

On the interaction of femtosecond laser pulses with layered dielectric materials

Présentée le 8 septembre 2023

Faculté des sciences et techniques de l'ingénieur
Laboratoire Galatea
Programme doctoral en manufacturing

pour l'obtention du grade de Docteur ès Sciences

par

Ruben RICCA

Acceptée sur proposition du jury

Prof. V. Michaud, présidente du jury
Prof. Y. Bellouard, directeur de thèse
Prof. P. Kazansky, rapporteur
Prof. S. Juodkazis, rapporteur
Dr A. Hessler-Wyser, rapporteuse

*Considerate la vostra semenza:
fatti non foste a viver come bruti,
ma per seguir virtute e canoscenza.*

Versi 118-120, Canto XXVI, Inferno, Commedia

Dedicated to my family...

Acknowledgements

I am deeply grateful to Prof. Yves Bellouard, my thesis supervisor, for welcoming me into his research group and supporting me throughout this four years-long journey. His guidance and vision were essential for the development of this project, providing mentorship on a topic that was novel to me. I also greatly appreciated his support for my career choices, which allowed me to expand my knowledge and experience outside of the specialized field of my PhD thesis.

I would like to thank the thesis committee, Prof. Véronique Michaud, Dr. Aïcha Hessler-Wyser, Prof. Peter Kazansky, and Prof. Saulius Juodkazis, for their meticulous work, their availability and their precious feedback. I would also like to thank the Swiss National Science Foundation for funding this research project.

I would like to extend my acknowledgements to the people at LCAV, notably Prof. Martin Vetterli, Dr. Michalina Pacholska, Dr. Adam Scholefield, Dr. Julien Fageot and doctors-in-progress Sepand Kashani and Eric Bezzam, for the fruitful discussions and the helpful suggestions in the framework of the *femtoLippmann* project collaboration, which is at the foundation of this thesis, and for introducing me to the world of signal processing. I would also like to thank the members of the *ClosedLoopLM* collaboration, especially Dr. Larissa Boie, for their support during the experiments at the μ -XAS beamline.

I am also grateful to various staff members at EPFL, who assisted me during experimental work, notably Dr. Richard Gaal, Dr. Arnaud Magrez and Dr. Wen Hua Bi, for their support during the use of their Raman and XRD equipment, Dr. Nicolas Descharmes, Dr. Raphaël Barbey and Joël Spitznagel, for the deposition of some of the samples studied in this manuscript, Dr. Cyril Cayron, Mathijs van der Meer and Priscille Bôle, for their support on the equipment at LMTM facilities, and the staff at CMi, notably Joffrey Pernollet, for his support on the focused ion beam. I would also like to thank Dr. Simone Frasca, for his help with sample depositions and for the discussions in the BM's guest room, and Dr. Francesco Gramuglia, for the insightful conversations and the crispy arancine.

This thesis heavily relies on the use of electron microscopy techniques. Henceforth, this would not have been possible without the precious help from the people at CIME, notably Dr. Lucie Navratilova and Dr. Rita Therisod, who trained me on the microscopes and gave valuable suggestions for the taming of these complex machines. I am also grateful to Dr. Victor Boureau,

Acknowledgements

with whom I spent many hours performing TEM observations, and who contributed to this work by sharing his vast knowledge on electron microscopy.

I had the opportunity of spending these years with amazing lab mates. First, I am grateful to Dr. Julien Gateau, with whom I collaborated in the framework of the *femtoLippmann* project during the first couple of years of PhD, and who patiently thought me many of the practical and theoretical skills needed in an optics lab. I also thank Dr. Olivier Bernard, for his side job as a laser nurse and for being a reliable *apéritif* buddy, and Dr. Gözden Torun, for sharing her knowledge in materials science and for the emotional support (and for baklava, of course). Ernesto Gribaudo, for the talks and for sharing the responsibilities of the SLM-task force, Dr. Antoine Delgoffe and Dr. Benedikt Hermann, for their resourceful comments and ideas, Samuel Benketaf and Dr. Daniel Talán Echarri for their support, as well as the former staff of Galatea, all of whom have enriched my life here in Neuchâtel: Dr. Enrico Casamenti, Dr. Pieter Vlugter, Dr. Saood Nazir, Dr. Arunkrishnan Radhakrishnan, Dr. Margarita Lesik, Dr. Andrea Kraxner, Dr. Manon Tardif, Dr. Tanveer Islam, Samuel Rey and Sacha Pollonghini, and finally our guest from distant lands, Dr. Daijiro Tokunaga. Also, I would like to thank Josiane Pachoud, who very efficiently solved all sorts of administrative nightmares. A special thank you goes to Antoine, Benedikt and Daniel for proofreading this manuscript and for providing insightful feedback on its content.

As a wise man once said, "*rire, c'est bon pour la santé*". I would add that surrounding ourselves with good people is determining for our own well-being and for maintaining an impression of sanity. For this reason, I would like to use these last lines to express my deep gratitude to my friends near and far, to the trio of the *sagra* Nicola, Pietro and Frankie, to the extended family of the *Rolex* gang Giulia, Lorenz, Flo, Moreno, Prisca, Nicolzza and Ale, and also to Viola, for her enduring support. To Lucile, for being a reliable friend and for the mountain adventures, and to the *herd*, Jack, Vanni, Paola, Gianni, Vasco, Ettore, Ollo, Idro, Silvio, Nich and Alex, for lifelong friendship and for the time spent together, throwing dices, listening to loud music and being worry-less. I am also infinitely grateful to Annika, for her grounding presence and support during the most intense days of this PhD, for the the visits to the yurts and for being a wonderful person overall.

I owe an immense debt of gratitude to my parents Felice and Irene, for their unwavering support, guidance, and love throughout my life, and to my brother Rossano, my steadfast companion and appointed *consul in aeternum*, for always being at my side. This work is dedicated to them.

Last, I want to express my sincere gratitude to everyone who has contributed to this journey, no matter how small their role, and who I may not have acknowledged explicitly in this text.

Lausanne, June 26, 2023

Ruben Ricca

Abstract

Materials properties are strictly dependent on their microstructure. The internal symmetries and the disposition of the constituting atoms of a material, which depend on its crystallographic structure, greatly affect its response to mechanical, electromagnetic and thermal stimuli. This dependence is notably exploited for the conception and fabrication of heterogeneous materials, where the coexistence of different components results in improved physical properties, or in the development of novel capabilities.

Here, we investigate the formation process of heterogeneous phases within dielectric multilayer structures, mediated through the exposure to femtosecond lasers. Thanks to the tight confinement of energy and the electric field-modulating effect of the layers themselves, laser exposure of layered dielectrics enables the localized formation of crystallites within the laser-affected area, effectively changing the material's properties at a microscopic scale.

The manuscript starts with a general introduction on the state of matter and on the fundamentals of femtosecond laser machining, providing the context of our research, the current state-of-the-art in thin films laser processing and explaining the experimental approach of the thesis. Given the complexity of these materials systems, a section of the manuscript is also consecrated to the illustration of the computational methods used in this thesis in order to calculate the propagation of light through the multilayer structures.

The occurrence of laser-induced crystallization is then studied more in detail, and the observation of extreme confinement of this modification type along the beam propagation axis is discussed. Specifically, it is shown that the multilayer structure is responsible for the modulation of the laser's electric field, which then results in localized energy maxima, promoting the confinement of the modifications. The investigation of such buried nano-structures with Third Harmonic Generation microscopy will also be discussed, as this non-destructive method enables fast and repeatable characterization of laser-processed samples.

Although femtosecond processing of dielectrics is, at the single pulse level, a non-thermal phenomenon, the accumulation of pulses at high repetition rates results in the observation of a thermal regime, where thermal relaxation occurs over the same, or longer, timescale than the inter-pulse time interval. To this end, this work also investigates the influence of thermal effects on crystallization, and traces a comparison between two different crystallization

Abstract

regimes, one based on non-linear absorption (with and without thermal influences) and a second one relying on linear absorption through exposure to a continuous-wave laser.

Finally, a case study illustrating the use of femtosecond lasers for phase engineering in the $\text{Al}_2\text{O}_3/\text{Nb}_2\text{O}_5$ multilayer system is presented, showcasing the nature of the laser-induced modifications.

In summary, this thesis offers a contribution towards a better understanding of the laser-matter interaction between femtosecond laser beams and multilayer dielectric materials. This is done with a particular focus on the modalities of laser-induced crystallization, and on the confinement of such material's modifications along the laser beam propagation direction.

Keywords: femtosecond laser, multilayer dielectric materials, phase transitions, electron microscopy, crystallization

Riassunto

Le proprietà dei materiali dipendono strettamente dalla loro microstruttura. Le simmetrie interne e la disposizione degli atomi costituenti un materiale, che dipendono dalla struttura cristallografica del materiale stesso, influenzano notevolmente la sua risposta a stimoli meccanici, elettromagnetici e termici. Questa dipendenza è sfruttata in modo significativo nella progettazione e fabbricazione di materiali eterogenei, in cui la coesistenza di diversi componenti porta ad un miglioramento delle proprietà fisiche o allo sviluppo di nuove funzionalità.

In questo studio, viene investigato il processo di formazione di fasi eterogenee all'interno di strutture stratificate di materiali dielettrici, mediato tramite l'esposizione a laser a femtosecondi. Grazie al confinamento dell'energia e all'effetto di modulazione del campo elettrico della pulsazione laser, derivante dalla struttura stessa dei materiali multistrato, l'esposizione laser di questi materiali consente la formazione localizzata di cristalli all'interno dell'area colpita dal laser, modificando efficacemente le proprietà del materiale su scala microscopica.

Questo manoscritto inizia con un'introduzione generale sulle proprietà della materia e sui fondamenti della fabbricazione con laser a femtosecondi, fornendo il contesto della nostra ricerca, illustrando lo stato dell'arte attuale nella lavorazione laser di film sottili e spiegando l'approccio sperimentale della tesi. Date le complessità di questi sistemi di materiali, una sezione del manoscritto è dedicata all'illustrazione dei metodi computazionali utilizzati per calcolare la propagazione della luce attraverso le strutture multistrato.

Il fenomeno della cristallizzazione indotta dal laser viene poi studiato in modo più dettagliato, così come viene discussa l'osservazione del confinamento di questo tipo di modifica lungo l'asse di propagazione del fascio laser. In particolare, viene discusso come il design della struttura multistrato è responsabile della modulazione del campo elettrico del laser, risultando nella localizzazione di massimi di energia in punti specifici della struttura, promuovendo il confinamento delle modifiche. Viene inoltre presentato l'utilizzo di tecniche di microscopia THG (Third Harmonic Generation) per l'investigazione di tali nanostrutture, in quanto questo metodo non distruttivo consente una caratterizzazione rapida e ripetibile dei campioni esposti al fascio laser.

Sebbene il trattamento con laser a femtosecondi di materiali dielettrici sia, a livello di un singolo impulso, un fenomeno non termico, l'accumulo di impulsi ad alta frequenza di ripe-

Riassunto

tizione porta all'osservazione di un regime termico, in cui il rilassamento termico avviene in un intervallo di tempo uguale o maggiore all'intervallo di tempo tra gli impulsi. A tal fine, questo lavoro investiga anche l'influenza degli effetti termici sui fenomeni di cristallizzazione e traccia un confronto tra due regimi di cristallizzazione diversi: uno basato sull'assorbimento non lineare (con e senza influenze termiche) e un secondo basato sull'assorbimento lineare attraverso l'esposizione ad un laser a onda continua.

Infine, viene presentato un esempio di applicazione dei laser a femtosecondi per il controllo delle fasi nel sistema multistrato composto da film sottili di Al_2O_3 e Nb_2O_5 , mostrando la natura delle modifiche indotte dal laser.

In sintesi, questa tesi offre un contributo per una migliore comprensione dell'interazione tra laser a femtosecondi e materiali dielettrici multistrato. Ciò viene fatto con particolare attenzione sulle modalità di cristallizzazione e sul confinamento di tali modifiche lungo la direzione di propagazione del fascio laser.

Parole chiave: laser a femtosecondi, materiali dielettrici stratificati, trasformazioni di fase, microscopia elettronica, cristallizzazione

Contents

Acknowledgements	i
Abstract (English/Italiano)	iii
1 Introduction	1
1.1 The nature of matter, and how to control materials properties	1
1.2 Heterogeneous, structured and multilayer materials	4
1.3 Femtosecond laser processing of dielectrics	6
1.4 Femtosecond laser-matter interaction in thin films	10
1.5 Thesis objectives and outline of the manuscript	13
I Methods	15
2 Light propagation through multilayer materials	17
2.1 Reflectance of layered media: computation with transfer matrix method	18
2.2 Pulse propagation simulations with FDTD	23
2.2.1 Examples of FDTD simulations	26
2.3 Summary	28
3 Experimental methods	29
3.1 Materials selection process	29
3.2 Multilayer fabrication process	31
3.3 Femtosecond laser processing setup	34
3.4 Electron microscopy and sample preparation by focused ion beam	38
3.5 Summary	43
II Experimental results	45
4 Modalities of laser-matter interaction in dielectric multilayers	47
4.1 Introduction	47
4.2 Experimental methods	48
4.3 Layer ablation	49
4.4 Evidence of laser-induced phase transitions	51

Contents

4.5	Inter-layer atomic intermixing	58
4.6	Ablation residues	60
4.7	Discussion	62
4.8	Summary	64
5	Laser-induced confined crystallization in multilayer systems	67
5.1	Introduction	67
5.1.1	Confined modifications in multilayers	68
5.2	Sample fabrication and experimental methods	70
5.2.1	Sample design, preparation and processing	70
5.2.2	Third Harmonic measurement principle	71
5.3	Nanometric confinement of the modifications	72
5.4	Modelling of pulse propagation	78
5.5	THG imaging of modified multilayers	81
5.6	Case studies for modifications confinement	84
5.7	Discussion	88
5.8	Summary	90
6	Crystallization dynamics and dependence on thermal regime	93
6.1	Introduction	93
6.1.1	Ionizing versus non-ionizing exposure conditions	93
6.2	Materials and methods	94
6.3	Experimental results	95
6.3.1	Femtosecond laser exposure at low and high repetition rate	95
6.3.2	CO laser exposure	99
6.4	Discussion	107
6.5	Summary	113
7	Case study: phase engineering in the Al₂O₃/Nb₂O₅ multilayer system	115
7.1	Introduction	115
7.2	Sample design and fabrication	117
7.3	Experimental results	118
7.4	Discussion	123
7.5	Summary	124
III	Conclusions	125
8	Conclusions and outlooks	127
8.1	Main results	128
8.2	Future outlooks and potential applications	129
8.3	Personal contributions	132
A	Samples thickness profiles	133

B Raman spectroscopy	135
Bibliography	137
Curriculum Vitae	157

1 Introduction

1.1 The nature of matter, and how to control materials properties

The nature of the universe, and the composition of the world surrounding us, have been fascinating humanity for millennia. At a time when scientific curiosity and philosophical activity often coincided, civilisations around the globe hypothesized that the constituting materials of the universe, with which we interact through our senses, were in fact composed by smaller units, whose composition, combination, concentration and distribution resulted in the different substances and materials populating the world. Earliest theories included the separation of all things into a restricted group of elements, such as fire or water, whose difference in proportions would result in the different physical aspects and properties of different materials.

Going further than this, the discretization of the world in smaller units of matter was famously proposed by the Greek philosophers Leucippus and Democritus, who suggested the existence of small, *indivisible* particles (in Greek $\alpha\text{-τομ\omicron}\nu$, or in-divisible) [1], which varied in shape and size, and that were considered to be constantly in motion. These atoms would be the fundamental building blocks of matter. With the formulation of more rigorous protocols for scientific research in the 19th century, more accurate models were proposed, in parallel with the establishment of the periodic table of the elements. It is known, today, that atoms are in fact composed by a variety of sub-atomic particles. That being said, in the vast majority of cases, to study the physical properties of materials it is sufficient to consider matter as composed by arrays of atoms, who themselves consist of a positively charged nucleus, surrounded by a negatively charged electron cloud. As a result, it is known that the atomic arrangement within a material has a great influence on its physical and chemical properties, and can generally be described as ordered or disordered.

Ordered systems are referred to as *crystalline*, and consist of a basic unit cell repeating periodically and infinitely, on all directions, on a lattice (see Fig. 1.1a). Mathematically, seven different crystal systems can be defined, and crystalline materials can therefore be described according to their lattice system, according to Bravais notation, and to their space group,

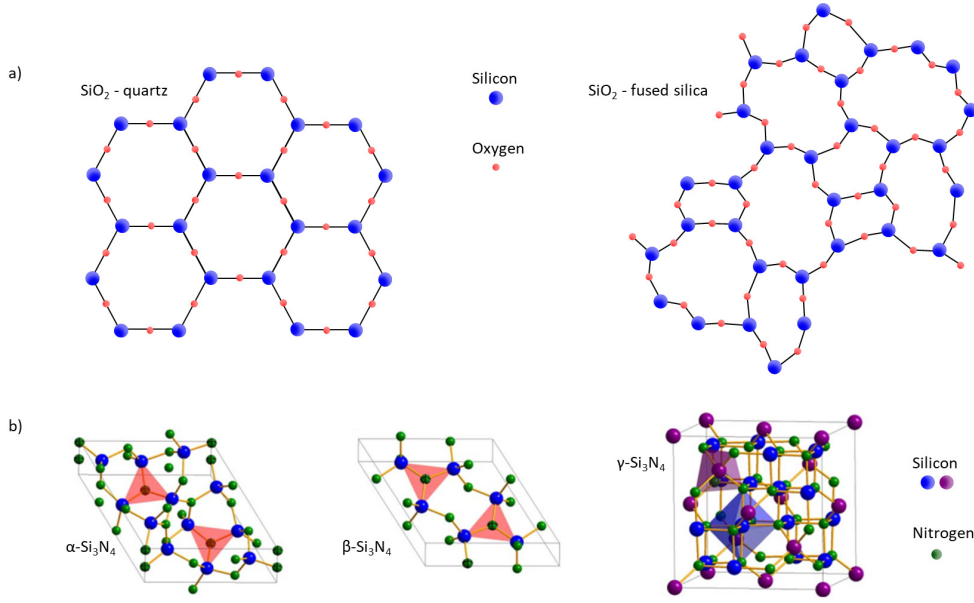


Figure 1.1: Illustration of polymorphism in materials. a) Crystalline (ordered) and amorphous (disordered) structures of SiO₂. b) Representation of the α, β and γ polymorphs of crystalline Si₃N₄, figures adapted from [2].

which defines the crystal symmetry. Crystalline materials can possess a very high degree of homogeneity, with well aligned atoms across the whole volume of the material (although with the possible presence of minor defects such as dislocations), in which case they are defined as *mono-crystalline*. Conversely, if the material is composed by multiple regions of differently oriented atoms (grains), the material is referred to as *poly-crystalline*. Crystals typically exhibit some degree of anisotropy, so that the ordering of atoms within the volume of a crystalline material affects the symmetry of its response to external stimuli, like mechanical forces or thermal gradients, according to the Curie-Neumann principle. This principle states that the symmetry operations of the physical properties of a material are included within the symmetry operations of its crystallographic structure, establishing a causal link between microstructure and physical properties. As a consequence, it is then possible to deduce many properties of a given compound by studying its microstructure. This principle simplifies the analysis of materials, for instance during tensorial calculations, as many elements of the tensors can be equalized or are equal to 0, depending on the crystals' geometry. An example of this phenomenon is visible in Eq. 1.1, where the second rank permittivity tensor describing the property of birefringence can be simplified once the crystal structure of the material is known (in this case, a material belonging to the cubic $m\bar{3}m$ space group).

$$\begin{bmatrix} K_{11} & K_{12} & K_{13} \\ K_{21} & K_{22} & K_{23} \\ K_{31} & K_{32} & K_{33} \end{bmatrix} \longrightarrow \begin{bmatrix} K & 0 & 0 \\ & K & 0 \\ & & K \end{bmatrix} \quad (1.1)$$

1.1 The nature of matter, and how to control materials properties

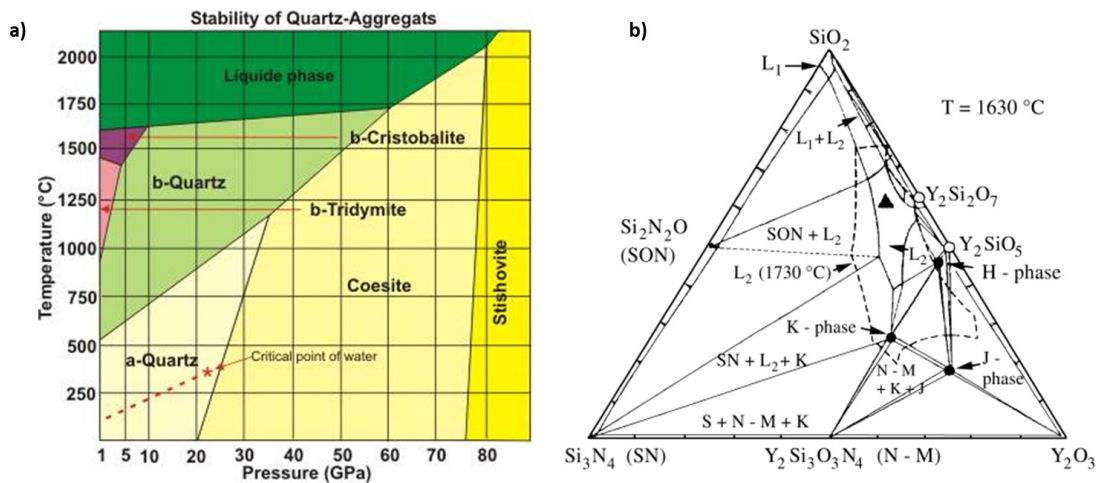


Figure 1.2: a) Pressure-temperature phase diagram of SiO₂ [3], showing thermodynamically stable phases for any given value of pressure and temperature. b) Ternary phase diagram of the SiO₂-Si₃N₄-Y₂O₃ materials system, at a temperature of 1630°C [4].

Conversely, *amorphous* materials lack long-distance order in their structure, effectively resulting in a disordered succession of atomic bonds, as visible in Fig. 1.1b. Due to the absence of well defined atomic planes, amorphous materials are isotropic, in that responses to external solicitations are independent from the material orientation.

Compounds of equal stoichiometric composition can exhibit radically different atomic arrangements, giving rise to a variety of *polymorphs*, which are material phases of same compositions, but different microstructures. Fig. 1.1c shows an example of such polymorphism, illustrating how crystalline Si₃N₄ can take different forms. Through modelling and experimental verification, it is possible to establish phase diagrams, showing the most thermodynamically stable phase of a given material within an interval of pressures and temperatures, for instance as shown in Fig.1.2a. In this specific example, it is possible to estimate the prevalence of a specific polymorphic phase of SiO₂ depending on experimental conditions. By combining information on multiple atomic species (or materials systems), one can also produce phase diagrams showing alloy phases and intermetallics formation as function of temperature (or, less often, pressure) and chemical composition. One such example is visible in Fig.1.2b, where a ternary phase diagram for the system SiO₂-Si₃N₄-Y₂O₃ shows the thermodynamically stable phases for any possible composition, at a temperature of 1630°C.

Depending on their composition and their thermodynamic properties, different compounds have different numbers of distinct phases. By locally inducing specific phase transitions in selected areas, it is possible to design materials with heterogeneous phase distributions, resulting in the presence of multiple, different phases, enabling the functionalization of different areas of the material. Consequently, materials systems with a large number of polymorphs or binary compounds are particularly suited for this type of processing.

1.2 Heterogeneous, structured and multilayer materials

Given the structural dependence of materials' responses, by controlling the microstructure of a material, it is possible to govern its physical properties and tailor them to suit desired applications. This control can be achieved in multiple ways. For instance, the microstructure of a crystal can be modified by introducing or removing defects, grain boundaries and precipitates, as done for example in metallurgical processes [5]. Additionally, semiconductor materials can be doped by introducing controlled amounts of impurities, which change the electrical properties of the material as a whole, while materials like quantum dots exploit the high surface-to-volume ratio (a result of their nanometric size) to improve their optical and electrical properties [6]. On a larger scale, composite materials, typically consisting of the combination of at least two distinct and homogeneous materials, enable the improvement of physical properties of both the matrix and the inclusions, resulting in new, better performing materials, the most notorious examples being concrete [7] and fibre-reinforced plastics [8].

Materials' structuring is widely exploited in optics and photonics as well, as it enables the fine tuning of the effective refractive index, and therefore the transmitting and light guiding properties of materials. This structuring can be topological instead than based on composition, as is the case of structural colouration, where the reflectance of an object is not determined by pigments, but rather by the surface's structure, whose conformation acts as a photonic crystal [9]. A relevant example of structural colouring can be found in the bright colors of the *Morpho* butterfly wings, which are caused by the scattering of incoming light from the scaled, lamellar structure of the wing's surface [10].

In the field of photonics, specifically, the need for the fabrication of mirrors and anti-reflective coatings promoted the use of dielectric thin films, and more specifically of multilayered structures. This class of optical components has several advantages over metallic mirrors, such as a higher damage threshold, making them suitable for applications involving higher peak power lasers, and tunable reflectance spectra. Depending on the application of choice, sequential depositions of dielectric thin films result in stacks of layers with arbitrary composition and thickness design. The number, nature and composition of the layers and of their interfaces influence the way the material reflects light. For instance, periodically spaced layers with regular thicknesses, like the distributed Bragg reflector (DBR) exemplified in Fig. 1.3a, can be designed to reflect a precise frequency bandwidth. The optical properties of these layered structures can be tuned by changing the layers composition and geometry, as shown, for instance, in the double DBR structure in Fig. 1.3b. Consequently, different multilayer designs result in different reflectance properties, and it is therefore possible to design narrow- or broad-band mirrors, chirped mirrors or filters by selecting the appropriate materials and layer thickness distribution [11].

Such multilayered structures have also been investigated as candidates for the controlled fabrication of nanocrystallites in solid matrices. For instance, intermixing phenomena in multilayers have been reported through thermal annealing processing, in metallic [16] or

1.2 Heterogeneous, structured and multilayer materials

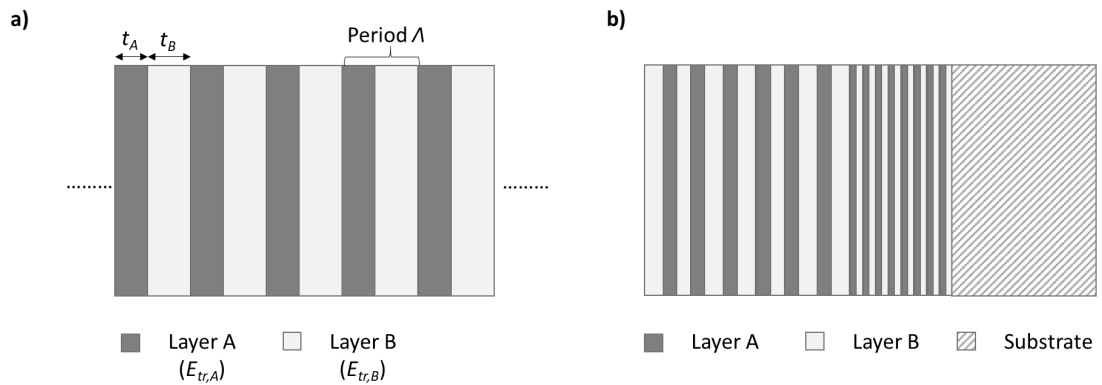


Figure 1.3: Schemes of dielectric multilayer samples. a) Distributed Bragg reflector, consisting of alternating layers of thickness t_A and t_B , repeating with a periodicity Λ . Layers A and B are composed by different materials, therefore have different values of refractive index and non-linear absorption threshold $E_{tr,i}$. b) Alternative design of multilayer sample, consisting of two Bragg reflectors of different periodicity and layers' thickness, stacked on top of each other and deposited on a substrate.

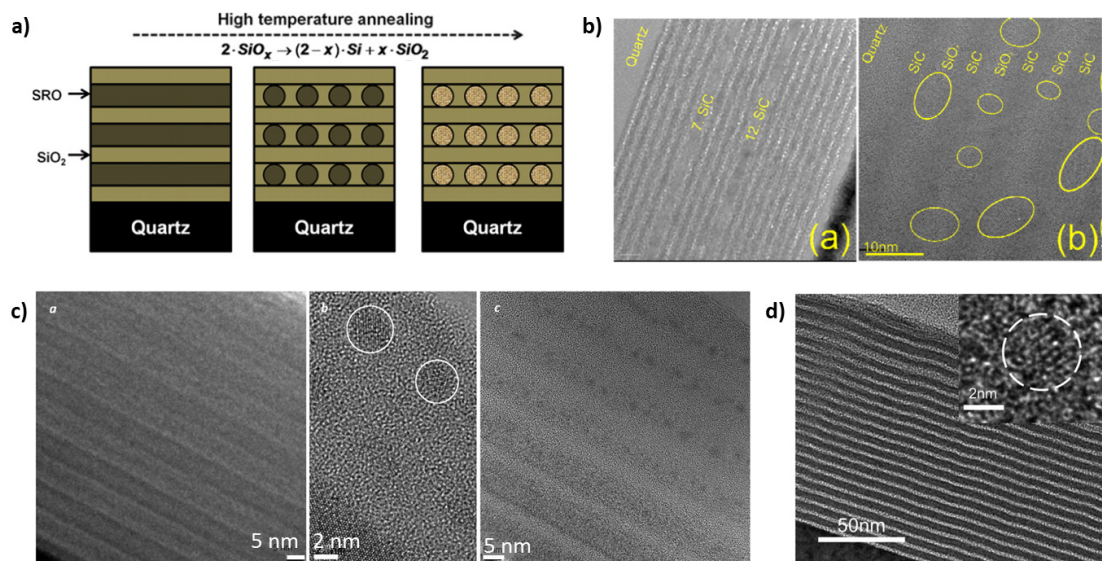


Figure 1.4: Examples of techniques for the processing of multilayer materials, in order to induce the formation of crystallites. a) Schematics of thermal annealing, illustrating the pathway for phase transformation of SiO_2 and Si-rich SiO_2 (SRO) into a mix of Si and SiO_2 regions [12], and b) transmission electron microscope image of post-annealing material, showing evidence of crystallization in SiO_2 -SiC heterostructures [13]. Other images show examples of c) ion bombardment in Si-SiO₂ structures [14] and d) excimer laser processing of Si-SiC multilayers [15]. Scalebars in image c) have been adapted to increase visibility.

semiconducting substrates, like the case of the formation of silicon quantum dots in SiC/SiO_x hetero-super-lattices [13, 17] (see Fig. 1.4a and b). Other suitable techniques for materials modifications are ion-beam-induced crystallization [14] and exposure to excimer lasers radiation [15, 18], shown in Fig. 1.4c and d, respectively. Both alternatives, and laser technologies in particular, offer a more localized processing method than thermal annealing done in a furnace, and therefore are more versatile if the goal is to functionalize different sections of a same material, or if this process is to be done at smaller scales.

The formation of nanocrystalline phases in a dielectric host under intense laser field conditions is motivated by the interest in having nanocrystals dispersed in a transparent and amorphous matrix (effectively creating a composite material), in which the nanocrystals are used to locally control electrical and optical properties [19, 20]. In these mixed systems, the dielectric layer not only defines a flat optical interface, but also shields the nanocrystals from their surroundings, preventing environmental degradation. These composites are suitable for photonics [21], photovoltaics [22] and memory applications [23], but also meta-lenses, anti-counterfeiting marking and high-density data storage in durable materials, among other applications. In this context, an intermixing process consisting in forming a new material compound by mixing multiple, stacked layers of various compositions is particularly interesting, as it offers a potential means to obtain arbitrary crystal compositions. Here, the motivation would be to create nanoscale crystallites and densified zones at predefined locations within the layers' stack, while keeping the integrity of the surface. For instance, silicon and titanium oxide nanocrystals, which will be discussed later in the manuscript, are being investigated for applications as single-photon emitters [24], in electronics and photovoltaics [25] and biological applications [25, 26], and would be excellent candidates for this kind of processing.

1.3 Femtosecond laser processing of dielectrics

Laser processing can be an effective tool to locally tailor materials properties. In this framework, femtosecond lasers demonstrate a high versatility and application range [27], as a consequence of the non-linear absorption processes that they trigger.

Transparent materials, notably dielectrics, possess a non-linear absorption threshold, above which light is absorbed rather than transmitted. Given the large bandgap of dielectrics, multiple photons are needed to provide enough energy for an electron to be excited to the conduction band; hence, the process is triggered as soon as the light beam can provide enough energy density for the multiphoton non-linear absorption process to occur [28]. This is the case of tightly focused, short-pulsed femtosecond lasers, whose high peak-powers enable non-linear absorption at the focal spot, rather than along the whole optical path like in the case of linear absorption (see Fig. 1.5a), and can result in different modifications of the exposed materials, such as densification or self-organization of nanostructures. Several mechanisms have been proposed to explain the phenomenon of non-linear absorption in transparent materials,

1.3 Femtosecond laser processing of dielectrics

depending on laser parameters, deposited energies and materials. The three main mechanisms are multiphoton ionization (Fig. 1.5b), tunneling ionization (Fig. 1.5c) and avalanche ionization (Fig. 1.5d).

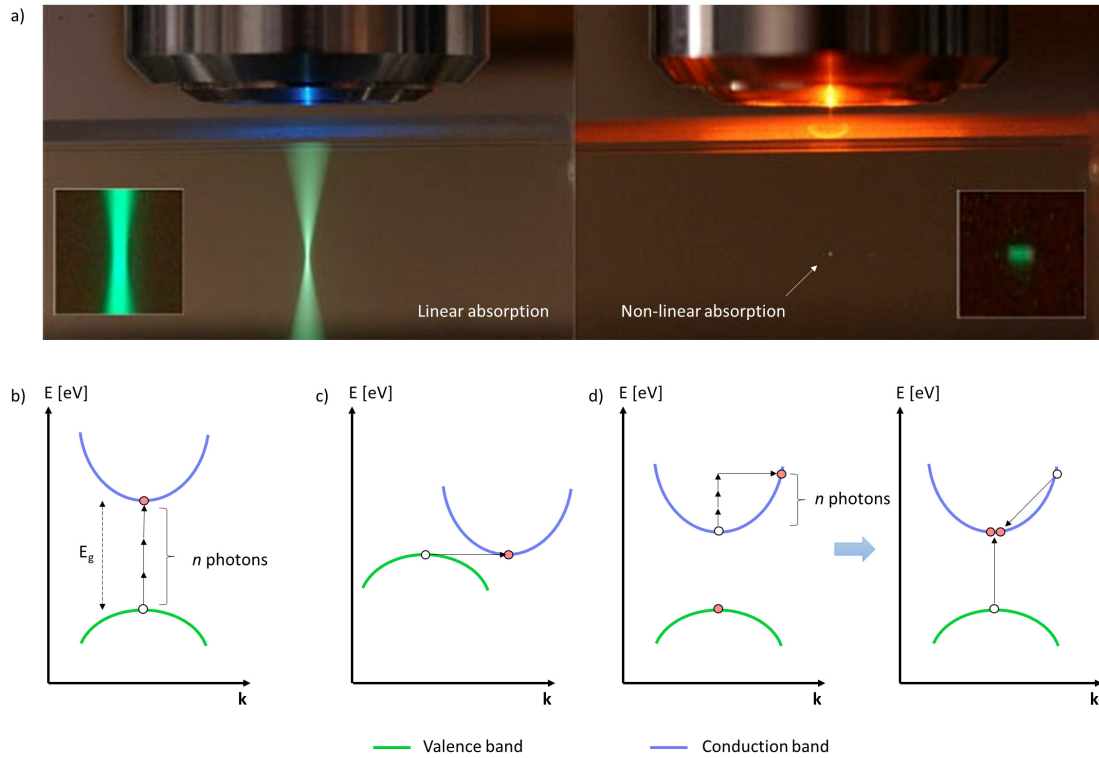


Figure 1.5: a) Representation of linear and non-linear absorption processes. Image adapted from [29]. The absorption mechanisms in dielectric materials during femtosecond laser exposure are shown below. b) Multiphoton ionization, c) tunneling ionization and d) avalanche ionization. Drawing based on an image from [27].

The first two ionization phenomena, commonly known as photoionization processes, are bandgap-dependent, and the dominance of one over the other is determined by the Keldysh parameter γ , which is proportional to the laser frequency and inversely proportional to the electric field amplitude. Around the threshold value of 1.5, both concurring mechanisms contribute to the ionization, but when the parameter value deviate from this figure, one of the two mechanisms becomes dominant [30]. Multiphoton ionization is the dominant mechanism at higher γ values, i.e. at lower intensity. As the name suggests, it consists of the absorption of multiple photons by a single electron, whose total energy matches the bandgap of the material. The higher the materials' bandgap, the larger the energy density needs to be, in order to trigger the non-linear absorption phenomenon. Notice that since the exposure of multilayers samples is done at low pulse energy, compared to the usual fluence values for the processing of bulk materials, we assume that multiphoton ionization is the dominant non-linear absorption mechanism in our case.

Introduction

For higher pulse energies (lower γ values) the ionization rate is rather controlled by tunneling ionization, where the potential well preventing the electrons to pass to the conduction band is reduced by the presence of the intense laser electric field, thus increasing the tunneling probability of the electrons and, therefore, enabling the ionization process to occur [28]. Avalanche ionization, on the other hand, is a two-step process consisting in a conduction band electron increasing its energy by photon absorption, ionizing in the process an electron of the valence band by direct collision. The “primary” electrons are promoted to the conduction band by heating defect centers, or because of previous multiphoton or tunneling ionization processes [28].

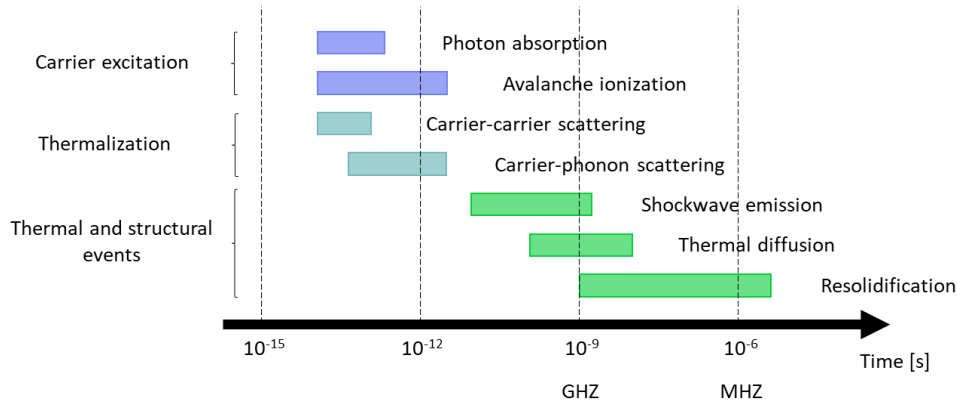


Figure 1.6: Schematic representation of physical phenomena induced by femtosecond laser exposure with a dielectric material, showing typical timescale ranges. Drawing based on an image from [31].

Regardless of the dominant process, the exposure to a femtosecond laser with energies above the non-linear absorption threshold results in the generation of a free electron gas (plasma) at the focal spot, which dramatically increases the temperature and pressure locally, thus allowing the transmission of energy from the electrons to the surrounding lattice through electron-electron collisions [32]. Given the short time-scale of this processes, the energy transfer is usually not phonon-mediated; hence, the modifications are limited to the focal spot and its immediate surroundings [33]. The time-scale of these events is an important parameter to consider; specifically, avalanche ionization has a greater role at longer pulse durations, since the pulse exposure interval is consistent with the carrier-phonon interaction timeframe, and therefore the electrons promoted to the conduction band by photoionization act as seed carriers for avalanche ionization [31]. It is also important to notice that the shape of the laser-affected zone, and specifically its symmetry properties, are a function of the pulse duration [34].

The full duration of the laser-induced effects goes well beyond the mere duration of the femtosecond pulse, which, as the name implies, is comprised between 10^{-15} and 10^{-12} s. As illustrated in Fig. 1.6, some physical phenomena can be initiated, and terminated, even microseconds after the onset of laser-matter interaction, representing a variation on the time-scale of up to 9 orders of magnitude. The extended time-scale of some of these physical

1.3 Femtosecond laser processing of dielectrics

phenomena, with respect to the pulse duration, is important to consider when dealing with laser-induced modifications.

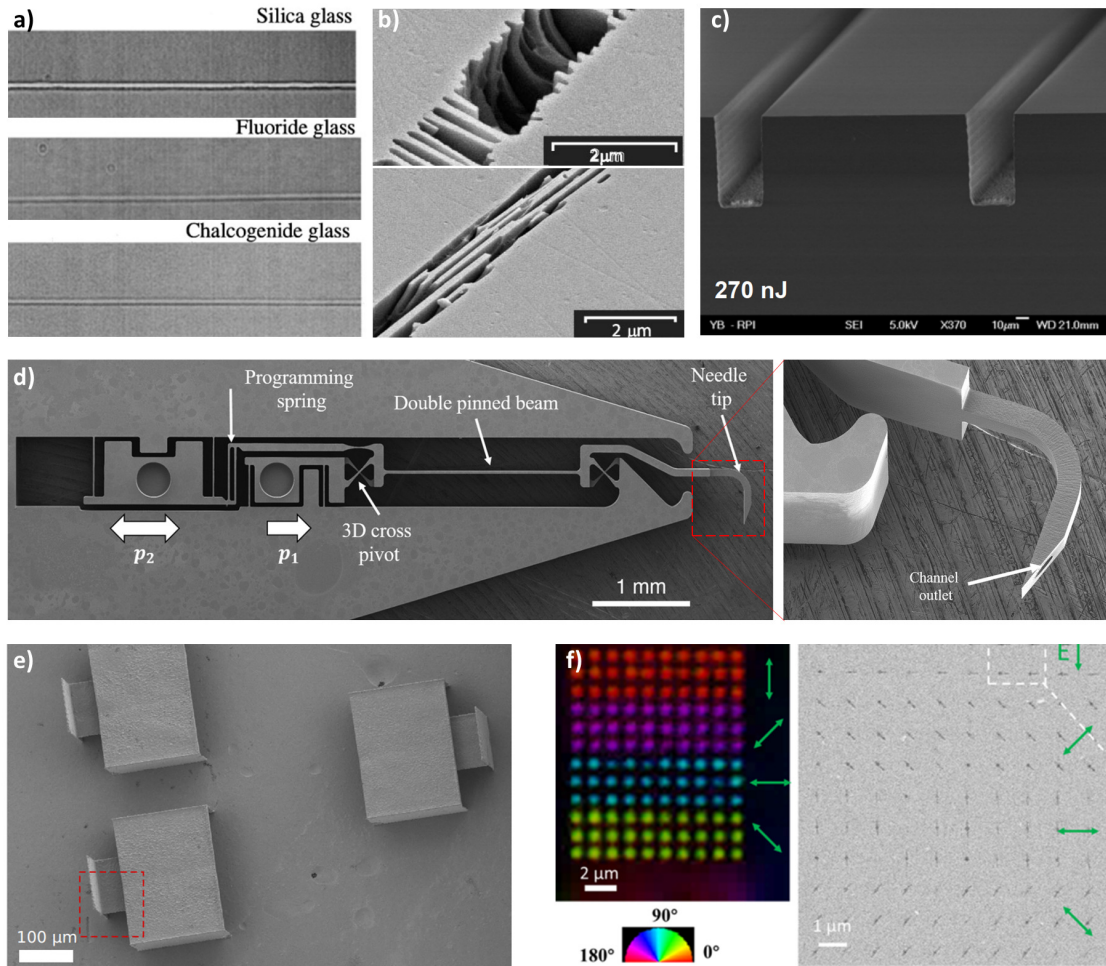


Figure 1.7: Examples of laser-induced modifications in dielectric materials, and their applications. a) Densification and creation of waveguides in different transparent materials [35]. b) Self-organization phenomenon (nano-gratings) in fused silica after exposure to a femtosecond laser, with polarization parallel (above) and perpendicular (below) to the writing direction [36]. c) Selective etching of laser-exposed fused silica in a HF solution [37]. This technique can be exploited for the fabrication of monolithic opto-mechanical devices, like the micro-needle shown in image d) [38]. This method can be combined with micro-infiltration of metals and glasses for casting, as exemplified by the metallic structures shown in e) [39]. f) Use of laser-induced modifications in fused silica as a potential data storage media [40].

The capability of femtosecond laser processing to deliver high peak power pulses into very localized volumes inside the materials' bulk enables a broad variety of technological and research applications: for instance, laser-induced densification has been successfully exploited for the direct writing of waveguides in a variety of glass systems [35], as visible in Fig. 1.7a, enabling the integration of waveguiding sections into optomechanical devices [41]. Self-organization phenomena, both in the bulk and at the surface of materials, have been reported [42, 43], where the laser's electric field discretizes the affected areas into regions of different

density or even composition, oriented according to the beam polarization state, like the nano-gratings visible in Fig. 1.7b [36]. Under certain irradiation conditions, laser processing can be coupled with chemical etching, resulting in the selective removal of the laser-exposed regions and the achievement of volumic micro-structuring, as shown in Fig. 1.7c [37]. If the laser-written pattern is developed into a specific design, this enables the conception and the fabrication of miniaturized and potentially extremely complex three-dimensional opto-electro-mechanical devices [44], like actuators [45], flexures (see Fig. 1.7d) [38], optical components [46] and microfluidic channels [47, 48]. Etching also open many possibilities for microcasting, both for the integration of other materials into the glass matrix [49], or for the use of the glass as a sacrificial mould [39], an example of which is shown in Fig. 1.7e. Finally, femtosecond laser machining is also an effective tool for writing nanometric-sized features, as exemplified by recent works in the framework of data storage research [40], like the image in Fig. 1.7f showing the retardance difference in laser-written features inside fused silica specimens.

1.4 Femtosecond laser-matter interaction in thin films

Femtosecond laser interaction with dielectric thin films differs from the case of bulk exposure, due the presence of multiple interfaces between the layers and with the substrate, resulting in the partial reflection of the beam. These interfaces disrupt the laser interaction process and introduce weak mechanical boundaries in proximity of, or at the laser-modified area. Laser-mediated nanostructuring of thin films has been studied with the goal of creating devices [50], an example of which is shown in Fig. 1.8a, where a thin film of silicon nitride is selectively ablated by exploiting the interference pattern created by the pulse reflecting from the substrate. In manufacturing, the effects of the absorption-induced shockwave on the ejection of the films were exploited to develop a deposition method called laser-induced forward transfer (LIFT), enabling localized deposition of a variety of compounds, as can be seen in Fig. 1.8b. In a related application, thin films are used as sacrificial materials for the structuring of a substrate's surface, for instance to improve the quality of laser-induced periodic surface structures (LIPSS) [51].

Dielectric mirrors are an important example of technological application of multilayer dielectric materials. This class of mirrors provides higher reflectance yields than metallic mirrors at the expense of a narrower frequency bandwidth, and is at the core of laser applications due to the tunable properties of the multilayers. Because of the technological importance of these optical components, there is a relatively large body of literature on the laser induced damage threshold (LIDT) of these structures upon exposure to femtosecond laser pulses. It has been reported that the intensity of the laser's electric field along the multilayer stack, which takes the form of a standing wave, can be computed and optimized to reduce its intensity at selected locations. The electric field intensity is, in fact, periodically modulated along the propagation axis according to the stack geometry and composition, and presents intensity minima and maxima. The weakest points of the multilayers are the interfaces and, due to

their lower bandgaps, the high index materials [52, 53]. This modulation can therefore be modified by changing the layers design, away from the usual quarter-wave ($\lambda/4$) design, where the thickness of each individual layer is proportional to one quarter of the wavelength. This change in design can result in a shift of the intensity peaks towards the low-index layers [54–58] (see Fig. 1.8d). The role of pits, scratches and defects in enhancing the electric field intensity has also been studied [59–61] (as shown for example in Fig. 1.8c, where the effect of defects on the energy bands of the material is explained), together with methods for reducing it [62]. The role of laser and materials parameters on the modifications [62, 63], as well as the dynamics of the laser-matter interaction [64, 65], have been investigated. The refractive index (constant and modification-dependent), the interlayer stress-state as well as geometrical parameters like thickness and number of layers have been linked with the intensity profile of the electric field, therefore with the materials modifications as well.

To better control the optical properties of such structures, the modes of interaction of a propagating electromagnetic wave through the layers' stack can be modeled. Given a periodic arrangement of alternating layers of different materials, due to the rotational symmetry with respect to the horizontal plane, a multilayer structure can be considered as a one-dimensional photonic crystal, whose dielectric function only varies along the vertical axis [66]. Therefore, the reflectance and transmittance of periodic multilayers can be modeled like a Bragg reflector [67]. However, it should be noticed that, in the case of femtosecond laser exposure, the different non-linear responses of the layers result in a higher level of complexity of the system, since the light is not only reflected or transmitted, but can also be absorbed through non-linear absorption mechanisms, if an energy threshold is overcome.

The crystallization dynamics of dielectric materials after exposure to femtosecond laser radiation is a source of debate, as the process itself is outside of thermodynamic equilibrium. Laser-induced crystallization has been studied in semiconductor films, notably on amorphous silicon [71], where uniform and localized crystallization could be induced, and germanium [72], where the suggested crystallization mechanism is linked to the preferential absorption of IR radiation by the Ge nanoclusters. Crystallization phenomena in semiconducting multilayers was also studied in [73], where the crystallization of Ge is linked to the destabilization of the lattice due to the local increase in temperature, and to the mismatch in thermal expansion coefficient between the two constituting materials. A previous study linked the crystallization of TiO_2 to the effect of local lattice defects, which act as nucleation points after localized laser-induced heating [74]. Here, however, it must be noticed that the light source used in this study was a continuous laser; consequently, thermal effects were predominant, with respect to the femtosecond case. Other studies were performed on bulk glass substrates using pulsed lasers in the picosecond regime, and have been linked to a thermal gradient as well [75], which is believed to induce a phase separation. Finally, Liu *et al.* [76] postulated a crystallization process mediated by local temperature gradients through thermal accumulation, in the femtosecond regime. Overall, the number of studies related to femtosecond lasers interaction with thin films reported in the literature remains limited.

Introduction

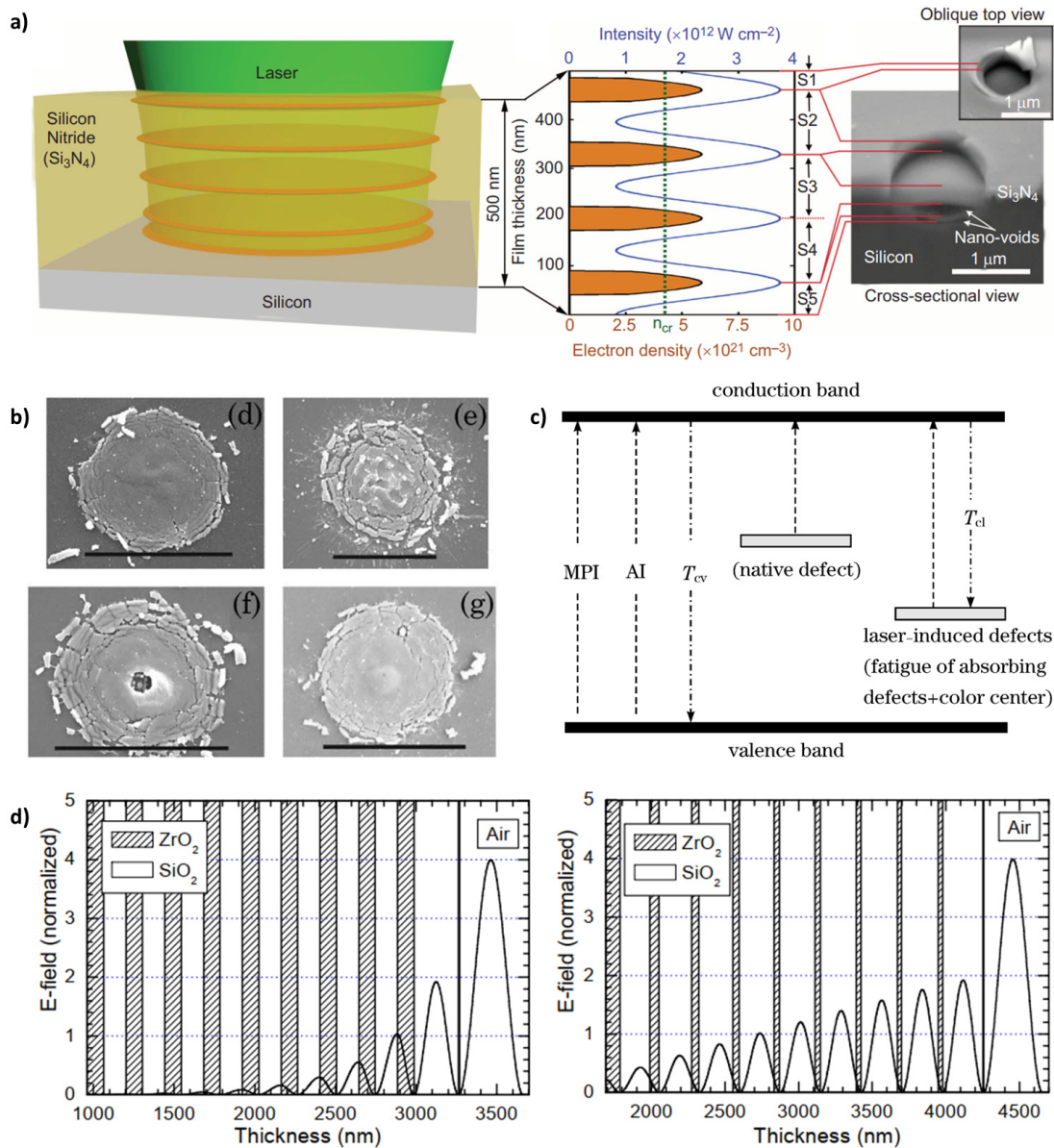


Figure 1.8: Examples from the literature, concerning the femtosecond laser processing of thin films and multilayer structures. a) Selective ablation of Si_3N_4 thin film for microfabrication [50]. b) Dielectric thin films deposited by laser-induced forward transfer [68]. c) Schematics of the effect of native and laser-induced defects on the laser-induced damage threshold of a multilayer, which introduce intermediate energy levels in the band structure [69]. d) Variation of the laser's electric field modulation after multilayer design change [70].

To summarize what has been presented so far, there is an interest in developing methods for phase engineering in materials, to optimize their optical, electric and mechanical properties: to this end, heterogeneous materials are a good foundation, as their structure can already be designed according to the prospective process. More precisely, multilayer materials offer the possibility of depositing a wide range of compounds, which can be combined according to

the desired final process output. A generalised processing method for this class of materials, with the capability of selectively modifying localized spots of the sample, and with a large range of tunable parameters, would be a versatile asset. Therefore, we suggest a laser processing method based on the exposure of structured, layered stacks of dielectric materials to a femtosecond laser, enabling localized and non-thermal modifications of the laser-exposed regions.

1.5 Thesis objectives and outline of the manuscript

This thesis aims at exploring purposeful laser-induced modifications of multilayer dielectric materials. The research plan is modelled around three main goals:

1. Describe the taxonomy of modifications that can be obtained by exposing dielectric multilayers to femtosecond lasers.
2. Investigate the modification dynamics by studying the influence of cumulative regimes on the modalities of phase transitions.
3. Demonstrate the possibility of introducing confined modifications within the layers stack, with nanometric dimensions, along the optical axis.

In addition, case studies on specific materials systems are presented, to provide illustrative examples of the peculiarities of this particular class of laser-matter interaction.

Following this introductory chapter, the second one introduces the theoretical background for the study of light propagation through multilayered structures. The focus is put on the computational methods used to calculate the reflectance of these structures, as well as to simulate the propagation of an electromagnetic field through the layers.

The third chapter illustrates the experimental methodology used in this work. Important information for the design of the layers and the choice of the constituting materials are presented, and the fabrication process of the samples is explained. This is followed by a description of the femtosecond laser exposure protocols and setup. As extensive use of electron microscopy techniques was made during this work, theoretical elements needed for the understanding of these results are introduced at the end of the chapter.

A review of the obtained materials modifications is presented in chapter four, where different outcomes of multilayer-laser interaction are presented with experimental evidence, and discussed with respect to the exposure parameters. Specifically, occurrences of surface ablation, atomic intermixing and crystallization are discussed.

The fifth chapter delves deeper into the study of laser-induced phase transitions, more precisely on the spatial confinement of nano-crystallization within the originally amorphous

Introduction

layers, and on THG microscopy, a non-destructive technique that can be used to detect the occurrence of tightly confined, sub-surface features.

This is followed by a sixth chapter focusing on the influence of thermal phenomena on the dynamics of crystallization, showing a comparison between laser-induced modifications obtained with femtosecond and continuous-wave lasers.

The seventh chapter presents a case study: the $\text{Al}_2\text{O}_3/\text{Nb}_2\text{O}_5$ materials system, its potential technological applications and the modalities of laser-based crystallization processes applied to this multilayer system.

Finally, the last chapter summarizes our findings, offering a comprehensive overview of the research on femtosecond laser-induced modifications in dielectric multilayers conducted over the course of the thesis, as well as the potential uses of these findings in academia, industry and for technological applications.

Methods **Part I**

2 Light propagation through multilayer materials

The development of ultrashort laser pulses has been a game-changing progress, with applications in waveguide writing, surface structuring, for the fabrication of optomechanical devices and for the implementation of permanent data storage. Based on the phenomenon of non-linear absorption, femtosecond laser processing results in strongly localized modifications, even in the bulk of materials, provided that the substrate is transparent to the laser's wavelength. We introduce a laser fabrication approach involving the exposure of layered materials to this class of lasers.

The proposed process is illustrated in Fig. 2.1, and can be generalized as follows: the starting material consists of a multilayer dielectric sample, composed by a substrate over which a number N of layers is deposited, each layer i being of thickness t_i and of arbitrary composition c_i . The substrate material can be selected arbitrarily as well, depending on the requirements of the experiment or the final product, and should not necessarily be limited to dielectrics only; in this specific study, the substrate is always a fused silica wafer. The material should be designed depending on the intended application, or on the basis of the desired modifications, as changing the thickness, the periodicity or the composition of some or all of the layers can result in different modifications patterns. The individual layer thicknesses are typically in the range between 10 nm and 500 nm, although these limits can be exceeded for specific applications.

Following the deposition of the materials, a femtosecond laser beam is tightly focused on, or in proximity of, the surface of the multilayers. The beam can be focused directly on the layers, or can be focused through the substrate first, if it is transparent to the laser's wavelength. Due to the high peak power of the pulses, non-linear absorption is triggered, and the material is locally modified. Exposure and confocal parameters such as the repetition rate of the laser, the pulse energy and duration, the sample scanning speed, the numerical aperture of the objective, the focal spot position and the pulse chirp can be exploited to influence the modification dynamics, or should be otherwise controlled to improve the repeatability of the process.

As a result of the complexity of this type of materials, and given the nature of the interaction of

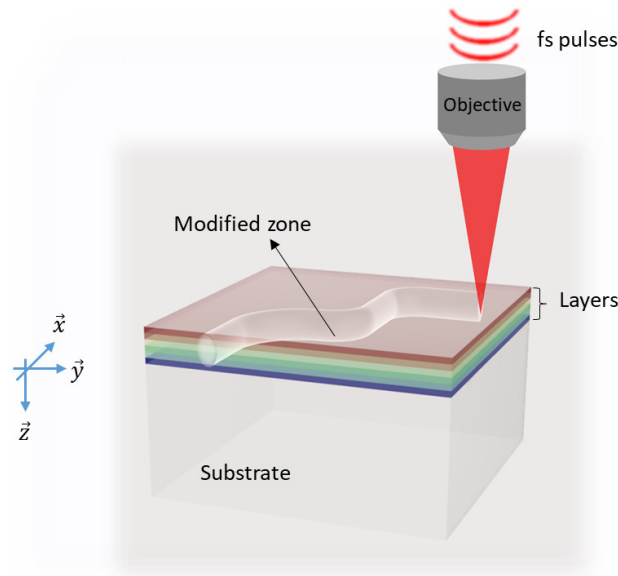


Figure 2.1: Generalized working principle of femtosecond processing of dielectric multilayers: the layered material, consisting of a substrate and an array of thin films deposited as a layer stack (visible in different colors, symbolizing different materials compositions), is exposed to a femtosecond laser beam, focused in proximity of, or at, the layers' surface. The non-linear absorption of the pulses leads to the formation of materials' modifications within, and around, the laser-affected area.

light with these structures, the use of computational methods enables a deeper understanding of the observed optical phenomena. Light propagation simulations are a common tool in the fields of optics and photonics, as they are helpful means to develop devices and study the light-matter interaction process. This chapter serves as starting point to understand these approaches, and to explain our work methodology. First, we will present the formalism used to calculate the reflectance of a layer stack, which was used extensively during the thesis, especially during the sample design process. Moreover, we will introduce the Finite-Difference Time-Domain computational method, which can be used to simulate the propagation of an electromagnetic wave through a material, together with some example simulations, illustrating the potential of the method.

2.1 Reflectance of layered media: computation with transfer matrix method

The spectrum of reflectance and transmittance of dielectric multilayer materials, when structured in periodically spaced bilayers, can be computed using methods developed for dielectric Bragg reflectors (DBR). Consequently, the following simulation approach models the reflectance of Bragg mirror-like structures as a function of layer geometry and composition, beam incident angle and light polarization. Note that this method can be modified to model

2.1 Reflectance of layered media: computation with transfer matrix method

non-periodic layered structures as well. The materials investigated here consist in multilayer stacks of thin films of different compositions, and hence of different refractive indexes. Some assumptions are made to simplify the model: the interfaces between the layers are assumed to be sharp (i.e. that there is an immediate index change at the boundaries instead of a gradient) and the refractive index is presumed to be homogeneous within individual layers.

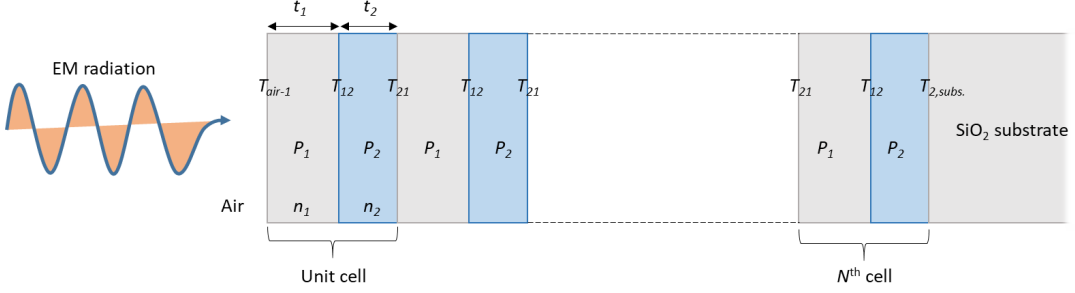


Figure 2.2: Scheme of a layered material and of its associated transfer and propagation matrices. The unit cell consists of a bilayer of materials with refractive indexes n_1 and n_2 , and thicknesses t_1 and t_2 , respectively, that is repeated N times. The propagation matrix P_i and the interface matrix T_{ij} are also indicated in the layers, and at the interfaces, of interest, with the corresponding indexes.

The propagation pattern of the electric field of the beam, and in particular the reflections at the interfaces between the layers, can be computed using the transfer matrix method (TMM) [77–80], as schematically shown in Fig. 2.2. As the electric field must be continuous at every point, in particular at the interfaces, this approach allows its calculation over the multilayer thickness. Due to the symmetry of the layers stack, the system is usually described in two dimensions; hence, the transfer matrix is a 2×2 matrix. The formulation of its elements is strictly dependent on the characteristics of the system, so that each particular multilayer material, with its own structure and composition, possesses a matching characteristic matrix describing light propagation through its core.

The mathematical description of the matrix changes according to the polarization of the incident light, i.e. if the incoming beam has its electric field transverse to the propagation direction (TE, or s-polarized) or if the transverse field is the magnetic one (TM, or p-polarized). Intermediate states of polarization can be described by a linear combination of these two extremes [81], and therefore the case of un-polarized light is modeled here as the arithmetic mean between the TE and TM modes. With this formalism in mind, let us first define the propagation matrix P_i as the matrix describing the propagation of light inside a uniform medium, therefore inside each individual layer i . Each layer is assumed to be homogeneous, without internal interfaces and phase changes, as would be the case of porous materials, for instance. The matrix simply describes the phase shift of the wave's electric field along the propagation direction, as illustrated in Eq. 2.1:

$$P_i = \begin{bmatrix} e^{-i\phi} & 0 \\ 0 & e^{i\phi} \end{bmatrix} \quad (2.1)$$

Chapter 2. Light propagation through multilayer materials

The phase difference $\phi = n(\lambda) \cdot \frac{2\pi}{\lambda} \cdot \cos(\theta) \cdot d$ is expressed as a function of the vacuum wavelength λ , the refractive index of the material $n(\lambda)$ (hereafter simply labelled as n), the incidence angle θ and position d along the layer thickness. To express the reflection and the transmission at the interfaces between layers, we further define the interface matrix T_{ij} , an operator describing the behaviour of the incident rays at the boundaries between a layer i and a layer j , therefore calculating the interference of the various reflections and transmissions at the interfaces, according to Fresnel equations [82]. The value of matrix T_{ij} , for the same materials and laser parameters, changes with respect to the polarization of light:

$$T_{ij} = A \begin{bmatrix} N_i + N_j & N_j - N_i \\ N_j - N_i & N_i + N_j \end{bmatrix} \quad (2.2)$$

where $N_i = n_i \cos(\theta_i)$ if in TE mode and $N_i = n_i / \cos(\theta_i)$ if in TM mode, corresponding to the effective indexes of refraction extracted from the Fresnel equations [82], and $A = 1/(2a_{ij}N_2)$ is a coefficient. a_{ij} is calculated as $\cos(\theta_i)/\cos(\theta_j)$ in TM mode, or as 1 in TE mode. The indices i and j refer to the layer media, therefore the matrix value will vary according to the conformation of the initial and final layer materials. The light angle after the crossing of the interface (θ_2) can be calculated with Snell's law.

The light propagation through N bilayers then writes:

$$M_{net} = \prod_{k=1}^N M_k = (P_i T_{ij} P_j T_{ji})^N = \begin{bmatrix} M_{net,11} & M_{net,12} \\ M_{net,21} & M_{net,22} \end{bmatrix} \quad (2.3)$$

where P_i is the propagation matrix in medium i , P_j is the propagation matrix in medium j , T_{ij} is the interface matrix between mediums i and j and T_{ji} is the interface matrix between mediums j and i . The product of these matrices results in the total transfer matrix of a bilayer, which is then elevated to the power N (the number of bilayers in the stack) to obtain the transfer matrix of the system. Notice that equation 2.3 is only valid for periodic multilayer structures, which can be broken down into a simple succession of periodically spaced, equally thick bilayers. If that is not the case, for example when layers of different thickness are introduced in the stack, the propagation and interface matrices P_i and T_{ij} **should be individually multiplied**.

Finally, the reflectance of the multilayer stack is given by the square modulus of the reflection coefficient r , itself given by the ratio between $M_{net,21}$ and $M_{net,11}$ (Eq. 2.4).

$$R = |r|^2 = \left| \frac{M_{net,21}}{M_{net,11}} \right|^2 \quad (2.4)$$

As discussed above, the reflectance of a multilayer stack depends on the refractive indexes and the thicknesses of the materials composing the layers, as well as on the light incidence

2.1 Reflectance of layered media: computation with transfer matrix method

angle and on the number of layers. As can be seen in Fig. 2.3a and Fig. 2.3b, the reflectance curves are plotted over a spectral interval, showing the reflectance intensity (from 0, total transmission, to 1, total reflectance) of the multilayer materials, here in the 300-1100 nm range of the spectrum. The reflectance spectrum shape depends on the polarization of the incident light, but for normal incidence ($\theta = 0$) there are no differences in reflectance between different polarizations. These curves have a few distinctive properties, such as the number, the position (along the wavelength spectrum) and the intensity of the maxima's peaks, the peaks' bandwidth, as well as the density of the fringe peaks (i.e. the bands of lower reflectance intensity) around the main stopband.

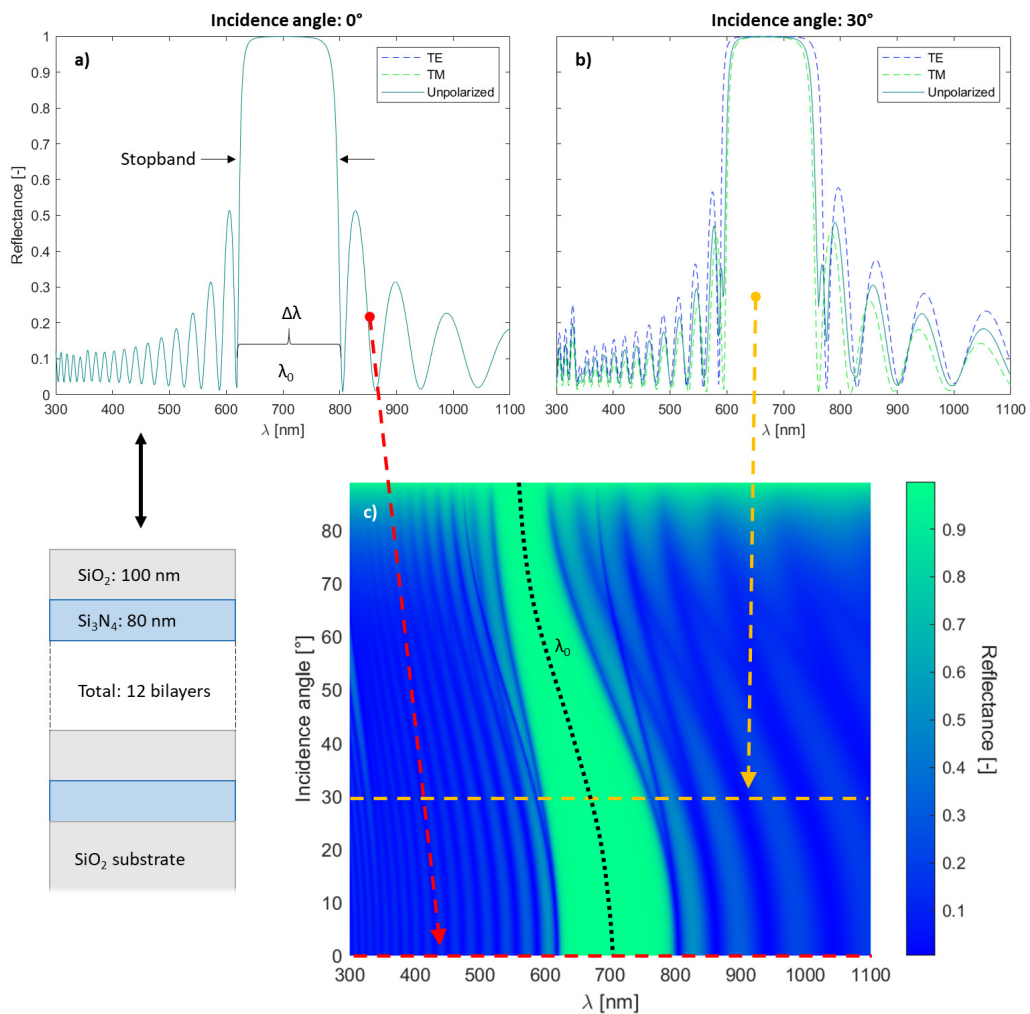


Figure 2.3: a) Reflectance intensity with respect to the incident wavelength, for a stack of 12 bilayers of SiO₂ (100 nm) and Si₃N₄ (80 nm), at a vertical incidence angle, for TE polarization, TM polarization and unpolarized light. A scheme of the layers' structure is visible below the graph, on the left. At this incidence angle, no difference between curves is observed. b) Reflectance calculation for the same material as in a), but with an incidence angle of 30°. The splitting of TE and TM modes becomes evident. c) 2D map of reflectance for the same sample, as a function of incident wavelength and angle, for unpolarized light. The material exhibits blue-shifting of the stopband with the increase of light incidence angle.

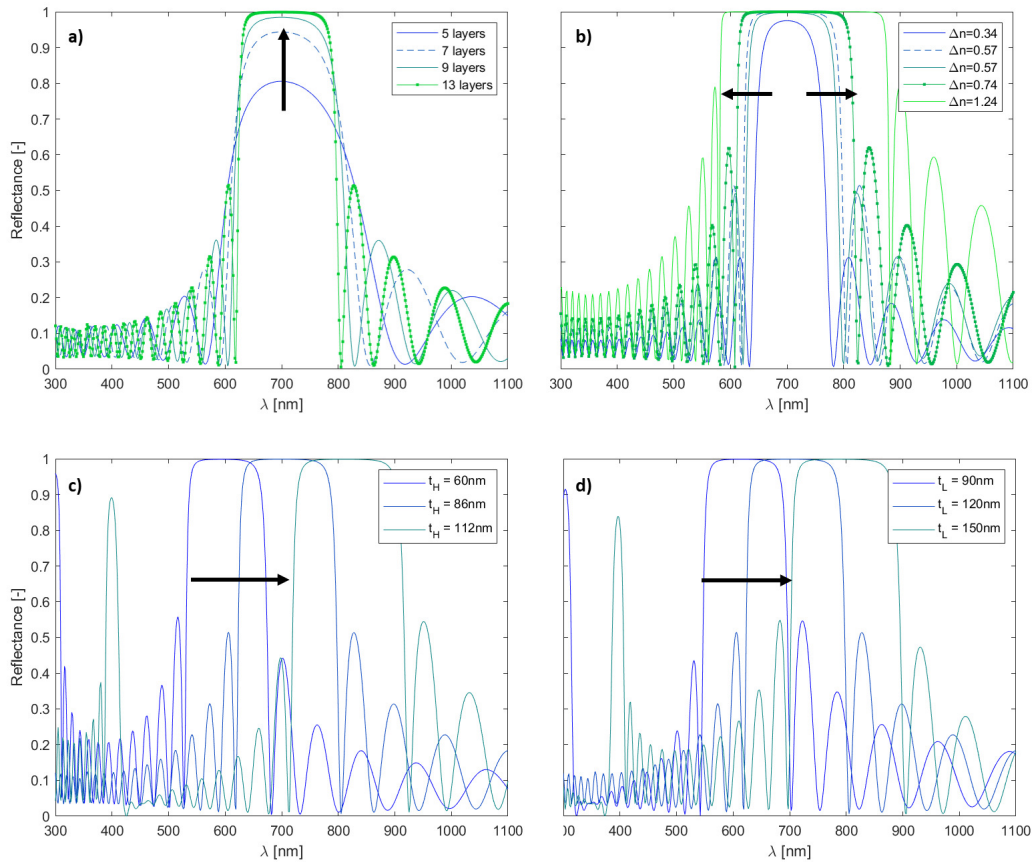


Figure 2.4: Dependence of the reflectance spectrum of a multilayer on its design parameters. a) Increasing the number of bilayers results in sharper peaks, while b) increasing the index contrast between the layers broadens the reflection bandwidth. Images c) and d) simulate cases where the thickness of one of the layer types, the low-index and the high-index material layers, respectively, is kept constant. The thickness of the other layer is increased, showing a red-shift of the main band with increasing layer thickness, in both cases.

A density map of the reflectance as function of both wavelength and incidence angle intervals can be plotted to better visualize the extent of the reflective efficiency of a given set of layers, as can be seen in Fig. 2.3c. This map is symmetric along the incidence angle axis, as one would expect, since the material structure is itself symmetric with respect to that axis. Therefore the plot is shown exclusively for positive angles $+\phi$, from 0° to 89° . The oscillating behavior of the reflectance percentage with the wavelength, already noticed in Fig. 2.3a and Fig. 2.3b, is here confirmed. With an increasing incidence angle, therefore with a decreasing orthogonality, a blue-shift in the position of the main stopband, which moves towards shorter wavelengths, is observed. By running the code with different geometrical and incident light parameters, we notice that TM polarized light is more sensitive to the angle of incidence than TE polarized light, as both the reflected intensity and the bandwidth decrease with the angle. Moreover, the peaks positions shift towards the red when the layer's thickness increases, while the number

of fringe peaks increases with the number of layers. Given the large spectrum of variation of the curves' features, it is therefore interesting to investigate the effect of the different input parameters on these properties, as it is possible to tune the position and shape of the reflectance bands by specifically changing some properties rather than others.

Figure 2.4 shows how layer design parameters can influence the reflectance of the material. For instance, Fig. 2.4a shows that increasing the number of layers results in a much sharper main stopband, since the larger number of interfaces multiplies the number of reflections. The effect of the refractive index contrast Δn between the two constituting materials is shown in Fig. 2.4b, where it is demonstrated how increasing the index difference results in the broadening of the main reflectance band. Finally, the effect of layer thickness increase is shown in Fig. 2.4c-d, where the thickness of one of the layer types, respectively the low- (high-)index material layers, is fixed at values $t_L = 120$ nm ($t_H = 86$ nm), while the other layer thickness is increased. This thickness modification results in a red-shift of the main peak.

2.2 Pulse propagation simulations with FDTD

The field intensity of a laser pulse propagating through a multilayer material is affected by the layers' structure. To model the amplitude of modulation of the electric field inside the multilayer stack and to localize the sites of field enhancement, we performed electromagnetic field propagation simulations using a finite-difference time-domain (FDTD) method. In practice, we used an open source Python package, Meep [83], and considered a chirp-free Gaussian source to simulate the pulse propagation.

The FDTD method is a computational approach that simulates the evolution of electromagnetic fields over a period of time. The simulation domain is divided into a mesh, which consists of an array of rectangles. At the beginning of the simulation, the fields are initialized, then finite-difference approximations are used to approximate the derivatives of Maxwell's equations at the center of each cell of the array. Typically, the fields are evolved for a large number of time steps, with the results being used to compute the electromagnetic field in the next time step. This iterative process is repeated until the simulation is completed [83, 84].

To be more specific, in the spatial domain, Maxwell's equations are discretized on a rectangular grid using finite-difference approximations. This allows the fields to be updated at each time step using the discretized Maxwell's equations, specifically in their time-derivative form as explained in [83]:

$$\frac{\partial \mathbf{B}}{\partial t} = -\nabla \times \mathbf{E} - \mathbf{J}_B \quad (2.5)$$

$$\frac{\partial \mathbf{D}}{\partial t} = \nabla \times \mathbf{H} - \mathbf{J} \quad (2.6)$$

Chapter 2. Light propagation through multilayer materials

Where t is the time, \mathbf{E} is the electric field, \mathbf{H} the magnetic field, \mathbf{D} the electric displacement, \mathbf{B} the magnetic induction and \mathbf{J} and \mathbf{J}_B the electric and magnetic current, respectively. In the time domain, an algorithm is used to evolve the fields, where the electric and magnetic fields are updated at alternate time steps, with the electric fields being updated at half time steps. This allows for the fields to be updated in a stable and accurate manner. As introduced above, the fields are null for times $t < 0$.

To enable the code to run on parallel platforms, the system cell is, in principle, divided into several chunks (see Fig.2.5a, on the left), that can therefore be assigned to different computational clusters. Each chunk is then divided into a certain number of points, depending on the resolution specified by the user, to form a $n \times m$ Yee grid. The Yee grid has the particularity that electric field and magnetic field evolution points are staggered, and can therefore be calculated independently [85]. This discretization of the computational cell enables the time-space evolution of the electromagnetic field at each point of the grid. This points can be divided into owned points, completely at the interior of a chunk, and non-owned points, which are shared between chunks (see Fig.2.5a, on the right) and for which, therefore, communication between chunks of the field values at this points is necessary. In our case, no parallelization of the algorithm was performed, as the computation time was short enough to allow running simulations on a single field laptop. One of the main advantages of the FDTD method is its flexibility. The method can be applied to a wide range of electromagnetic problems, including the simulation of electromagnetic wave propagation in complex geometries.

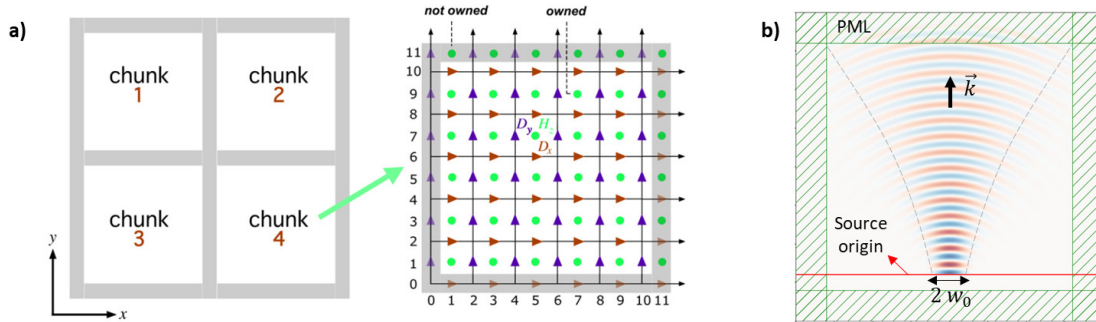


Figure 2.5: a) Representation of the system discretization, which is based on the partition of the Yee grid into smaller chunks. Each chunk is then divided into further points, which can be owned (that is, their time-evolution is computed within the chunk) or non-owned, and where therefore communication of the field values between chunks is necessary. The image is taken from [83]. b) System under study, consisting of a square geometry, surrounded by PML layers to ensure full absorption of radiation at the boundaries. The red line represents the source origin, which propagates orthogonally. The source is modelled as a Gaussian pulse with $\lambda = 1030$ nm and τ_p variable between 250 and 500 fs, depending on the simulation requirements.

Concretely, Meep requires several input parameters to perform the simulations. Specifying the dimensions of the system and the resolution of the rectangular grid is the first important step, and its resolution should be adapted to the dimensions and the complexity of the system under study: it should be high enough to ensure the convergence of the simulation, and to increase the finesse of the results. However, the computing time scales with the resolution

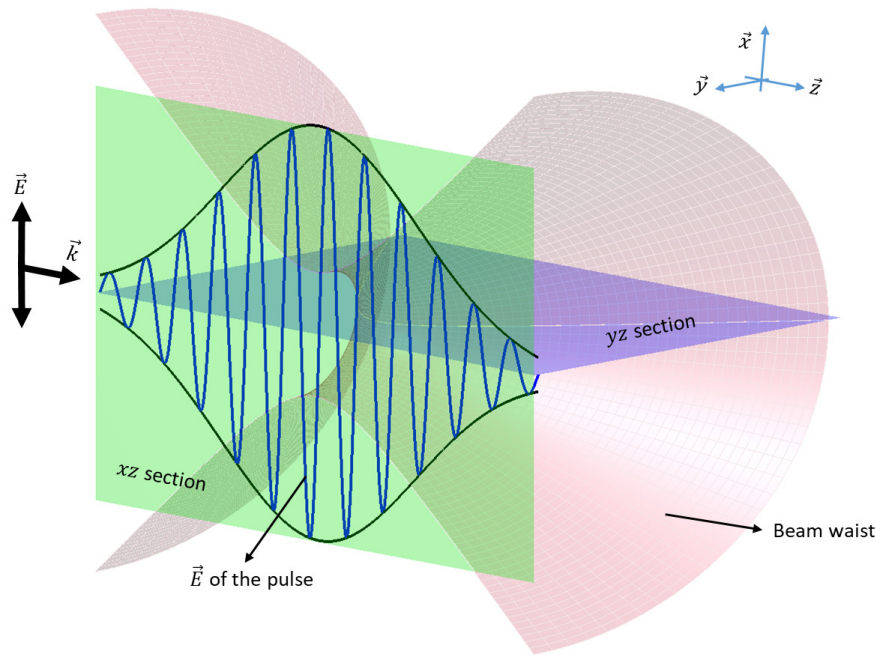


Figure 2.6: Superposition of the pulse's electric field (blue line) with the Gaussian beam envelope (pink surface), at the focal position, to schematize the simulation. The beam profile shows the Gaussian shape of the beam along the \mathbf{k} direction: the contraction of the beam at the focal spot is evidenced. The blue yz and the green xz planes correspond to the cross-sections of the beams that can be visualized with the help of the simulations.

value. It is worth noting that the package works with dimensionless units and is fully scalable.

Boundary conditions should also be specified; in our case, this is achieved by inserting an artificial absorbing layer at the edges of the system, with sufficient thickness to prevent back-reflections, as shown in Fig.2.5b. This fictitious material is called perfectly matched layer (PML), and is defined as reflectionless, so that it effectively acts as a boundary condition.

Another important parameter is the geometry of the system, describing the location, dimensions and composition of each material. In our case, it involves the specification of all the layers of the stack. A materials library is available, providing data for the most common materials, but it is also possible to add materials or to modify existing parameters, as was the case for TiO_2 , whose properties had to be manually specified according to the data presented in [86].

Finally, the nature, position and propagation parameters of the light source should be specified. Here, we consider a Gaussian pulse, without chirp, focused as a Gaussian beam and travelling towards, and orthogonal to, the multilayer stack. The origin of the source is considered to be the focal spot of the laser beam, as illustrated in Fig.2.5b. A scheme of the simulated pulse is shown in Fig. 2.6, showing a representation of the different visualization planes for a femtosecond pulse focused as a Gaussian beam, located at the focal position. The beam

profile is shown in pink, while the electric field of the pulse is traced with a blue line. The blue yz and the green xz planes correspond to the cross-sections of the beam that can be visualized with the help of the simulations, as exemplified in Fig. 2.7. Here, the origin of the source is located a few microns outside of the multilayers surface.

In a first approximation, we neglect the refractive index dependence (Kerr effect) on the pulse intensity. The chromatic dispersions are also neglected. These approximations are reasonable in this case, since we are interested in the low-energy pulse regime (just above the absorption threshold), for which the non-linear component of the refractive index remains small. To justify these assumptions, we can estimate the extent of the Kerr effect, knowing that the refractive index evolves according to the following formula [87]:

$$n = n_0 + n_2 I, \quad \text{where the intensity is } I = \frac{2E_p}{\pi\tau w_0^2} \quad (2.7)$$

Here, n_0 is the linear refractive index, E_p is the pulse energy, τ the pulse duration and w_0 the beam waist. The values of the non-linear refractive index n_2 for the simulated materials (SiO_2 , SiN_x , TiO_2) are $n_{2,\text{SiO}_2} = 2.19 \cdot 10^{-20} \text{ m}^2 \text{ W}^{-1}$ [88] (at $\lambda=1030 \text{ nm}$), $n_{2,\text{SiN}_x} = 24.00 \cdot 10^{-20} \text{ m}^2 \text{ W}^{-1}$ [89] (at $\lambda=1.55 \mu\text{m}$) and $n_{2,\text{TiO}_2} = 18.20 \cdot 10^{-20} \text{ m}^2 \text{ W}^{-1}$ [90] (at $\lambda=1.55 \mu\text{m}$). For a pulse energy of 100 nJ (standard value for the processing of multilayer samples in this work), a pulse duration of 500 fs and a beam waist radius of 0.9 μm , this results in a refractive index increase comprised between the two extremes of $3.44 \cdot 10^{-3}$ (for SiO_2) and $3.77 \cdot 10^{-2}$ (for SiN_x). Hence, for the purpose of the simulations, we neglect such small changes.

It is important to notice that these simulations are **restricted to the case of a single pulse propagating through the multilayers**. A multi-pulse regime would imply to consider a feedback mechanism, as each pulse gradually modifies the structure through which it propagates. In practice, the simulation should also incorporate evolving material properties after the passage of each pulse, such as a varying refractive index. Here, we limited ourselves to simulating the first step of the process, which is to compute the passage of a single pulse and localize the regions where non-linear absorption is more likely to take place, according to the local electric field's intensity distribution, and to correlate these simulated zones of enhancement with experimental observations.

2.2.1 Examples of FDTD simulations

To exemplify the versatility of FDTD as a simulation tool, this section illustrates some examples of pulse propagation through multi-material systems. These designs were not investigated in the context of this thesis, but are closely related to our samples either in composition or geometrical design. All simulations shown in Fig. 2.7 are at a timestamp of 180 fs after the wavefront reaches the position 0 μm along the beam propagation direction (i.e. the beginning of the multilayers' surface), while the focal spot of the beam is located at the position -5 μm

2.2 Pulse propagation simulations with FDTD

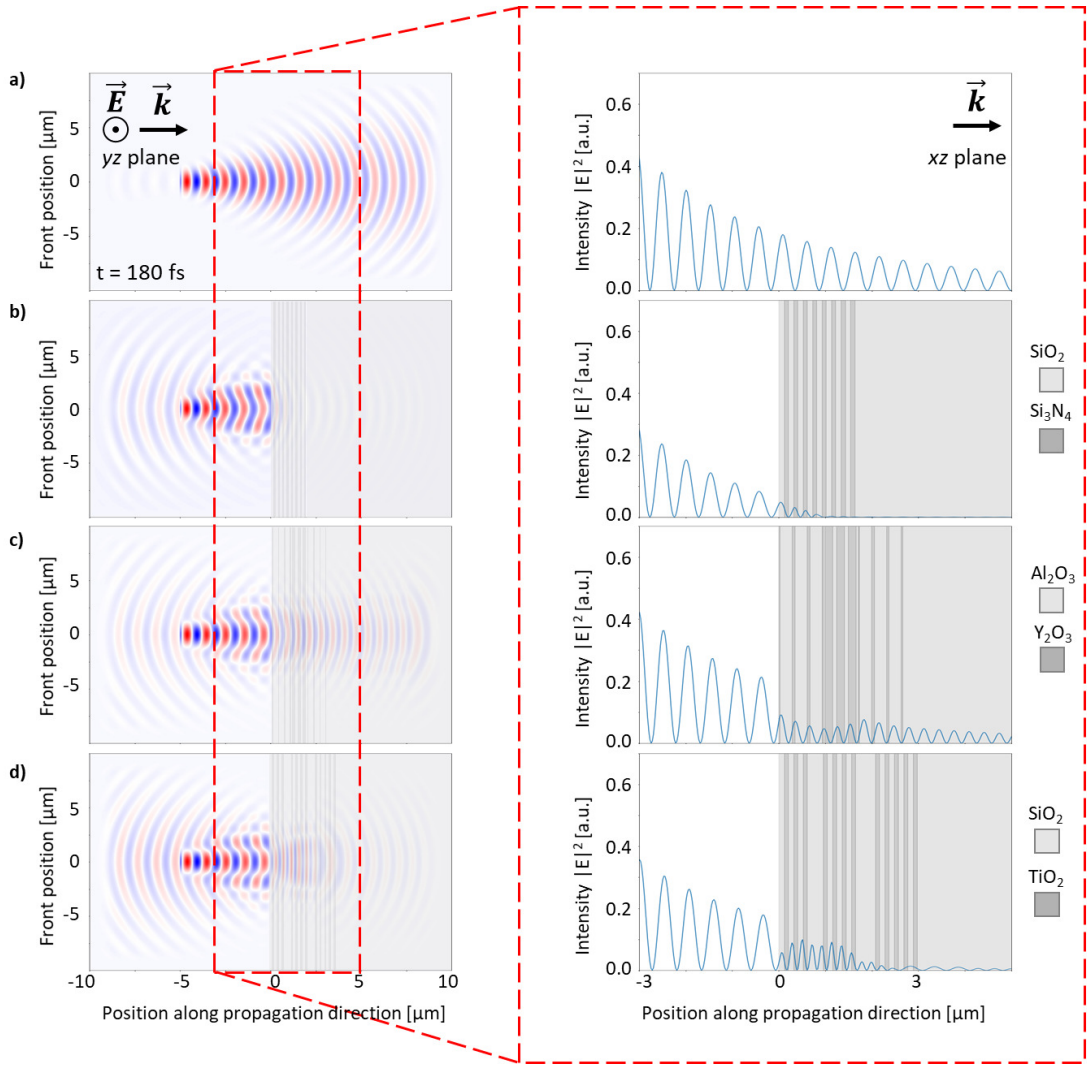


Figure 2.7: Examples of FDTD simulations applied to the propagation of a 500 fs pulse, taken at a timestamp of 180 fs after the wavefront reaches horizontal position $0 \mu\text{m}$. Left: 2D plots of the electric field as it propagates, where the field's orientation is orthogonal to the image plane. Right: cross-section at front position $= 0 \mu\text{m}$, consisting in the magnification of the area marked by the red rectangle, showing the intensity of the field. a) Case of propagation through air, while b) shows the case of a $\text{SiO}_2/\text{Si}_3\text{N}_4$ DBR with thicknesses $t_{\text{SiO}_2} = 120 \text{ nm}$ and $t_{\text{Si}_3\text{N}_4} = 90 \text{ nm}$. c) Case of a triple DBR specimen, composed by layers of Al_2O_3 and Y_2O_3 , with the lateral DBRs having thicknesses $t_{\text{Al}_2\text{O}_3} = 272 \text{ nm}$ and $t_{\text{Y}_2\text{O}_3} = 83 \text{ nm}$, and the central DBR having thicknesses of $t_{\text{Al}_2\text{O}_3} = 56 \text{ nm}$ and $t_{\text{Y}_2\text{O}_3} = 175 \text{ nm}$. Finally, d) is the case of a regular $\text{SiO}_2/\text{TiO}_2$ DBR, with the addition of two larger spacers along the stack. Here, $t_{\text{SiO}_2} = 119 \text{ nm}$ and $t_{\text{TiO}_2} = 89 \text{ nm}$, while the spacers have a thickness $t_{\text{spacer, SiO}_2} = 357 \text{ nm}$.

on the same axis. The thickness values of each individual layer of the stacks can be found in the description of the image. The left-hand side of the figure shows the propagation of the electric field of the pulse on the plane orthogonal to the field's orientation, corresponding to the yz plane defined in Fig. 2.6, while the images on the right show the intensity ($I \propto |E|^2$) of the field along the propagation axis (that is, at front position $0 \mu\text{m}$), corresponding to the xz

plane. Here, the limits of the horizontal axis are restricted between -3 and $+5$ μm . Notice that the intensity values are taken from a specific cross-section, at front position 0 μm , and not integrated over the whole surface.

The first simulation example concerns the propagation of the pulse through air, as seen in Fig. 2.7a, which serves as benchmark for all other simulations. Here, the spatial distribution of the field is unaffected by external structures, and the pulse is free to propagate without partial reflections or modulations. This changes in Fig. 2.7b: the structure introduced here is a standard DBR, consisting of 8 $\text{SiO}_2/\text{Si}_3\text{N}_4$ bilayers, which affect the propagation of the pulse by introducing a decay of the intensity within the first few sets of layers. The reflected beam also interferes with the incoming field, as visible in the interference patterns in the figure on the left.

Conversely, the structures introduced in Fig. 2.7c and Fig. 2.7d show a different propagation dynamics, even though the trend shows an overall reduction of the intensity inside the material, like in the case of a single DBR. The $\text{Al}_2\text{O}_3/\text{Y}_2\text{O}_3$ specimen shows shifts in electric field intensity at the interfaces between the three DBR stacks. Similarly, the $\text{SiO}_2/\text{TiO}_2$ structure shows a modulation of the field intensity, with localized enhancement of the field. It can therefore be concluded that, in accordance to the literature presented in the introduction, the presence of several subsequent interfaces affects the propagation dynamics of a femtosecond pulse inside a multilayer material, and that FDTD simulations are useful to locate the areas of field enhancement.

2.3 Summary

The computation of pulses propagation through multilayer samples enables a deeper understanding of the laser-induced modification processes occurring within these materials. Two different approaches were explored here. First, the transfer matrix method was used to calculate the reflectance spectra of the designed samples, to identify the positions of the stopbands and to assess the quality of the layer deposition processes. This method consists in calculating the reflection, the transmission and the propagation at every layer interface, adding them to obtain a full reflectance profile, over a given wavelength interval.

Second, the FDTD computational method was used to estimate the evolution of the electric field of a single pulse propagating through a multilayer structure. This involved the discretization of the system into a regular mesh, over which the evolution of the electromagnetic field was calculated both in spatial and temporal domains. Examples of FDTD simulations were also shown, involving various materials systems and illustrating the potential of this computational method in describing the pulse's electric field modulation inside a multilayer stack.

3 Experimental methods

This chapter summarizes the experimental methods used in this work, from the materials selection to the laser processing setup, including an introduction on the fundamentals of electron microscopy.

3.1 Materials selection process

As illustrated in the previous chapter, the dielectric, optical properties of materials, especially their refractive index, are of the utmost importance when designing a multilayer sample. However, given the thermo-mechanical nature of laser-thin films interaction, other properties should be considered too, like thermal expansion coefficient or elastic modulus. The potential candidates for dielectric multilayer deposition are countless, and range from simple oxide and nitride compounds to complex glass-ceramic systems. Based on a survey of the most common materials used in the micro-technology industry, it was decided to focus on the following compounds, and to select the constituting materials from this restricted group: SiO_2 , Al_2O_3 , HfO_2 , GeO_2 , TiO_2 , Ta_2O_5 , Nb_2O_5 , Y_2O_3 , ZrO_2 , Si_3N_4 , MgF_2 .

The index contrast between layers is the most important parameter to consider, as it determines the propagation dynamics inside the multilayer stack, as seen in Fig. 2.4, but also affects the initiation of non-linear absorption, as explained in Section 2.2. In the context of our research, low-index materials can be defined as materials with $n < 1.8$. Some materials possess remarkably high refractive indexes (TiO_2 and Nb_2O_5 , for instance) and are therefore particularly suitable to be deposited, as the index contrast is greatly increased. Note that a high Δn can also be related to mismatching lattice constants, therefore resulting in increased stress-strain states after layer deposition. The evolution of the refractive index of the eligible materials with the wavelength is visible in Fig. 3.1, in the 300 to 800 nm spectral range.

The materials selection process can also involve the study of several other physical properties, such as Young's modulus and elastic limit, coefficient of thermal expansion, thermal transport properties or lattice constant. These parameters can be important to consider when dealing

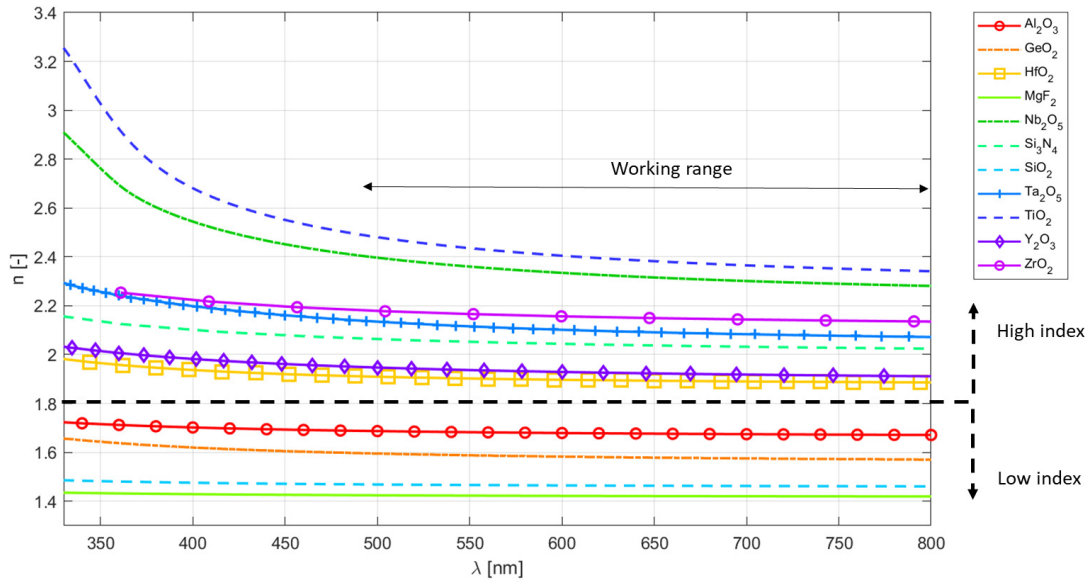


Figure 3.1: Real part of the refractive index as a function of incident wavelength for the group of potential constituting materials candidates, in the interval between 300 and 800 nm. Data of refractive indexes are taken from [91–100]

with the stress-strain state of a material after laser exposure, or when the exposure conditions involve the presence of thermal accumulation. Examples of such maps can be seen in Fig. 3.2, showing the distribution of the elastic modulus E and the coefficient of thermal expansion α_{th} , in function of the refractive index, for the group of materials considered here.

From an application perspective, it is also beneficial to gather information on the reported polymorphs of the candidate compounds, as well as the on polymorphs of potential intermixed phases, for an efficient functionalization of the laser-affected area. By knowing the composition and the physical properties of the desired laser-induced phase, one can design the layer thickness distribution and the materials composition such that the process output corresponds to the desired target material.

Note that these physical properties can **change considerably** with the stoichiometry and porosity of a material, and with its crystallographic structure (crystalline/amorphous, polymorphs, ...), all of which depend on the deposition method of choice, on the precursors used, as well as on the thickness of the layers. The values gathered here, and used during the simulations, are taken from the literature, hence do not fully represent the real values of our own samples. That being said, they offer a valid starting point for the design and the simulation of the laser exposure process, and the analysis of the experimental results.

From a technological and practical point of view, the materials' availability, as well as the compatibility between materials systems, is also important. If different deposition machines or techniques are required for different materials, the fabrication of a multilayer structure

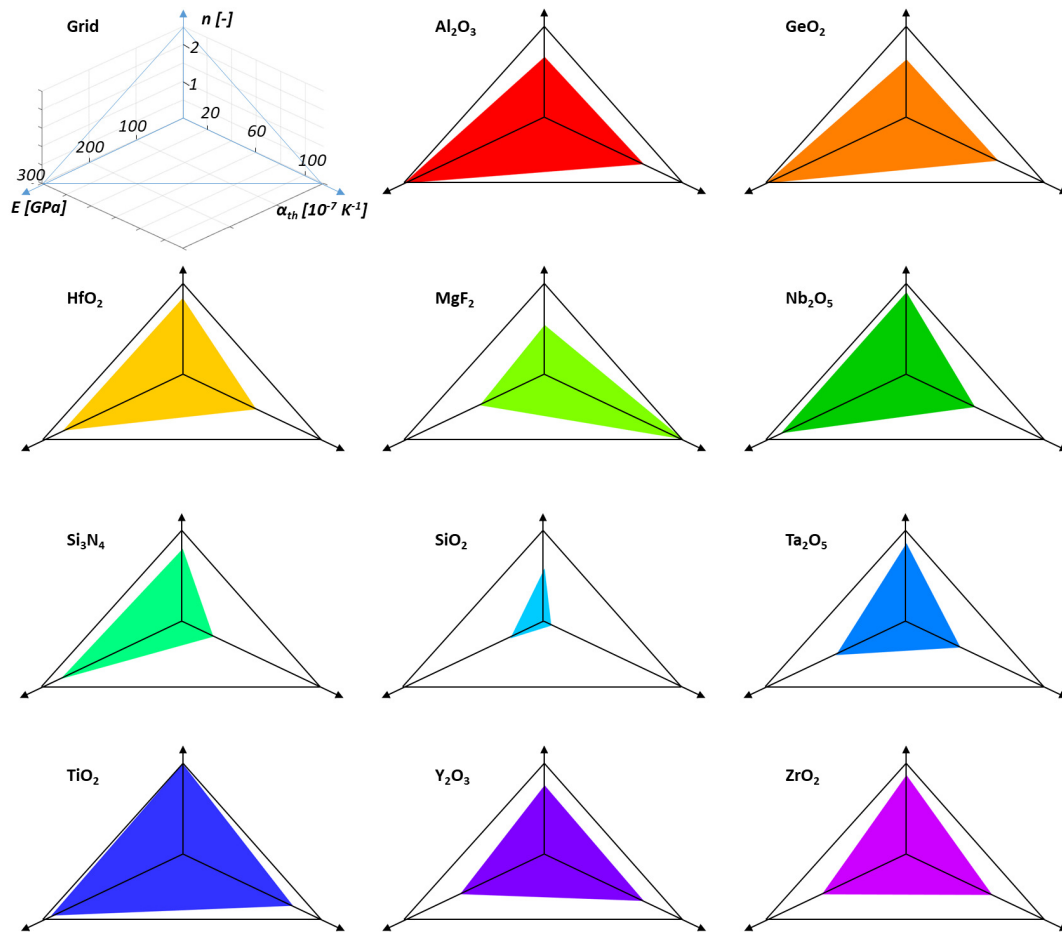


Figure 3.2: Examples of physical property mapping, with a triangular plot showing the elastic modulus E , the coefficient of thermal expansion α_{th} and the refractive index n (at $\lambda=1030$ nm), for the group of materials under consideration. Data retrieved from [101–118].

becomes extremely complex and time-consuming, as well as prone to contaminations. For this reason, it was decided to restrict the sample design to materials systems that could be deposited using the same equipment.

Taking into account all of the above parameters, it was chosen to focus on the following compounds: SiO_2 , Al_2O_3 , TiO_2 , Nb_2O_5 and Si_3N_4 . More specifically, and as will be explained more in detail in the following section, multilayer systems under study during the course of this thesis are $\text{SiO}_2/\text{Si}_3\text{N}_4$, $\text{Al}_2\text{O}_3/\text{Nb}_2\text{O}_5$ and $\text{SiO}_2/\text{TiO}_2$.

3.2 Multilayer fabrication process

A summary of the investigated sample's compositions and geometries can be found in Table 3.1. Visual representations of both the multilayer structures and their reflectance spectra can

be found in Fig. 3.3 (for the $\text{SiO}_2/\text{SiN}_x$ samples) and in Fig. 3.4 (for all other materials). The motivation for each specific design will be discussed in the following chapters.

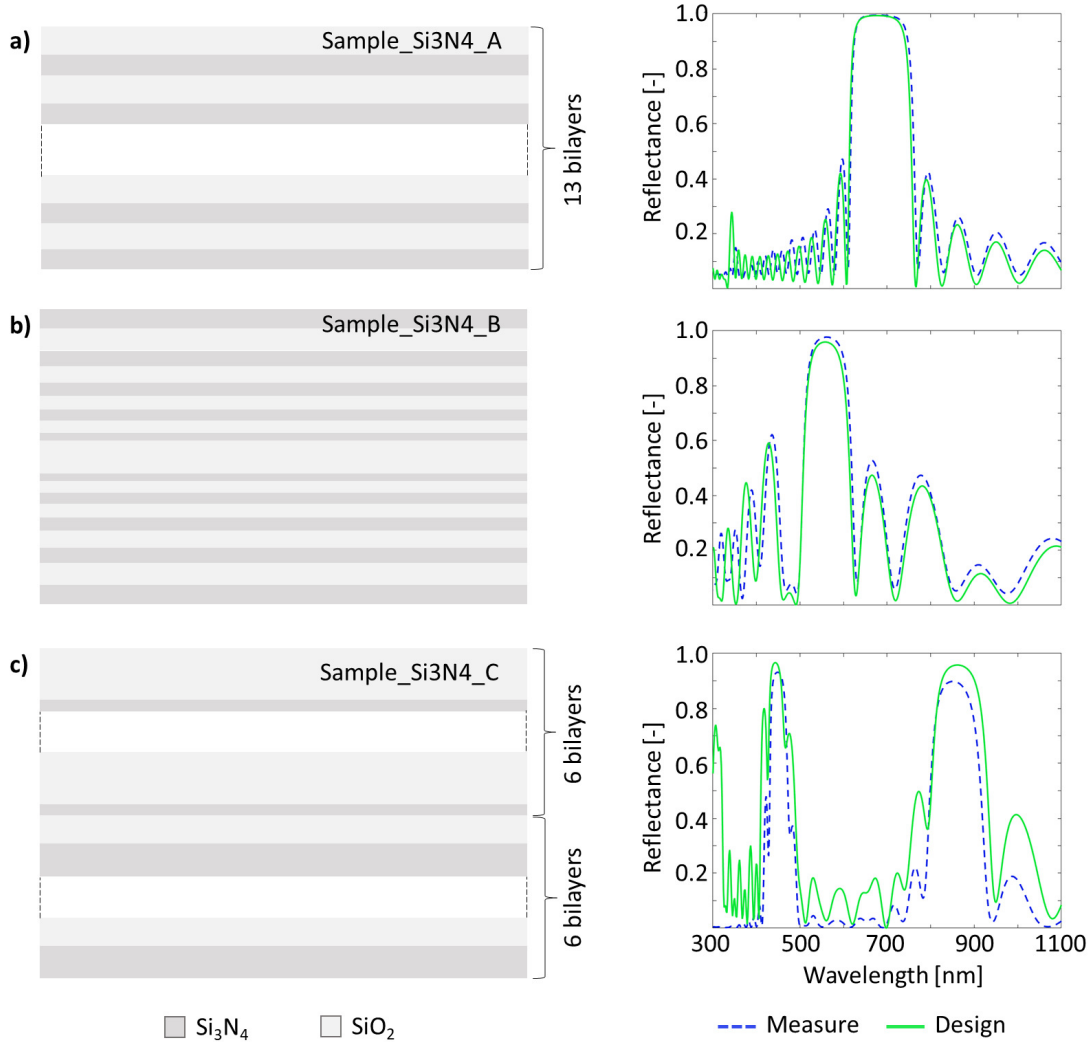


Figure 3.3: Visual representations of the $\text{SiO}_2/\text{SiN}_x$ multilayer samples studied during the course of the thesis (left) and their corresponding reflectance spectra (right), as measured with a spectrophotometer (dotted blue lines) and as designed with the transfer matrix method (continuous green lines). Image a) corresponds to Sample_Si3N4_A, while b) corresponds to Sample_Si3N4_B, and c) to Sample_Si3N4_C.

Thin film fabrication technology is a well established field of applied physics, with several different techniques that can be selected and adapted depending on the deposition constraints, such as the choice of materials, the thickness range, the uniformity of the layers, the desired deposition rate, and the required adhesion strength to the substrate. To this end, several deposition techniques have been developed over the years and have become industry standards, such as sputtering, plasma-enhanced chemical vapor deposition (PE-CVD), evaporation, atomic layer deposition (ALD) and reactive sputtering.

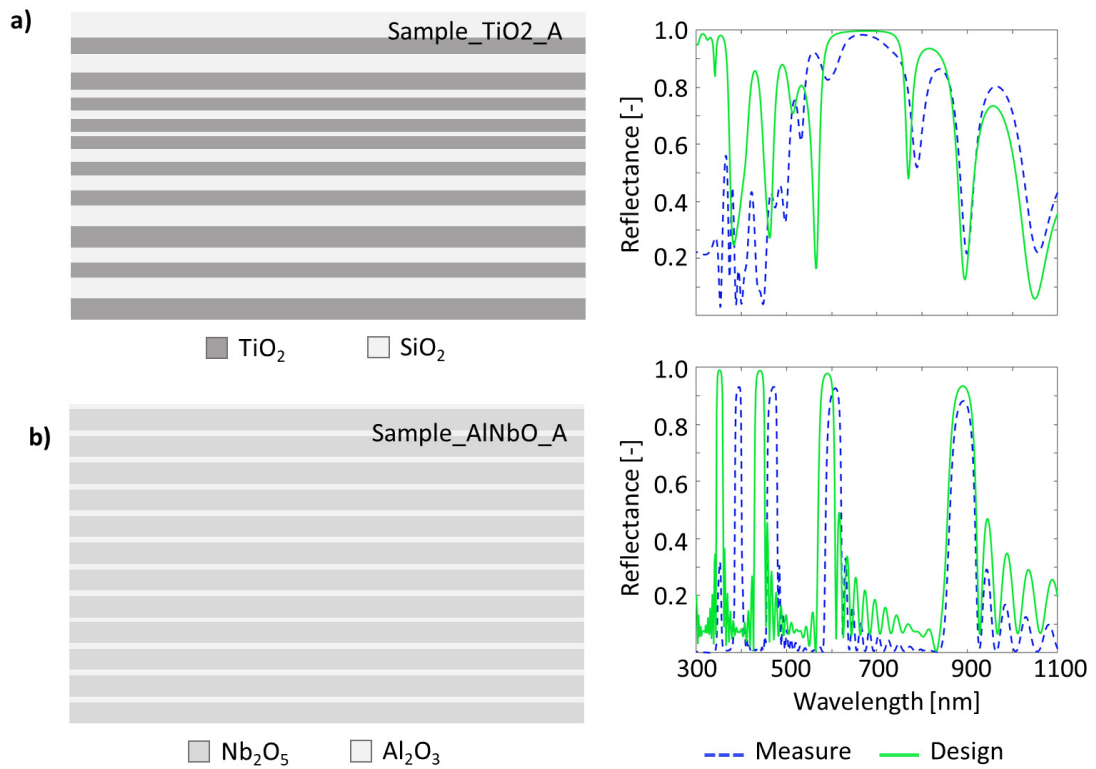


Figure 3.4: a) Visual representations of the $\text{SiO}_2/\text{TiO}_2$ multilayer sample (Sample_TiO2_A) and b) of the $\text{Al}_2\text{O}_3/\text{Nb}_2\text{O}_5$ multilayer sample (Sample_AlNbO_A) (left side of the figure). Their corresponding reflectance spectra, as measured with a spectrophotometer (dotted blue lines) and as designed with transfer matrix method (continuous green lines), are shown next to the corresponding layered structure.

Sample_TiO2_A was deposited by magnetron sputtering using a Kenosistec system at the III-V lab at EPFL (Switzerland). All $\text{SiO}_2/\text{SiN}_x$ samples, i.e. Sample_Si3N4_A-C, were deposited by PECVD with an Oxford Plasmalab machine in the cleanroom of the Microcity building in Neuchâtel (Switzerland). The deposition was done at a temperature of 300°C , and the resulting layers consisted of stoichiometric SiO_2 and Si-rich Si_3N_4 . For this reason, the pristine layers of silicon nitride are defined by the more generic formulation SiN_x , which is more accurate than the stoichiometric formula, since x is on the order of 0.5. Last, the $\text{Al}_2\text{O}_3/\text{Nb}_2\text{O}_5$ multilayer sample (Sample_AlNbO_A) fabrication was outsourced to Schott AG in Yverdon-les-Bains (Switzerland), and done by magnetron sputtering.

For deposition with the Oxford Plasmalab, the deposition rate of each individual material was measured thanks to a profilometer. After deposition of the actual samples, the thicknesses of the individual layers of two selected samples (Sample_Si3N4_B and Sample_TiO2_A) were measured by analysing their cross-sections with transmission electron microscopy, and can be found in Appendix A.

Chapter 3. Experimental methods

Sample's name	Composition	Geometry	Layers thicknesses [nm]
Sample_Si3N4_A	SiO ₂ /SiN _x	$\lambda/4$ DBR	120 nm (SiO ₂) / 86 nm (SiN _x)
Sample_Si3N4_B	SiO ₂ /SiN _x	Central symmetry	See Appendix A
Sample_Si3N4_C	SiO ₂ /SiN _x	Double DBR	250 nm (SiO ₂) / 100 nm (SiN _x) and 100 nm (SiO ₂) / 150 nm (SiN _x)
Sample_TiO2_A	SiO ₂ /TiO ₂	Irregular	See Appendix A
Sample_AlNbO_A	Al ₂ O ₃ /Nb ₂ O ₅	DBR	56 nm (Al ₂ O ₃) / 343 nm (Nb ₂ O ₅)

Table 3.1: List of samples studied during the course of the thesis, including the sample name, layer composition, stack geometry and layer thicknesses. The individual layer thicknesses of Sample_Si3N4_B and Sample_TiO2_A are too complex to fit in this table, and can be found in table A1, in Appendix A.

3.3 Femtosecond laser processing setup

Two different laser systems were used to process the multilayer samples. First, a 270 fs fiber ytterbium laser (Yuzu from Amplitude Systèmes), emitting at a wavelength of 1030 nm, was employed. Its repetition rate can be controlled with a AOM (located within the laser cavity) and can be set up between 1 kHz and 3 MHz. The second source is a 500 fs Yb laser (Yuja from Amplitude Systèmes), also emitting at 1030 nm, and set at a repetition rate of 240 kHz. In addition, a continuous wave CO laser from Coherent was used to compare the effects of linear and non-linear absorption (its specifications will be introduced in Chapter 6, which will focus on the modifications induced by this laser).

The lasers' wavelength of 1030 nm is generally well transmitted through the fabricated multilayer structures, as visible in Fig. 3.3 and Fig. 3.4, showing the stopbands location and width, for all samples. Using different wavelengths (second or third harmonic, for example) would have resulted in stronger reflection effects in some samples. Comparative studies using these wavelengths would nevertheless be interesting outlooks of this work. The pulse duration lies within the usual range for ultrashort pulse -induced phase transition studies in dielectrics, enabling the occurrence of non-linear effects with less thermal effects and lower individual pulse energies, preventing excessive damage of the multilayers, with respect to the ps or ns case.

Laser processing was performed on a dedicated platform, shown in Fig. 3.5, where the power is controlled by a motorized half-wave plate and a polarized beam splitter, while the polarization of the beam can be controlled by another motorized half-wave plate placed just before the objective. The focal spot position with respect to the sample is controlled by motorized stages, enabling movement along the propagation direction and on the orthogonal plane, with a nominal precision of 100 nm. The scan speed limit is determined by the maximum velocity of the stages, which in principle can be as high as 100 mm s⁻¹. However, higher speeds require longer acceleration times, therefore scan speeds between 0.1 and 10 mm s⁻¹ were deemed more suitable for our experiments. The focal spot position with respect to the sample's surface is determined with a third harmonic generation (THG) detector, since the interaction of the

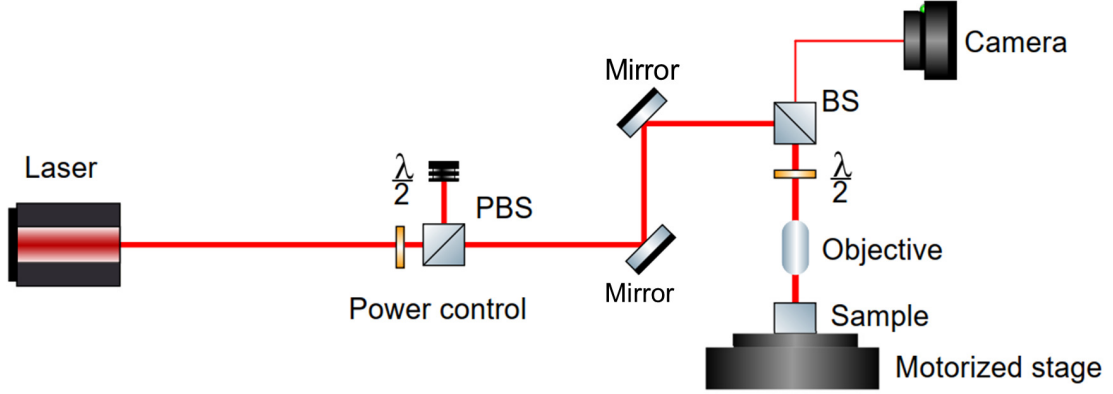


Figure 3.5: Scheme of the optical setup of the laser platforms. Power control is achieved with a first combination of half wave-plate (labeled $\lambda/2$) and polarized beam splitter (PBS), while the beam polarization is controlled by another wave-plate just before the objective. Image created using the component library of Alexander Franzen (<http://www.gwoptics.org/ComponentLibrary>).

laser with the material at the interface material/air generates THG signal. Alternatively, it is also possible to align the focal spot with the sample surface by moving it along the propagation direction and tracking the ablation marks with a camera.

Given the variety of experimental parameters, establishing reliable metrics to characterize the energies used during laser processing is important, especially in the perspective of comparing the work of different authors. To this end, to quantify the amount of energy transferred by the laser beam, useful parameters include the exposure dose (or net fluence) E_d [119], which takes into account the repetition rate and the sample scan speed, the individual pulse fluence F , useful to highlight the influence of a single pulse electric field's strength, and the peak irradiance P_p , defined to include the pulse duration parameter. The equations relative to these quantities are expressed as follows:

$$E_d = \frac{4E_p f}{\pi w v} \quad [Jcm^{-2}] \quad (3.1)$$

$$F = \frac{2E_p}{\pi w^2} \quad [Jcm^{-2}] \quad (3.2)$$

$$P_p = \frac{0.94E_p}{\pi \tau_p w^2} \quad [Wcm^{-2}] \quad (3.3)$$

Where E_p is the pulse energy, f is the laser repetition rate, v is the scan speed, w is the beam waist at the focal spot and τ_p is the pulse duration.

For an objective of numerical aperture (NA) equal to 0.4 and a laser at 1030 nm, the beam

Chapter 3. Experimental methods

waist at the focus is $0.9 \mu\text{m}$, a value that has been established by calculations, simulations and experimental evidence, as illustrated in the supplementary material of Torun *et al.* [120]. This, in turn, leads to a calculated Rayleigh length z_R of $2.47 \mu\text{m}$ (see Eq. 3.4). This value is corrected according to the quality factor, or M^2 value, of the laser. As the nominal vertical movement resolution of the stage is lower than 100 nm , the positioning accuracy along the vertical direction is assured with respect to the dimension of the Rayleigh length and to the total thickness of the multilayer stacks, which varies between 1 and $3 \mu\text{m}$.

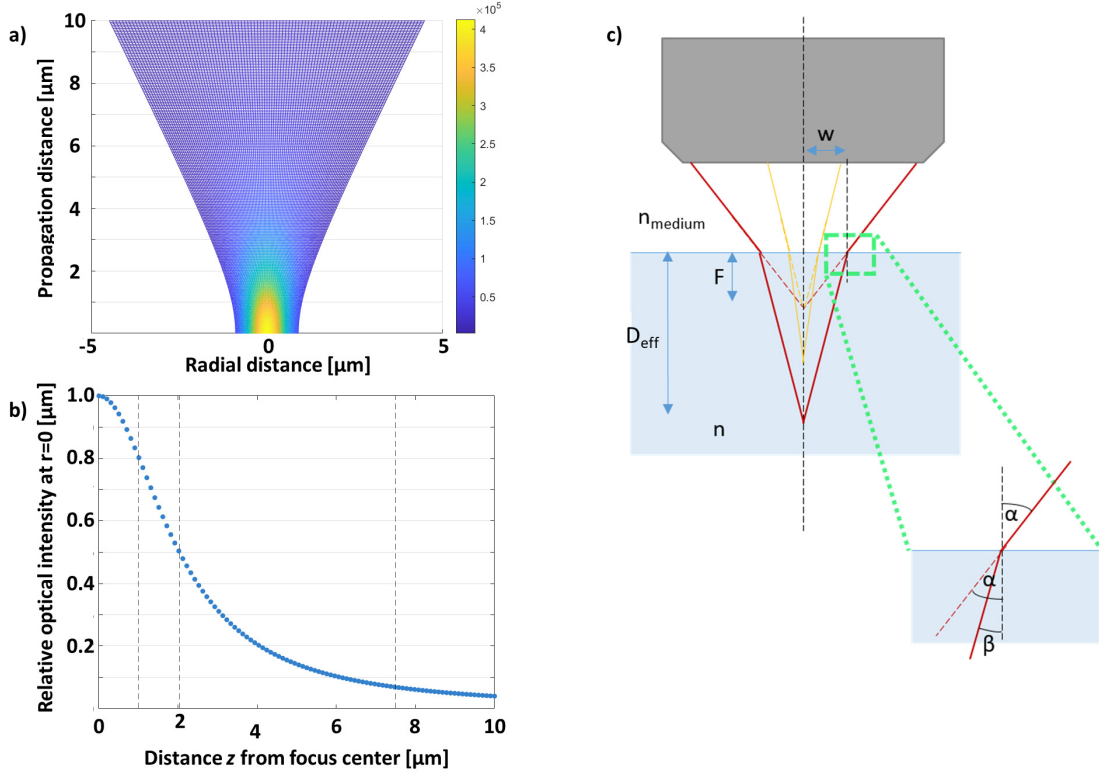


Figure 3.6: a) Intensity of a Gaussian beam as a function of the propagation distance, and the radial distance from the optical axis, resulting from Eq. 3.5. In b), the drop of the optical intensity with the distance from the focal spot, along the optical axis, is further illustrated. c) Scheme of the vertical correction of the beam's focal spot, resulting from the distortion caused by refraction at the interface between the medium of light propagation, and the material under processing.

Assuming a Gaussian pulse of $M^2=1.2$, a Rayleigh length z_R , a beam waist w_0 and a circular profile of the beam (shape confirmed by a beam profiler), the beam radius as a function of the propagation distance z can be calculated with the following formula [121]:

$$w(z) = w_0 M^2 \sqrt{1 + \left(\frac{z}{z_R}\right)^2}, \quad \text{where } z_R = \frac{\pi w_0^2}{\lambda} \quad (\text{in air}) \quad (3.4)$$

The beam radius is defined as the distance from the beam center to where the intensity value drops to $1/e^2$ of the initial value. The optical intensity at a radial distance r from the beam

focus center and, subsequently, its fraction at any position along z can then be calculated as follows, and then visualized in Fig. 3.6a [121]:

$$I(r, z) = I_0 \left(\frac{w_0}{w(z)} \right)^2 e^{-2r^2/w(z)^2}, \quad \text{where } I_0 = \frac{2P}{\pi w_0^2} \quad (3.5)$$

$$f(r=0, z) = \frac{I(z)}{I_0} = M^2 \frac{w_0^2}{w(z)^2} \quad (3.6)$$

Here, I_0 is the maximal intensity at the beam center, while P stands for the average power of the laser pulses. The M^2 factor in Eq. 3.6 is included to balance the fact that w_0 is already calculated with respect to a M^2 factor of 1.2. The evolution of the optical intensity at the beam center ($I(z)/I_0$) is illustrated in Fig. 3.6b. Assuming that the pulse is not absorbed (i.e. the condition for non-linear absorption is not reached), the optical intensity is conserved. Consequently, the intensity profile across the beam radius for a fixed z can be estimated as the ratio between the optical intensity of a given radial distance r and the intensity at the central point ($r=0$), for the same z value.

Understanding the distribution of energy and its relationship with the Rayleigh length is crucial to understand how modification dynamics are affected by the position of the focal spot. This is particularly significant in cases of extreme confinement of the modifications in single layers, as discussed later in Chapter 5. Even though the laser intensity at distances larger than z_R should be lower than the non-linear absorption threshold, it can still cause absorption due to local field enhancement effects.

Finally, the change in refractive index between the medium (usually, air) and the material results in the elongation of the beam, as the light rays are refracted at the interface. The magnitude of this distortion can be estimated by computing the amount of refraction at the edges of the beam, assuming a triangular shape of the focused beam, with the lower edge located at the focal spot. This elongation phenomenon becomes important when exposing the multilayer samples from the backside of the specimens, with the beam propagating through the thick substrate (relative to the multilayers thickness). This approach does not take into account the profile at the focus, i.e. the presence of a beam waist. According to the scheme in Fig. 3.6c, the distortion of the beam can be calculated using the numerical aperture of the objective, which is defined as $NA = n_{medium} \sin(\alpha)$, and Snell's law, applied at the interface between the medium and the material:

$$n_{medium} \sin(\alpha) = n \cdot \sin(\beta) \quad (3.7)$$

Hence, the ratio between the effective focusing distance D_{eff} , which marks where the focal spot will actually be, and the "ideal" focal spot F as would be *in-air*, can be expressed as:

$$\frac{D_{eff}}{F} = \frac{\tan(\alpha)}{\tan(\beta)} = \frac{\sin(\alpha) \cdot \cos(\beta)}{\sin(\beta) \cdot \cos(\alpha)} = n \cdot \frac{\sqrt{1 - \sin(\beta)^2}}{\sqrt{1 - \sin(\alpha)^2}} = \sqrt{n^2 \frac{1 - (\frac{NA}{n})^2}{1 - NA^2}} \quad (3.8)$$

This eventually leads to an effective focusing distance of:

$$D_{eff} = F \sqrt{\frac{n^2 - NA^2}{1 - NA^2}} \geq F \quad (3.9)$$

In the case of fused silica ($n=1.45$), the elongation of the beam can be quite relevant when focusing deeply inside a material, and should be taken into account if laser processing is done through the backside of the specimen. The use of adaptive optics could potentially reduce the effect of the refractive index. However, no such setup was used in the course of the project, as most of the materials modifications were directly written on the multilayers' surface. Nevertheless, it should be noticed that exposure from the backside of the specimens, with the laser beam propagating through the substrates (with thicknesses ranging from 300 to 500 μm), is far more susceptible to this kind of aberration.

3.4 Electron microscopy and sample preparation by focused ion beam

Optical microscopes are diffraction limited, their resolution being bound to the wavelength and to the numerical aperture of the objective in use. Hence, feature resolution by this technique is fundamentally thresholded at around 100-200 nm, in the visible range. This makes the observation of nanometer-sized crystallites or single layer modifications extremely challenging with conventional optical means. Electron microscopy offers a solution to this problem, as the wavelength associated to an electron is inversely proportional to its momentum, $\lambda = h/mv$. For example, an electron at an acceleration voltage of 30 kV has a wavelength of 7 pm, resulting in a resolution lying within the Angstrom range. This is for instance exploited in scanning electron microscopy (SEM), where an electron beam is accelerated and focused through a set of magnetic lenses, and then scanned across the surface of the sample under investigation, or in transmission electron microscopy (TEM), where the beam is transmitted through a thin specimen and the contrast is constructed using both transmitted and diffracted electrons.

A detailed scheme of the architecture of a SEM can be found in Fig. 3.7a, where the locations of the electron source, the electromagnetic lenses and the detection units are shown. In case of non-conductive samples, electrons cannot be easily evacuated from the sample's surface and therefore affect the contrast and resolution of the image, a phenomenon called *charging effect*. To reduce the importance of charging effects, non-conductive samples should be coated with a few nm of conductive materials such as Cr, C or Au, prior to observation.

3.4 Electron microscopy and sample preparation by focused ion beam

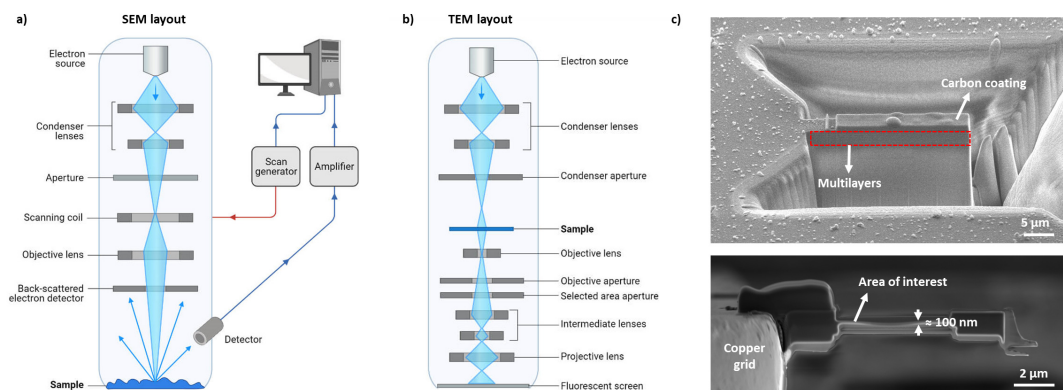


Figure 3.7: a)/b) Layout of a standard scanning/transmission electron microscope architecture, showing the electromagnetic lens system used to shape and control the electron beam, as well as the location of the main detectors [122]. In c), the top image shows a cross-section of a multilayer sample (area outlined in red) during the preparation of a TEM lamella, while the bottom image shows a top view of a finished TEM lamella, with the thinned down area of interest in the middle of the sample, whose thickness is reduced to around 100 nm. The copper grid holding the sample is visible on the left side of the image.

The different modes of interaction of the electrons with matter are shown in Fig. 3.8a, which details the scattering of electrons and the generation of radiation upon impact, and the relative penetration depth of the beam's electrons inside the material. Different types of scattering can be exploited to gather different types of information in scanning electron microscopy [123]. Specifically, the most common detection systems of a SEM rely on two specific outcomes of electron-matter interaction, the emission of secondary electrons (SE) and the generation of backscattered electrons (BSE).

Secondary electrons result from the inelastic scattering of electrons of the primary beam, which transfer a considerable amount of energy to the lattice and result in the ejection of SEs from the material itself. These newly generated electrons are then guided towards, and collected by, a detector placed on the side of the sample. SE are most useful to image the topography of a sample, as the contrast depends on the number of SE attracted by the detector, which can be screened by the surface's features. Backscattered electrons (BSE), on the other hand, are electrons of the primary beam which are elastically scattered by large angles and travel back, in the general direction of the emission source. Since the amount of backscattering is dependent on the atomic number of the species constituting the sample (as heavier nuclei will exert a greater force on the primary electrons), BSE imaging is not only useful to obtain topographic information, but is also an effective tool to obtain chemical contrast, with heavier elements appearing brighter than lighter elements.

Thanks to these two contrast modes, SEM enables precise topography and composition analysis of a wide array of samples, with a potential resolution around 5 nm. However, there are instances where more advanced characterization techniques are needed, to push the resolution limit and to gain deeper insights into the fundamental structure of the specimen under study. To this end, TEM techniques enable a higher level of spatial resolution, as its

resolution is truly limited by the electron's wavelength, and not by the probe size, like in the SEM case. The configuration of a TEM is visible in Fig. 3.7b, and consists of an array of coils, acting as electromagnetic lenses, and a set of apertures that can be inserted or removed, depending on the analytical tool of choice. Since the electrons are transmitted through the specimen, the detectors are located after the sample position.

The main imaging tools in a TEM, providing contrast between amorphous and crystalline parts of the specimen, are bright field (BF) and dark field (DF) TEM imaging modes [124]. The switching between these two modes can be done by moving the objective aperture over specific diffraction points: if the primary beam is chosen, then a BF image is created, with crystals and thick areas appearing in darker hues, or black, because of the scattering of the electrons. If a diffracted beam is selected by the objective aperture (usually, by tilting the beam), only the crystals responsible for these specific diffracted electrons will be imaged with a lighter contrast, resulting in a mapping of crystallites with the same composition and orientation, in DF contrast.

Several other techniques, associated to TEM imaging, were used during the course of the thesis, notably selected area electron diffraction (SAED), high-resolution TEM (HR-TEM), high-angle annular dark field imaging (HAADF) and electron-dispersive X-ray spectroscopy (EDS). The following paragraphs briefly introduce each of these techniques.

SAED consists first in inserting an aperture after the sample to limit the electron beam passing through the material and towards the screen [124, 126]. As is the nature of TEM imaging, electrons are either diffracted by the materials' structure, or they pass through the sample without being scattered (see Fig. 3.8c). The electrons are then collected on the back focal plane, where the diffraction pattern of the material can be recorded. Amorphous materials result in diffused, ring-shaped patterns expanding from the center, as the absence of order prevents the concentration of diffracted electrons in specific points. This is visible, for instance, in the upper image of Fig. 3.8d. Conversely, monocrystalline materials exhibit a regular pattern of dots, each one corresponding to a specific crystalline phase and orientation. Polycrystalline materials show ring-shaped, but sharp patterns, due to the random orientation of the crystallites: the distance of the diffraction points from the center is the same, but their angle varies, creating the ring shapes (see lower image in Fig. 3.8d). The higher the number of crystallites, the more solid the lines look like. The location and spacing of the diffracted dots relies on Bragg's law:

$$n\lambda = 2d_{hkl}\sin(\theta_B) \quad (3.10)$$

Here, n is the order of the reflection ($n \in \mathbb{N}$), d_{hkl} is the interplanar spacing of a set of planes with Miller indices hkl and θ_B is the angle at which the equation is satisfied. The expression for d_{hkl} varies depending on the crystal system. For the convenience of the reader, the interplanar distance formulation is explicated in the following lines, for two common cases, the cubic and tetragonal systems [127]:

3.4 Electron microscopy and sample preparation by focused ion beam

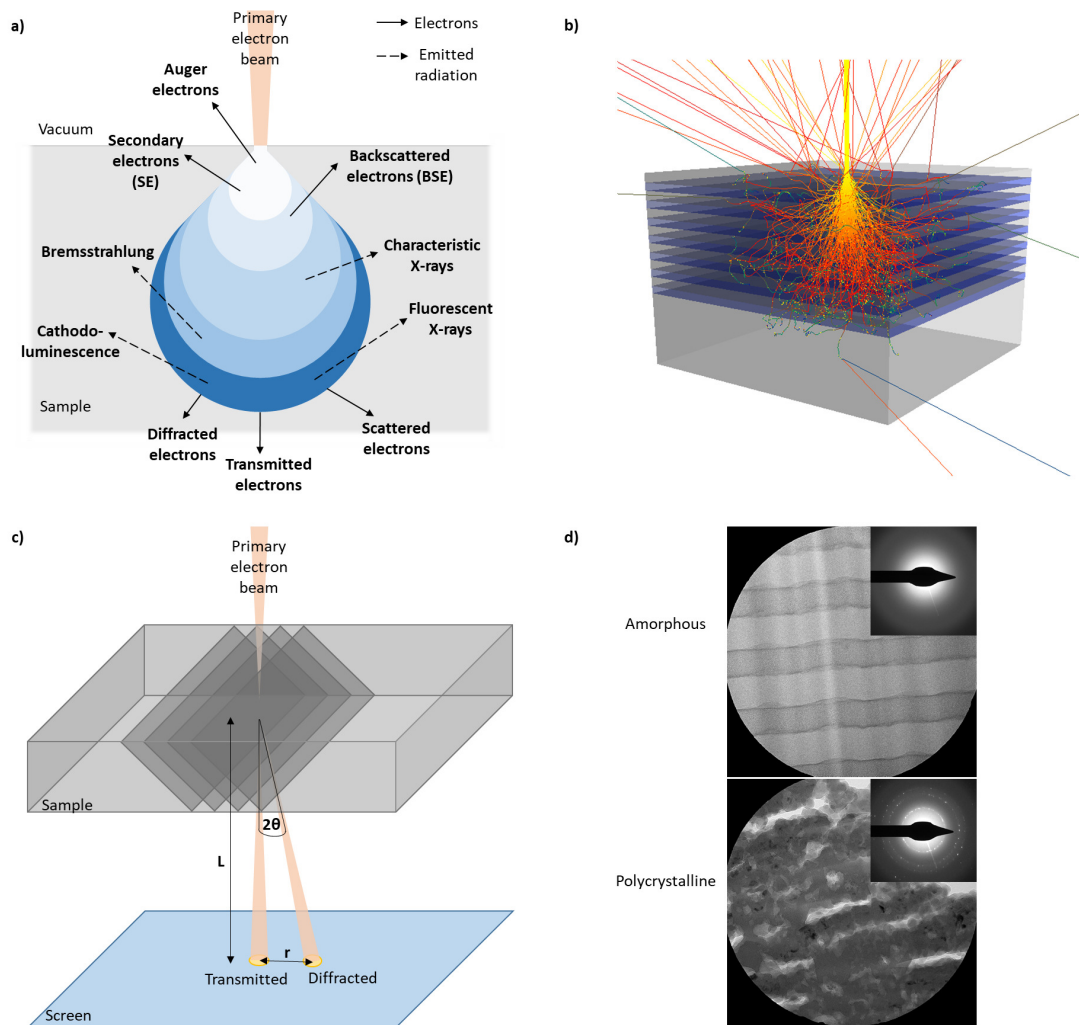


Figure 3.8: a) Interaction volume of the electron beam with a material, and its resulting effects, involving the generation and scattering of electrons, as well as the emission of radiation. b) Monte Carlo simulation of ionic interaction volume within a multilayer sample, at an acceleration voltage of 12 kV, as if the material was processed with a focused ion beam. The simulation was performed with the Casino software [125]. Image c) shows the principle of electron diffraction: the electron beam passes through a fine lamella of material, where the presence of ordered atomic planes results in elastic scattering of the electrons according to Bragg's law. This results, in the back focal plane, in the formation of a spotted image, where the location of each dot is typical of a certain phase and crystalline orientation. In d), two examples of diffraction patterns obtained on a $\text{SiO}_2/\text{SiN}_x$ multilayer sample: the pristine, amorphous material (as deposited) results in a diffuse ring pattern, typical of structures without long-distance atomic order. Conversely, a polycrystalline sample (the crystallites having a black contrast in the image) results in a diffraction pattern with well defined points, spaced from the center in proportion to the spacing between the planes. The ring pattern visible here arises from the sum of multiple points due to the random orientation of the crystallites.

$$d_{hkl}(\text{cubic}) = \frac{a}{\sqrt{h^2 + k^2 + l^2}} \quad (3.11)$$

$$d_{hkl}(\text{tetragonal}) = \frac{a}{\sqrt{h^2 + k^2 + l^2(a^2/c^2)}} \quad (3.12)$$

where a is the lattice parameter, and c is the vertical lattice parameter in the tetragonal system.

If BF and DF contrasts result from the choice of either the primary beam or the diffracted beam, HR-TEM imaging results from the interference of both beams, such that phase contrast is obtained and it is possible to register images of the lattice planes [124, 126], gaining information on the orientation of the crystals, their microstructure (i.e. plane spacing) and the state of the crystal-matrix boundaries.

Conversely, HAADF is a scanning technique where the beam is convergent and scanned across the desired area, imaging pixel-by-pixel [126]. Here, the detector is a ring with a large central aperture, placed after the sample. Consequently, as the name suggests, only highly scattered electrons are imaged. HAADF is intimately linked to EDS mapping, which also takes advantage of the scanning technique; the beam is scanned over the area of interest, promoting the creation of electron-hole pairs [126]. When an electron of the outer shell comes down to a lower energy level to fill the hole position, the corresponding release of X-ray radiation can be detected, and the atom can be identified on the basis of the radiated energy value. Scanning of the beam over the surface allows for the reconstruction of the atomic composition of the investigated area, resulting in the elemental mapping of a given location of the sample. As this analysis technique requires an electron beam to function, it can be employed both in a SEM or a TEM. In the framework of this thesis, only EDS analysis in TEM mode was performed, as the study was concerned with the state of the cross-sections of the layers, not with the samples' surfaces.

Finally, focused ion beam (FIB) processing enables the precise manipulation of a sample's surface, the exposure of the cross-section of a specimen for further characterization and the fabrication of specimens for TEM observations [128]. Here, a source filament is heated and subjected to a potential difference resulting in the ejection of ions (most often Ga^{3+}), which are then accelerated and focused on the sample's surface through a set of electromagnetic lenses. Depending on the energy of the ions, the interaction volume can change, and the ions will be scattered around the exposed zone, as illustrated by the simulation in Fig. 3.8b. It is then possible to carve the surface and to reveal the cross-section of the substrate under analysis. Combined with the insertion of gaseous precursors, it is also possible to deposit a variety of materials; for instance, the ionic deposition of a thin carbon layer over the area of interest is a necessary step before ionic bombardment, to reduce unwanted damaged to the structures of interest.

Given the geometry of our samples, being able to expose the cross-section of the layers without

damaging the surroundings is fundamental for a thorough analysis of the laser-affected areas [129]. FIB is also the tool of choice for the preparation of TEM specimens, as the lamellas are required to be extremely thin. The area of interest can therefore be carved out of the processed sample (see Fig. 3.7c), where a suitable specimen can be removed from the area and attached to a sample holder, and subsequently thinned down to the desired thickness with a series of gentler ionic swipes.

3.5 Summary

The materials' selection process involved the study of several candidate compounds, consisting of a variety of oxides and nitrides. Materials were sorted with respect to relevant physical properties, such as their refractive index, elastic modulus and coefficient of thermal expansion, but also depending on technological constraints, such as their availability and the required deposition techniques. The selected compounds were then deposited, resulting in the fabrication of three $\text{SiO}_2/\text{SiN}_x$ multilayer samples with different layer thickness distributions, as well as a $\text{SiO}_2/\text{TiO}_2$ and a $\text{Al}_2\text{O}_3/\text{Nb}_2\text{O}_5$ samples.

Laser processing was done using two distinct femtosecond lasers, emitting at a wavelength of 1030 nm and with pulse durations of 270 and 500 fs. The samples were mounted on motorized platforms to ensure mobility in all three directions. Three energy parameters, the exposure dose, the individual pulse fluence and the peak irradiance, were defined to express the amount of deposited energy.

Last, several scanning and transmission microscopy techniques were described, more specifically secondary electron and back-scattered electron contrast modes in SEM, as well as various TEM imaging modes such as bright-field, dark-field, high-resolution, selected area electron diffraction, high-angle annular dark field imaging and electron-dispersive X-ray spectroscopy. The fundamental characteristics and limitations of these techniques were discussed. These microscopy techniques have been extensively used throughout the this work.

Experimental results **Part II**

4 Modalities of laser-matter interaction in dielectric multilayers ¹

4.1 Introduction

We identify three predominant modification mechanisms occurring during femtosecond laser exposure of dielectric multilayers. The most visible one is layer ablation, where one, multiple or all the layers are removed from the laser-affected area, leaving a crater that can be bigger than the laser's beam waist, and that can also affect the substrate below it. Secondly, atomic intermixing between adjacent layers can be observed upon irradiation, under certain conditions. There, ionic diffusion during the non-linear absorption process results in a redistribution of the atomic species, effectively creating a solid solution composed by the different constituting elements of the layers. Laser-induced phase transitions, and notably crystallization from the amorphous state, represent a third modality, where under the influence of the femtosecond pulses, nm-sized crystallites are allowed to nucleate and grow. A fourth observed modification modality, consisting in the creation of nanopores embedded within the layers thickness, will be discussed more in detail in Section 5.7.

These first three types of modifications can also occur concurrently, with different locations within the laser-affected volume showing different responses to the laser exposure. For instance, depending on the exposure parameters, the top layers of a laser-affected area might be ablated, while the volume below could show a high degree of intermixing, and simultaneously being interspersed with crystallites. A notable example of synchronous modification phenomena is presented at the end of this chapter, in section 4.6, where the ejection of crystalline material from the layers' surface will be discussed.

In the present chapter, we investigate the use of femtosecond laser exposure to induce localized crystallization and elemental redistribution in amorphous dielectric multilayers, composed of alternating SiN_x and SiO_2 layers of sub-micron thickness. Specifically, we report on the occurrence of a laser-induced elemental intermixing process and on the presence of localized silicon nanocrystals clusters within the multilayer structure. The spatial distribution of these

¹Part of this chapter has been published in "R. Ricca, V. Boureau, and Y. Bellouard, *Ultrafast laser interaction with transparent multi-layer $\text{SiO}_2/\text{Si}_3\text{N}_4$ films*, Journal of Applied Physics, vol. 130, p. 243105, 2021" [130]

clusters goes significantly beyond the zone under direct laser exposure, providing evidence of energy being channeled transversely to the laser propagation axis, possibly through the interfaces between the nanoscale layers.

4.2 Experimental methods

Femtosecond laser exposure was performed using the setup described in section 3.3, with a 270 fs laser emitting at 1030 nm. The samples were exposed to the femtosecond laser in two different ways: in one case, the laser beam was directly focused on the stack's surface (see top side of Fig. 4.1), in what can be referred to as "top illumination". As such, the air-layer interface is mostly affected. Conversely, in a "bottom illumination" approach (see bottom side of Fig. 4.1) the laser beam has to propagate through the fused silica substrate first, before being focused in proximity of, or at, the layer-substrate interface.

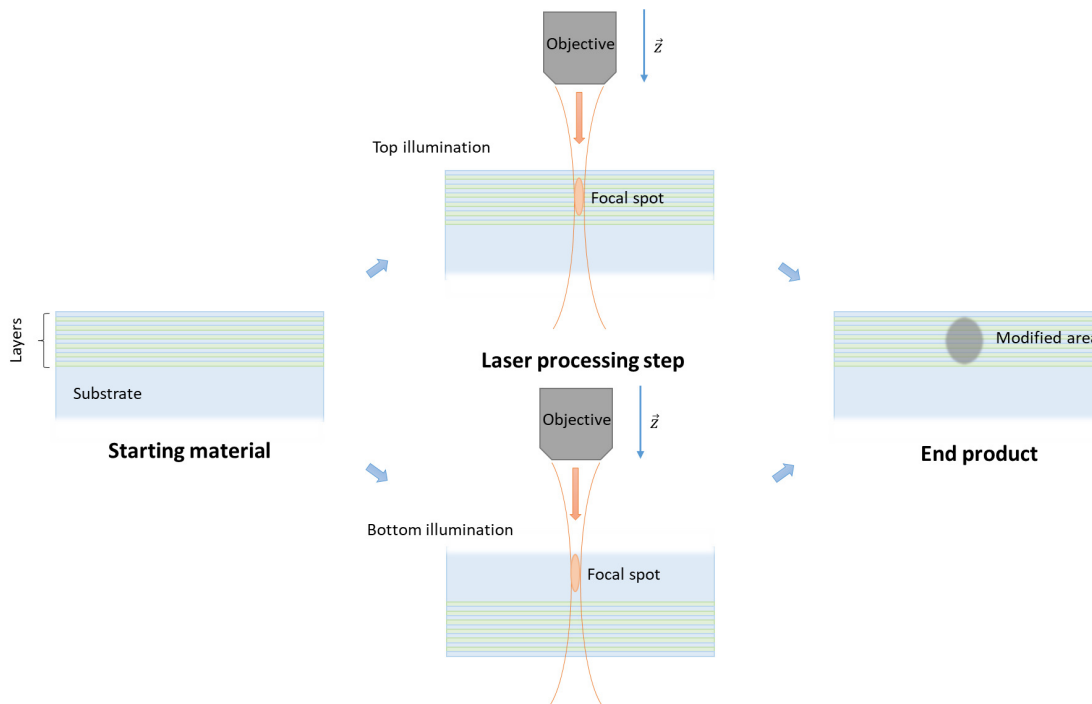


Figure 4.1: Scheme of the two modes of exposure: starting from its pristine, amorphous state, the multilayer sample can be exposed in a top illumination configuration, with the laser directly focused on the layers' surface, or a bottom illumination configuration, with the laser passing through the substrate before being focused in proximity of, or at, the layer-substrate interface. Both cases can result in laser-induced modifications, albeit with substantially different outcomes.

The purpose of this second exposure approach is to study the effect of the pulse propagation through the bulk substrate on the modifications dynamics. Here, the focal spot can be located several microns below the interface. In both cases, the laser beam is scanned over the specimen at constant speed.

We also define the metrics of *exposure overlap* as the number N_c of subsequent pulses emitted at a frequency f and translated at a velocity s , impacting the area defined by the beam waist w_0 , such that $N_c = w_0 f / s$. Here, on average, between 450 and 900 pulses impact a same zone, depending on the repetition rate used (250 or 500 kHz), and considering a scan speed of 1 mm s^{-1} , meaning that under this experimental configurations cumulative exposure is achieved.

The experiments presented in this chapter were conducted on Sample_Si3N4_A, consisting of a $\text{SiO}_2/\text{SiN}_x$ multilayer sample in $\lambda/4$ DBR configuration, so that the individual layer thicknesses are 119 nm (SiO_2) and 87 nm (SiN_x), respectively; a total of 13 double layers were deposited. Samples with similar designs were for instance used in Bloch wave propagation experiments [131]. With this choice of individual thickness values, the multilayer stack displays its maximal reflectance (at normal incidence) around the 700 nm mark, while showing a high transparency with respect to the laser's wavelength (1030 nm). This particular stopband interval corresponds to a maximum in sensitivity for standard imagers and for the wavelength range of the laser, after travelling through the silica substrate (in the case of backside illumination).

The changes in the microstructure were studied using Raman spectroscopy, SEM and TEM, while the specimen preparation was done with a FIB. Raman spectroscopy was performed with a Horiba Jobin-Yvon LabRam HR instrument, using a laser excitation wavelength of 532 nm, and the beam was focused with a 0.9 NA objective. The excitation laser average power was capped at 4 mW to limit local heating of the specimen during the Raman analysis, which might have otherwise artificially altered the laser-induced nanostructures during observation. SEM observations and cross-sections cuts were done on a FEI Nova 600 NanoLab dual-beam SEM/-FIB, running at 5/30 kV respectively. Samples preparation for TEM imaging was realized with a Zeiss NVision 40 dual-beam SEM/FIB, to produce lamellas from specimen cross-sections, thinned down to thicknesses of about 100 nm. TEM observations were done using a Talos F200S from ThermoFisher operating at 200 kV.

4.3 Layer ablation

Albeit not being the main interest of the thesis, layer ablation is the most visible and easily obtainable material's modification in these multilayer systems; to achieve this, it is sufficient to increase the exposure dose until some, or all, material is removed from the surface. From the characterization point of view, ablation is also easily observed. The laser affected area has a radius comparable to the laser's beam waist, or larger, hence optical microscopy is sufficient to spot ablation marks thanks to the contrast given by the index difference. If higher resolution is needed, a standard SEM is sufficient to gain insight on the topography of such modifications.

The amount of removed material depends on the composition of the layers and on the exposure dose. Materials more susceptible to non-linear absorption will develop a higher plasma intensity, and consequently a larger internal pressure, which will lead to a stronger ejection of material, even for lower pulse energies. Furthermore, delamination processes are also linked to the mechanical properties of the films.

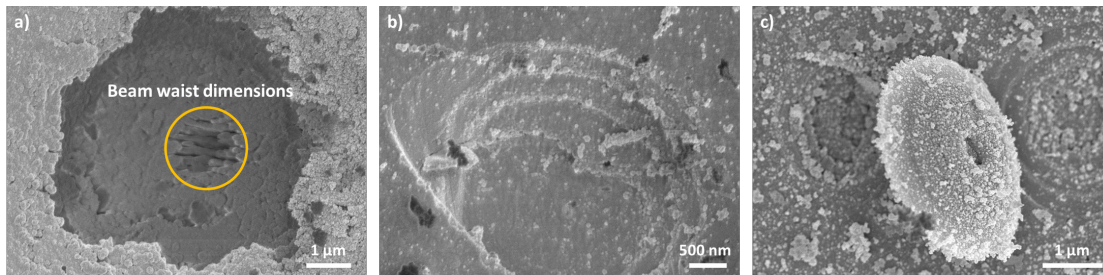


Figure 4.2: SEM images showing examples of laser-induced surface ablation on multilayers. a) Ablation/delamination of the layers, exposing the underlying fused silica substrate. At the center of the ablated spot, partial self-organization induced on the substrate is visible. b) Partial ablation of several layers, resulting in a terraced topography of the laser-affected spot. c) Residue of ablation remaining on the surface, shaped like a semi-open lid.

Examples of ablation are presented in Fig. 4.2, for spots exposed to a beam with a repetition rate of 750 kHz. For high exposure doses, not only the layers are removed, but the underlying substrate can be damaged as well. This is exemplified by the SEM image in Fig. 4.2a, showing a spot exposed at a pulse energy of 140 nJ, in top illumination condition. Here, the $\text{SiO}_2/\text{SiN}_x$ layers are removed from the exposed area and laser-induced self-organized patterns (nanogratings, as explained in Section 1.3) are inscribed in the fused silica substrate, at the center of the damaged zone, corresponding to the location of highest intensity of the beam.

Layer-by-layer ablation can also be observed, for energies low enough, so that one or more layers are delaminated and removed from the rest of the stack, as visible in Fig. 4.2b, resulting in a stair-like topography of the ablated site. This specific spot was also exposed in top illumination condition, but at a pulse energy of 30 nJ. This behaviour is visible, for instance, when analysing the cross-sections of the exposed areas, especially for low fluences, as shown in the next chapters on SEM and TEM images of laser-exposed samples, with several observations of partial ablation, with sharp limits between layers' interfaces. On very particular occasions, delamination residues can be found on the processed surface; this is the case shown in Fig. 4.2c, where the removed top layer is beautifully in display, like a micrometric pot lid, still partially attached to the surface. In this particular case, the sample was exposed from the background (i.e. bottom illumination configuration), with a pulse energy of 23 nJ.

Overall, ablation of the multilayers is easily obtainable and observable, but not very relevant for our studies. The ablation threshold varies for each sample design, but has been observed to be as low as 20 nJ, for a repetition rate below 1 MHz. Despite not being a central part of this thesis' work, ablation marks were used on our samples to determine the focal spot position with respect to the top surface of the layers, and to act as markers to find processed areas during SEM observation or FIB processing.

4.4 Evidence of laser-induced phase transitions

Non-ablative modifications are more challenging to study than ablated regions, as their contrast (both from topography and optical properties) is lower. Direct observation in the plane perpendicular to the beam propagation direction, as would be the case for ablated spots, does not provide enough information, since the evolution of the laser-affected zone around the location of the focal spot, and along the beam path, cannot be easily imaged. Therefore, given the orientation of the modified zones and the dimensions of the laser-induced features, the visual analysis of the modifications necessitates electron microscopy techniques.

To this end, cross-sections of the laser affected zones were observed using a SEM to examine the post-exposure morphology of the multilayers, both in top (Fig. 4.3a) and bottom (Fig. 4.3b-d) exposure configurations. Prominent features are visible depending on the exposure conditions, including evidences of cracking and partial ablations (see surface topography in Fig. 4.3e), formation of periodic micro-voids (see cross-section in Fig. 4.3c and d), intermixing between layers (Fig. 4.3a, b, d), cracks across layers (Fig. 4.3b) as well as damages at the layer-substrate interface (Fig. 4.3b-d). Additionally, Fig. 4.3d shows a more pronounced confinement of the modifications in the nitride layers, suggesting that non-linear absorption is initiated in SiN_x , at a lower energy threshold than SiO_2 .

The cases of bottom illumination shown in Fig. 4.3c, d and e are particularly interesting. The effective wavelength of the incoming laser beam travelling in the substrate is approximately 710 nm, given the original laser wavelength of 1030 nm and the refractive index of the fused silica substrate ($n = 1.45$). This wavelength value lays within the peak reflectance band of the Bragg reflector, as visible in Fig. 3.3a. As a result, the incoming light is strongly reflected at the interface. The first layers of the Bragg mirror are subjected to the highest energy and consequently are the first to be affected, as is confirmed in images c and d. Higher pulse energies and shorter layer-focal spot distances are expected to enhance the ionization rate and result in broader modifications, as visible in image b. Finally, in the case of image e, the rapid plasma expansion may explain the formation of cracks distributed symmetrically and normally to the shockwave front (expected to propagate from the layers-substrate interface).

SEM observations were supplemented by Raman spectroscopy measures along, and perpendicularly to, the laser-written lines. As more thoroughly explained in Appendix B, this technique explores the nature of the chemical bonds within a material, as the intensity of scattered radiation (Stokes and anti-Stokes scattering) depends on the vibrational energy of a bond, and can be traced for different probe wavelengths. This results in a continuous spectrum showing a series of peaks, which are more or less sharp depending on the crystalline content of the material.

The position, height, width and shift of the peaks give useful indications related to the state of the material and its microstructure, as well as the presence or absence of defects and residual stresses. During the measurements, we had to carefully limit the intensity of the probe beam, to prevent further modifications of the area under study. The Raman spectrum of the bare

Chapter 4. Modalities of laser-matter interaction in dielectric multilayers

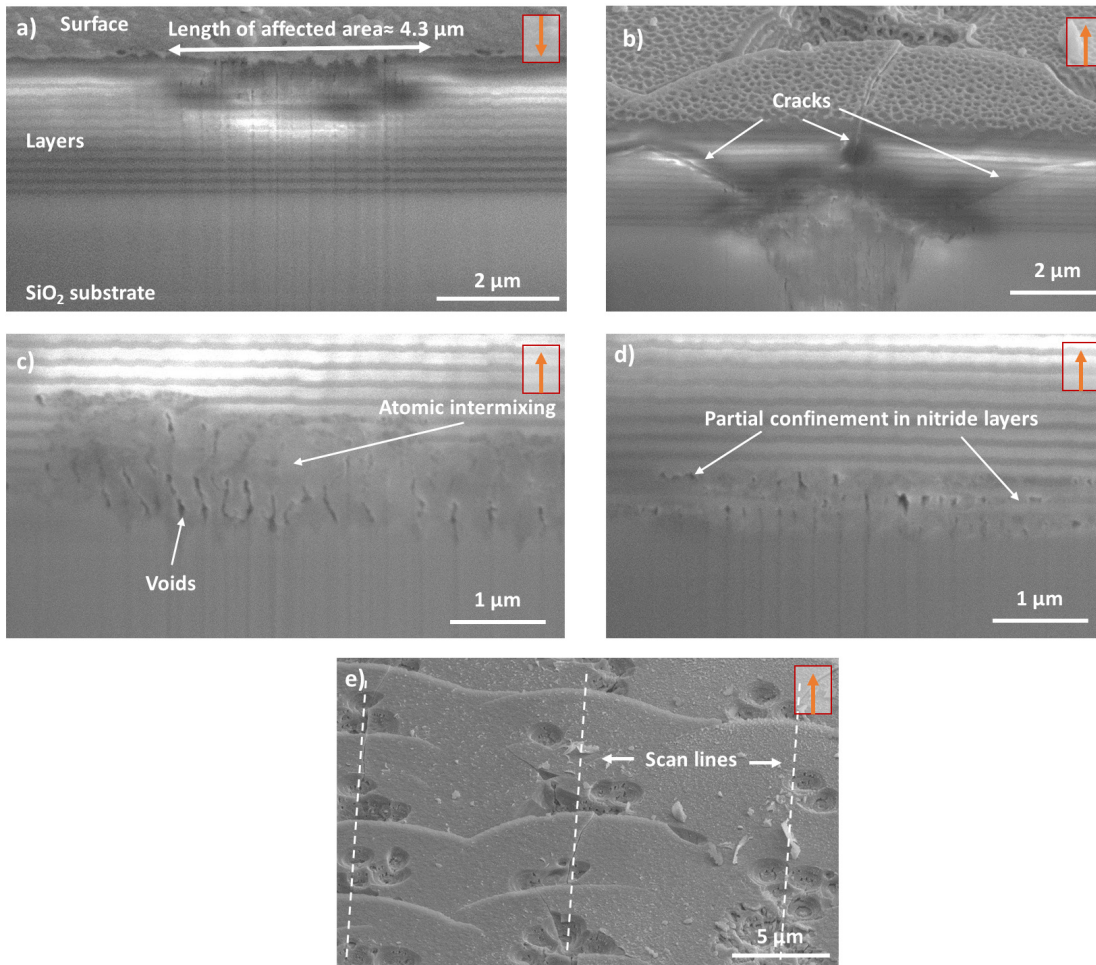


Figure 4.3: SEM images of laser-exposed regions. Images a)-d) show cross-sections, obtained through FIB milling of the surface at the locations of interest. The orange arrows (top right corner of each image) show the beam propagation direction, corresponding to one of the two exposure configurations presented in Fig. 4.1. Specifically, a) shows the result of top illumination of the multilayer sample, with a central section of greater intermixing of the layers and an affected area larger than the beam size. b-d) Modified zones in bottom illumination mode, at a repetition rate of 100 kHz and scan speed of 1 mm s⁻¹. The pulse energies are of 500 nJ in c), 250 nJ in b) and d) (deposited energies 7.07 and 3.54 kJ cm⁻², pulse fluence 78.6 and 39.3 J cm⁻², peak irradiance of 68.4 and 34.2 TW cm⁻², respectively) while the distance between layers and focal spot is 10 μm in b), 40 μm in c) and d). e) Specimen's top surface, in the case of a bottom illumination exposure processing, showing localized fractured pits and longitudinal cracks, transversely to the scan direction.

substrate, used as a reference, is shown in Fig. 4.4a. A noticeable shift and narrowing of the main band is observed after deposition of the multilayers (Fig. 4.4b). We attribute these effects to the presence of residual deposition stresses between layers and between the stack of layers and the fused silica substrate. Near and within laser-affected zones, the presence of a narrow and intense peak, centered around 515 cm⁻¹ (Fig. 4.4c) indicates the occurrence of a localized crystallization event, which can be attributed to a crystalline silicon phase (c-Si) [132].

4.4 Evidence of laser-induced phase transitions

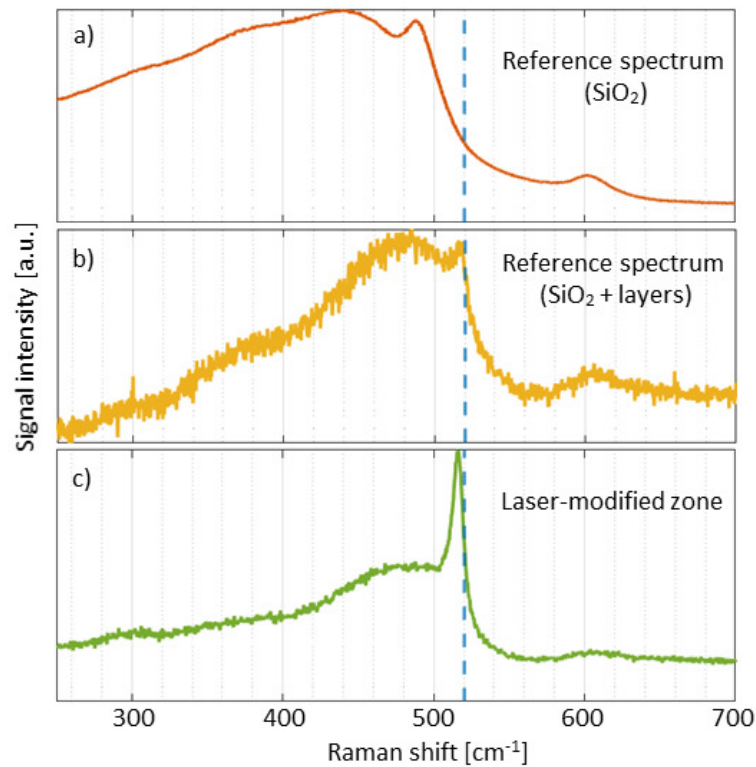


Figure 4.4: Raman spectra of un-exposed and exposed regions. a) Reference curve of an amorphous silica (SiO_2) substrate, measured on the backside of the samples, far away from the multilayers. b) Pristine multilayers' surface, and c) measured spectrum from a laser-affected zone. The dotted blue line shows the position of the crystalline silicon peak (at 520 cm^{-1}), for reference [132]. Due to the low intensity of the Raman laser, which has been limited to preserve the structural integrity of the features of interest in the specimen, the spectra related to multilayer regions are noisier than the reference curve.

A small, but persistent shift in the interpreted Si peak position, if compared to the reported c-Si values ($5\text{-}10 \text{ cm}^{-1}$), is observed, on average up to 20 cm^{-1} , and is attributed to residual stress induced by the lattice mismatch between crystalline regions and the surrounding matrix [133]. More specifically, sharper peaks are shifted towards wavenumbers higher than 515 cm^{-1} , while the shallower peaks (indicating a lighter presence of crystallites) are shifted towards lower wavenumbers.

TEM observations of cross-sections of the exposed regions were used to confirm the presence of crystalline regions within the laser-affected zones, and to map their location and distribution. A first observation was done on a sample exposed in the top illumination configuration, at a repetition rate of 250 kHz , a scan speed of 1 mm s^{-1} , an exposure dose of 2.49 kJ cm^{-2} , a pulse fluence of 5.54 J cm^{-2} and a peak irradiance of 4.8 TW cm^{-2} . A BF-TEM image of the sample is shown in Fig. 4.5a. The various layers are clearly visible, with the SiN_x layers (darker) alternating with the SiO_2 layers (lighter). Empty spaces appear white, while the crystallites appear as small dark regions, when oriented in strong diffracting conditions. At a first glance, the presence of nano-crystalline regions observed in Raman measurements is confirmed by the

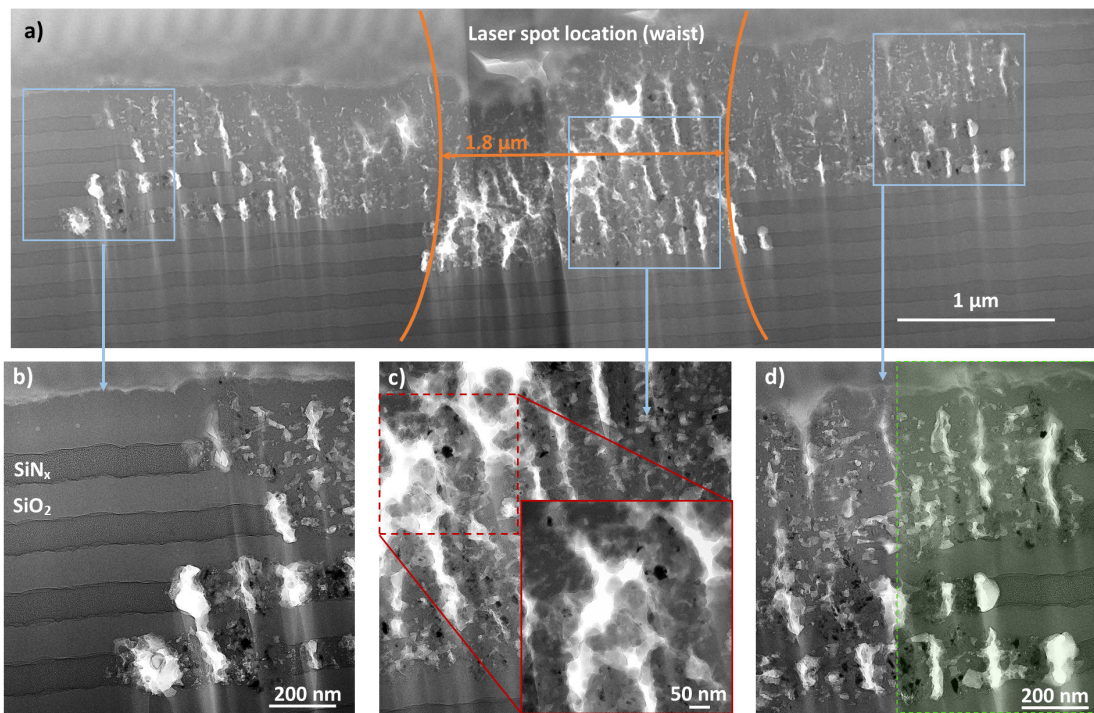


Figure 4.5: a) BF-TEM image of a sample exposed in top illumination configuration, corresponding to a cross-section of a written line. The laser spot location and the size of the beam waist are shown in orange. Three distinct areas (highlighted in blue) are further magnified in images b)-d), showcasing examples of the left, central and right parts of the damaged region. In d), the section highlighted in green is further analysed by EDS mapping in Fig. 4.8.

presence of isolated dark clusters in the BF images. The dimensions of these nano-crystallites vary significantly, but do not exceed 50 nm in diameter, as evidenced in the magnifications of the left, center and right regions in Fig. 4.5b-d.

It is remarkable that the dimensions of the damaged area exceed several times the dimensions of the laser beam waist at the focal point, suggesting that part of the incoming laser energy was propagated away from the zone under direct laser exposure through the denser layers. The location of the beam waist is highlighted in orange in Fig. 4.5a, and is assumed to be located at the center of the modified zone, due to its mirror symmetry. This central zone experienced higher intensity and corresponds to a zone where the deepest (in terms of penetration through the layers) modifications are observed. The average width of this modified central portion is $2 \pm 0.25 \mu\text{m}$, which is in good agreement with the measured beam waist at the focus. The modified region then extends further, both on the right and on the left of the beam waist location, by approximately $2 \mu\text{m}$ in each direction. Remarkably, crystallites are also found in these locations. These nano-crystalline phases observed with the TEM are assumed to be at the origin of the crystalline peak found in the Raman spectra (see Fig. 4.4).

Other salient features to be observed on the TEM images are the sharp boundaries between

4.4 Evidence of laser-induced phase transitions

modified and pristine regions, both along and transversely to the laser propagation direction, defining the edges of the damaged zones. Here, modifications are most often confined in the higher index layers (SiN_x), and stop abruptly in the transverse direction a few microns away from the focal waist. This lack of gradual transitions is also observed along the propagation direction. Note that the non-linear nature of the interaction is illustrated by the abrupt transition between modified/non-modified SiN_x layers. Although it is based on post-exposure investigations, this observation brings evidences that part of the incoming laser beam energy was channeled away over significant distances from the beam waist through the higher index SiN_x layers. This happened in a non-thermal regime as the modification remained mostly confined in the SiN_x nano-layers, as evidenced by the distinctly visible boundaries within the SiO_2 layers, and by the absence of ion migration between layers outside of the beam waist location.

This observation suggests an ionization mechanism driven by evanescent-like and coupled waves propagating in the denser SiN_x layers. The initiation and partial confinement of the modifications in the SiN_x layers is consistent with the properties of a quarter-wave design Bragg reflector, for which the pulse's electric field intensity is modulated in such a way to have maxima preferentially located in the higher-index layers [52, 53], therefore increasing the probability of localized ionization taking place there. Taking into account the lower band-gap of SiN_x layers and the Bragg reflector properties, damages are expected to be first initiated in the SiN_x layers, a hypothesis that was confirmed by the TEM observations. Furthermore, as seen in figures 4.5a-d, the void regions are distributed periodically and stretch along the vertical direction (i.e. beam propagation direction), extending along the length of the damaged area.

The crystallographic structure of the crystallites found in the central region of the sample (i.e. the beam waist highlighted in orange in Fig. 4.5a) was investigated by registering their diffraction pattern through SAED, as visible in Fig. 4.6a. Here, a sequence of well defined ring patterns is observed, a phenomenon that can be explained by the random orientation of the crystal grains, as introduced in Section 3.4. The spots are well organized in the reciprocal space, with positions measured from Fig. 4.6b. The comparison of the peaks distribution with the literature [134] hints at a diamond-structured silicon phase, with no other ordered phases detectable. More specifically, experimental and theoretical values agree within a maximum deviation of 1.4%, as reported in Table 4.1.

Table 4.1: Comparison of values of interplanar distances, as measured and as calculated for diamond-Si, in nm^{-1} .

Corresponding plane	Measured	Theoretical
(111)	3.21	3.189
(220)	5.28	5.208
(113)	6.15	6.107
(004)	7.44	7.365
(133)	8.08	8.026

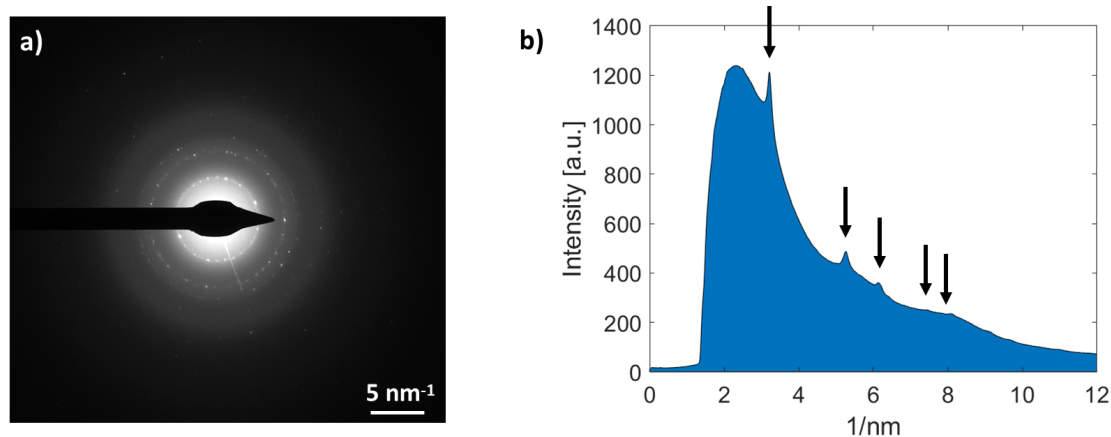


Figure 4.6: a) SAED pattern of a 850 nm-diameter region of the damaged region and b) its corresponding rotational averaging, showing the positions of the crystal peaks over the diffuse background.

In the case of bottom illumination exposure, depending on different laser parameters and on the location of the beam waist with respect to the layers, three types of modifications were induced: local damages in the form of voids and intermixed/crystallized regions, internally confined explosions, and layer ablation, respectively. Sets of lines were written with the laser beam focused through the substrate and focused below the multilayers' interface, with the same repetition rate and scan speed, but varying the pulse energy (from 50 to 200 nJ) and the focal spot position (from 50 μm to 0 μm below the surface, in steps of 5 μm). An example of surface topography after laser exposure is visible on the bottom image of Fig. 4.7a, showing the alternation of localized ablations and pristine surface along the writing direction. The cut location of the lamella shown in Fig. 4.7c and Fig. 4.9 is also indicated. The presence of crystallites was rapidly assessed with Raman spectroscopy by scanning perpendicularly to three written lines, and the results are shown in Fig. 4.7b, presenting sharp peaks that can be assigned to crystalline Si, clearly demonstrating the occurrence of crystallization processes.

In this case as well, TEM observations were performed to gain further insights on the nature of the modifications; the focus of our attention was brought to the case where no top layer ablation occurred, as visible in Fig. 4.7c. This specific case corresponds to an irradiation with laser pulses fired at a repetition rate of 500 kHz, a scan speed of 1 mm s^{-1} and a pulse energy of 100 nJ, resulting in an exposure dose level of 10.61 kJ cm^{-2} , a pulse fluence of 23.58 J cm^{-2} and a peak irradiance of 20.5 TW cm^{-2} . The focal point is localized approximately 7.5 μm below the substrate/layers interface. Like in the previous exposure conditions, crystallites appearing as dark clusters on TEM images (Fig. 4.7c) are noticed, well spread around the modified area. Just like for top illumination, the region affected by the laser is several times wider than the actual beam waist. Here, however, the modified zone shows a circular symmetry and a greater degree of homogeneity. For instance, damage propagation is still preferentially targeting the SiN_x layers, but to a much smaller extent than in the case of top illumination exposure. It is worth noting that the presence of crystals is confirmed not only within the multilayers, but also in the fused silica substrate. Furthermore, the SAED analysis in multiple locations of

4.4 Evidence of laser-induced phase transitions

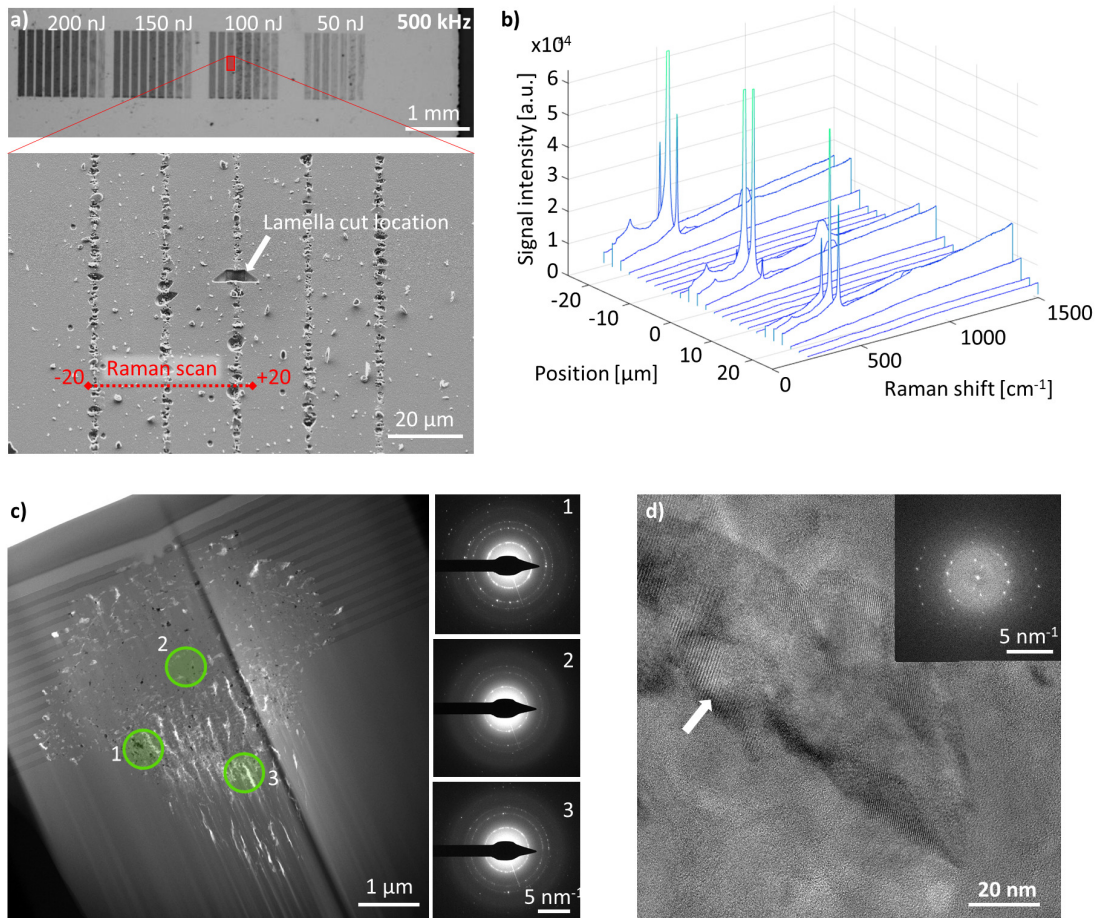


Figure 4.7: a) Optical micrograph of a sample exposed at a repetition rate of 500 kHz and in bottom illumination configuration. Each set of line blocks is written at different pulse energies, and within each block there are sets of lines written at decreasing distances from the multilayer-substrate interface. One of these sets of lines is highlighted in the SEM image just below, corresponding to the location of the lamella shown in c) as well as in Fig. 4.9. b) Raman mapping of the surface, showing clear crystalline peaks at the location of the lines. The scan has been performed perpendicularly to the three lines left of the line set, as evidenced in image a). c) BF-TEM image of the lamella, confirming the presence of crystallites within the intermixed volume. The SAED patterns on the right, corresponding to the locations 1 to 3 on the lamella, prove that the same crystalline phase is obtained in the whole laser-affected area, both in the substrate and in the volume previously occupied by the multilayers. Image d) shows a high-resolution TEM image of the bigger crystallite in area 1 (indicated in image c), with its Fourier transform in inset, evidencing the distribution of the crystal planes.

the cross-section shown in Fig. 4.7c (green circles 1 to 3), confirms that the crystallites are diamond-lattice silicon, showing the same diffraction pattern as the one analysed in Fig. 4.6a.

Finally, Fig. 4.7d shows a high-resolution TEM image of a large crystallite inside the amorphous matrix, located within the green circle number 1 in Fig. 4.7c. The arrangement of the atoms along well ordered planes is evident, with their Fourier transform shown in the inset (corresponding to the plane periodicity), confirming that the crystals are composed by pure Si.

4.5 Inter-layer atomic intermixing

Previous SEM and TEM images evidenced the presence of substantial ion exchange between layers, with blurring or even disappearance of boundaries between the SiO_2 and SiN_x layers. To better investigate the extent of the intermixing process, elemental mappings were performed by scanning TEM (STEM) energy-dispersive X-ray spectroscopy (EDS) analysis.

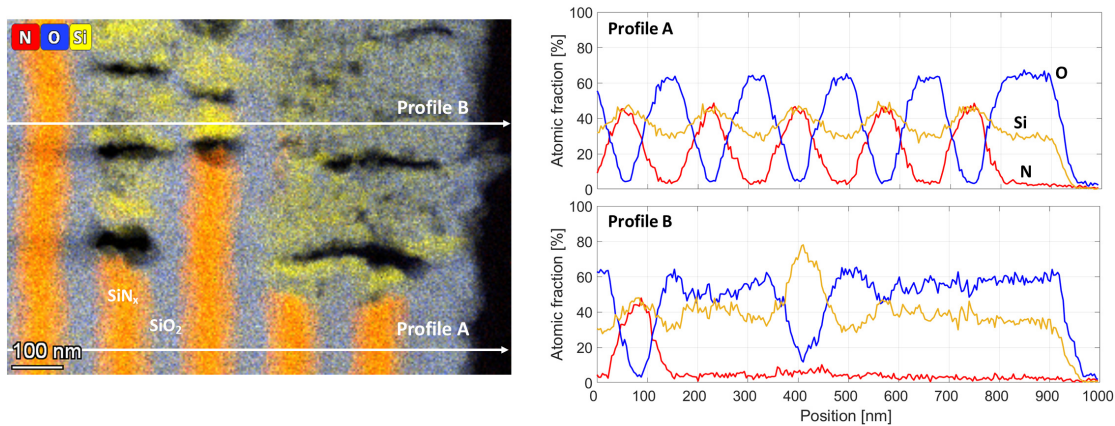


Figure 4.8: EDS elemental color-map (net counts) of the right part of the damaged region, indicated in green in Fig. 4.5d, rotated 90° clockwise for better visualization of the scan profiles. Two profile scans are traced along the unmodified (A) and modified (B) regions, with an integration width of 35 nm, and the corresponding evolution of the atomic fractions is plotted on the right.

Figure 4.8 shows such a map for the right-hand side of the sample exposed in top illumination condition, which is highlighted in green in the BF-TEM image in Fig. 4.5d. Here, it is possible to notice how, in the damaged zones, the nitrogen content decreased, being substituted both by oxygen and silicon. The accuracy of the atomic fraction profiles can be estimated using profile scans, that trace the atomic fraction of the selected elements and plot them over the position along the scan length. For instance, profile A shows the elemental distribution within the undamaged region, as indicated in the left-hand side image. In the SiO_2 layers, the atomic percentage of Si and O is measured to be 34% and 66%, respectively, corresponding to the nominal stoichiometry of SiO_2 . For SiN_x , the ratio between elements is more balanced, with approximately 50% of both elements. This confirms that the deposited nitride layers are slightly more rich in silicon than the stoichiometric compound. Things change when scanning over the modified region, as visible in profile B; here, the depletion of N atoms is evident, with the laser-affected area having, on average, a composition of Si-rich SiO_2 . A remarkably high concentration of Si is measured at the position 400 nm, corresponding to the location of a Si crystallite. It is possible that gaseous N_2 , after separation from the Si, found itself trapped into the voids, and was then subsequently released into the atmosphere during FIB machining, due to the cutting process and the exposure to the environment.

The case of bottom illumination exposure condition is equally interesting; EDS mapping of the elemental distribution was done on the same lamella already shown in Fig. 4.7c. The modified volume can be separated into three distinct regions, named I to III, according to their

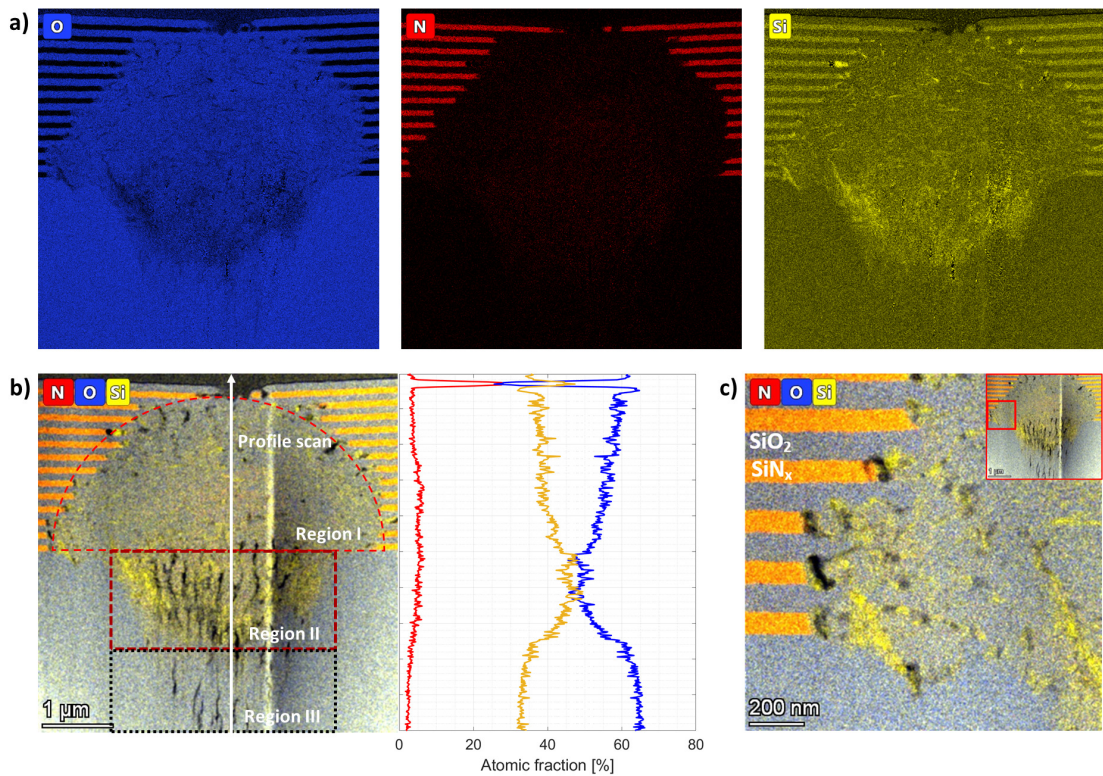


Figure 4.9: a) EDS elemental mapping of a laser-exposed sample in bottom illumination mode, with isolated maps for Si, O and N atomic distributions. Image b) shows the combination of these three maps, together with a plot of the atomic fraction along a vertical line on the center of the affected area. The image is divided into three distinct regions, named I to III, which show specific modified features. In c), a magnification of the layer-substrate interface on the left side, shows the abrupt modified-pristine interface within each layer.

modification pattern. Similarly to the case of top illumination, the modified area as a whole is almost fully depleted of nitrogen (Fig. 4.9a). On the one hand, a nitrogen atomic content of 4% is measured on average in the upper 1 μm of region II, increasing to 5% when going deeper in region II and in the top of region I (see profile of Fig. 4.9b). Detection of nitrogen within the modified region of the substrate indicates a migration of this element from the SiN_x layers into the substrate during laser exposure. On the other hand, the concentration of Si increases in the damaged areas (see profile of Fig. 4.9b). Although it was originally composed by stoichiometric amorphous SiO_2 (atomic O/Si ratio of 2), like also measured in the lower part of region III, average atomic ratios of O/Si of 1.5 and 1.1 are measured in region I and in the top of region II, respectively, confirming a strong increase in Si concentration.

The characteristic dome shape of region I, symmetric with respect to the optical axis, and the somewhat homogeneous mixing of atomic species in its volume, suggest that the Bragg mirror gradually ruptured as ionization of the substrate started. This could lead the broadband radiation scattered from the interface to propagate homogeneously within the dome volume without a preferential direction, giving rise to the circular symmetry of the modified region.

Silicon clusters regions, showing higher fractions of Si compared to the initial stoichiometry of SiO_2 and SiN_x , are clearly identifiable and distributed along the laser-modified zones, inside and outside the optical beam waist. Within these regions, the concentration of Si atoms reaches up to 80%. Note that pure Si regions are not observed in EDS maps due to projection effects of the TEM measurements over the lamella's thickness, which at 100 nm is thicker than the Si clusters. Generally, oxygen is present in a relatively homogeneous concentration, just slightly lower than the stoichiometric SiO_2 , most probably due to the same TEM projection effects. It is also possible to notice the abrupt limit between modified and pristine material, especially visible in Fig. 4.9c, with the absence of a transition region.

Layer intermixing is, therefore, observed for both exposure conditions, with EDS measurements enabling the mapping of the distribution of the atomic species and the tracing of the probable migration route of the ions, after the formation of the laser-induced plasma.

4.6 Ablation residues

Although different in nature, ablation, crystallization and intermixing phenomena can happen simultaneously, successively, or can partially overlap in time. Studying the composition of ablation residues, after laser processing, is a potential approach to gain better knowledge over the timeline of these modifications, since the particles might show evidence of crystallization and/or intermixing.

In both exposure configurations described in Fig. 4.1, ejection of particles was observed at high pulse peak fluence and deposited energies. Although the presence of these residues signals a transition towards an ablative regime and, as such, is of less practical interest, their compositions offer further insights on the modification dynamics. The ejecta concentration logically depends on the exposure dose and, in the bottom-illumination case, on the focal point position, i.e. the closer is the focusing to the substrate-multi-layer interfaces, the higher is the residues concentration in the ejecta.

These ejected particles accumulate on a collecting substrate (here, a borosilicate microscope slide), located at a fixed distance from the multilayers and within the laser beam path (Fig. 4.10a-b). Note that as the laser beam is unfocused at the collecting substrate, and hence, the energy density is not sufficient to trigger non-linear absorption, no modification of this substrate occurs. The collected material (Fig. 4.10c) is subsequently analyzed with Raman spectroscopy by scanning the probe beam on the surface with a $3\ \mu\text{m}$ -spacing between measurement points (Fig. 4.10d).

A selection of the Raman spectra is shown in Fig. 4.10d. These curves are chosen to highlight various spectral occurrences qualitatively, but do not contain quantitative information related to the crystallites distribution. The residues' Raman spectra exhibit crystalline peaks positioned around $515\ \text{cm}^{-1}$, consistent with our previous observation of non-ablated exposed regions (Fig. 4.4). Further referring to the previously shown TEM images, the ejecta contain

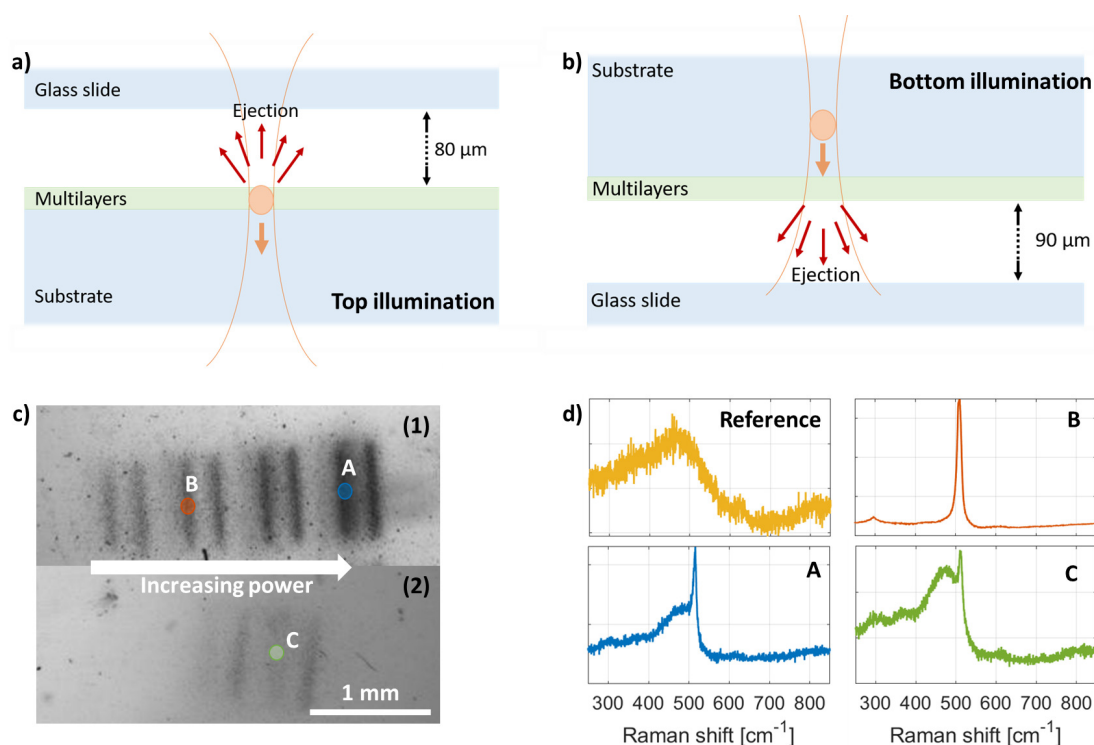


Figure 4.10: a-b) Configurations of the experimental setups for the laser-induced crystallite ejection, showing the respective direction of ejection of ablated residues, in the top and bottom exposure cases, respectively. The optical microscope image in c) shows the accumulation of ablated particles on the glass sample holder after bottom illumination (c1), showing the particles concentration increasing with pulse energy, and the same after top illumination (c2). The coloured circles and letters refer to the Raman spectra shown on the right, in image d). The yellow spectrum is provided as a reference and corresponds to the pristine glass slide collector substrate.

crystallites of the same phase identified in the non-ablated cases, as described in the previous paragraphs. These results confirm that both top and bottom exposure conditions lead to similar crystallization conditions. The presence of crystalline clusters in the ejecta logically indicates that the crystallization took place in the early steps of the interaction, before ablation effectively took place. As these experiments are not done with single pulses, crystallization may have gradually occurred, before the particles are propelled outside of the modified zone.

This experiment is somewhat similar to a Laser-Induced Forward Transfer (LIFT) process, in which ultrafast laser pulses are used to eject material from a selected thin film, effectively resulting in a controlled and localized deposition process [135]. Previous works in this field include the observation of the deposition of crystalline particles starting from an amorphous source [136, 137] as well as the deposition of transparent layers [68]. Here, starting from controlled multilayers compositions and thicknesses, the ejection process can potentially be exploited to deposit particles with exotic compositions, blending compounds from the various nanolayers.

4.7 Discussion

Before proposing a phenomenological interpretation of the events unfolding in these experiments, let us first summarize the main results of our observations. It is important to note that these are based on post-mortem analysis and, as such, do not provide indications on the exact sequence of events leading to the final phase.

In both exposure configurations, strong intermixing of the atomic species of the layers occurring within the modified zones is observed, together with the formation of a silicon nanocrystalline phase. A prominent feature is that the dimensions of the damaged areas are significantly exceeding the actual focal spot beam waist, with no evidence of delamination between nano-layers. Top illumination exposure displays a discrete damage morphology propagating far-off the laser-exposure site within the SiN_x layers, and defining sharp boundaries between damaged layers. This is particularly visible at the tail of the modified zone, with no evidence of diffusion from one layer into the adjacent one, suggesting localized energy confinement in the films with faster dynamics. The extent of these modifications and their confinement to the high-index layers suggest the presence of a coupled evanescent wave propagating sideways with sufficient intensity to cause localized ionization and plasma formation. The nature of this coupled wave can be multiple and is discussed further below.

Bottom illumination yields a structure considerably different from the top illumination case. The most noticeable difference is the prevalence of homogeneous atomic intermixing in the modified zones, instead than discretized modifications confined in particular layers, as it is mostly the case in the top illumination approach (at least, outside of the focal spot location). We labelled "region II" and "region III", in Fig. 4.9b, the modified regions localized within the substrate. The two regions are considered separately because region II has a particularly high fraction of Si with respect to the surrounding substrate, while region III is in line with the SiO_2 stoichiometric ratio, and only shows the presence of voids and cracks. In both regions, periodic self-organized voids forming nanoplanes are observed, stopping at a rather well-defined boundary where the interface between the first nano-layer and the substrate was previously found. Above it, a somewhat homogeneous (in sharp contrast with the previous case) dome-shaped area of several microns in diameter is found (labelled "region I" in Fig. 4.9b) that corresponds to a region where strong atomic intermixing occurs. The dome-shaped structure spreads over a region significantly bigger than the laser waist. As we do not see evidence of thermal dissociation of the material, the plasma was likely confined in a region that is now defining the regions I to III in the end-product. We also note that nitrogen diffused into the substrate in a rather homogeneous manner (see atomic fraction profile in Fig. 4.9b), which may indicate that towards the end of the process the plasma expanded in the direction of the bulk. Despite the fact that the interface between the substrate and the nano-layers vanished (interface between region I and II), the two regions are still clearly distinguishable and, given the presence of N in the substrate, this suggests that region I was formed first, while regions II and III followed afterwards. Region I may have formed first since the multi-layers absorption threshold is lower than in the silica bulk.

In both cases, the fine composition analysis indicates that SiN_x ionized first. This is particularly visible in the top illumination case, when observing the interfaces between the pristine layers and the modified ones. The SiN_x layers act as "wicks", feeding the surrounding material with ionized nitrogen and silicon. This observation is expected as the band gap of SiN_x is effectively lower than for SiO_2 (typically around 5 eV for SiN_x versus 9 eV for SiO_2) [138, 139]. As SiN_x has a significantly higher index, the existence of a guided mode in the confined layer is also to be expected in certain cases, corresponding to the photonic bandgap formed by the layer's structure (as is the case of Bloch-waves). The samples are designed as quarter-wave stacks, therefore a lower modification threshold of the SiN_x layers would be consistent with the modulation of the lasers' electrostatic field inside the multilayers, which is more intense towards the higher-index layers, as reported in the literature, also for layers of sub-micron dimensions [52, 53]. This would lead to the formation of a plasma early on, during the pulse-matter interaction, where the power contained in the pulse's tail is enough to reach the energy threshold for non-linear absorption in these precise locations. In the bottom exposure case, this can explain the presence of modifications both in the bulk and in the multilayers stack, this effect being potentially enhanced by the beam elongation induced by the pulse's propagation through the substrate, as explained at the end of Section 3.3.

In Fig. 3.3a, the measured reflectance spectrum of Sample_Si3N4_A presents a short but noticeable peak around 1030 nm, equivalent to 18% of reflectance. This means that multiple reflections of a fraction of the incoming pulses between the various layers are possible. This may explain the peculiar shape of the modifications visible in Fig. 4.5, where the top layers, exposed to a greater amount of secondary reflections, are more likely to get damaged than the lower layers, and multiple reflections can partially explain the propagation of the modifications along the surface plane of the layers.

In the following summary, we draw a few hypothesis to explain the formation of these complex structures. This scenario remains phenomenological and would require further dynamical observations to confirm some of its key features. Keeping these reservations in mind, a possible sequence for both plasma formation and material modifications is as follows:

1. Seed electrons are initially produced through multiphoton absorption in the SiN_x layers due to the modulation of the laser's electrostatic field by the Bragg reflector, as well as the lower ionization threshold of silicon nitride compared to silicon oxide. This is valid for both exposure conditions, top and bottom. However, in the case of bottom illumination, the Bragg reflector acts as a mirror for the effective laser wavelength, as the beam propagates inside SiO_2 instead of air. This would explain why in the case of bottom illumination, the first layers to be modified are always at the boundary between the Bragg reflector and the multilayer. These layers rapidly build up a plasma, through subsequent ionization processes, which is confined in the layers through additional electron excitation mechanisms.
2. As the confined layered-plasma structure density increases, the dielectric function

acquires a metallic behaviour and favors the propagation of energy sideways, along the $\text{SiN}_x/\text{SiO}_2$ interfaces. It may share similarities with plasmon-polariton coupling reported at interfaces between layers supporting transverse optical Tamm states, in the case of normal incidence exposure [140].

3. To support intermixing events, we propose the following mechanism; as the plasma builds up into a more homogeneous volume and in temperature, ions gain a sufficiently high energy to diffuse between multilayers as well as in the supporting substrate, as noticed in the case of bottom illumination, mimicking an ion-implantation process. To support these observations, we note the presence of nitrogen down to a few microns within the substrate itself in the case of bottom illumination, where it was not present in the first place, and the redistribution of oxygen throughout the modified zones for both exposure configurations.
4. As multiple pulses impact a same exposure zone at an average rate of 352 - 176 pulses μm^{-2} with a time separation of 2 - 4 μs (depending on the repetition rate), pulse-to-pulse additive effects occur, and may account for some of the self-organized structures observed, just like in the case of nanogratings formation described previously in bulk silica [36, 42, 141, 142], possibly enhanced and stimulated by the presence of the Bragg reflector.
5. The fast intermixing and the ionic mobility produces the seeds for nanocrystalline silicon phase formation. In both cases, these nanocrystalline phases seem to have nucleated preferentially in the vicinity of interfaces. A possible explanation is that these are regions of higher pressure confinement and higher defect density, hence higher phase nucleation probability.

4.8 Summary

This chapter reported on the interaction of ultrafast lasers with stacked $\text{SiO}_2/\text{SiN}_x$ sub-wavelength thick layer coatings, deposited on a fused silica substrate as a one-dimensional periodic structure. The exposure conditions led to strong and controlled intermixing between layers, and to the formation of cubic-diamond silicon nanocrystals dispersed within the laser-affected zones. The characteristics of elemental mixing, crystallization and ablation were discussed, together with a case study on the crystallites found in ablation residues.

Two exposure cases were considered, leading to a different behaviour related to the properties of the Bragg reflector. Top illumination configuration, i.e. with the laser beam travelling through the multilayers first, led to laser-induced modifications initiated in the SiN_x layers, propagating into the SiO_2 layers and stretching laterally significantly more than the beam waist at the focus. This unravels a strong coupling between the incoming wave and a coupled mode in the SiN_x , higher density, layers. Bottom illumination mode, where the laser beam was focused just below the layers after travelling through the whole substrate, yielded

another outcome, and was characterized by a more homogeneous volume where strong intermixing occurred. Moreover, diffusion of atoms from the multi-layers into the substrate was observed, with the addition of a self-organization phenomenon within the same substrate, whose formation is possibly enhanced by the presence of the Bragg reflector.

In conclusion, the exposure of multilayer dielectric substrates to femtosecond lasers potentially offers a powerful method for a selective and confined formation of crystalline compounds in amorphous dielectric matrices, starting up from discrete elements of well-defined composition and benefiting from the intrinsic advantages of non-linear absorption.

5 Laser-induced confined crystallization in multilayer systems ¹

5.1 Introduction

In bulk substrates, spatial confinement of a Gaussian beam along the optical propagation axis can be achieved by tightly focusing it using high numerical aperture lenses [144], as shown in Fig. 5.1a. However, the extreme peak power of the highly confined beam also leads to extreme pressures (estimated to TPa in certain cases [145]), making it difficult to induce stable material modifications without inducing cavitation. Overly tight focusing may also lead to undesired filamentation effects. Moreover, the tight focusing of the beam is generally only able to confine the energy of the laser, and therefore also the extent of the modified area, on the plane orthogonal to the beam propagation direction, while the dimensions along this axis can still extend for several μm . By exploiting the index-dependence of the absorption threshold, we can try to confine the energy, and therefore the modifications, along the propagation direction as well, by creating a succession of i areas of different $E_{th,i}$, for example a binary system of layered materials where $E_{th,1} \gg E_{th,2}$, as shown in Fig. 5.1b. It can be argued that, by creating systems that alternate several layers of materials with different E_{th} , it should be possible to control the distribution, size and structure of the modified regions, by tuning parameters such as the layers thicknesses and the refractive index contrast between the layers. In this case, the dimensions of the modified zone (labelled W_i , for width, and L_i , for length, as seen in the figure), especially the length, would be smaller than in the case of high-NA processing.

Here, building on the observations reported in the previous chapter, we propose a method based on stacked layers. Specifically, by exploiting the index-dependence of the absorption threshold, we confine the energy, and therefore the modifications, *along* the optical propagation axis.

¹Part of this chapter has been published in "R. Ricca and Y. Bellouard, *Single-Layer Subwavelength Femtosecond-Laser-Induced Confined Nanocrystallization in Multistack Dielectrics*, Physical Review Applied, vol. 19, p. 044035, 2023" [143].

5.1.1 Confined modifications in multilayers

For a single pulse travelling through a layered stack, the succession of interfaces results in multiple Fresnel reflections, reducing the intensity of the transmitted beam, through destructive interference between the reflected light and the rest of the incoming pulse. The reflection can be partial or total, depending on the wavelength of the laser, the choice of materials and the thickness and number of layers. This layered construction principle is commonly used in highly efficient DBRs that reflect narrow spectral bands of light. Technically, the layered construction modulates the propagating beam's electric field, with localized intensity minima and maxima, located within specific layers (see Fig. 5.1b). Consequently, a non-linear absorption threshold for a layer in the stack can be reached in specific locations [55]. As discussed in Section 1.4, in quarter-wave distributed Bragg gratings, non-linear absorption is generally initiated within the high index materials, due to their lower laser-modification threshold [146]. It was also shown how the electric field can be further modulated by adapting the thickness and the composition of the layers [61], leading to a shift of the high-intensity peaks positions. This approach has been exploited as a means for reducing the laser-induced damage threshold of optical components, as illustrated in [58, 64, 70, 147].

In such cases, in addition to the multiple reflections at the layers' interfaces, a feedback phenomenon arises from the pulse overlap when multiple pulses are shone on the same area. Indeed, each pulse induces structural changes in a pulse-to-pulse dynamically changing landscape. When the time separating two consecutive pulses is shorter than the thermal relaxation time in the focal volume, the temperature gradually rises and a heat-dominated regime is observed, producing laser-affected zones significantly bigger than the spot size. In the opposite case, the structure evolves step-wise, after each pulse, regardless of the time separating them, and in regions that can be smaller than the spot size. In both cases, though, each pulse interacts with a dynamically evolving landscape.

As mentioned above, most of the focus on the design of multilayer dielectric materials has been directed towards improving the damage threshold of these optical components. Reported femtosecond laser-induced modifications in multilayers typically have minimal dimensions ranging from just below the beam waist up to the Rayleigh length. However, achieving confined crystallization and other types of modifications in specific layers of the stack would represent a significant technological advancement. This would make it possible to precisely localize the modified regions within a few tens of nanometers, potentially opening up applications in high-density data storage and anti-counterfeiting, acting as an "ink" invisible to conventional microscopy. By working on layered dielectrics with non-regular layer stacking thicknesses (and with each individual layer having typically sub-wavelength dimensions), we aim to influence the process of laser-matter interaction, so that the resulting laser-induced modifications can be confined to a single layer. The goal of this chapter is to demonstrate that such extreme localization of the modifications is possible, and to explore how the design of the multilayers can influence the confinement of the electric field's intensity in one or few specific layers of the multilayer stack, thus confining the occurrence of laser-induced modifications along the

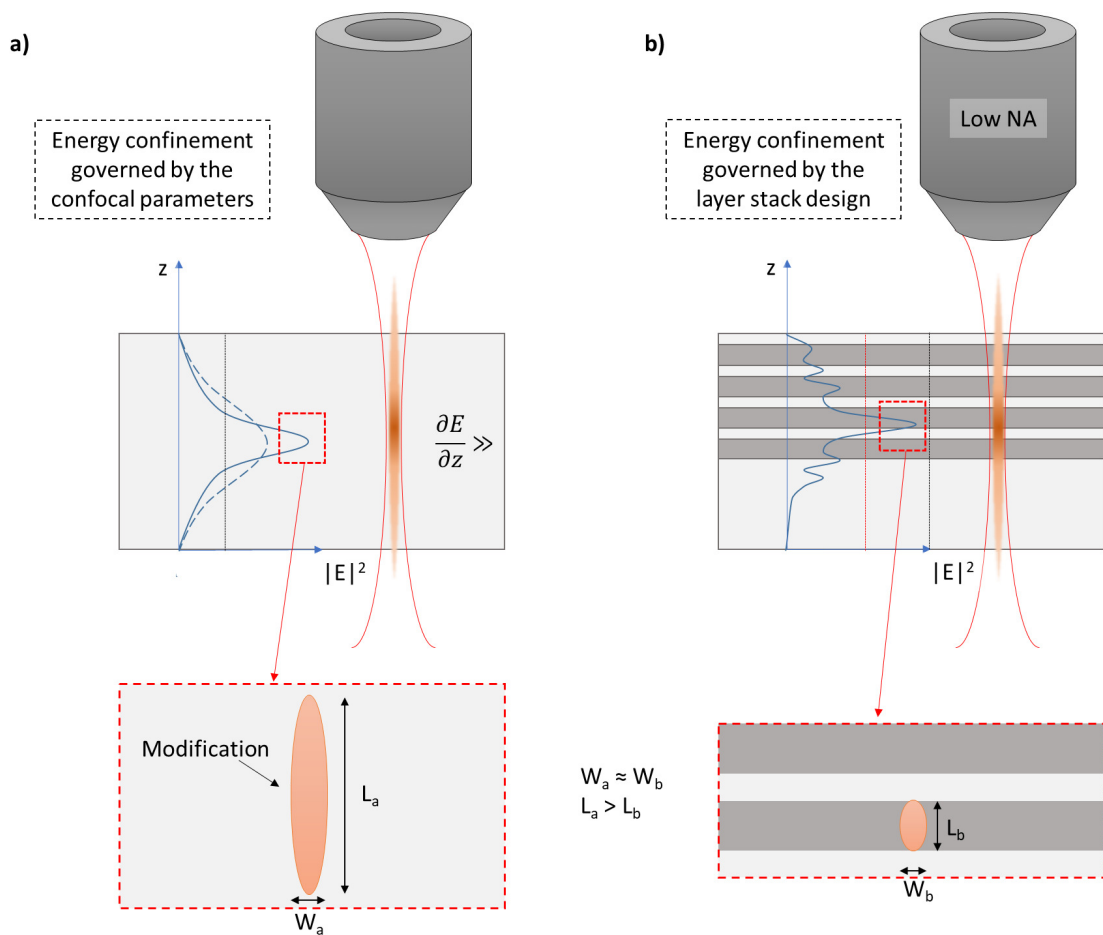


Figure 5.1: a) Electric field intensity ($|E|^2$) distribution along the beam propagation direction, inside a homogeneous dielectric material. The continuous line corresponds to a high numerical aperture (NA) objective, while the dotted line corresponds to a lower NA value. The absorption threshold is represented as a black vertical line. Depending on the NA value, the dimensions of the affected area can vary. The higher the NA, the sharper the intensity gradient and the smaller the non-linear affected zone. Conversely, image b) illustrates the concept of the modification process introduced in this paper. Consider a multilayer dielectric stack exposed to a femtosecond laser and designed to modulate the optical intensity profile as light propagates through it, due to the multiple reflections at the layers' interfaces. The electric field modulation is schematically shown in blue: combined with the different absorption threshold of the constitutive materials, this modulation enables a localized energy confinement along the propagation axis, and, if exceeding the absorption threshold, also the formation of laser-induced modifications limited to a specific layer(s) (see sketch in the bottom right), as opposed to an elliptical volume stretched along the optical axis (see sketch in the bottom left), as observed when using a focusing technique based on a high NA objective. In this illustration, the absorption threshold of the most sensitive material is represented as a red vertical line, while the threshold of the material most resistant to the laser radiation is shown in black.

optical propagation axis to a region of sub-wavelength dimensions.

5.2 Sample fabrication and experimental methods

5.2.1 Sample design, preparation and processing

The ways in which the layers' thickness arrangement influences the location of high electric field intensity within the material have been previously discussed; this phenomenon can enable a better control of the laser-induced damage threshold in dielectric mirrors. According to the theory related to dielectric Tamm waves, described in [148, 149], a localized field enhancement along the propagation axis in a specific location can be obtained if a rupture of periodicity is introduced in the multilayer design. As an illustration, Kavokin *et al.* [148] demonstrated that two periodic dielectric stacks with different periodicities (see for instance Fig. 1.3b) can effectively trigger a localized field enhancement effect nearby the boundary between the two stacks. Inspired by this work, we explore how these concepts can be used to trigger localized laser-induced modifications in selected locations within a multilayer.

Specifically, we considered three sets of thin-film stacks, belonging to the $\text{SiO}_2/\text{SiN}_x$ materials system (Sample_Si3N4_B and Sample_Si3N4_C) and the $\text{SiO}_2/\text{TiO}_2$ system (Sample_TiO2_A), respectively. Sample_Si3N4_B consists of an organized structure, with layers thicknesses decreasing towards the center of the stack until reaching a thick SiO_2 spacer, and then increasing again, symmetrically. The dimensions of each individual layer are listed in Table A.1 in Appendix A. The second case, Sample_Si3N4_C, has a double DBR geometry, the first DBR, with thicker SiN_x layers, lays next to the substrate interface, while the second one (with thinner SiN_x layers) is deposited towards the surface/air interface. This design is comparable to the geometry proposed by Kavokin [148]. Finally, the $\text{SiO}_2/\text{TiO}_2$ sample consists of a nearly random stacking of layers of different thicknesses and was accidentally produced. Interestingly, this specimen resulting from serendipity, as we will show in the following sections, offers a perfect illustration of the confinement effect occurring in an aperiodic structure. Here as well, layers dimensions can be found in Table A.1 in Appendix A. All depositions were done on 4-inch fused silica wafers. Furthermore, samples' structures and reflectance spectra are visible in Fig. 3.3b-c and Fig. 3.4a.

The light source is the femtosecond laser presented in Section 3.3, emitting a linearly polarized beam at 270 fs and 1030 nm. The samples were exposed in the top illumination condition. In this configuration, and considering the M^2 value of the laser, the Rayleigh length can be calculated as being 2.47 μm . In the present study, the repetition rate was chosen to be low enough so that no thermally cumulative effects would occur. In all cases considered in this paper, the scan speed s was kept at 1 mm s^{-1} . When using the laser processing platform described in Section 3.3, Sample_TiO2_A and Sample_Si3N4_B were processed at repetition rates of 500 kHz and 1 MHz, respectively. However, samples Sample_TiO2_A and Sample_Si3N4_C were also investigated with the THG detection setup described in the next

section, at repetition rates of 60 and 240 kHz. The femtosecond laser pulse train was focused in proximity and on the surface of the multilayers (distance chosen depending on the confocal parameters), and the combination of laser confocal parameters and layers' design resulted in the confinement of the modifications within a single layer, as explained in the scheme in Fig. 5.1b.

The processed samples were analysed with SEM and TEM techniques. As was already the case in Chapter 4, the TEM lamellas were prepared with a focused ion beam, specifically with a Zeiss NVision 40 dual-beam SEM/FIB, by slicing cross-sections of the multilayers and thinning them down to ~ 100 nm. TEM observations were done on a Talos F200S from ThermoFisher operating at 200 kV. Raman spectroscopy measurements were done on a Horiba Jobin-Yvon LabRam HR, using a wavelength of 532 nm and a 0.9 NA objective.

5.2.2 Third Harmonic measurement principle

Third Harmonic Generation (THG) is a non-linear phenomenon observed when a beam of light interacts with a material. Here, three photons of frequency ν_0 are re-combined as a photon of higher frequency $\nu_f = 3\nu_0$. To be effectively exploited for imaging, this requires light sources of high peak power, such as femtosecond lasers. The effect is enhanced when the laser beam is focused at materials interfaces, and is therefore suited for the analysis of heterogeneous materials.

As THG signal is generated at the interfaces, it can be exploited to detect the presence of such interfaces within a material [150], and it applies to dielectric materials and multilayers alike [151], as visible in Fig. 5.2a, as well as to biological samples [152]. The non-linear dependence of THG signal on the probe beam intensity means that the generation of appreciable signal is only enabled near the focal spot. By scanning at different positions along the propagation axis, it is then possible to reconstruct a 3D image of the volume under observation, similarly to a tomographic measurement [153, 154]. Moreover, the same femtosecond laser source can be used for both processing and THG signal detection [155], allowing both processes to be performed on the same experimental setup, as is our case.

The equipment used for THG microscopy employs a laser with a wavelength of 1030 nm, resulting in a THG signal emitted at 343 nm. The experimental setup is shown in Fig. 5.2b, and shows notably the location of the AOM (for pulse frequency control) and of the detector. Since the THG signal lies in the UV range, the objective is custom made to be adapted to this wavelength [156]. The sample can be moved in three dimensions by a micrometric stage, while fine movements during the processing and the measure steps are ensured by a piezoelectric stage, with a range of 100 μm in both orthogonal directions, and 30 μm along the beam propagation direction. With the help of this experimental setup, bi-dimensional THG intensity maps of a laser-exposed area of up to $10^4 \mu\text{m}^2$ can be registered, as well as tomography measures along the cross-section of the layers.

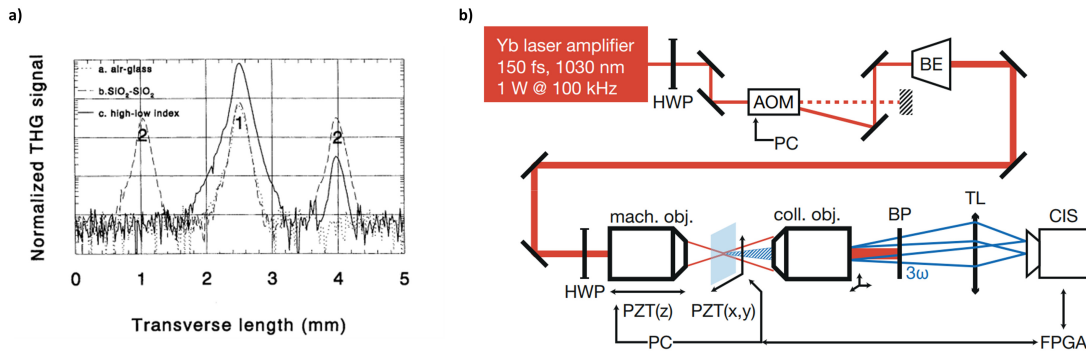


Figure 5.2: a) Schematics of THG signal collected from various interfaces: at the air-glass interface, between two SiO_2 samples separated by air, and for a $\text{SiO}_2/\text{HfO}_2$ multilayer structure on fused silica, showing their corresponding THG signal intensity as function of the focal spot position. Image adapted from [151]. b) Scheme of the THG measure setup. Notice that the laser source in the scheme is different than the one we used. Image adapted from [156].

5.3 Nanometric confinement of the modifications

Laser-induced modifications in specimen Sample_Si3N4_B are highlighted by the BF-TEM image in Fig. 5.3a. This area was exposed to the laser at a repetition rate of 1 MHz, scan speed $s=1 \text{ mm s}^{-1}$ and a pulse energy of 100 nJ, which in turn corresponds to a peak fluence of 7.86 J cm^{-2} and an exposure dose of 14.15 kJ cm^{-2} . The writing was performed diagonally across the surface, starting from a point outside the sample and moving gradually towards the multilayers, along the vertical direction, and along the length of the written line, finally ending below the level of the multilayer stack.

Following the exposure of this sample, modifications are observed within a single layer of the high-index material, SiN_x , while the rest of the layers and the top surface of the sample are remarkably unaffected by the laser, so that the modifications reside exclusively within the stack itself. In BF-TEM mode, as visible in Fig. 5.3a, highly diffracting crystalline structures appear darker, due to the contrast created by diffracted electrons. Hence, the modified zone consists of alternating nano-voids (visible in white) and intermixed/crystallized regions visible as dark spots, alternating with an approximate periodicity of 200 nm. The presence of crystallites within the modified zone is confirmed by the SAED pattern, visible in the inset of Fig. 5.3a, and by HR-TEM (Fig. 5.3b), showing a globular-like crystallite with visible atomic planes. This image was further processed to produce a fast Fourier transform (FFT) image (visible in the inset in Fig. 5.3b) to obtain the frequency domain of the signal, resulting in discrete spots that can be used to retrieve the interplanar distance d_{hkl} for various planes of index hkl . The d_{hkl} values for different planar orientations are listed in Table 5.1. The calculations were performed using Bragg's law in the hypothesis that the observed phase consists of (diamond) silicon, which has a FCC structure with additional sites at positions $x, y, z = \frac{1}{8}, \frac{1}{8}, \frac{1}{8}$, resulting in a total of 8 atoms per cell, and a lattice parameter $a = 0.543 \text{ nm}$ [134]. Table 5.1 shows that there is a good correlation between experimental and theoretical data, with maximal deviations of 2.26%,

5.3 Nanometric confinement of the modifications

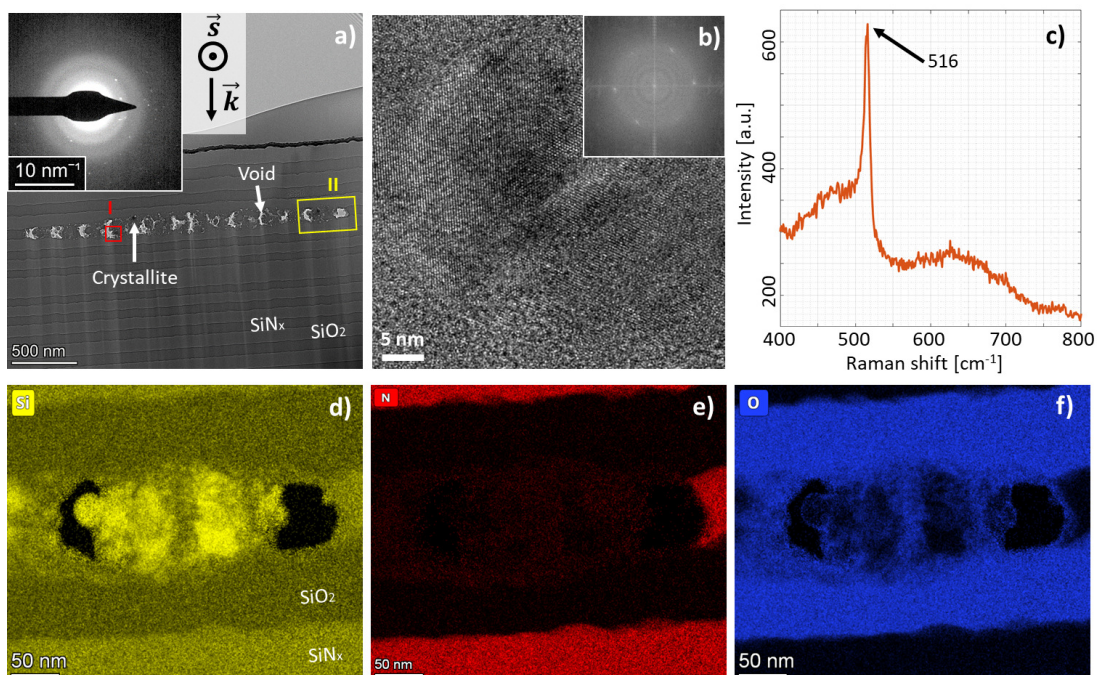


Figure 5.3: Confined modifications observed within Sample_Si3N4_B, with a BF-TEM image of the affected area in a) and the corresponding SAED pattern in the inset. The cut corresponds to the orientation of the xy plane, as defined in Fig. 2.6. Zone I (red square) is further magnified in image b), where a high-resolution image of the area is visible, showing the presence of oriented atomic planes corresponding to a crystalline material. The FFT of the HR image is shown in the inset. A Raman spectrum of the full laser-affected area is shown in c), with a sharp peak at 516 cm^{-1} corresponding to the main peak of crystalline diamond silicon. Images d)-f) illustrate the elemental distribution within zone II (yellow square) as measured with EDS, showing a sharp decrease in concentration of nitrogen, infiltration of oxygen (perhaps resulting from an oxidation process of the walls of the void regions) and clustering of silicon in the area.

which are likely due to lattice distortions induced by residual stresses and volume mismatch between the crystallites and the surrounding amorphous matrix. Therefore, it can be stated that the laser-induced phase transition results in the creation of crystalline silicon clusters, as further evidenced by the Raman spectrum of the laser-affected zone visible in Fig. 5.3c. The position of the sharp peak at 516 cm^{-1} , indicating the presence of crystallinity, is compatible with the spectrum of crystalline silicon [132]. In this sense, the formation of Si crystals is comparable to the phase transitions reported in the previous chapter. The presence of silicon clusters is further illustrated by EDS elemental mapping, showing a higher concentration of Si atoms within some locations of the modified zone (Fig. 5.3d), corresponding to the locations of the crystallites. Conversely, the behaviour of nitrogen and oxygen (Fig. 5.3e and f, respectively) is antithetical: while N atoms are getting depleted from that region, O atoms are infiltrating the modified area. This suggests a laser-induced modification phenomenon occurring in multiple steps, with bond breaking resulting from ionization at the beginning, followed by ionic migration and then recombination of a new crystalline phase.

Chapter 5. Laser-induced confined crystallization in multilayer systems

Corresponding plane	Measured	Calculated	Difference [%]
Rutile [157]			
(110)	3.357	3.247	+3.39
(101)	2.473	2.487	-0.56
(200)	2.259	2.296	-1.61
(210)	2.089	2.054	+1.70
(400)	1.141	1.148	-0.61
Diamond-Si [134]			
(111)	3.200	3.135	+2.07
(202)	1.900	1.919	-0.99
(212)	1.800	1.810	-0.55
(103)	1.700	1.717	-0.99
(113)	1.600	1.637	-2.26

Table 5.1: Comparison of measured and calculated interplanar distances for tetragonal rutile TiO_2 and FCC-diamond silicon, for a set of planar orientations, as well as the difference between these values (in %). Values of both measured and calculated interplanar distances are expressed in Å.

Sample_TiO2_A was also investigated. Several sets of lines were written on the surface of this multilayer sample; each set was written at a different focal spot position, above, at, and below the surface of the multilayers (see Fig. 5.4a). The focal spot position was varied from 10 μm below, to 10 μm above the surface, in intervals of 5 μm . The resulting lines are visible in Fig. 5.4b. The exposure was performed at a repetition rate of 500 kHz, a pulse energy of 234 nJ and a scan speed of 1 mm s^{-1} . A different repetition rate was chosen for the $\text{SiO}_2/\text{TiO}_2$ specimen, with respect to Sample_Si3N4_B, to accommodate for the different threshold repetition rate towards thermal accumulation for this specimen. Four locations were exposed by FIB cutting, named A) to D), corresponding to cross-sections of lines exposed to laser beams focused 5 μm below the surface (A), at the surface level (B) and 5 μm above the surface (C and D).

The cross-section of location A) (see Fig. 5.4c) shows a large ablated spot on the left side, which completely removed the layer stack, reaching the substrate interface. There, we notice the propagation of modifications from the ablated mark towards some of the TiO_2 layers (here, appearing with a brighter hue). Remarkably, the presence of two nanovoids is even observed a few microns away from the ablated spot, close to the layers-substrate interface. Similarly, the cross-sections shown in Fig. 5.4d and e show the presence of partial layer ablation on the top surface, and of confined modifications in one, or more, layer(s) below, specifically targeting the TiO_2 layers. Location D), as visible in Fig. 5.4f, presents the most interesting case, where sub-surface modifications are confined within a single layer, without affecting other layers or the top surface. Here, the modified region is effectively hidden within the multilayer structure.

Following these preliminary measures, higher resolution TEM images of Sample_TiO2_A were taken; for this, a lamella was extracted from the same written line where cut C), in Fig. 5.4e, was done, albeit not in the same location, but 50 μm away, in a region where no surface ablation was visible. Figure 5.5a shows a BF-TEM image of this lamella, exposing the structure of the

5.3 Nanometric confinement of the modifications

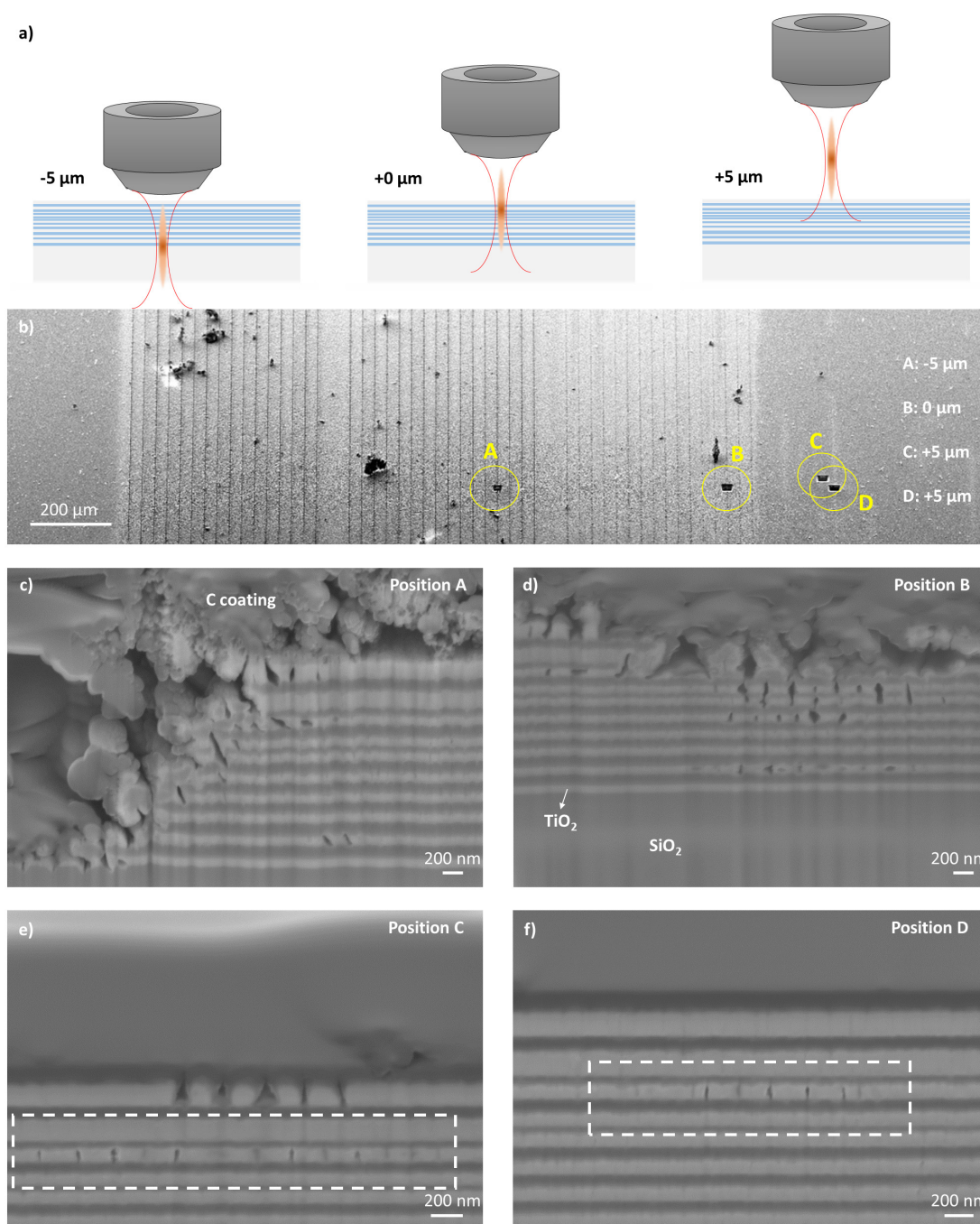


Figure 5.4: a) Scheme of the process, showing how the focal spot of the laser beam can be focused below, at and above the layers' surface. b) SEM image of the surface of the processed Sample_TiO₂_A specimen, illustrating sets of lines with increasing distance from the surface. Four different FIB cut positions are highlighted, position A, where the focus was 5 μm below the surface, position B, with the focus right at the surface and positions C and D, where the beam was focused 5 μm above the surface. The repetition rate was fixed at 500 kHz, the pulse energy at 234 nJ and the scan speed at 1 mm s⁻¹. Images c)-f) show SEM cross-sections at the spots A)-D), showing the extent of the modified zones. Several instances of ablation (totally or partially removing layers, depending on the deposited energy) are visible, and the presence of modifications confined in specific layers is confirmed.

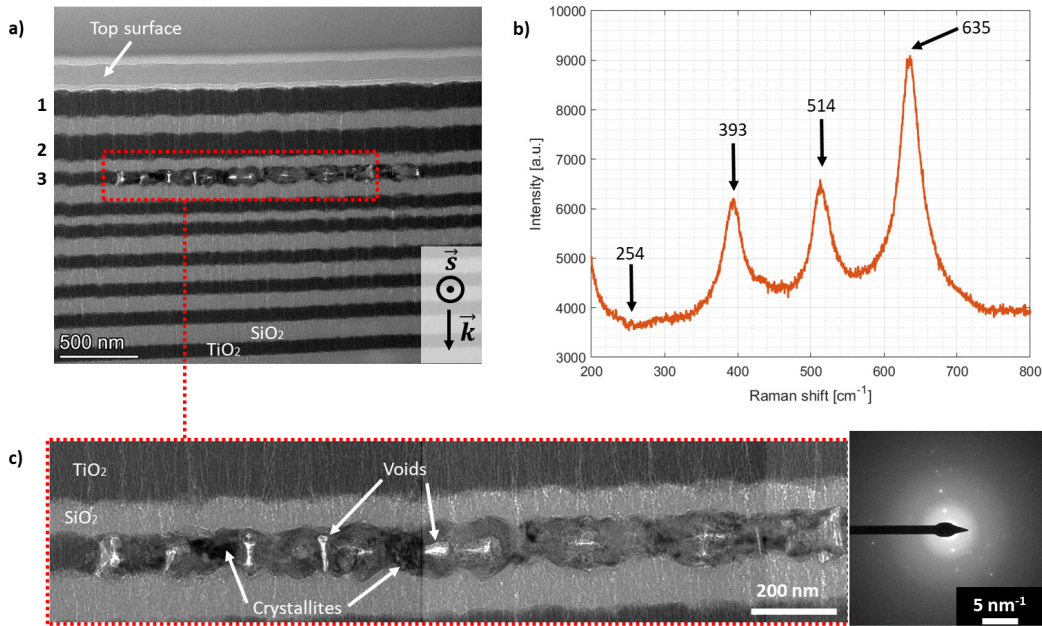


Figure 5.5: a) BF-TEM image of the laser-modified $\text{SiO}_2/\text{TiO}_2$ multilayer stack and illustration of the beam propagation direction. Here again, the cut corresponds to the orientation of the xy plane, as defined in Fig. 2.6. The laser-induced modifications are confined to the third TiO_2 layer from the top. b) Raman curve measured at the exposed location, showing peak positions in agreement with a rutile- TiO_2 phase. In the BF-TEM image in c), magnification of the modified zone showing the presence of both nano-crystallites and nano-voids, together with an inset showing a SAED pattern with clear spots, attributed to electron diffraction from crystalline structures.

multilayers and of the laser-induced modifications. As written above, this particular region was irradiated with a repetition rate of 500 kHz, a scan speed of 1 mm s^{-1} , and a pulse energy of 234 nJ, resulting in a peak fluence of 18.39 J cm^{-2} and an exposure dose of 16.55 kJ cm^{-2} . The beam was focused $5 \pm 1 \mu\text{m}$ above the top surface. Note that the actual exposure dose is reduced by a factor $(\frac{w}{w_0})^2$, as the irradiated area grows larger with the distance from the beam waist. As a result, at a distance of $5 \mu\text{m}$, the beam waist reaches a value of $2.01 \mu\text{m}$, resulting in an exposure dose of 3.32 kJ cm^{-2} , or 5 times lower than at the focal spot. The uncertainty about the positioning of the focal spot is caused by the tilt of the sample's surface with respect to the optical axis, which in principle is measured and taken into account during the laser processing step; however, given that the deposited energies lie around the non-linear absorption threshold, micrometric displacements along the pulse propagation direction can still play a role in the triggering, or not, of non-linear absorption.

As observed in the case of the $\text{SiO}_2/\text{SiN}_x$ sample, the modified zone is confined along the vertical direction within 100 nm, while the Rayleigh length in that case was $2.47 \mu\text{m}$, or 25 times larger. The presence of crystalline zones within the confined modifications is confirmed by Raman spectroscopy (Fig. 5.5b), with the measured curve showing a peak profile comparable to the one of rutile [158], with deviations with respect to the literature data comprised between

5.3 Nanometric confinement of the modifications

-1.1% and +2.8%. These deviations can be explained by the strain induced by the crystallites being surrounded by a continuous amorphous matrix and by periodic nano-voids, resulting in localized strain and therefore in minor peak shifts [133].

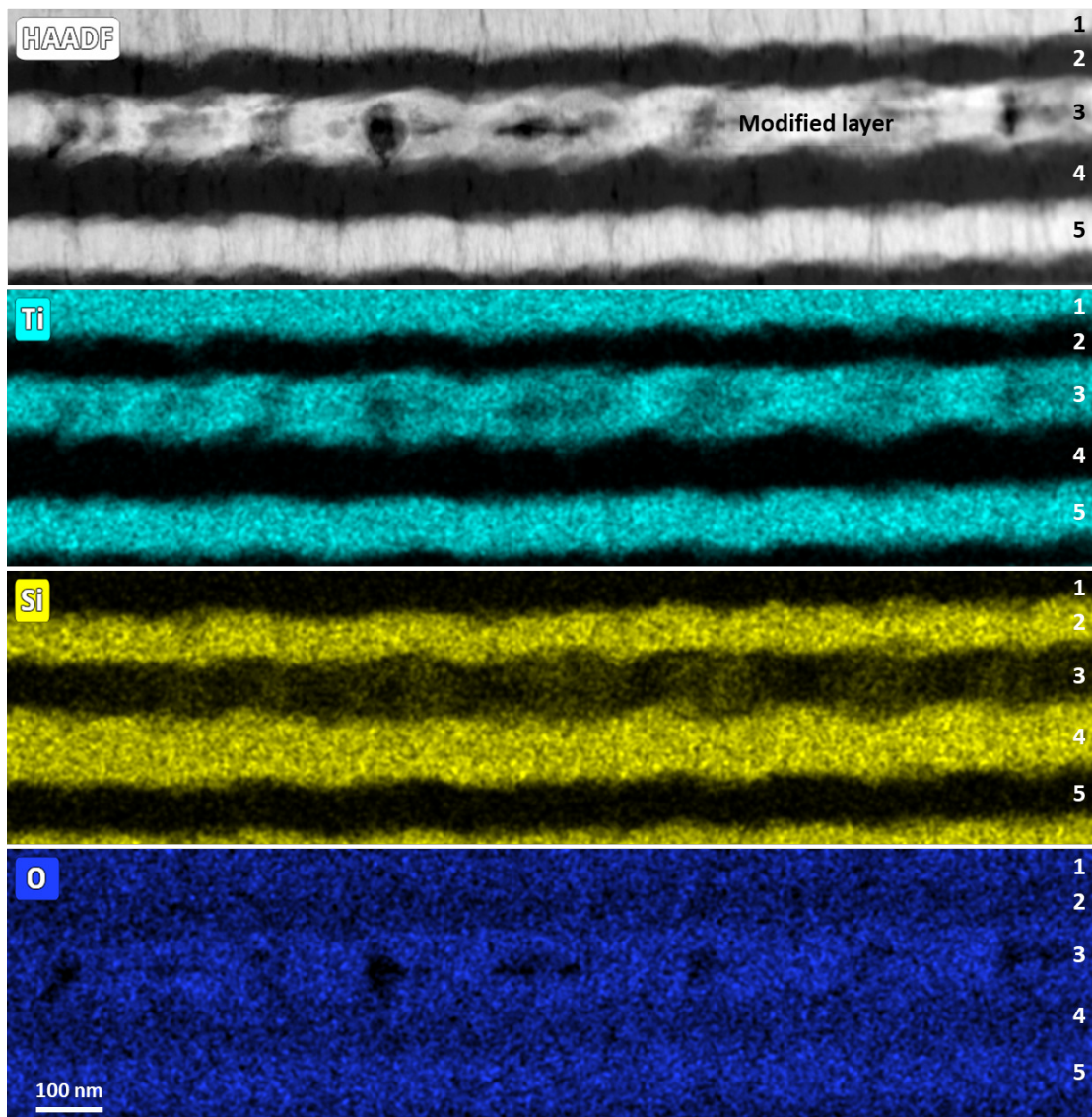


Figure 5.6: HAADF image and EDS maps, showing the elemental distribution of Ti (top), Si (middle) and O (bottom) atoms through a cross-section of the $\text{SiO}_2/\text{TiO}_2$ multilayers exposed to the laser.

A larger view of the modified region is visible in Fig. 5.5c, where the crystallites appear as darker spots within the TiO_2 layers. The presence of nano-voids (appearing in white), periodically spaced by around 150 nm, can also be noticed, as there is an alternating pattern of crystalline regions and voids along the length of the layer. In this sense, the features of the modifications are similar to what has been observed in the $\text{SiO}_2/\text{SiN}_x$ sample (Fig. 5.3), albeit with smaller void regions. The inset shows a discrete SAED pattern, typical of a crystalline material, which can be used to infer the interplanar distance for a set of planar orientations. Using Bragg's

law, it is then possible to calculate the theoretical values of interplanar distances for the same set hkl of Miller indices, and to compare them to the experimental values. Since the Raman observations suggested the presence of a rutile phase, calculations were done according to the rutile crystal structure, which consists of a tetragonal phase with lattice parameters $a = 0.4593$ nm and $c = 0.2959$ nm [157]. Ti atoms occupy the corners, while O atoms occupy the sites at the positions $x, y, z = 0.3046, 0.3046, 0$. As visible in Table 5.1, there is a good agreement between measured and theoretical values of interplanar distances, with minimal differences (between 0.56 and 3.39 %) that, similarly to what has been observed with Raman spectroscopy, can be attributed to residual stresses remaining after the phase transition process, due to lattice mismatch at the crystalline-amorphous interface, and to instrument calibration precision.

Figure 5.6 consists of an HAADF image of the modified area, followed by EDS elemental maps showing the distribution of Si, Ti and O atomic species in the same zone, comprising both pristine and laser-modified layers of the lamella shown in Fig. 5.5. As such, the modified layer corresponds to the third TiO_2 layer from the top. There is a moderate degree of infiltration of silicon atoms in the modified layer, mostly located around the nano-voids. It is therefore possible that Si-O bonds at the interface between the SiO_2 and TiO_2 layers are also affected by the plasma developing in the TiO_2 layer, and the resulting Si ions are able to diffuse at the edges of the voids. This is also supported by the presence of bulges around the nano-voids location, which can be the result of a combined effect of pressure, i.e. stresses induced by material shrinking (crystallization) and void creation, and plasma. Given that the phase transition does not involve the nucleation of a heterogeneous phase, but instead involves the crystallization of amorphous TiO_2 into a crystalline polymorph of the same chemical composition, the concentration of O atoms does not appear to change noticeably, if at all, in the modified layer with respect to the pristine ones.

5.4 Modelling of pulse propagation

To model the amplitude of modulation of the electric field inside the multilayer stack and to localize the sites of field enhancement, we performed electromagnetic field propagation simulations using a finite-difference time-domain (FDTD) method, as explained in Section 2.2.

Materials properties were sourced from Meep's own database, even though in the case of TiO_2 the parameters were customized according to the literature [86]. The resulting simulations show the pulse propagation through the layered structures, and can be displayed in two main ways; a first possibility for visualization is a cross-section showing a bi-dimensional illustration of the electric field, as is the case in Fig. 5.7, corresponding to the yz section plane, as defined in Fig. 2.6. Otherwise, the simulations can also be visualized in the form of the electric field intensity as function of the position along a section of the multilayers, as shown in Fig. 5.8, corresponding to the xz plane.

Simulations results for two $\text{SiO}_2/\text{SiN}_x$ materials systems, with the focal spot located $4 \mu\text{m}$ away

from the layers' surface, and at 90 fs of interaction, are shown in Fig. 5.7. The image in Fig. 5.7a concerns a simulation with a multilayer structure consisting of a $\lambda/4$ DBR of 8 bilayers, with individual layer thicknesses of $t_{\text{SiO}_2}=120$ nm and $t_{\text{Si}_3\text{N}_4}=90$ nm. This configuration is similar to the layer thickness distribution of Sample_Si3N4_A. Below, in Fig. 5.7b, the structure is symmetric around its central SiO_2 layer, from where subsequent layers thicknesses increase gradually, and corresponds to the structure of Sample_Si3N4_B. Both layer designs are visible on the left side of the figure.

The central and right sides show 2D maps of the laser beam's electric field profile, as it propagates through the multilayers. Here, the incoming and reflected waves interfere and result

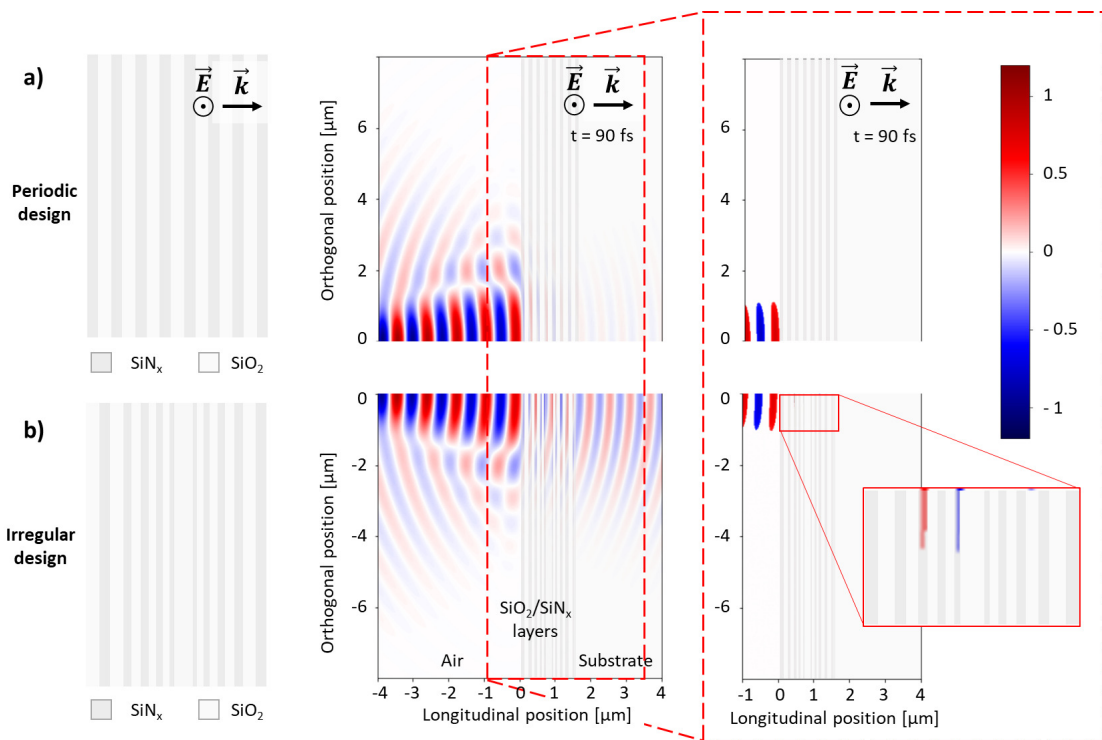


Figure 5.7: a) Illustration of Gaussian beam propagating in a regular DBR and b) through a $\text{SiO}_2/\text{SiN}_x$ multilayer with an aperiodic layer arrangement. As the k -vector axis defines an axis of symmetry for the electric field, only half of the field distribution is shown in both cases. The periodic design is a DBR corresponding to a $\lambda/4$ design ($t_{\text{SiO}_2}=120$ nm, $t_{\text{Si}_3\text{N}_4}=90$ nm), similar to the geometry of Sample_Si3N4_A, while the irregular one corresponds to the geometry of Sample_Si3N4_B. The exposure case simulated here is the one of a linearly polarized Gaussian beam propagating from left to right and corresponding to a 500 fs laser pulse. The field intensity distribution is shown at a simulation time-stamp of $t=90$ fs, defined from the time the pulse first entered the material. The visualization plane is defined as perpendicular to the electric field orientation and along the k -vector. The right figure shows a filtered intensity map for a pre-defined absorption threshold, concentrating on the region between -1 and 4 μm along the longitudinal position. This particular time-stamp corresponds to the case where a maximum electric field intensity is observed in one of the layers. The simulation predicts, first, a field-enhancement only in the case of the aperiodic design and, second, that the first layer along the propagation axis in which such enhancement occurs is the third SiN_x layer (see inset), which effectively agrees with the experimental observations reported in Fig. 5.3.

in characteristic patterns, visible at the left of the multilayers (i.e. in air). More specifically, the two images on the right show exactly the same simulation as the images in the center, but where the electric field has been filtered in regions where the intensity is lower than an arbitrary threshold of 50% of the maximal intensity of the pulse. Thanks to this filtering, the effect of the layers' design on the field enhancement is more clearly visible: whereas in the case of the $\lambda/4$ design, the electric field decays rapidly within the first few layers, in the second case the presence of the enhanced field is observed in specific locations within the layers' stack.

Conversely, Fig. 5.8a shows the simulated movement of a femtosecond pulse through Sample_TiO2_A, showing how the electric field is visibly enhanced in the third TiO₂ layer from the sample's surface. The field of view is not along the laser's electric field any more, but corresponds to the xz section, as defined in Fig. 2.6. The timestamp for this situation is 145 fs after the pulse reaches the multilayers' surface, corresponding to the first instant in which the simulated electric field intensity locally overcomes the (arbitrary) threshold. To better visualize the electric field intensity evolution, snapshots of previous timestamps are magnified and shown in Fig. 5.8b. As introduced in the previous paragraphs, we argue that the field's intensity at that location is above the non-linear absorption threshold (as indicated by the horizontal red line), resulting in the laser-induced modifications reported in Fig. 5.5a and c. Conversely, the pulse energy is still below the absorption threshold of the second material (SiO₂). It should also be noticed that the threshold shown in the image is arbitrary, since its value has been chosen to illustrate qualitatively the field modulation process.

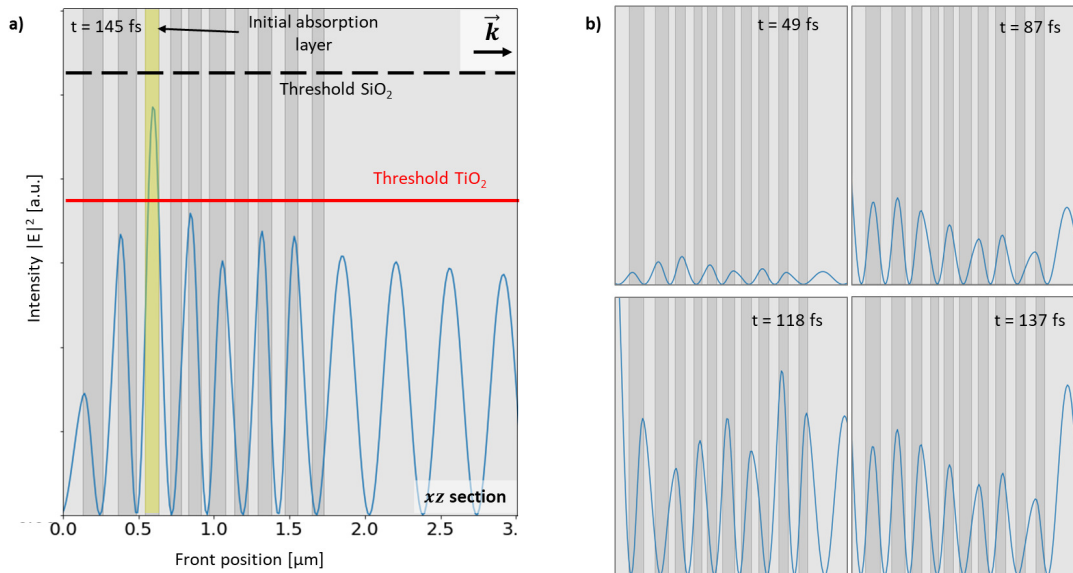


Figure 5.8: a) Electric field profile inside Sample_TiO2_A. The horizontal lines represent the hypothetical laser-induced modification thresholds for the layers' materials. The high-index material (TiO₂) is shown in dark grey, the low-index material (SiO₂) is shown in light grey. b) Intensity evolution for previous times, i.e. before the non-linear absorption process is triggered.

With the help of these simulations, we argue that the field intensity reaches the modification threshold of the "weakest" material of the system, which is the high-index material, in a specific layer, where non-linear absorption is initiated. The lack of modifications in the other material (low-index material) and in the following layers of the weak material can be explained, respectively, with a highest modification threshold of the low-index material, which is not reached, and the absorption of the pulse energy in the first high-index layer where the threshold is reached, which is therefore screening the following layers from the pulses.

5.5 THG imaging of modified multilayers

Sample_TiO2_A was tested first. The specimen was processed and imaged at a repetition rate of 240 kHz. The exposure condition was designed to result in the writing of a matrix of points, whose parameters were varied as illustrated in Fig. 5.9a. Along the horizontal axis, the pulse energy E_p was varied, starting from the maximal value and decreasing to the minimal desired value. Along the vertical axis, the focal spot position z_f was also changed. The first row of dots was written with the focal spot outside of the sample, which was then gradually approached to the surface and beyond, until the last row of dots, which were written with the focal spot located below the layers' surface. Each dot was written with a burst of pulses, whose number was controlled by an AOM, enabling the selection of pulse numbers as low as a single pulse.

Several arrays of dots, written with different numbers of bursts, were written on the layers. The number of pulses doubled each time, from a single pulse to a train of 8 pulses, as visible in Fig. 5.9 (the cases of bursts of 2 pulses has been omitted from the figure). Here, the vertical displacement was comprised between $+6\ \mu\text{m}$ and $-6\ \mu\text{m}$, and the energy interval between 60.9 nJ and 31.0 nJ (corresponding to deposited energies between 1.24 and $0.63\ \text{J cm}^{-2}$), in steps of $\approx 2\ \text{nJ}$ (this value is approximate because the relationship between applied input and output power is not perfectly linear). Lines have been traced in Fig. 5.9a to improve the visibility of the modified spots, but have been omitted in images b and c, to avoid overcharging the images. The number of ablated spots, clearly visible as dark dots in the digital microscopy images, increases with the pulse number, and similarly the whole array becomes more symmetric with respect to the focal spot position on the surface. Some sub-surface modifications are already visible in these micrographs, and are indicated by a more diffuse brown color. However, as exemplified by Fig. 5.9b and c, for these hidden modified zones, THG microscopy offers a greater degree of information than simple optical or digital microscopy. As highlighted by the white areas, THG imaging hints to the presence of a larger number of sub-surface modifications, that are not visible with conventional microscopy techniques.

However, at this point THG imaging alone is not sufficient to prove in a definitive manner the presence of sub-surface laser-induced modifications, as the signal intensity variations might be the effect of artifacts. Without further characterization of the modified zones, it is not possible to understand the nature of the modifications based solely on THG images. To demonstrate the correlation between THG maps and sub-surface modifications, the cross-section of an

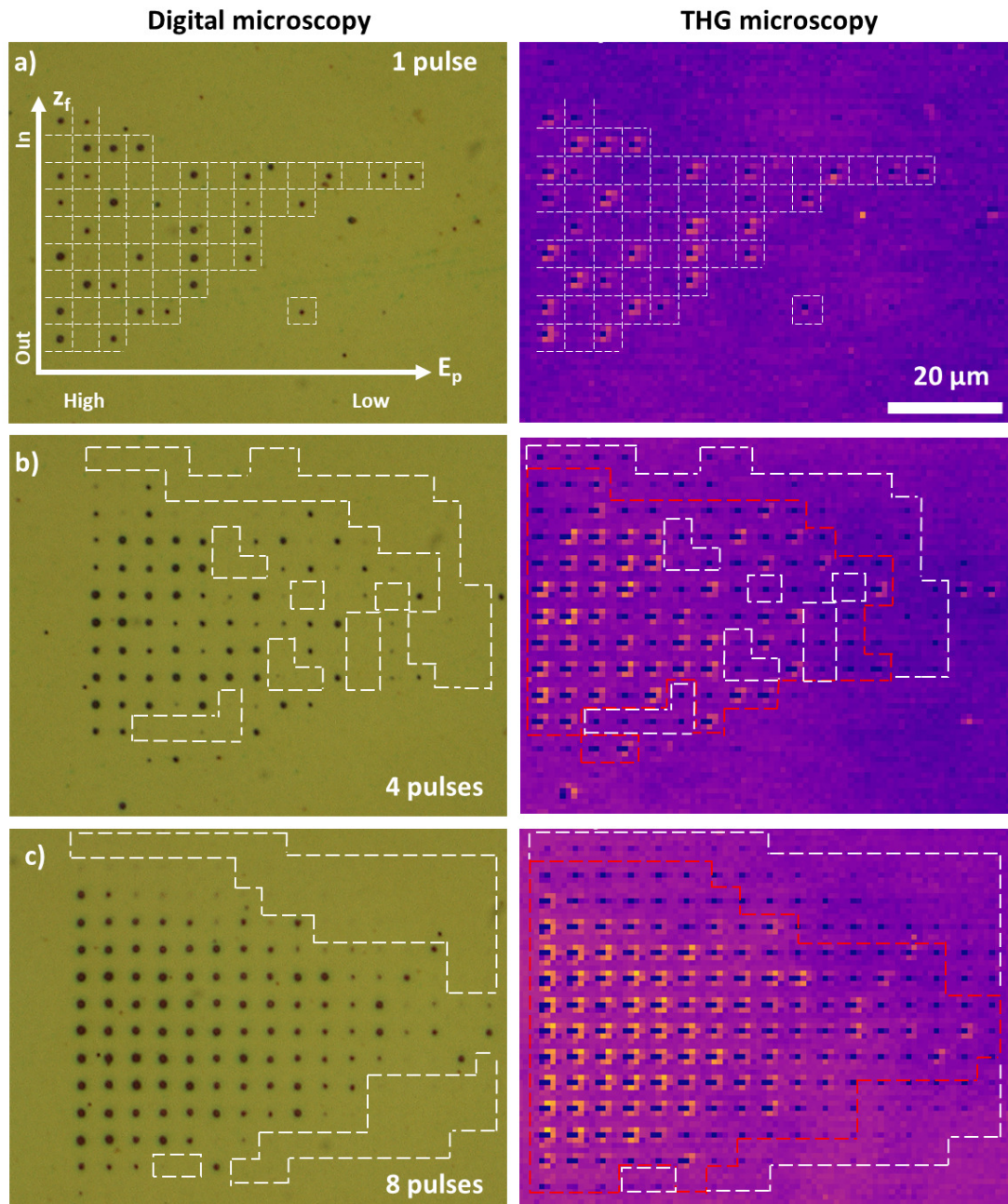


Figure 5.9: THG mapping of the $\text{SiO}_2/\text{TiO}_2$ sample exposed to a matrix of points. Image a) also shows the matrix design, with the pulse energy E_p varied along the horizontal axis, and the focal spot position z_f varied along the vertical axis. Images a) to c) show the results of bursts of increasing number of pulses (1 to 8, respectively). The left side of every image corresponds to a digital micrograph of the exposed area, while the right side (more pink in color) corresponds to the THG intensity map. Images b) and c), in particular, show the potential of THG microscopy for the analysis of laser-induced modifications in dielectric multilayers: modifications detected with both techniques are highlighted in red in the THG images, while areas only visible with THG microscopy are highlighted in white.

5.5 THG imaging of modified multilayers

array of dots was processed by FIB, and a lamella was prepared for TEM observations. As these confined modifications are small and localized, FIB processing had to be done cautiously, using very gentle sweeps, to prevent the removal of the whole affected area.

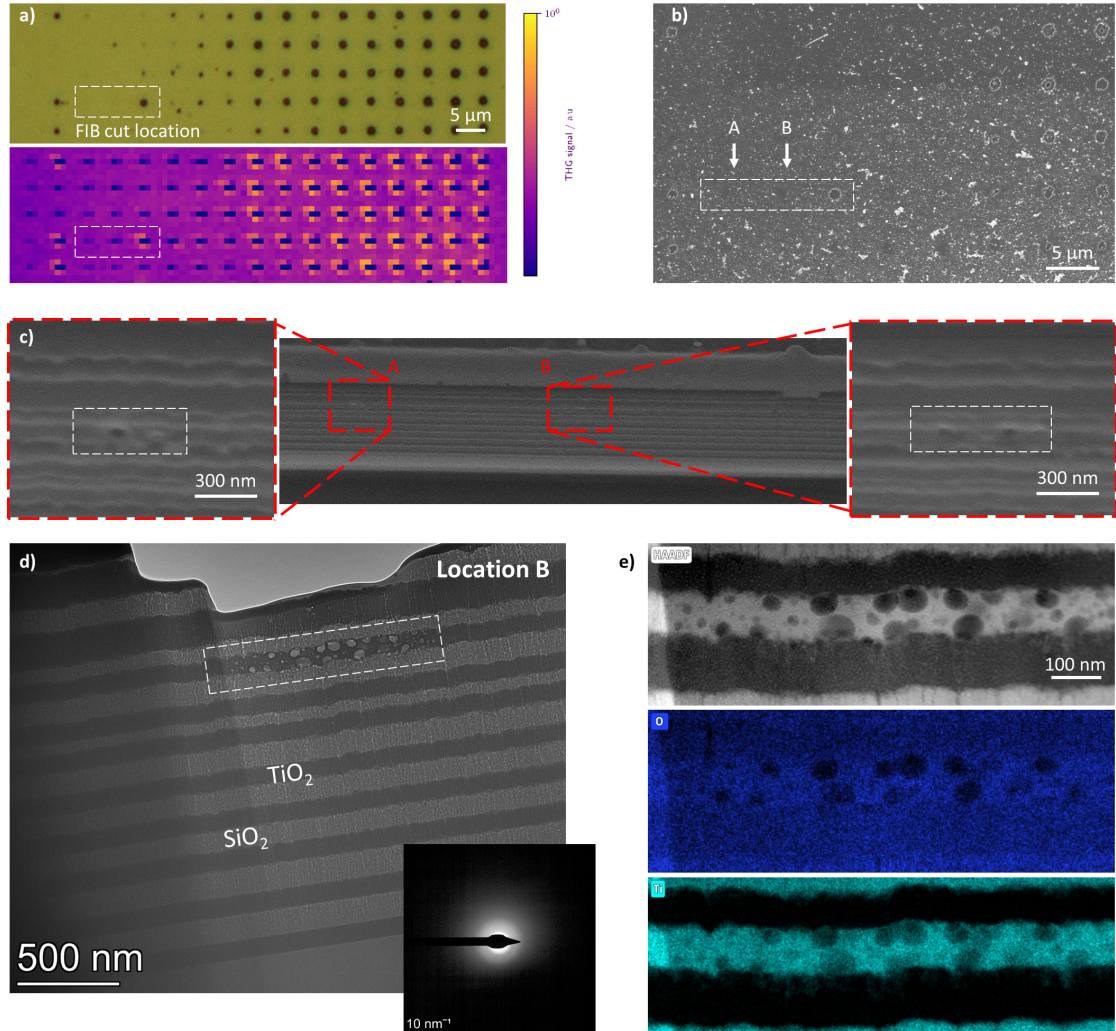


Figure 5.10: Correlation between THG imaging and the nature of the materials modifications. a) Mapping of the matrix of points with a digital microscope (above) and its THG signal (below). The scalebar for the THG intensity can be found on the right. The cut location is surrounded by a white dotted box in both cases. b) SEM image of the same sample, showing the location of the FIB cut, and the locations (A and B) of the sub-surface modifications. c) FIB-exposed cross-section, confirming the presence of sub-surface modifications at locations A and B, which are further magnified in the left and in the right insets. d) BF-TEM image of location B, and its corresponding SAED pattern (in inset, bottom right). The pattern is diffuse, indicating that the material is fully amorphous. e) HAADF image and EDS elemental maps (for O and Ti) of the modified layer, showing the presence of voids, with no trace of crystalline grains and very limited ion diffusion.

This specific sample was exposed to the same laser conditions seen in Fig. 5.9c, with bursts of 8 pulses, also at a repetition rate of 240 kHz. As before, the energy interval was fixed between 60.9 nJ and 31.0 nJ, while the focal spot position was varied between +6 μm and -6 μm . The

resulting digital micrographs and THG maps are visible in Fig. 5.10a, with additional spots visible in the THG image, suggesting the presence of sub-surface modifications. The position of the FIB cut is also showed, both in these two images and in the SEM picture of the sample surface in Fig. 5.10b. Positions A and B correspond to the points of interest, where, according to the THG image, there should be sub-surface modifications, despite the absence of visible contrast in these places in the digital microscope image.

The existence of these confined modifications is confirmed in Fig. 5.10c, where in both locations (A and B), SEM images of the cross-section show the presence of nano-voids, which appear to be confined within a single layer. It is also worth noting the clean surface ablation process of the partially-ablated spot on the right, which is also visible in Fig. 5.10b, where only a few layers were removed, leaving a sharp interface behind.

Fig. 5.10d shows a BF-TEM image of the modification in location B, which is indeed confined within a single TiO_2 layer (the same layer that was modified in the experiments shown in Fig. 5.5). This area, around $1\ \mu\text{m}$ long, shows the distribution of several void pockets, and no visible grain boundaries. The absence of clear contrast within the modified area suggests that in this occasion, no crystallization occurred. The SAED pattern in inset confirms the absence of crystalline particles, as the pattern is smooth and diffuse, indicating the presence of an amorphous phase. Finally, HAADF and EDS maps in Fig. 5.10e illustrate the conformation of the modified zone, as well as the elemental distribution of O and Ti atomic species. The contrast in the HAADF image suggests the presence of nano-pores, or nano-voids (their definitions depending on their content). Unfortunately, due to the nature of the observations, the pores were slice-opened and then exposed to the environment, so that the original gas content of the pores, if existing, cannot be measured. The nature of the modifications is confirmed by EDS chemical mapping, as neither O or Ti atoms are registered at the location of the pores. Diffusion of Ti atoms is also noticeable, going towards the SiO_2 layer below the modification.

5.6 Case studies for modifications confinement

Having developed a methodology to obtain confined modifications in multilayer samples, and after the confirmation that THG microscopy can be used as a non-destructive means to probe such structures, we decided to develop this work further by including two distinct case studies. Specifically, the first one concerns the writing of text under the layers' surface, to prove the potential of this laser-processing technique as a means of printing text or images *inside* the layers' structure. The logo of EPFL was selected for this proof-of-concept. Secondly, a new $\text{SiO}_2/\text{SiN}_x$ sample was designed and produced, to test this methodology with a double DBR layer configuration.

The logo of EPFL was inscribed inside the $\text{SiO}_2/\text{TiO}_2$ multilayer specimen, Sample_TiO2_A, at a repetition rate of 240 kHz, a focal spot position of $4.4\ \mu\text{m}$ above the surface and a pulse energy of 18.5 nJ, resulting in an exposure dose of $0.38\ \text{J cm}^{-2}$. THG imaging of the laser-exposed area

5.6 Case studies for modifications confinement

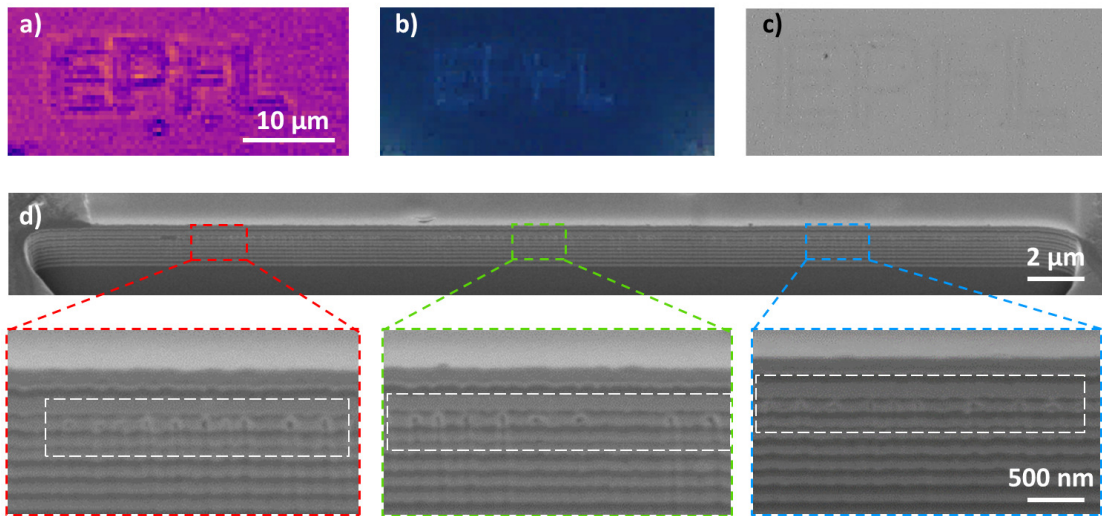


Figure 5.11: Writing of more complex patterns as sub-surface modifications. The string "EPFL" is inscribed below the top surface, with a repetition rate of 240 kHz, a focal spot position of 4.4 μm above the surface and a pulse energy of 18.5 nJ. The resulting modifications are imaged with different microscopy techniques, notably a) THG microscopy, b) cross-polarized optical microscopy, and c) digital microscopy. The cross-section of the logo is then exposed with a FIB cut, as visible in image d), and the contrast is confirmed to be caused by the presence of sub-surface modifications.

was done at 240 kHz, and the resulting map is shown in Fig. 5.11a, where, according to the results described in previous paragraphs, the contrast indicates the presence of sub-surface modifications creating the desired text. This map can be compared to the cross-polarized optical microscopy image in Fig. 5.11b, showing the presence of minor retardance in the modified structure. Conversely, under observation with digital microscopy, the writing is barely visible, as shown in Fig. 5.11c.

Finally, Fig. 5.11d shows SEM images of a cross-section of the logo, cut transversely to each letter. Three distinct regions are magnified, showing the presence of sub-surface modifications confined within a single layer of the stack, and proving that this laser-processing method can effectively result in the writing of information within the layers' structure, without affecting the top surface of the sample. The nature of the modifications has not been investigated further, but these preliminary observations suggest the presence of nano-voids, while the occurrence of crystallization processes remains speculative.

It should be noticed that the writing of bi-dimensional shapes, like the EPFL's logo, involves changes of direction and accelerations of the stages. For this reason, calculating the deposited energy in every point of the modification can be complicated, since the speed of the platform during the writing of the text is not linear, and the pulse overlap cannot be easily calculated. Even if that was the case, due to the absence of visible features on the surface after the coating of the conductive layer, the exact location of the FIB cut with respect to the EPFL logo geometry would be difficult to establish.

Chapter 5. Laser-induced confined crystallization in multilayer systems

The second case study involved the design, deposition and processing of a new sample, inspired by the design proposed by Kavokin *et al.* [148], consisting of the superposition of two $\text{SiO}_2/\text{SiN}_x$ DBRs of different periodicity. A visualization of the layers' structure and the reflectance spectrum of this specimen (Sample_Si3N4_C) can be seen in Fig. 3.3.

Similarly to the experiments carried out in Section 5.5, the exposure processes aimed for the creation of an array of dots, where the pulse energy was varied along the horizontal axis between 70.0 nJ and 31.0 nJ (meaning deposited energies between 1.43 and 0.63 J cm⁻²), and the focal spot position was varied between +6 μm and -6 μm along the vertical axis. The sample was processed at a repetition rate of 60 kHz, in order to improve the stability of the laser output during bursts of low pulse number, while the imaging step was still done at 240 kHz. Bursts of 8, 16 and 32 pulses were used, and their effect on the sample's surface is shown in Fig. 5.12a-c, respectively. Each image is subdivided in a right part (with an optical microscope image on top, and a THG map on the bottom, showing the position of the FIB-cut cross-section) and a left part, consisting of SEM images of the exposed areas.

Specifically, Fig. 5.12a shows the sample after exposure to bursts of 8 pulses. The modifications appear to be confined to the lighter layer, corresponding to the high-index material (SiN_x), consistently with what has been observed so far. The presence of partial layer ablation is also observed, in locations 8-A and 8-B; in this second case, the ablation is limited by the modified region, which acts as stopping point. This, together with the inclined walls of the ablated spot, might indicate that crack propagation from the modified area could be at the origin of the layers removal process. A similar case of figure is observed in Fig. 5.12b, showing the case of exposure to bursts of 16 pulses. Here, layer ablation damage is much more visible, and often larger than the beam waist. Once again, modified regions are mostly confined within a SiN_x layer, even though the damages do extend towards neighbouring layers, notably in the case of position 16-B. The cross-section in position 16-D also hints to the presence of laser-induced modifications, even though the resolution is not sufficient to clearly identify their nature. Finally, Fig. 5.12c shows the exposure case of bursts of 32 pulses, which generated more ablation than the two previous cases. A SEM image of the surface is presented on the right, showing the surface topography at the location of four partially ablated spots. The terraced layout of the ablation is clearly visible. Moreover, the SEM image taken in position 32-A shows the presence of a large, confined modified area, appearing to be at the origin of both the initiation of some partial ablation at the center of focal position, and of the crack propagation at the edges of the modification. As suggested for the 8 pulses burst case, this diagonal crack propagation is likely to explain the terraced topography of the ablated spots, as its angle, position and dimensions can be correlated with the conformation of the partially ablated spots (see for example 8-B and 16-A).

The advantage of THG imaging over conventional microscopy is less evident with this specimen, as the THG and digital microscope images tend to showcase the same patterns, with fewer points that are only found in THG maps. The nature and the extent of the modifications is more pronounced than in the $\text{SiO}_2/\text{TiO}_2$ case, which might explain why many sub-surface

5.6 Case studies for modifications confinement

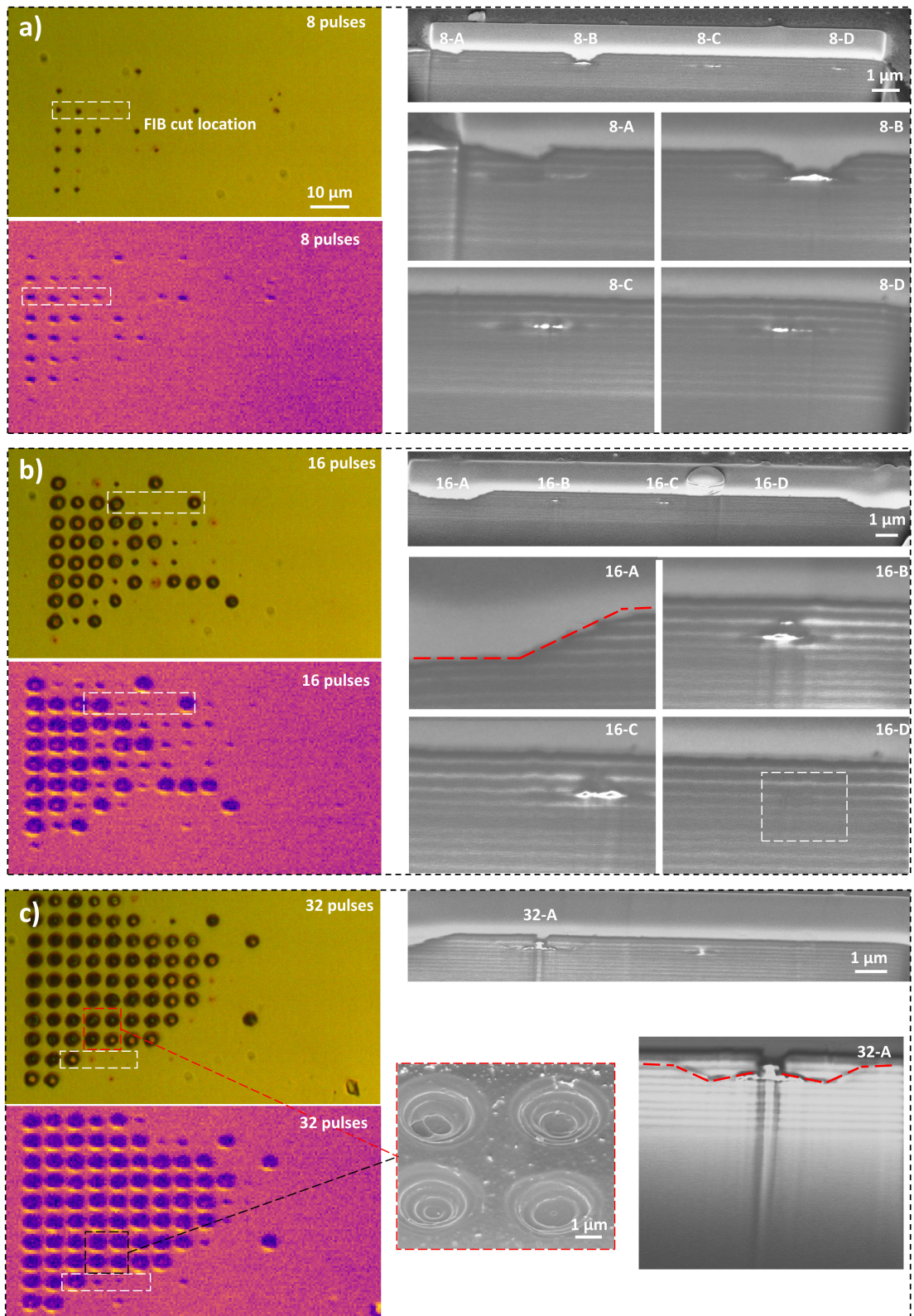


Figure 5.12: Correlation between THG imaging, optical microscope and SEM, for Sample_Si3N4_C. The description of the figure is found in the main text.

features are not only visible with THG imaging, but with digital microscopy as well.

5.7 Discussion

The correlation between FDTD simulations and experimental observations, in the case of $\text{SiO}_2/\text{TiO}_2$ sample, is appreciable. The enhancement of the electric field in the third layer of TiO_2 , starting from the surface (shown in Fig. 5.8a), suggests that non-linear absorption could have been initiated in this specific location, as is then demonstrated by the TEM images in Fig. 5.5. The proposed modification dynamics is as follows: the femtosecond beam is focused at a certain distance from the multilayer surface, such that the exposure dose is kept below the non-linear absorption threshold of the layers' materials. While travelling through the multilayer stack, the geometry and dielectric properties of the layers result in a local enhancement of the electric field of the pulse, in particular inside this specific TiO_2 layer, where non-linear absorption is triggered and ionization occurs. Further absorption in the following layers is inhibited by the existence of a localized plasma that acts as a mirror within the initially modified layer (that sees its damage threshold decreasing). The initiation of damage at the location of highest intensity was also suggested in similar thin film systems and for similar exposure conditions [50, 60], although these studies focused on the laser-induced damage threshold, and on the ejection of material, rather than on localized crystallization and controlled modification as we do here. As thoroughly argued by Zhang *et al.* [159], the electron density distribution is correlated to the electric field's intensity, and is dependent on the material's bandgap. Their proposed model also included modules for the ionization mechanism (dependent on the beam intensity) and the material modification mechanism.

In the case of Sample_Si3N4_B, unfortunately, the focal spot accuracy along the optical axis compared to the size of the multilayers does not allow for a precise correlation with the FDTD simulations, since the location of the beam waist with respect to the stack's surface is not known with certitude. However, a confinement is obtained in the layers where higher electric field was expected, and it manifests itself with the occurrence of nano-crystallites as visible in Fig. 5.3, despite the short interaction time of the laser.

As introduced in Section 1.4, the dynamics of femtosecond laser-induced crystallization is a complex subject, due to the short times of interaction and the presence of plasma at the spot of non-linear absorption. In previous studies, crystallization was believed to be linked to localized laser-induced heating and thermal gradients, which in non-cumulative femtosecond regime are very localized, inducing phase separation or destabilizing the lattice. In this work, femtosecond laser exposure of dielectrics stacks is also proven to be effective in promoting nucleation sites for crystallization, even though the crystallization dynamics remains elusive due to the current lack of real-time observations. In this case, and compared to these previous studies, there is no thermal-process occurring beyond the focal volume, as evidenced by the absence of intermixing, or evidence of melting, in the post-mortem observations. The repetition rate of the laser was chosen to be in a range where no thermal-cumulative effect

is observed. The energy is also chosen such that the energy is confined only in a single layer. In addition, TEM observations along with elemental distribution mapping clearly show that adjacent layers are unaffected during the process, hence demonstrating that no thermal degradation occurred and that the temperature in these layers remained lower than any critical temperature for melting or softening.

As expected, there is a difference in crystallization dynamics between the two materials systems, as laser exposure of Sample_TiO₂_A resulted in a TiO₂ crystalline polymorph (rutile) while exposure of Sample_Si₃N₄_B originated a Si crystalline phase. Hence, in the TiO₂ case the stoichiometry of the material was maintained, as the material likely underwent a laser-induced ordering of its own microstructure. The local increase in temperature, as well as the compressive pressure applied by the surrounding layers, enabled the overcoming of the energy barrier necessary for the phase transformation. The rutile phase is, generally, energetically more stable than other TiO₂ polymorphs [160, 161], which would explain the preferred transformation of the non-ordered material into this specific phase. Interestingly, previous reports suggest that anatase should be the preferred phase for nanoparticles of diameter of the order of 10 nm, due to the lower surface energy of this phase compared to rutile [162]. It has also been shown that anatase might have a faster kinetic of crystallization and therefore, might be favored at lower temperatures, at the early stage of classical phase transition processes (e.g. in a furnace) [160]. Here, however, due to the nature of the laser-matter interaction, it is likely not the case, suggesting a more dramatic phase transformation mechanism, from a 'nano'-plasma phase to a crystalline one. As we do *postmortem* analysis of the crystallized samples, however, we are not able to observe the crystallization process as it happens, which may involve multiple steps (e.g. for instance amorphous to anatase, then to rutile) as the structures are produced by multi-pulses exposure.

A slight migration of Si atoms towards the modified TiO₂ layer is also observed (see Fig. 5.6), even though it is mostly confined around the void regions, and therefore might be explained by the diffusion of atoms towards available "empty", low-surface energy space. The concentration of oxygen does not appear to be altered between the affected and non-affected zones, which is consistent with the fact that the stoichiometry of the new phase is unchanged with respect to the original amorphous material. In the case of Sample_Si₃N₄_B, however, it is evident that the Si-N bonds in the affected SiN_x layer were broken at a certain point of the process, as the Si atoms subsequently recombines into Si crystallites, while the N atoms diffuse outside of the affected zone, with a fraction of them probably escaping the material in gaseous form through micro- and macro-cracks along the above layers, or during the lamella preparation process. Such cracks were observed at some locations along the laser-written lines, indicating that some places might exhibit larger damages across multiple layers and up to the surface. Of relevance is also the diffusion of O inside the modified zone, indicating that the surrounding SiO₂ layers were partially affected as well.

Another interesting phenomenon is the formation of nano-pores, observed for low pulse cycles, as illustrated in Fig. 5.9 for a burst of 8 pulses. This is an addition to the cases of crystallization

and elemental intermixing described in the previous chapter. While the role and the formation mechanism of these nano-pores is not yet clear, it can be argued that they could be precursors for the formation of nano-voids, whose development, in turn, leads to crystallization of material in between them, due to compression and localized heating. This multi-step process is consistent with the visual appearance of the modified zones, especially visible in Fig. 5.3, Fig. 5.5 and Fig. 5.6, with regularly spaced nano-voids surrounded by crystalline clusters. However, the lack of sufficient experimental evidence, and especially the study of different exposure conditions with increasing pulse numbers, hinders the establishment of a definitive answer. In this perspective, a parametric study mapping the evolution of the layers' stack with an increase in burst pulse number would be beneficial for the understanding of the initiation of the crystallization process. That being said, FIB/SEM and TEM observations are expensive, time-consuming, destructive and very delicate to perform on such small modifications. The development of THG microscopy on dielectric multilayers could potentially address this issue.

Finally, Fig. 5.12c highlighted an interesting crack propagation pattern, whose directionality can be compared to the topography of the ablated blisters on the same specimen's surface. This partial ablation of the surface, consisting of the ejection of blisters, was especially noticeable in Sample_Si3N4_C, for bursts of larger number of pulses. Due to reflection from the plasma, energy accumulation above the modified region is likely to cause the ejection of the top layers, facilitated by the presence of the cracks at the edge of the blisters. This could also explain the distinct and clean delamination observed between layers, which would be promoted by preferential crack propagation along layers' interfaces. This proposed mechanism can, for instance, be compared to the phenomenon described by Kumar *et al.* [50], where the localized and finely controlled ejection of SiN_x thin films was promoted by tuning the interference between incoming and reflected parts of the beam.

5.8 Summary

Exploiting a phenomenon of localized field enhancement in 1D aperiodic arrangements of layers, we demonstrated a method to achieve high spatial confinement of laser-induced modifications along the optical propagation axis, without the use of a tightly focused beam. Specifically, we showed that laser-induced modifications in dielectric multilayers, notably localized crystallization, can be confined in one layer of a multilayer stack without affecting the surface of the material. The crystalline zones are much smaller than the wavelength of the processing laser, and are as little as 25 times smaller than the Rayleigh length for the focusing objective considered here.

The confinement is demonstrated in two different materials systems, namely $\text{SiO}_2/\text{SiN}_x$ and $\text{SiO}_2/\text{TiO}_2$ multilayer samples, with different layers thickness arrangements, confirming that this phenomenon is essentially driven by the layer thickness distribution and validating the hypothesis of field enhancement effect. The experimental observation of field confinement has been confirmed and predicted using a FDTD propagation model. The presence of laser-

induced nano-pores, for exposure conditions with few pulses, is also observed, suggesting that their formation could be within the first steps of the crystallization process, in case of cumulative exposure. Also, the topography of partially ablated spots on one of the samples was correlated with the propagation of transversal cracks, from the sub-surface modifications towards the surface.

Imaging of the confined modifications with THG microscopy was successfully demonstrated, and the intensity of THG signal could be correlated with the presence of sub-surface modifications. However, the correlation between the nature of such modified areas, and the intensity or quality of the signal is still to be investigated. As the conversion efficiency of THG signal depends on the interface state between two different media, the difference in their physical properties matters. As such, interfaces between nano-pores, crystallites, densified areas and amorphous material could, in principle, give rise to different THG signals.

The method is generic and can be applied to a broad variety of layers assemblies. Although not investigated here, but nevertheless commonly observed for bulk-nanogratings formation (see for instance [42]), the polarization state of the beam may also offer an additional parameter for controlling the formation and possibly the orientation of the crystallites. Finally, this controlled high confinement capability in the bulk of layered materials opens interesting opportunities in various field, including high-density durable data storage, meta lenses and nanocrystals for quantum emitters.

6 Crystallization dynamics and dependence on thermal regime ¹

6.1 Introduction

Laser-induced crystallization provides a finer control of the modifications dimensions and distribution, with respect to other methods such as thermal annealing. Here, we investigate the characteristics of modifications induced by different laser exposure conditions, notably involving ionizing and non-ionizing absorption processes, and the presence, or absence, of thermally cumulative irradiation regimes.

6.1.1 Ionizing versus non-ionizing exposure conditions

Here, we explore laser-induced crystallization phenomena through three different laser exposure modalities. Specifically, we investigate the role of non-linear absorption-induced ionization in crystallization processes by comparing it to a purely temperature-driven process. In addition, we further consider the case where the temperature gradually builds up, by successive and cumulative femtosecond laser pulses exposure, fired at a rate sufficiently high for preventing thermal relaxation to occur in between pulses (as illustrated in Fig. 6.1). This exposure regime is interesting, as it offers an opportunity to highlight the role of ionization as a precursor for thermally-driven crystallization processes and to compare the role of ionization in such cases, with respect to an annealing process purely based on thermal excitation.

When the repetition rate of the laser is increased above a certain material-dependent threshold, the thermal profile around the laser-affected zone becomes gradually more important, resulting in what is known as thermal regime, where a thermally-induced feedback phenomenon affects the structure, size and distribution of the laser-modified volumes [164, 165].

At the opposite side of the spectrum, continuous wave (CW) lasers are linearly absorbed by the materials, as the lack of temporal confinement prevents the achievement of the peak powers

¹Part of this chapter is being published in "R. Ricca, V. Boureau and Y. Bellouard, *Influence of ionization and cumulative effects on laser-induced crystallization in multilayer dielectrics*, in preparation, 2023" [163].

needed to initiate non-linear absorption. As a result, CW laser-induced modifications are non-ionizing, contrarily to the case of femtosecond laser exposure, and are fully thermally driven.

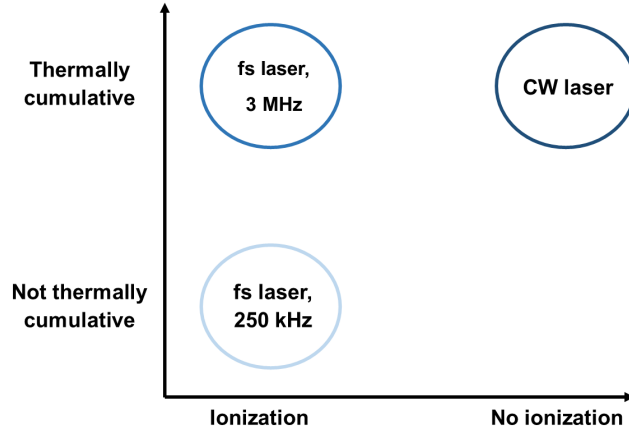


Figure 6.1: Scheme of the three laser exposure regimes used in this study: a laser source with exclusively non-linear absorption effects and no thermal accumulation effects (femtosecond laser, 250 kHz) the same non-linear source but at higher pulse frequencies (femtosecond laser, 3 MHz), enabling the presence of thermal effects, and a different laser source, where the absorption is non-ionizing and purely thermal (continuous-wave laser).

Therefore, the work presented in this chapter aims to explore the difference in crystallization outcomes between both low and high repetition rate femtosecond exposure, and linear exposure, and compare these two cases with the low-repetition rate exposure results presented in Chapters 4 and 5.

6.2 Materials and methods

The investigated specimen is Sample_Si3N4_A, consisting of alternating SiO₂ and SiN_x thin films, with the SiO₂ layers having a thickness of 119 nm and the SiN_x layers of 87 nm. The total thickness of the multilayer stack is 2.68 μm. The layers were deposited on a fused silica substrate (4" wafer) by PECVD using an Oxford Plasmalab, at a deposition temperature of 300°C, and the wafer was cut into smaller samples using a dicing blade. The microstructure of the layers after deposition was probed with Raman spectroscopy and resulted to be amorphous.

Two laser sources have been used in this study: the first one is a femtosecond fiber YAG laser with pulse duration of 270 fs and a wavelength of 1030 nm, as described in Section 3.3, used at a repetition rate of 3 MHz. This increase in repetition rate, with respect to the usual pulse picker frequency of 1 MHz, resulted in the broadening of the pulse duration, which has been measured to be 300 fs at this frequency, showing an increase of 11%. As this difference is minimal, we consider that it does not affect the physical phenomena behind phase transitions between exposures at low and high repetition rates regimes. Both beam intensity and beam

polarization can be controlled by motorized half-wave plates, and the laser is focused on the sample by a high-power objective (20X, NA 0.4).

The second laser source is a continuous-wave CO laser, Diamond C-55-5 from Coherent, emitting light at a wavelength of 5 μm and with a maximum power of 40 W. The power intensity profile, the shape of the signal (step function or sinusoidal) as well as the exposure time, are controlled through a Matlab-Simulink interface. The beam is focused on the sample through a ZnSe lens (focal length 35 mm, beam diameter approximately 300 μm), and the sample can be translated using a micrometric stage that can be controlled both manually or through the Matlab interface. The complex refractive indexes k of SiO_2 and Si_3N_4 at 5 μm are $k_{\text{SiO}_2} = 0.00076$ and $k_{\text{Si}_3\text{N}_4} = 0.00445$ [166], respectively. The absorption coefficient α can be calculated as $\alpha = 4\pi k/\lambda_0$, so that at the laser's wavelength, $\alpha_{\text{SiO}_2} = 1.91 \cdot 10^3 \text{ m}^{-1}$ and $\alpha_{\text{Si}_3\text{N}_4} = 11.18 \cdot 10^3 \text{ m}^{-1}$, showing that the nitride phase is about 6 times more absorbing than SiO_2 . At this wavelength, the single photon energy is 0.248 eV, more than an order of magnitude lower than the bandgap of both layers considered here. Ionization would require at least 20 photons for the SiN_x - which has the lowest bandgap. Furthermore, the power density is at most 180 kW cm^{-2} , much lower than the femtosecond laser peak-power at 1030 nm, preventing any non-linear absorption effects to take place.

The characterization of the materials was done by SEM and TEM observations. A Zeiss NVision 40 dual-beam SEM/FIB was used to slice the cross-sections across the surface, to observe the exposed sections in SEM mode and to prepare the TEM lamellas, thinning them down to a final thickness of ~ 100 nm. The lamellas were observed with a Talos F200S TEM, at an operating voltage of 200 kV; techniques of observation included bright-field TEM (BF-TEM), dark-field TEM (DF-TEM), selected area electron diffraction (SAED) and energy-dispersive X-ray spectroscopy (EDS) scanning-TEM techniques. Scanning precession electron diffraction (SPED) measures were also realized, using an Astar system installed on a FEI Tecnai Osiris TEM, for local phase and orientation mapping of the crystallites in the specimen [167, 168]. The SPED measurements were conducted at 200 kV, with a beam current of 12 pA, a precession speed of 100 Hz at an angle of 0.6° , a dwell time of 20 ms and a step size of 3.75 nm.

6.3 Experimental results

6.3.1 Femtosecond laser exposure at low and high repetition rate

Femtosecond laser exposure of this $\text{SiO}_2/\text{SiN}_x$ sample, at low repetition rates, has already been discussed in Chapter 4. To enable a better visualization of the differences between low and high repetition rates, we included parts of this previous findings in Fig. 6.2a and b. Here, the BF-TEM images show a location that has been exposed to the femtosecond laser at a repetition rate of 250 kHz, scan speed of 1 mm s^{-2} and pulse energy of 137 nJ, resulting in a deposited energy of 2.49 kJ cm^{-2} . These images correspond to what has been shown in Fig. 4.5.

As visible in Fig. 6.2a, the laser-modified area extends a few microns away from the beam waist

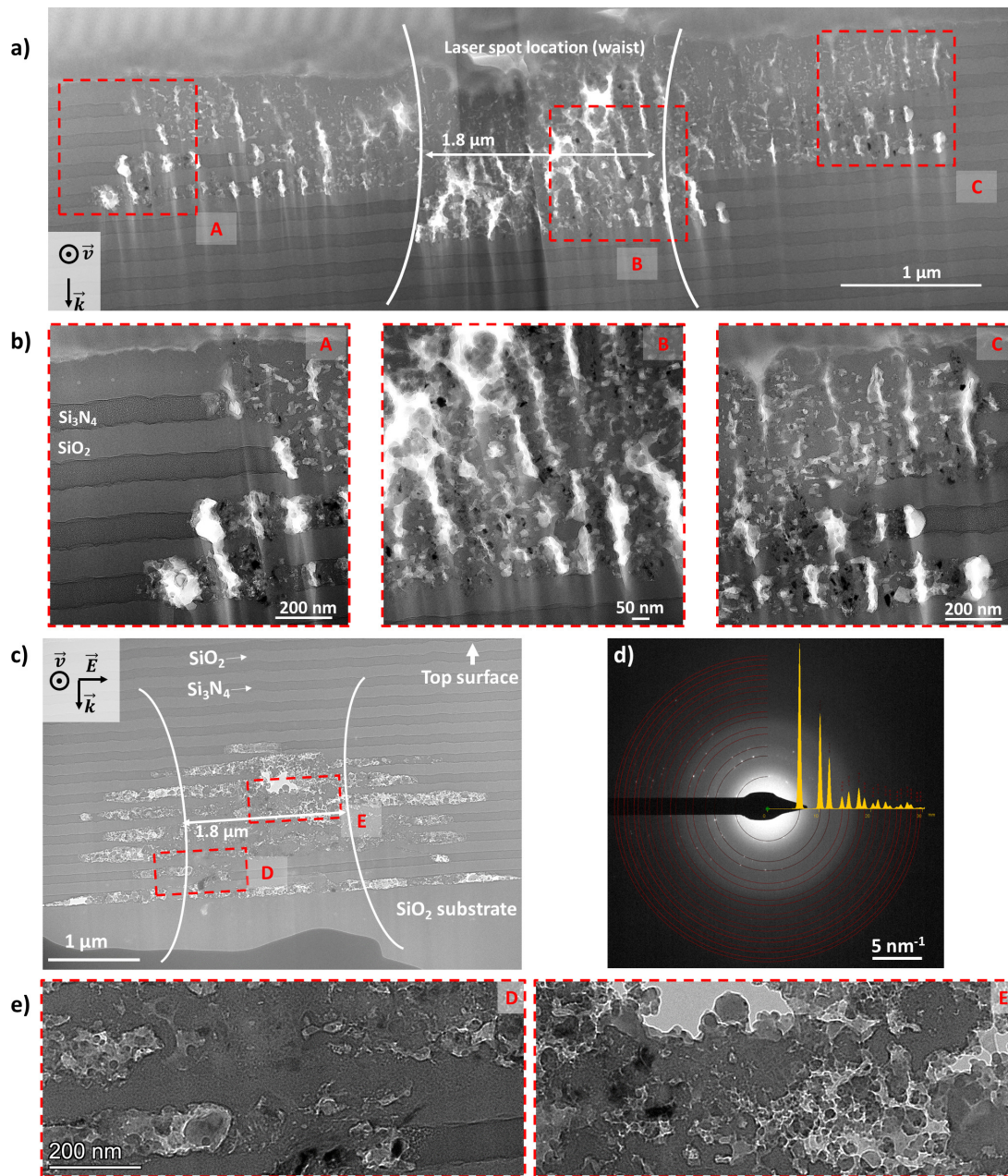


Figure 6.2: a) BF-TEM image of SiO₂/Si_x multilayers exposed to femtosecond laser pulses, at a repetition rate of 250 kHz and pulse energy of 137 nJ. The Si_xN_y layers appear darker. b) Higher magnification BF-STEM images of regions A, B and C, as highlighted in red in figure (a), showing the distribution of the silicon crystallites within the laser-affected area. c) BF-TEM image of the same multilayers exposed to femtosecond laser pulses, at a repetition rate of 3 MHz and a pulse energy of 16 nJ. Besides a central area (indicated by the approximate location of the beam waist), showing higher levels of intermixing, most modifications are confined to the high-index Si_xN_y layers. d) SAED pattern originating from the modified area, evidencing the presence of multiple crystallites of Si with random orientation. e) BF-TEM magnifications of areas D and E, as highlighted in red in figure c).

location (indicated in white on the image). Voids are visible, spaced with a relatively regular periodicity, and especially present in the SiN_x layers. The higher-magnification BF-TEM images shown in Fig. 6.2b, corresponding to locations A, B and C of Fig. 6.2a, confirm that atomic intermixing between the layers occurs within most of the laser-affected area, excluding the edges, where the damages are mostly located in the SiN_x layers. In the intermixed region, both the location and dimensions of the voids distribution is less homogeneous. Pure silicon crystallites with dimensions lower than 50 nm, shown by a darker contrast, are observed spread around the modified volume, without a clear preferential distribution in the layers.

Conversely, the high repetition rate sample was exposed to the femtosecond laser at a pulse frequency of 3 MHz, a scan speed of 10 mm s^{-1} , a beam polarization perpendicular to the writing direction and a pulse energy of 16 nJ, resulting in a deposited energy of 0.34 kJ cm^{-2} , or 7.3 times lower than the previous case. Here, the modifications were concentrated around the lower section of the multilayer stack, probably due to a minor misalignment of the focal position. Given the order of magnitude of the layers thicknesses, an error of $\pm 1 \text{ }\mu\text{m}$ induced by a slightly tilted surface can heavily affect the position of the modifications within the stack. As visible in Fig. 6.2c, it is worth noting that, outside of the central part of the laser-affected zone (which shows a great extent of intermixing), the damages are more concentrated in the SiN_x layers with respect to the low repetition rate case, with large portions of the modifications being confined in this material without heavily affecting the surrounding SiO_2 layers. Nevertheless, the modifications also extend towards the SiO_2 layers around the center of the beam waist location. The SAED pattern of the laser-affected area is shown in Fig. 6.2d, evidencing the presence of crystallites with random orientations. The pure Si, cubic diamond crystal phase, shows a good fit of the discrete ring pattern observed in the specimen.

Figure 6.2e shows BF-TEM magnifications of areas D and E, which are highlighted in red in Fig. 6.2c. Here, the presence and distribution of crystallites is indicated by the darker areas. Based on our previous findings [130], which were presented in Chapter 4, and on the EDS maps presented in Fig. 6.3a, that show a sharp increase in Si concentration within the laser-affected zone, we compared the interplanar distances measured from Fig. 6.2d with the calculated values for crystalline Si [134], as illustrated in Table 6.1, with a good agreement between the values. The SAED pattern proves the presence of Si crystallites within the modified area, similarly to what has been reported in [130].

Corresponding plane	Measured	Calculated	Difference [%]
(111)	3.096	3.135	-1.24
(212)	1.832	1.810	+1.22
(222)	1.595	1.567	+1.79
(223)	1.321	1.316	+0.38
(313)	1.235	1.245	-0.80

Table 6.1: Measured interplanar distances for the laser-induced crystallites in the $\text{SiO}_2/\text{SiN}_x$ sample exposed to the high-repetition rate femtosecond laser (from Fig. 6.2d), and comparison with the calculated values for FCC-diamond silicon (in Å).

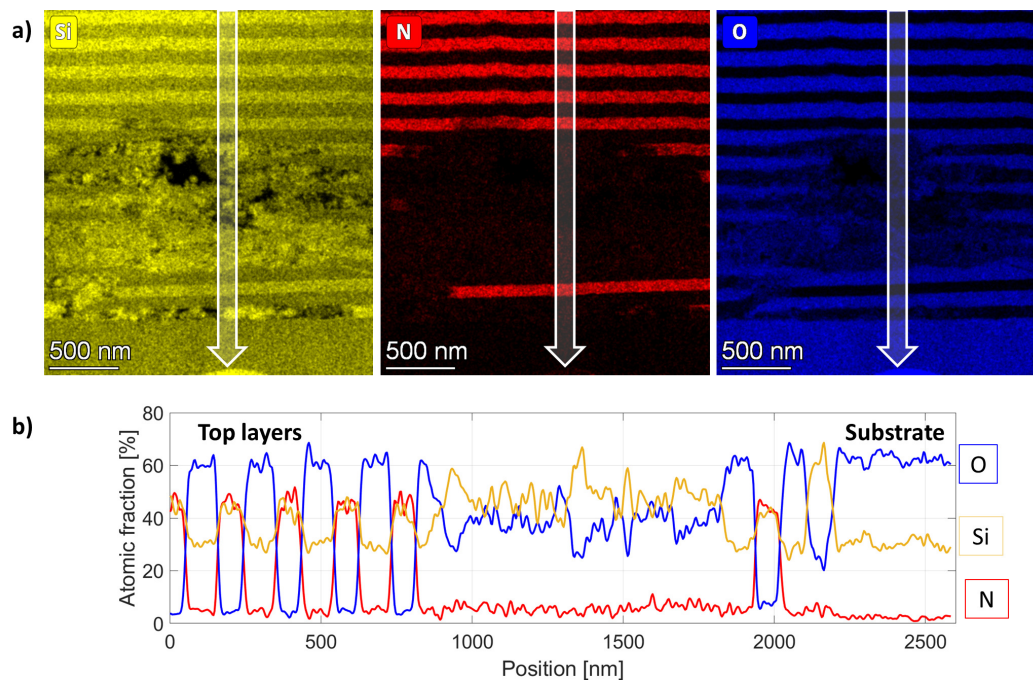


Figure 6.3: a) EDS elemental mapping of Si, N and O atoms across the laser-affected area, illustrating the redistribution of both silicon and oxygen, and the depletion of nitrogen. The white arrows represent the location of the profile of composition shown in b), where the atomic fraction of the atomic species is plotted as a function of the depth in the specimen. The width of the arrow represents the integration width of the profile.

The EDS images in Fig. 6.3a show the elemental distribution of Si, O and N within the same cross-section of the laser-affected zone. The nitrogen concentration, in particular, drops dramatically in the modified area, despite being 1 μm below the surface. This is probably due to a combination of elemental redistribution (homogeneous redistribution of N atoms within the modified volume) and, possibly, evacuation through cracks, pores and ablated regions located along the laser-written line, or by degassing during lamella preparation. On the contrary, Si and O species remain in high concentrations and are redistributed around the laser affected volume, with Si clusters observed at the location of the crystallites, in agreement with the data provided by the SAED pattern. The white, downward arrows represent the location and direction of the profile scan shown in Fig. 6.3b, tracing the atomic fraction of each species across the multilayer stack. The removal of N from the laser-affected volume is particularly visible, as its share goes below 10% in the whole area: if N atoms would have been simply redistributed, this value should have been in the range of 25-30%.

By comparing the TEM image of the two samples, multiple phenomena are noticeable. First, increasing the repetition rate seems to reduce the homogeneity of the elemental intermixing outside of the focal spot location, and to promote the preferential modification of the nitride layers. Moreover, the voids in the high repetition rate specimen are much more chaotically distributed, without any evidence of self-organization. Conversely, in both cases, the absence

of preferential distribution, and the relatively small dimensions (diameter ≤ 50 nm) of the crystallites are comparable. The extension of both modified areas in the longitudinal and transversal directions is also similar, spanning between 1.1 μm and 1.6 μm (transversal) and 6.0 μm and 5.3 μm (longitudinal), for the low and high repetition rate cases, respectively. It should be highlighted that both the pulse energy and the deposited energy are much smaller in the case of high repetition rate exposure, therefore the presence of such a large modified volume can be attributed to the presence of a thermal accumulation effect.

To summarize, femtosecond laser exposure at a repetition rate of 3 MHz resulted in the formation of Si crystallites distributed across the modification volume, together with an intermixing of silicon and oxygen atoms, and the depletion of most of the native nitrogen from the affected areas. With respect to previously reported cases, concerning the exposure at lower repetition rates, SiN_x layers were affected the most by the laser, and in a large portion of the exposed volume they could be selectively modified.

6.3.2 CO laser exposure

To study laser-matter interaction at the thermal, non-ionizing level, the sample was exposed to a CO laser, in two different modalities: either by scanning the laser over the surface, or by irradiating a single spot.

Due to the configuration of the experimental conditions, the energy of the laser beam could not be recorded, as the powermeters were not adapted to the task. Although it was not possible to directly measure the energy of the laser beam due to limitations on the experimental setup, we were able to control the power percentage and use it as a basis for comparison between different experimental conditions. By varying the power percentage, it was possible to explore how different levels of power affect the outcome of the experiment. Moreover, the laser power value could be modulated as an arbitrary function, as illustrated in Fig. 6.4a, showing the laser power profile (power percentage as function of time) in the case of linear scans A and B, whose trace on the multilayers' surface is shown in Fig. 6.4b. Scan A consists of a case where the power is increasing linearly, until reaching a plateau at 14% of the power. Conversely, scan B is more similar to a step function, but with a linear increase instead then a vertical step, in the first half of the process. Here, the maximal power is fixed at 12%. The scan distance was 6 mm, while the scan speed was 40 $\mu\text{m s}^{-1}$ for line A, and 25 $\mu\text{m s}^{-1}$ for scan B.

Under these conditions, laser irradiation in scanning mode resulted in the features shown in Fig. 6.4b. Line A consists of barely visible (with an optical microscope) modifications at the beginning, which gradually become more distinguishable, until suddenly resulting in periodically spaced melted dots along the writing line, which at this point has a width of approximately 300 μm . The presence of cracks, spreading several tens of microns away from the melted spots, is observed. Line B was written more slowly but also at lower power, and shows a lower degree of surface damage, with a limited amount of locations with heavy surface modifications.

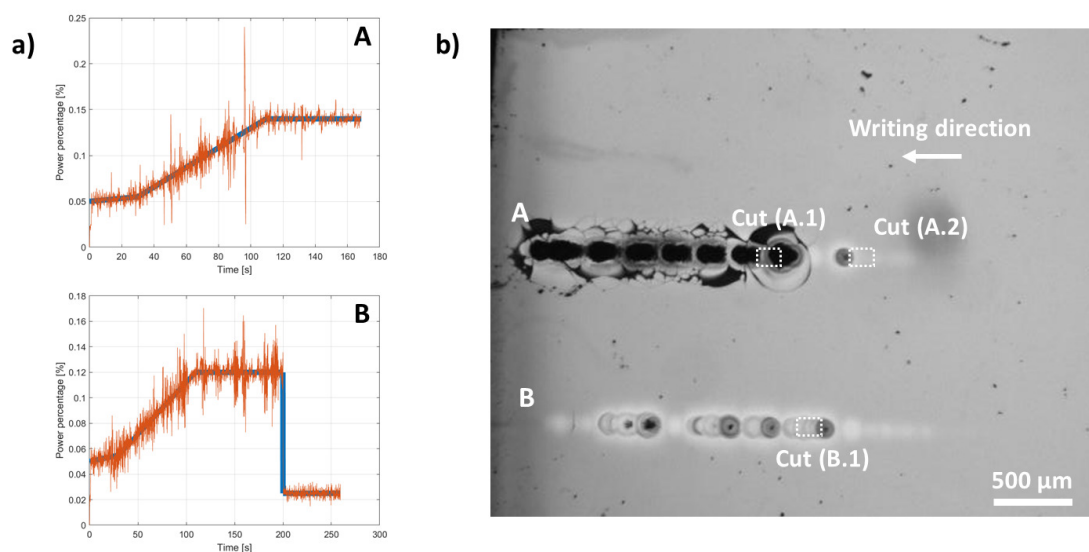


Figure 6.4: a) Example of laser power profiles, showing how laser power evolves with time. The blue curves represent the theoretical power evolution, while the orange curves represent the actual monitored data. b) Optical micrograph of the corresponding CO laser-written lines, on the surface of Sample_Si3N4_A. Two lines are shown, A and B, corresponding to the energy profiles shown in a). The locations of FIB cuts, shown in the following Figures, are indicated and labelled as A.1 and A.2 (on laser-written line A) and B.1 (on line B).

A magnification of the features observed along line A is shown in Fig. 6.5a, where SEM imaging evidences the presence of the melted spots, and of the cracked areas around them, arising from thermally-induced stresses. The length of the line can be followed from left to right, and top to bottom, keeping in mind that the writing direction is opposite to the orientation of the line, in this image. The location of FIB cuts A.1 and A.2 is also shown here.

Figure 6.5b specifically shows the cross-section of location A.1, at the edge of one of the melted spots, cut and exposed along the writing direction. Due to the extreme heating, the layers at the melted spot are mixed and partially ablated, resulting in a relatively deep crater, while part of the melt spilled over to the surrounding surface. Outside of the crater, the layers' geometrical structure is largely maintained, as no signs of delamination, plastic deformation or ablation are clearly visible. However, the crystallographic structure of the constituting materials is heavily affected, as illustrated by the dark spots visible within the layers (which are even more visible in the magnified image in Fig. 6.5c), corresponding to laser-induced crystallites. Cross-sections of the two other FIB-processed locations, A.2 and B.1, are visible in Fig. 6.5d and e, respectively. Here again, the layers' constituting materials were clearly subjected to a phase transition process, indicated by the presence of black spots dispersed within the stack. It is worth noting how the density of crystallites appears to be higher in location A.2 than in B.1, suggesting correlation between the laser power and the amount of crystalline material. However, given the absence of statistical significance, this correlation is purely speculative, and a definitive conclusion would require further investigations and an

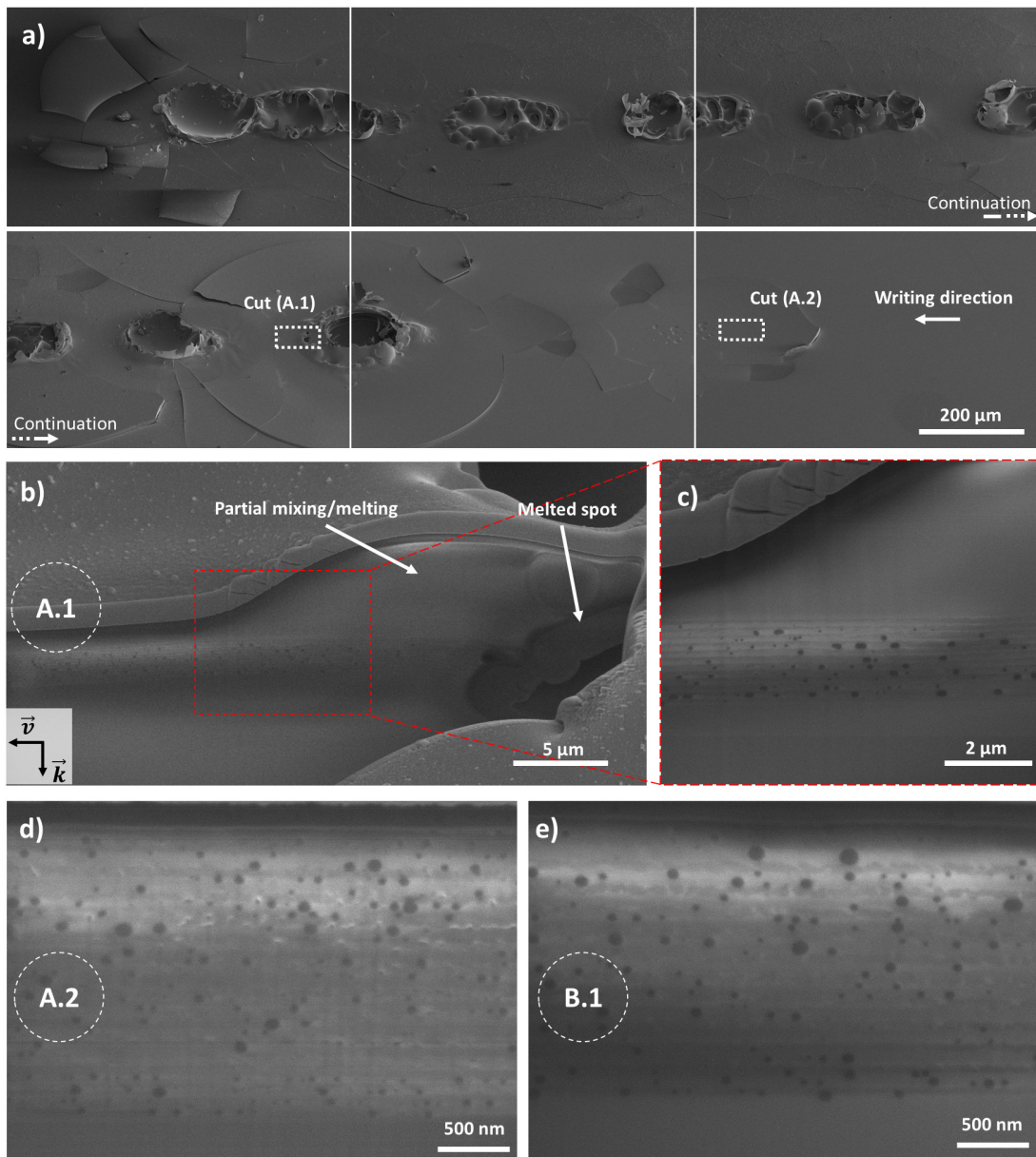


Figure 6.5: a) SEM image of laser-written line A, as defined in Fig. 6.4a, showing the alternation of craters, cracks and sub-surface modified areas. FIB cut locations A.1 and A.2 are also indicated. b) SEM image of a cross-section of the material after exposure to the CO laser, corresponding to location A.1. The focal spot position is shown far on the right, where the crater is visible. The layers' structure, with crystallites visible as black spots, is relatively consistent until the crater, while a considerable volume of melted material can be found above part of the layers, just next to the crater's boundaries. This material has been transferred from the crater location onto the nearby surface during the laser-induced localized melting of the layers. The interface between layers and melt is further magnified in c). Images d) and e) show SEM images of cross-sections of cut locations A.2 and B.1, respectively, evidencing the presence of crystallites throughout the whole laser-affected area.

increased number of data points.

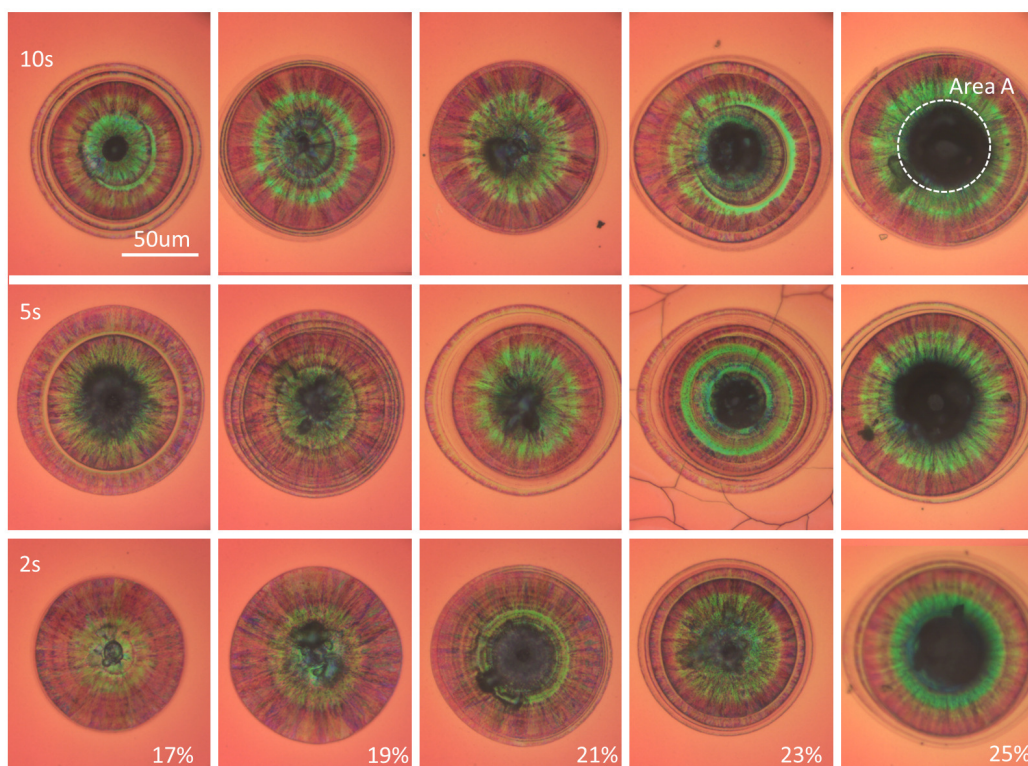


Figure 6.6: Optical microscope observation of single spot CO laser exposure mode, at different laser powers (along the horizontal axis) and exposure times (along the vertical axis). On the top right, area A is highlighted, and corresponds to the crater next to the lamella cutting location illustrated in Fig. 6.7a. The colors indicate both a change in material's structure, and a deformation of the layers, in proximity of the craters.

Likewise, laser exposure in single spot mode resulted in the creation of partially ablated spots, forming craters of dimensions up to 40 μm of diameter, with the presence of cracks and sub-layer modifications around the laser-melted area, which are due to thermal stresses following the irradiation and the rapid cooling of the material. Examples of such exposure conditions are shown in Fig.6.6, consisting of a matrix of points with varying laser powers (from 17% to 25%) and exposure times (from 2 s to 10 s). The black spots in the middle of the images correspond to the molten areas, while the coloured parts around it reflect the gradient of modifications in the surrounding area. The extent of the damages increases with power, however no remarkable trend is noticeable on the vertical axis. That being said, the instability of the laser power needs to be considered, as the repeatability of the data points might be hindered by fluctuations of the beam power. A lamella for TEM observation was cut out of a sample exposed at 25% power for 10 s, whose molten spot is indicated as *area A* in Fig. 6.6. The location where the lamella was cut is comprised within 25-45 μm from the crater's edge, as indicated in Fig. 6.7a.

A BF-TEM image of this lamella is shown in Fig. 6.7b, showing how the laser affected the totality of the layers of the stack, without evidence of preferential modification dynamics. A

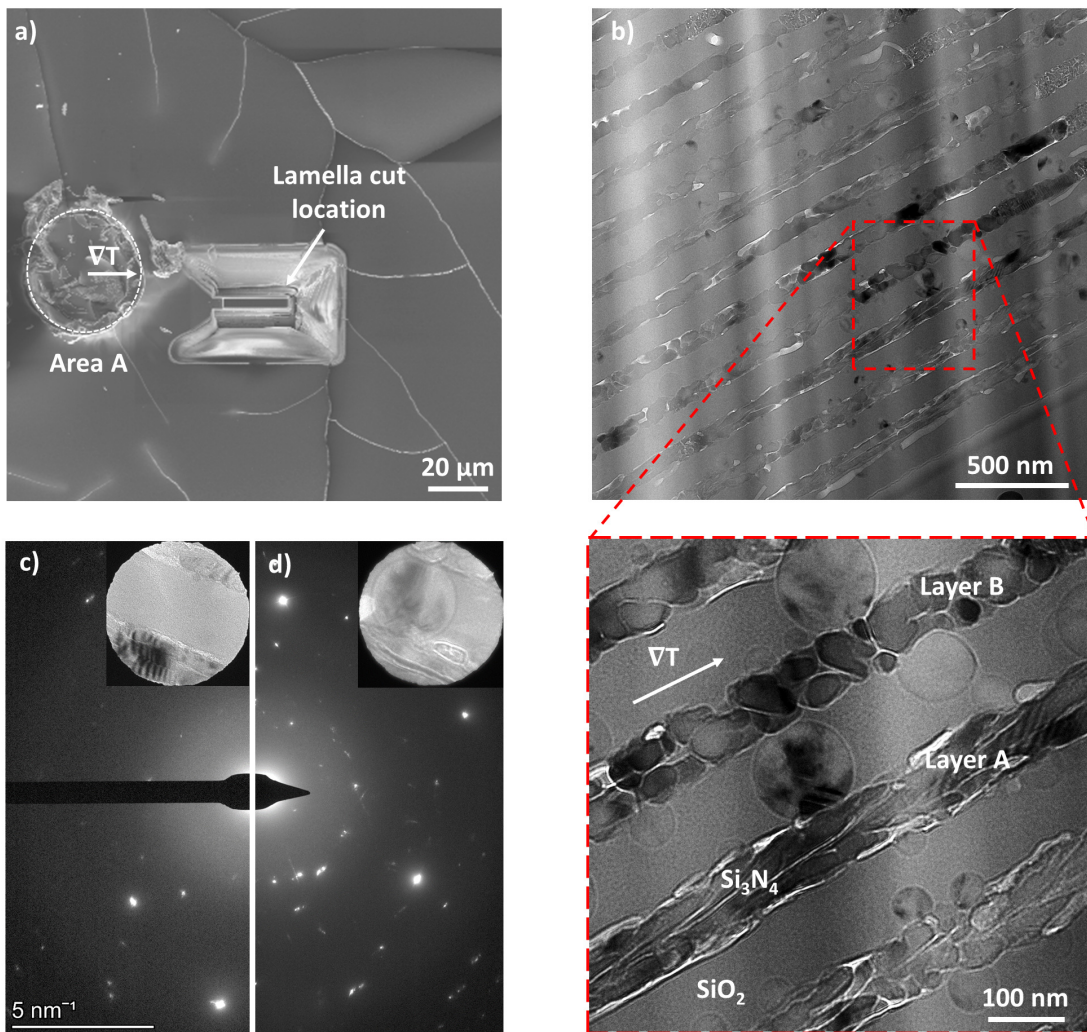


Figure 6.7: a) Location of the TEM-analyzed region, i.e. where the TEM lamella was fabricated, with respect to the position of the focal spot of the laser. b) BF-TEM image of the multilayers exposed to CO laser radiation, with grain structures clearly visible in the SiN_x layers and globular crystallites growing inside the otherwise amorphous SiO_2 layers. A magnification of a portion of the lamella is visible in the image below, showing the direction of the thermal gradient. Images c) and d) show halves of the SAED patterns of a region with modified SiN_x layers, and of a region with a modified SiO_2 layer, respectively (the regions are shown in inset). Both diffraction images show high crystallinity content.

portion of the image is further magnified below, where the growth of crystallites inside the SiN_x layers is highlighted by the presence of clear grain boundaries, with some of the grains stretched along the length of the layers. This orientation could indicate a preferential growth direction that follows the general direction of the temperature gradient, as visible along *layer A* (indicated in the image). Conversely, in *layer B* the grains show a more isotropic shape, or are possibly also elongated but with an orientation perpendicular with respect to the thermal gradient. Within the SiO_2 layers, it is possible to notice the presence of spherical crystallites of varying size, which seem to nucleate, generally, at the interface between the two materials

Chapter 6. Crystallization dynamics and dependence on thermal regime

These spheroids correspond to the black spots visible in the SEM images in Fig. 6.5.

The SAED patterns corresponding to these layers are visible in Fig. 6.7c-d. Specifically, Fig. 6.7d shows the diffraction pattern of two crystallized SiN_x layers, separated by an amorphous SiO_2 layer, while Fig. 6.7e shows the pattern corresponding to a blend of SiO_2 and SiN_x layers. Due to technical limitations of the equipment (namely, the minimal dimensions of the selective aperture), isolating the contribution of the SiO_2 layer alone was unfortunately not possible. Moreover, from the analysis of this patterns alone, it was difficult to define a most probable candidate for phase matching, as the different spots could be assigned to different polymorphs, due to the high uncertainties on the values of the interplanar distances.

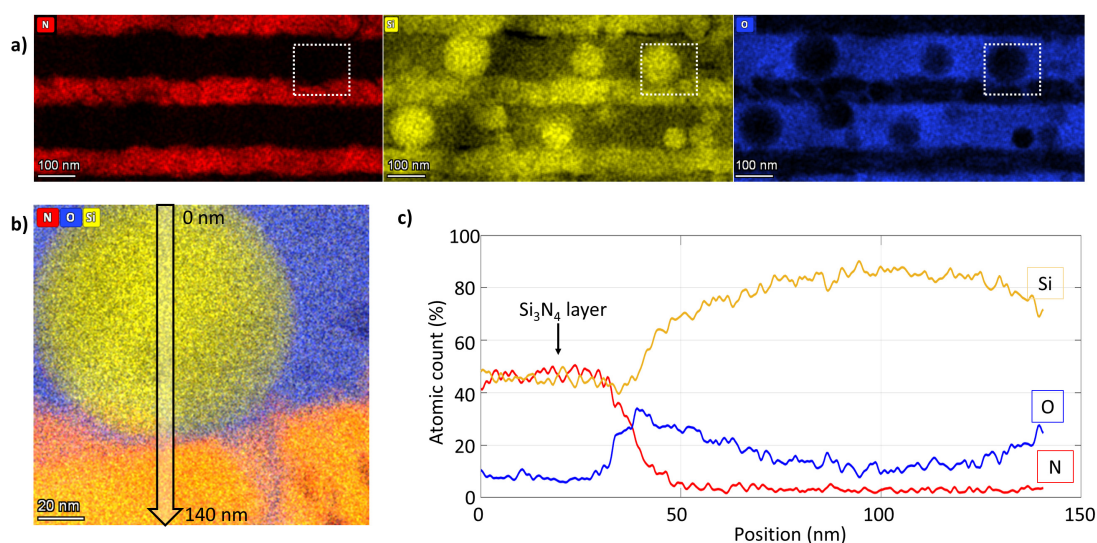


Figure 6.8: a) EDS elemental mapping of N, Si and O atoms across a volume exposed to the CO laser. b) EDS composite elemental map at the interface between an amorphous SiO_2 layer including a Si crystallite and a crystalline Si_3N_4 layer, at the location of the white rectangle depicted in figure a). c) Profile of the atomic fraction of N, O and Si, traced by the black arrow in image b).

EDS chemical mapping of the modified area is visible in Fig. 6.8a, with three images of the same cross-section detailing the atomic concentrations of N, Si and O. The structural integrity of the SiN_x layers is generally preserved, as no relevant elemental intermixing is observed between the layers. The images evidence the absence of oxygen from the spheroids inside the SiO_2 layers, and the presence of a silicon "surplus" in the same locations. Moreover, there is also evidence of oxygen infiltration at the grain boundary level in the SiN_x layers, as corroborated by the fine blue pattern visible in these layers. Figure 6.8b shows a magnification of the area indicated by the white rectangle in Fig. 6.8a, consisting of the interface between a SiO_2 layer, a SiN_x layer and a Si crystallite. The ratio of atomic species in the SiN_x layer is comparable to the stoichiometry of the pristine material, indicating that the phase transition involves the transformation of the amorphous phase into a crystalline polymorph of Si_3N_4 . However, the upper part of the image proves that inside the SiO_2 layer there is the occurrence of nucleation and growth of a heterogeneous phase of silicon. The elemental distribution

along a vertical line, indicated by the black arrow, is plotted in Fig. 6.8c, and confirms these observations.

The complete analysis of the nature and the phase of the different crystallites was not possible by SAED for the CO laser-exposed specimen. Thus, a scanning precession electron diffraction (SPED) configuration of the TEM was used, allowing the scanning of the specimen with a small electron probe while recording the pseudo-kinematical diffraction patterns with a camera, at each location in the specimen. The processing (using the Astar software suite [168]) of each diffraction pattern allows for the determination of the crystal phase and orientation distribution in the specimen, with a spatial resolution of 8 nm in the case of our experiment.

The investigated areas are indicated by BF-TEM images in Fig. 6.9a, and are named *Area 1* to 3. The presence of widespread crystalline zones is highlighted by the darker shades. Areas 2 and 3 are partially superposed, and the common area is indicated by the yellow shade indicated in the TEM images. Figure 6.9b shows the correlation maps of the investigated areas [169]. These maps display contrasts based on the change in the diffraction patterns, and thus are good tools to evidence the distribution of crystal grains with different orientations. We observe here that the spherical Si crystallites are in fact polycrystalline. Based on the EDS results presented above, crystal phase and orientation mapping were performed considering the presence of d-Si and α , β and γ polymorphs of Si_3N_4 . The maps of the crystal phase distribution display the diamond silicon in red, the α - Si_3N_4 in green and the β - Si_3N_4 in blue, as visible in Fig. 6.9c. The presence of spherical crystallites of pure Si within the SiO_2 layers, highlighted by EDS maps in Fig. 6.8, is confirmed. Moreover, the phases composing the nitride layers are a combination of both α - and β - Si_3N_4 , while no γ phase could be observed. This is in line with the literature, since the γ phase is known to be formed at high pressures and temperatures [170]. Evidently, although high temperatures were reached during CO laser exposure, the required conditions for the formation of this polymorph were not met. Remarkably, the two Si_3N_4 polymorphs are alternating, with successions of different grains belonging to the same phase extending for several hundreds of nanometers. There is no strong evidence of preferential phase formation, as the ratio between the phases is relatively homogeneous. The simultaneous occurrence of both phases explains the difficulty in correlating the measured interplanar distances with the theoretical ones, with SAED analysis.

Crystal orientation maps, visible in Fig. 6.9d, can be interpreted with the help of the orientation charts visible at the bottom of the figure. These maps are used for for the calculation of the 001 pole figures shown below, as each color encodes a specific orientation of the local crystallites. Since the three phases in presence belong to different lattice systems, Si is cubic, α - Si_3N_4 is tetragonal and β - Si_3N_4 is hexagonal, the crystal symmetries impose three different color legends, each one corresponding to a specific phase. Thus the corresponding crystal phase map is needed to read the absolute orientation of a crystallite at a specific location of the orientation map. The orientation of the Si_3N_4 phases is more uniform than the Si phase, as substantiated by the homogeneous color distribution within crystals of the same nitride phase.

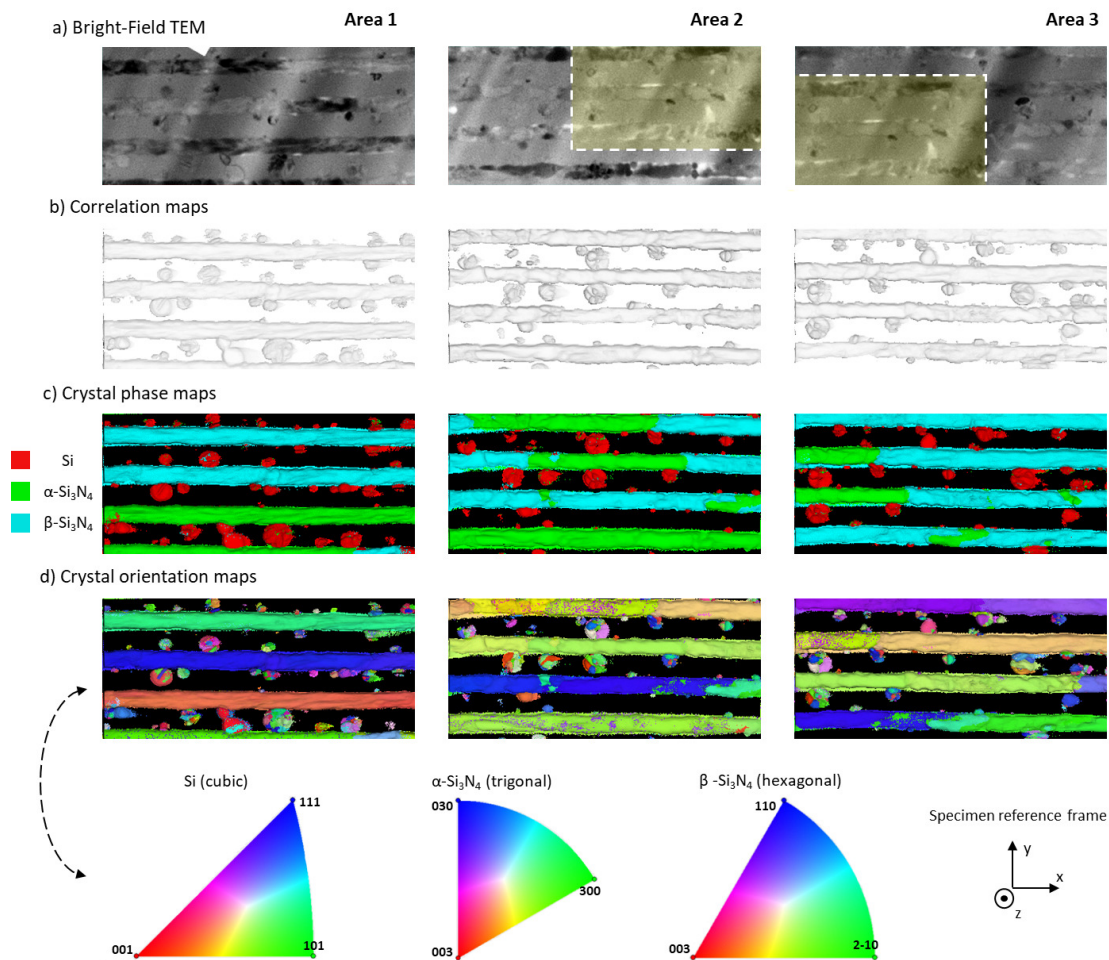


Figure 6.9: a) BF-TEM images of the lamella, indicating the locations investigated with the Astar technique, labelled Area 1 to 3. Areas 2 and 3 partially overlapped, as indicated by the common, yellow area. b) Correlation maps, showing the same features but highlighting their borders, rather than their details. c) Crystal phase maps, showing the phase distribution of Si, α - Si_3N_4 and β - Si_3N_4 across the investigated areas. d) Crystal orientation maps. At each location of the map, the color refers to the orientation of the local crystal phase, as reported in the legend. Black regions on the maps refers to an amorphous phase. Since each phase belongs to a different crystal system, color correlation between different phases is not consistent, so that the orientation of each phase should be studied individually with the help of the orientation charts at the bottom of the figure.

Conversely, the variety of colors inside the Si crystallites suggests that these are composed by several competing and differently oriented grains.

To better visualize the crystal orientation distribution of a sample, it is possible to plot pole figures, which represent the orientation density maps, with respect to an axis of reference. These figures consist of stereographic projections of the orientations of the crystallites [172], and their construction principle is shown in Fig. 6.10: depending on the chosen reference frame (which incorporates the rolling, transverse and normal directions, RD, TD and ND), selected crystalline planes of the sample diffract electrons at a certain angle, and their position

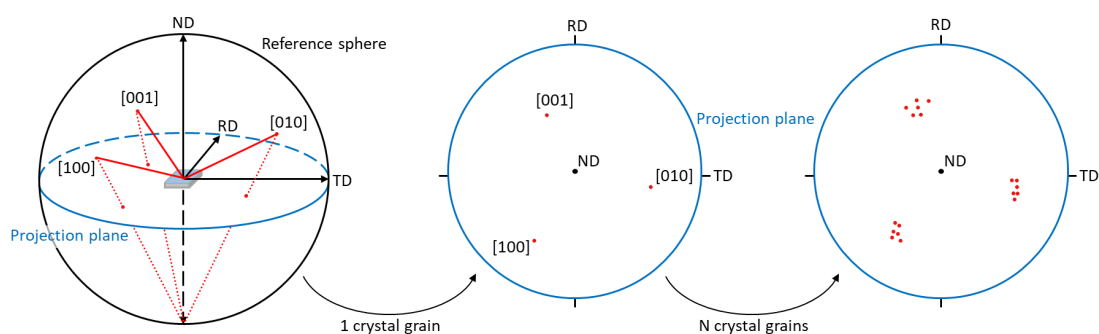


Figure 6.10: Principle of stereographic projection, and examples of **100** pole figures. The starting point is the reference sphere, indicating the rolling direction (RD), transverse direction (TD) and normal direction (ND). Diffraction points from crystalline planes are projected towards the south pole of the reference sphere, and the pole figure is created at the interpolation between the projection lines and the projection plane. The projection plane views for one crystal grain, and for N crystal grains, are also visible, in the center and the right of the figure, respectively. The image mapping N crystallites corresponds to the case of a material with preferential orientation, as visible from the clustering of the spots in specific locations. Drawing based on an image from [171].

can be traced on a reference sphere. These points can then be projected onto a 2D plane (the *projection plane*) by converging the spots towards the south pole of the reference sphere, and recording their footprint on the projection plane. By repeating the scan on different locations on the sample, multiple points (arising from multiple crystallites) are recorded, resulting in the mapping of the crystal orientation distribution. It is worth noting that, due to the definition of the stereographic projections, and since the three phases belong to different crystalline systems, the internal symmetries of the pole figures change with respect to the material composition.

The density plot of the 001 pole figures of the different crystal phases are visible in Fig. 6.11, for every investigated area. They display a statistical representation of the orientation of the crystallites, extracted from the orientation maps shown in Fig. 6.9. The higher the color-scale the bigger is the area covered by crystallites with this orientation. The pole figures of the α - and β - Si_3N_4 phases show a very strong texture, with the 001 orientations of all Si_3N_4 crystallites being aligned in the same orientations, whereas the textures of the Si pole figures do not evidence a preferential orientation of the Si crystallites, which seem to be randomly oriented. The spatial distribution in the pole figures is comparable between all investigated areas.

6.4 Discussion

From the results presented above, we conclude that $\text{SiO}_2/\text{SiN}_x$ multilayers laser exposure results in a variety of crystallization processes, depending on the regime of the laser-matter interaction. A comparison of the laser-induced modifications between the three explored exposure conditions is visible in Fig. 6.12. In a thermal, non-linear absorption regime, when the laser exposure results in ionization of the material, crystalline regions of pure Si are formed

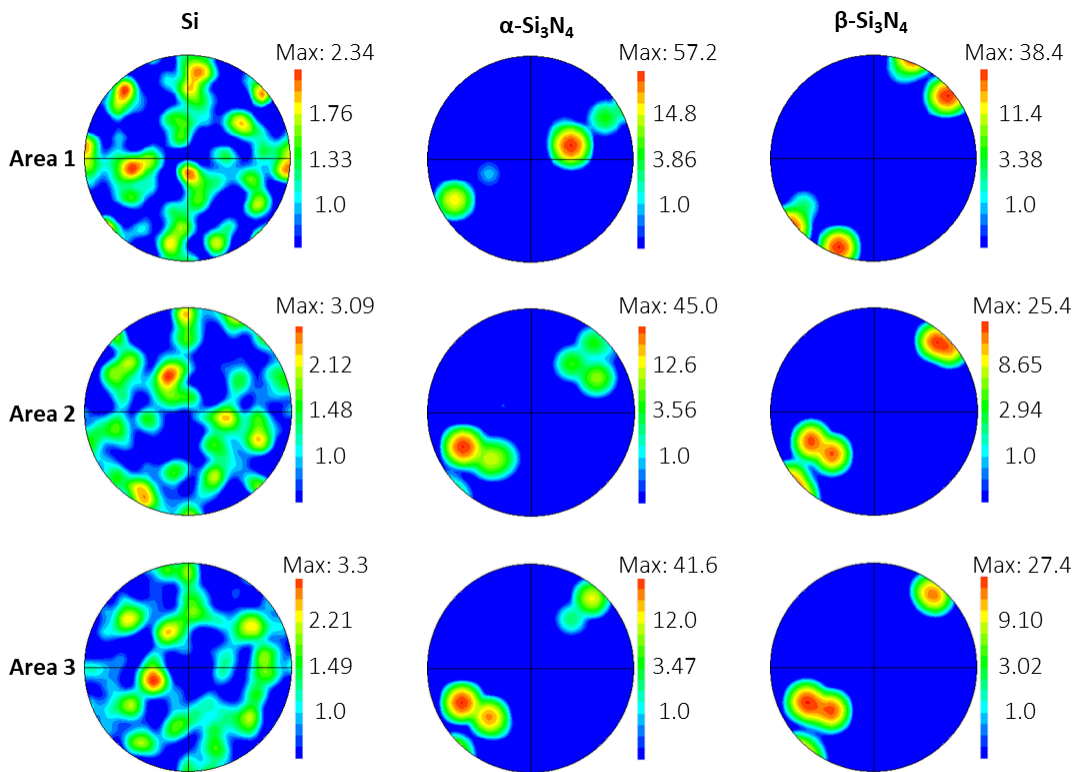


Figure 6.11: Pole figures for the **001** direction, for each phase and for each investigated area, as an indication of crystalline orientation distribution. Pole figures correlated with the Si phase are relatively homogeneous, while pole figures associated with both Si₃N₄ phases are highly directional.

within the laser-affected zone, preferentially targeting the SiN_x layers, as their absorption threshold is lower than the surrounding SiO₂ layers. After exposure to the same laser source, but at lower repetition rates, the confinement effect is restricted to the edges of the modified zone, which shows a higher degree of elemental intermixing than the case at high repetition rate. In a thermal, linear absorption regime, both constituting materials are affected, but with different outcomes: a phase transition from amorphous to crystalline is observed in the SiN_x layers, specifically resulting in a mix of α - and β -Si₃N₄ phases, as evidenced by various TEM observations. Conversely, in the SiO₂ layers, a heterogeneous Si phase grows within the layers, which remain otherwise amorphous.

To help the discussion on these observations, a set of relevant structural, mechanical and thermal properties of both materials is listed in Table 6.2. Some of the values are more indicative than quantitative, as they refer to quantities measured on crystalline bulk samples rather than on amorphous thin films. It must also be noticed that even values recorded for amorphous films should not be taken as definitive, as they vary with layer deposition conditions such as density, porosity, residual stresses at the interfaces, or the stoichiometry of the compounds. These values also change with temperature [173], so they are not representative of the material properties during the full duration of the laser-exposure, which can span an interval of several

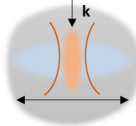
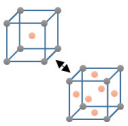
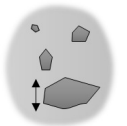
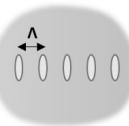

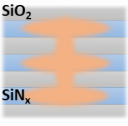
	Extension of the modified zone	Polymorphs in presence	Crystal size range	Self-organization phenomena	Elemental intermixing	Preferential SiN _x layers modification
Femto, 250 kHz, 137 nJ	 1 x 6 μm ²	 Si	 < 50 nm	 Yes (voids)	 Extending out of the focal spot position	 Limited to the edges of the modified zone
Femto, 3 MHz, 16 nJ	1.5 x 5 μm ²	Si	< 50 nm	Not observed	Limited to focal spot position	Strong
CO laser	Several 100s μm along layers	Si, α-Si ₃ N ₄ , β-Si ₃ N ₄	Si: ≤ layer thickness Si ₃ N ₄ : several 100s μm along layers	Not observed	Not observed	Strong

Figure 6.12: Summary of the main laser-induced modification features in multilayers, as observed by TEM, for the three considered exposure cases: femtosecond laser exposure at 250 kHz and 3 MHz, and CO laser exposure.

hundreds kelvins. The effects of thermal expansion at high temperatures and plasma creation at the focal spot also reduce the accuracy of these values. Nevertheless, they offer a starting point for the evaluation of different materials characteristics, and for initial correlation between materials properties and their response to laser irradiation.

Physical quantity	SiO ₂	Ref.	Si ₃ N ₄	Ref.
Band gap E_g	9.1 eV	[174]	4.5-6.5 eV	[175]
Refractive index (at $\lambda=1030$ nm) n	1.45	[176]	1.97 (β)-2.08 (α)	[177]
Absorption coefficient (at $\lambda=5$ μm) α	$1.91 \cdot 10^3 m^{-1}$	[166]	$11.18 \cdot 10^3 m^{-1}$	[166]
Permittivity ϵ	4.4	[178]	8.16	[179]
Density ρ	$2.20 g cm^{-3}$	[180]	$3.17 g cm^{-3}$	[180]
Young's modulus E	70 GPa	[181]	307 GPa	[181]
Melting temperature T_m	1713°C	[180]	1900°C	[180]
Glass transition temperature T_g	~1200°C	[182, 183]	950-1100°C	[184, 185]
Thermal expansion coeff. α_{th}	$0.65 \cdot 10^{-6} K^{-1}$	[181]	$2.30 \cdot 10^{-6} K^{-1}$	[181]
Heat capacity C_p	$0.76 J g^{-1}K^{-1}$	[89]	$0.7-0.8 J g^{-1}K^{-1}$	[186, 187]
Thermal conductivity k	$1.4 W m^{-1}K^{-1}$	[89]	$30 W m^{-1}K^{-1}$	[188]
Thermal diffusivity D_T	$0.725 \cdot 10^{-6} m^2 s^{-1}$	[189]	$8.605 \cdot 10^{-6} m^2 s^{-1}$	[190]

Table 6.2: Structural, mechanical and thermal properties of SiO₂ and Si₃N₄.

Increasing the repetition rate of a femtosecond laser to 3 MHz, effectively promoting the occurrence of a thermal regime, results in different modification pathways with respect to the non-thermal, "low" repetition rate scenario. If for non-thermally cumulative regimes the laser-affected zone appeared more homogeneous, with a greater degree of layer intermixing, the occurrence of a sort of voids' self-organization phenomenon and the presence of Si crystallites spread over the entire area [130], at higher repetition rates the absence of complete thermal relaxation between subsequent pulses results in a higher selectivity of the modification process, where the SiN_x layers are preferentially modified by the laser, and account for most of the

Chapter 6. Crystallization dynamics and dependence on thermal regime

crystallized regions. This can be explained by the higher absorption coefficient, thermal expansion coefficient, thermal conductivity and diffusivity of this material with respect to SiO_2 (see Table 6.2), as heat would tend to be distributed along these layers, which can therefore be modified further away from the focal spot. Moreover, the individual pulse energy is remarkably lower than usual values for low repetition rates, at 16 nJ. The accumulation of energy of subsequent pulses is likely to play a role here, as at 3 MHz and for 10 mm s^{-1} there are 300 pulses impacting every μm .

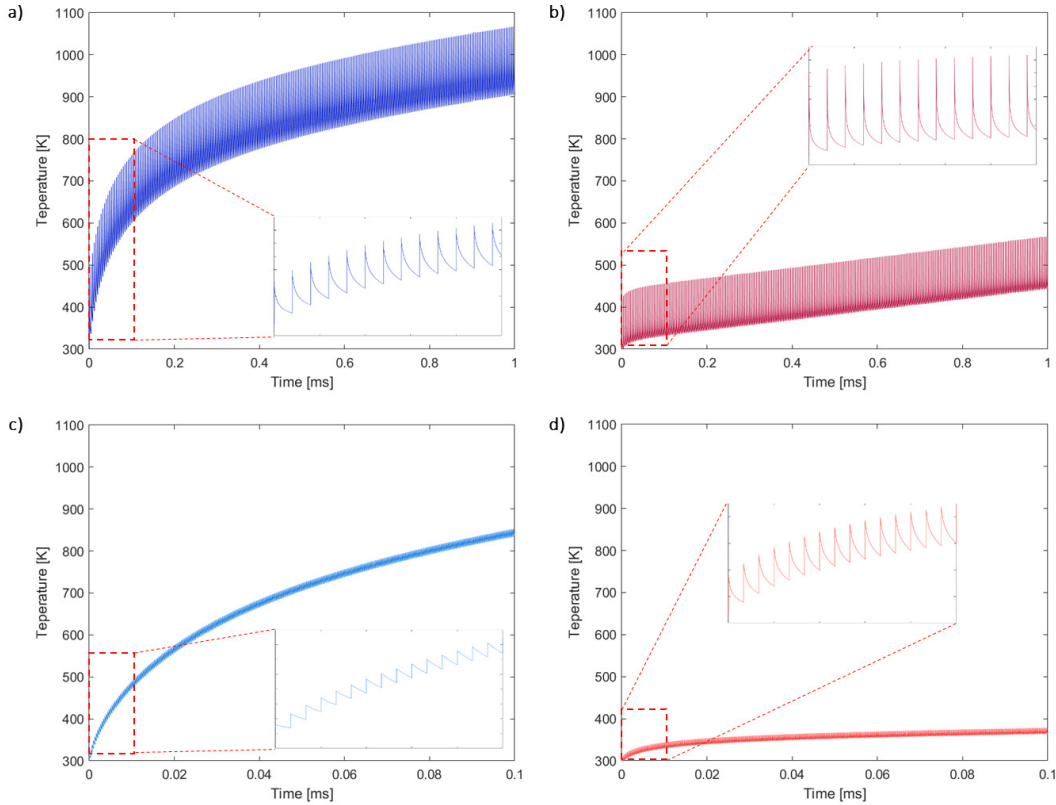


Figure 6.13: Simulated temperature increase in a bulk material during femtosecond laser exposure, calculated with the two temperature model. (a) Bulk SiO_2 at 250 kHz, 137 nJ and 1 mm s^{-1} , within 1 ms of exposure. (b) Bulk Si_3N_4 at 250 kHz, 137 nJ and 1 mm s^{-1} , within 1 ms of exposure. (c) Temperature increase in bulk SiO_2 at 3 MHz, 16 nJ and 10 mm s^{-1} , within 0.1 ms of exposure. (d) Bulk Si_3N_4 at 3 MHz, 16 nJ and 10 mm s^{-1} , within 0.1 ms of exposure.

To estimate the laser-induced local increase in temperature, the exposure process was simulated in Comsol with the two-temperatures model method, based on the work presented by Shimizu *et al* [191]. The simulated systems are composed by bulk SiO_2 and Si_3N_4 . While these basic systems cannot fully describe our complex multilayer system, simulating each material separately can give insights on the thermal behaviour of the constituting compounds of our layered material. The model simulates different exposure conditions: first, a repetition rate of 250 kHz, a pulse energy of 137 nJ and a scan speed of 1 mm s^{-1} , whose results are visible in Fig. 6.13a and b, for SiO_2 and Si_3N_4 , respectively. The second laser exposure condition is

a repetition rate of 3 MHz, a pulse energy of 16 nJ and a scan speed of 10 mm s^{-1} , whose results are visible in Fig. 6.13c (for SiO_2) and d (for Si_3N_4). These parameters correspond to the femtosecond laser exposure conditions presented in Section 6.3.1. The simulation time was adjusted to represent the time needed for the laser pulses to travel $1 \mu\text{m}$ of length, and is therefore set at 1 ms (for exposure at 250 kHz and 1 mm s^{-1}) and 0.1 ms (for exposure at 3 MHz and 10 mm s^{-1}).

The simulation results show the evolution of the specimen's temperature with time, during the absorption of the pulse train. Noticeably, the cases of high repetition rate show a temperature increase slightly lower than the cases of exposure at low repetition rate (for example, at around 850 K instead than 900 K, for bulk SiO_2). Despite this wide pulse energy gap, the difference in temperature over $1 \mu\text{m}$ is in the order of 10%, evidencing the effect of thermal accumulation in increasing the thermal energy of the system. It should be noted that while the considered distance is $1 \mu\text{m}$ in both cases, the actual exposure time is 10 times lower in the high repetition rate case. The comparison between the two materials systems proves that SiO_2 is more prone to thermal accumulation than Si_3N_4 , a behaviour that is expected, according to the thermal properties listed in Table 6.2. The faster dissipation of heat in the SiN_x layers can partially explain how the absorbed energy can be channelled through the nitride layers, and why this results in a preferential modification of this material.

Notice that the estimation of the maximal local temperature reached by the system, in the cumulative regime, is well below 1000°C . This is much lower than the crystallization temperature for both layers, yet crystallisation is observed in both cases. This confirms that multiphoton absorption (and the resulting ionization phenomenon) enable the occurrence of phase transitions in materials below their actual crystallisation temperature. It is not yet clear if the crystals nucleated in this condition may have a different structure and composition than crystals nucleated through classical thermally-driven processes.

In the CO laser exposure case, despite the absorption of CW radiation, and the thermal nature of the laser-matter interaction, there is no evidence of generalized liquid-induced diffusion of atoms between the two different materials, as there is little intermixing between the layers. This signifies that crystallization took place as a solid-state transition, with ordering (in the SiN_x layers) and crystal growth (in the SiO_2 layers) occurring without an intermediate melting step *over the whole multilayer volume*. However, given the lower melting temperature of SiO_2 (see Table 6.2), partial melting, or softening, of these layers could, in principle, have happened. In this case, the growth of the crystalline Si phase would evolve directly from the melt.

Previous studies on laser-induced crystallization, namely in the case of femtosecond laser exposure, have been conducted on a variety of oxides [192–197], suggesting the occurrence of crystallization due to a variety of thermal effects. Here, as discussed in previous sections, the position of the lamella cut is comprised between 35 and $55 \mu\text{m}$ from the central position of the focal spot. This means that, besides the laser absorption happening *in situ*, the crystallization dynamics is influenced by the heat transfer from the focal spot towards the surrounding

volume, after the irradiation, possibly following the thermal gradient.

The β phase is considered the most stable polymorph of Si_3N_4 , and is estimated to be so up to temperatures above 4000 K [198]. Conversely, the α phase (once considered a stable, low-temperature polymorph) is metastable with respect to the β phase, and is generally formed for kinetic reasons, but is later depleted due to the occurrence of a $\alpha \rightarrow \beta$ transition [2, 199], at temperatures around 1700°C [200]. De facto, no $\beta \rightarrow \alpha$ transition has been reported under normal stoichiometric conditions. The occurrence of the amorphous $\rightarrow \alpha$ phase transition has been reported for temperatures comprised between 1150 and 1370°C, depending on the properties of the starting amorphous material [201], and this reaction is known to possess a lower activation energy than other glass systems based on SiO_2 , at 300 kJ mol⁻¹ [200, 202]. This transition from the metastable α - Si_3N_4 to the stable β - Si_3N_4 is not evident from our results, since we can only analyse the final result of the phase transition process, and since the ratio between the nitride phases appears to be relatively homogeneous. That being said, the α phase is more scattered than the β phase, possibly due to the transformation process breaking up the continuity between α - Si_3N_4 crystallites. It should also be remembered that the three locations analysed with the Astar technique (see Fig. 6.9a) are in close proximity and located on a small lamella, several micrometers away from the focal spot position. It is likely that in the volume between the lamella location and the laser-induced crater (visible in Fig. 6.7a) the α/β ratio fluctuates, representing different stages of the $\alpha \rightarrow \beta$ transition. In the absence of experimental evidence, however, this hypothesis remains speculative.

Equally of importance is the presence of oxygen at the grain boundaries within the SiN_x layers, as evidenced by EDS imaging, indicating a lower activation energy for diffusion with respect to the $\text{SiO}_2/\text{SiN}_x$ interface. It is also well known that grain boundaries enable a faster diffusion of atomic species, due to their larger lattice distortion and defect density [203–205], effectively acting as diffusion highways across the layers. Conversely, silicon atoms from the Si-rich SiN_x layers can diffuse towards the SiO_2 layers, as the formation of crystalline Si_3N_4 phases results in the ejection of excess silicon. By moving along the grain and layer boundaries, these atoms are then available for crystal growth within the SiO_2 layers (perhaps promoting the nucleation of crystalline seeds), or for recombination with the oxygen that diffuses towards the nitride layers.

Although difficult to analyse dynamically through *post mortem* analysis of the laser-exposed areas, the preferential orientation of the Si_3N_4 crystals is remarkably visible from the pole figures, and can be correlated with the presence of a thermal gradient. As indicated in Fig. 6.7a and b, this gradient propagates radially from the laser-induced crater, and is oriented along the length of the lamella, or along direction x , according to the specimen reference frame indicated in Fig. 6.9d. As shown in Table 6.2, silicon nitride has higher values of thermal conductivity and diffusivity, hence is more affected by the magnitude and orientation of the thermal gradient than the SiO_2 layers. It should also be noted that each SiN_x layer is mechanically constrained by the SiO_2 layers surrounding them, and by the rest of the stack. This, coupled with the directionality of the temperature profile, can explain the higher degree

of homogeneous crystalline orientations within the nitride phases.

On the other hand, the more diverse orientation distribution of the Si phase can be explained by the formation mechanism of these crystallites. If nucleation is promoted at the layers boundaries, and on defect sites, the orientation of the initial crystal seeds is, in principle, arbitrary. The growth process, especially if occurring in a matrix that is still at least semi-solid, also hinders the re-orientation of the planes on the short term. As such, Si crystals coalescence results in the formation of polycrystalline globular clusters.

There is a noticeable difference between the outputs of femtosecond and CO laser processing. As was reported in previous cases [130], femtosecond laser exposure, regardless of the occurrence, or not, of thermal coupling effects, shows evidence of energy transfer, in a sort of plasmonic coupling along the layers interfaces. This is more noticeable in the case of processing at low repetition rate, suggesting that the introduction of a thermal regime hinders this mechanism. Moreover, it should be noticed that femtosecond laser exposure involves the occurrence of material ionization and the generation of shock-waves, subjecting the modified material to physical processes that are not commonly seen in studies on phase transitions. The promotion of ionization and the presence of pressure gradients favor the intermixing of elements and the creation of the Si phase, while the prevalence of thermal effects, occurring during CW laser exposure, does not involve atomic intermixing and results in more homogeneous formation of Si_3N_4 polymorphs. Overall, the influence of thermal effects on the modifications is important for both non-linear and linear absorption cases. However, the larger importance of heat transfer during CW irradiation leads to broader and more pervasive modifications across the multilayer stack, with respect to the femtosecond case. The exposure time also plays a role, as in the case of CO laser exposure, each spot was irradiated for 10 s, enabling all sorts of materials processes to happen during the energy transfer. Conversely, in the case of femtosecond laser exposure the high scanning speed (10 mm s^{-1}), and the intrinsic short-time duration of the pulses, are too fast to promote enough heating of the SiN_x to induce a generalized crystallization of the layers.

6.5 Summary

In this study, we could show how the crystallization dynamics for a same materials system differs widely, depending on the exposure parameters, most notably on the thermal regime of laser irradiation, which affects the ability of the sample to dissipate heat during the process. Three different exposure modalities were explored, low and high repetition rate femtosecond processing, which results in local ionization, and continuous-wave CO laser processing, resulting in a purely thermal energy transfer.

In the case of femtosecond pulses exposure, there is a difference between non-thermal regimes, as reported in [130], and the thermal regime occurring at high pulse repetition rates. Notably, the modification of the layers is more selective, targeting preferentially the SiN_x layers, in reason of the different thermo-mechanical properties of this material with respect to the

Chapter 6. Crystallization dynamics and dependence on thermal regime

silicon oxide. The occurrence of periodic voids, reported in the case of low repetition rate exposure, is not observed when increasing the pulse density. Moreover, the concentration of nitrogen drops dramatically within the laser-affected area, indicating the presence of an escape pathway enabling the removal of N atoms. However, there are also similarities, as in both cases the crystallization process results in the formation of crystalline Si clusters.

In the case of continuous-wave CO laser, layer modifications are much larger than the femtosecond case, spanning tens if not hundreds of μm , due to the confocal parameters (which result in a much larger beam) and the thermal nature of the interaction. The focal spot location undergoes partial melting and ablation of the layers, and cracks are observed propagating around the laser-affected area. Surface cross-sections analysis indicates the presence of crystallites in the whole multilayer structure. Remarkably, unlike the cases reported in previous chapters, crystallization is observed in both layers, but with different resulting polymorphs depending on each layer's composition: in the SiO_2 layers, a heterogeneous crystalline Si phase is nucleated within the amorphous, original material, which then grows into spherical crystallites, pushing the oxygen towards the surrounding volume. In the SiN_x layers, a transition from amorphous- SiN_x to a mix of $\alpha\text{-Si}_3\text{N}_4$ and $\beta\text{-Si}_3\text{N}_4$ is observed, with the two competing phases alternating along the layers length. The orientation of the crystals has been studied, and is much less homogeneous in the Si grains than in the Si_3N_4 crystals.

In summary, thermal regimes heavily affect the crystallization dynamics of laser-exposed multilayers, for both linear and non-linear absorption cases, resulting in the formation of various polymorphs during the process.

7 Case study: phase engineering in the $\text{Al}_2\text{O}_3/\text{Nb}_2\text{O}_5$ multilayer system

7.1 Introduction

As illustrated in previous chapters, femtosecond laser processing of dielectric multilayers can be used as a tool to obtain specific laser-induced phase transitions in this kind of materials systems. As a result, one can design the starting materials in such a way to obtain a variety of functional, localized regions within the multilayer matrix, for instance by creating electrically conductive or waveguiding paths, surrounded by a pristine material.

As a case study for this process, we investigated the $\text{Al}_2\text{O}_3/\text{Nb}_2\text{O}_5$ multi-material system (bandgaps of approximately 7 eV and 3.4 eV, respectively) and its behaviour under femtosecond laser exposure. An objective of this study was to investigate the potential of the method to specifically obtain the Nb_3Al phase (see Fig. 7.1a). This phase is technologically relevant, thanks to its superconducting behaviour below a critical temperature T_c of up to 18.8 K [206], and its good mechanical and irradiation resistance properties [207]. Uses of this material for specific applications in high-energy physics and nuclear engineering have been proposed, for instance as constitutive material of superconductive cables (Fig. 7.1b).

The properties of this phase are highly dependent on the thermal history of each sample. Specifically, the T_c depends on the phase transformation processes, both in the alloying and, if present, sintering/heat treatment steps [208]. Parameters such as the stoichiometric ratio, size of the crystallites, grain coalescence and mechanical strain [209] affect the maximal temperature at which superconductive behaviour is observed. In particular, during mechanical alloying it has been observed that superconductivity can disappear after quenching, but then suddenly reappears after an annealing step, thus indicating the importance of a fine and homogeneous microstructure for the manifestation of this physical phenomenon [207].

The effective T_c of Nb_3Al usually ranges from 14 to 18 K, depending on the fabrication methods, which can be classified into three distinct categories [212]: low-temperature and high-temperature processing, as well as rapid quenching and annealing (RHQT). Low-temperature

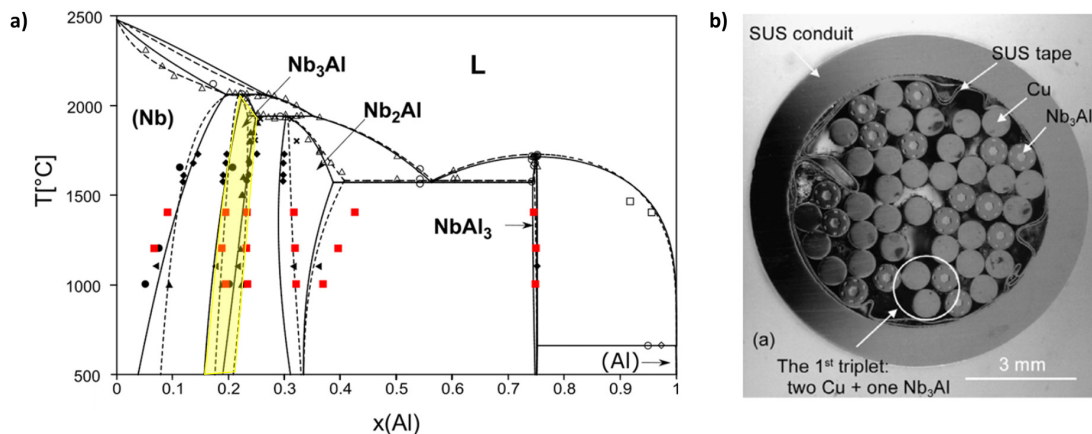


Figure 7.1: a) Phase diagram of the Nb/Al system [210]. The Nb_3Al superconducting phase is highlighted in yellow. b) Application example of the Nb_3Al phase, showing the cross-section of a conductor cable, as might be used in particle accelerators or nuclear power plants [211].

processing refers to more conventional methods, such as mechanical alloying, where powders of Nb and Al are milled with steel balls, and where the characteristics of the obtained Nb_3Al phase depend on the powder characteristics (size distribution, shape, surface to volume ratio) and the parameters of the milling process [213–215]. On the other hand, the standard RHQT method involves the extrusion of Al-Nb precursor powders, which then undergo rapid ohmic heating and rapid quenching, usually in a Ga bath [216]. After this, an annealing step can be done to stabilize the phase. Finally, high-temperature processing involves the use of laser, electron or ion beams to process materials at higher temperatures than conventional mechanical means, or even ovens. Notably, laser-based process have been proposed, albeit with continuous CO_2 lasers [217–219], with a Nb-Al tape or filament produced by powder metallurgy as starting material. Laser processing is followed by a thermal treatment to refine the microstructure, resulting in an improvement of the T_c . Heating and cooling rates are important parameters to control, and as a consequence the scan speed should be adapted. The advantage of laser-processing over mechanical alloying or RHQT is the scalability of the process, especially for the fabrication of wires, as the materials can be continuously fed under the laser beam.

Multilayer systems have also been investigated, by superposing sheets of Al and Nb, whose thicknesses correspond to the desired stoichiometry [220, 221]. It has been reported that the phase transition sequence depends on the layers thicknesses, hence by changing the layers design, it is possible to avoid, or promote, intermediate crystalline structures.

Contrarily to these previous works, our goal is to use oxides of these two elements as precursors, since their transparency to the laser's wavelength is a prerequisite for non-linear absorption of the femtosecond beam, and to explore the possibility of creating this specific phase with different precursors and heating techniques. As a result, a $\text{Al}_2\text{O}_3/\text{Nb}_2\text{O}_5$ multilayer sample was designed and fabricated, and a preliminary set of tests and characterization steps were

performed to study the modifications phenomena occurring in this materials system.

7.2 Sample design and fabrication

To promote specific phase transitions, the atomic content of Al and Nb within the multilayers should be calibrated to achieve a ratio as similar as possible to the final stoichiometric ratio. As suggested by its chemical formula, the Nb₃Al phase has a base composition of 1 Al atom for every 3 Nb atoms. From this ratio, knowing the tabulated values of the volumic density of amorphous, as-deposited, Al₂O₃ and Nb₂O₅, it is possible to estimate the layer thickness necessary to obtain this specific stoichiometry. The atomic density is defined as the number of stoichiometric compounds per volume unit, is expressed in [nm⁻³], and can be calculated as:

$$\rho_{at} = \frac{\rho_{vol}}{m_{at}} \quad (7.1)$$

Where ρ_{vol} is the volumic density and m_{at} the atomic mass of the chemical compound. Materials data were sourced from the *Materials Project* database [179]. The densities are $\rho_{vol,Al_2O_3} = 3.69 \cdot 10^{-21} \text{ g nm}^{-3}$ [222] and $\rho_{vol,Nb_2O_5} = 4.3 \cdot 10^{-21} \text{ g nm}^{-3}$ [223], while the atomic masses are, respectively, $m_{at,Al_2O_3} = 16.94 \cdot 10^{-23} \text{ g}$ and $m_{at,Nb_2O_5} = 44.1 \cdot 10^{-23} \text{ g}$. This results in the following atomic densities: $\rho_{at,Al_2O_3} = 43.5 \text{ nm}^{-3}$ and $\rho_{at,Nb_2O_5} = 19.5 \text{ nm}^{-3}$.

The multilayer stack has two mirror symmetries along the layers plane (perpendicularly to the beam propagation direction), so that volume changes between the layers can be expressed solely as function of layer thickness t . In addition, for each molecule the same ratio of Al and Nb is present. Consequently, the density ratio can be expressed in terms of layer thickness:

$$t_{Nb_2O_5} = 3 \frac{\rho_{at,Al_2O_3}}{\rho_{at,Nb_2O_5}} t_{Al_2O_3} \approx 6.67 t_{Al_2O_3} \quad (7.2)$$

Several layer structures with this ratio were simulated to design a multilayer stack which would not be overly reflective at the laser's wavelength (1030 nm). As a consequence, and taking into account technological factors linked to the deposition process, the layers' design consists of 12 bilayers of Al₂O₃, with a thickness of 51.4 nm each, and Nb₂O₅, with an individual layer thickness of 343.0 nm each. For the calculations, refractive indexes of $n_{Al_2O_3}=1.666$ [224] and $n_{Nb_2O_5}=2.256$ [225] were used. Notice that density and refractive index values are only indicative, as they correspond to tabulated values that do not reflect the real structure of the deposited layers. Nevertheless, they represent a good starting point for the estimation of the desired layer thicknesses. This specimen was labelled Sample_AINbO_A, and a visual representation of its structure, and its calculated and measured reflectance spectra, are shown in Fig. 3.3b. Due to technological constraints in the availability of materials, the deposition of the layers was outsourced to Schott Suisse AG, located in Yverdon-les-Bains.

7.3 Experimental results

The sample has been exposed to a femtosecond laser emitting pulses of 270 fs at 1030 nm, with a repetition rate of 500 kHz, a scanning speed of 1 mm s^{-1} , a pulse energy of 188 nJ and the beam polarization perpendicular to the scan direction. The laser beam was focused on the surface in top illumination condition. As it is possible to see in the SEM image of the cross-section of the laser-written line, in Fig. 7.2a, these exposure parameters resulted in the partial removal of the top layers and in a strong modification of the area surrounding the ablated region. Giving evidence of the high pressures generated by the ionization process, a crack propagated from the center of the laser-written line, where the beam intensity was higher, towards and inside the substrate, along the beam propagation direction. There is a clear transition from the ablation mark, where the original layered structure disappears in favour of an intermixed region consisting of several grains, to the un-exposed volume, which conserves the initial geometry and composition. At the frontier between the intermixed and the un-affected areas, it is also possible to notice a large concentration of nano-voids, represented as black spots under secondary electron contrast.

The left side of the cross-section (highlighted by a red line) is further magnified in Fig. 7.2b, where a BF-TEM image shows the microstructure of the laser-affected volume in more detail. Specifically, the area can be separated in three distinct sections: towards the ablation mark with the re-crystallization region (labelled as *region III*), where the constituting elements of the layers are intermixed and form well distinguished crystalline grains, as also confirmed by the SAED pattern in the inset image. As already seen in the SEM cross-section, far away from the laser-affected zone, the layers structure is preserved, so that the area can be defined as a non-affected region (*region I*). In between these two extremes, we find a transition region (labelled *region II*), where modifications, such as void creation and elemental mixing, can be observed, but the layers' structure is not as heavily affected as in proximity of the ablation mark.

The presence of crystalline grains of different orientation and composition is further illustrated by the DF-TEM image in Fig. 7.2c, with crystallites sharing the same microstructure and orientation appearing in white, while the remaining material is shown with a darker contrast. As evidenced by the uniform presence of white spots, the distribution of crystallites with the same structure is relatively homogeneous around the affected volume. The area around the larger grain visible on the image, and highlighted in red, is magnified in Fig. 7.2d with a BF-TEM image, confirming the presence of a variety of crystalline grains separated by well defined grain boundaries.

As shown in the previous chapters, scanning-TEM techniques, and in particular EDS elemental mapping, are powerful tools to visually assess the distribution of the elements across the section of interest, and to investigate atomic intermixing phenomena within the laser-affected zone.

A HAADF image of the lamella is visible on the top left of Fig. 7.3, together with elemental

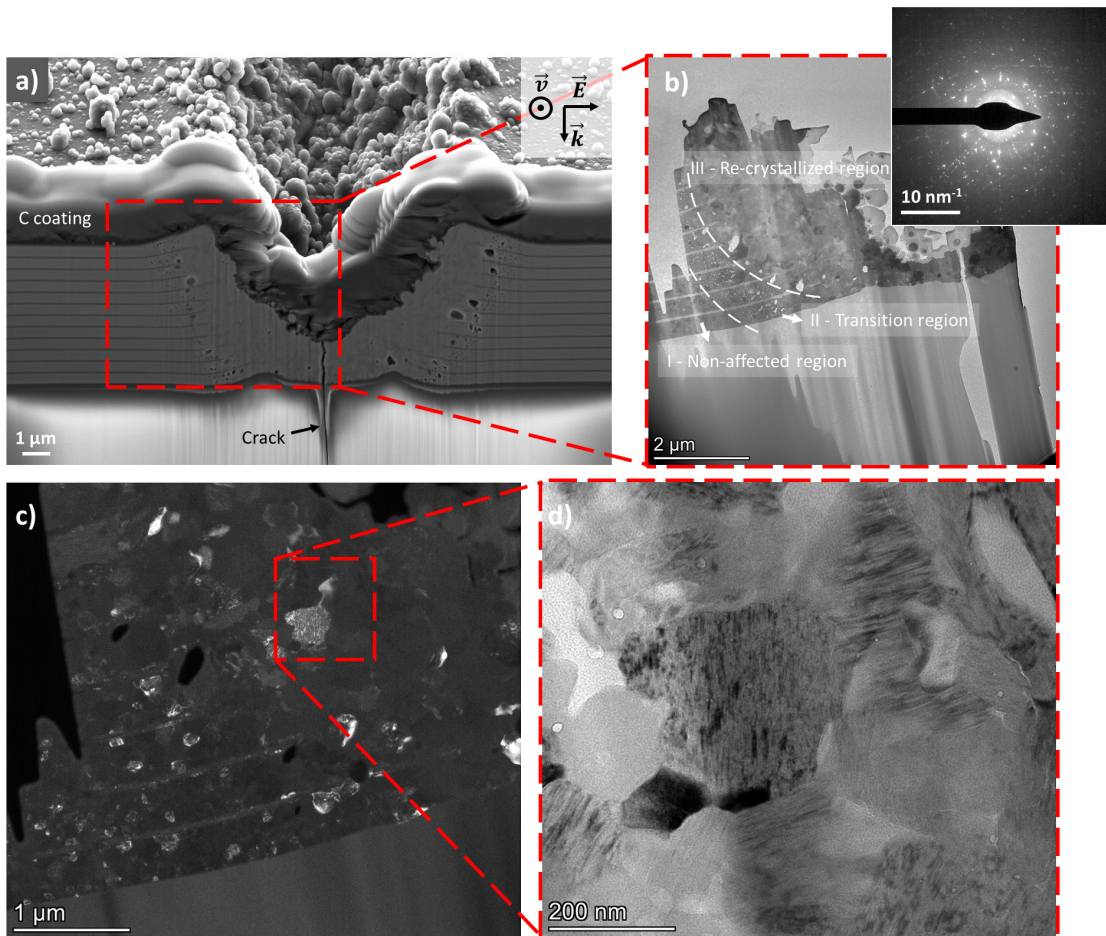


Figure 7.2: a) SEM cross-section of a laser-exposed region. The profile is relatively symmetric with respect to the center of the partially ablated line. A crack is visible, spreading along the propagation direction of the laser beam. The area highlighted in the red square was processed into a lamella and is shown in b) with a BF-TEM image, showing the transition from the non-affected area on the left, through a transition region and to the laser-affected area on the right, where the layers are fully intermixed and the crystalline grains are visible. The presence of crystallites is confirmed by the SAED pattern in inset. c) DF-TEM image of the laser-affected area, where white/light zones correspond to the same specific planar orientation. There, the crystallites are homogeneously spread around the modified volume. The area bordered with red is further magnified in the BF-TEM image in d), evidencing the presence of distinct grain boundaries.

maps of the same region for atoms of C, Si, Nb, Al and O. The residual presence of the carbon coating, deposited on the sample after laser exposure in order to render the surface conductive (for SEM/FIB manipulation), is restricted to the upper surface of the lamella, as expected. Similarly, silicon atoms are exclusively found inside the fused silica substrate, indicating the absence of ion migration from the substrate to the layered structure, during laser irradiation. The behavior of the constituting elements of the layers is more noteworthy: if both Nb and O diffuse relatively homogeneously across the whole laser-modified volume, albeit with local minima and maxima of concentration, Al atoms are segregated only in part of the crystallites, as evidenced by the jagged profile of the orange color. This means that the re-crystallized area

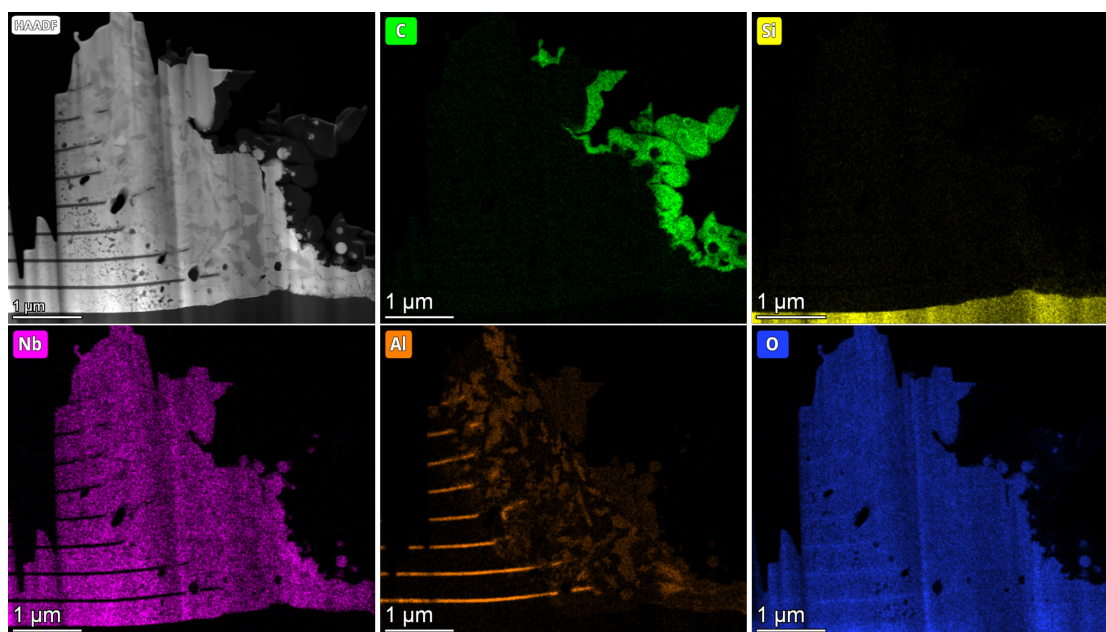


Figure 7.3: HAADF image (top left) and EDS elemental maps of the laser-affected area, in net counts. Shown are the constituting elements of the multilayer sample (Al, Nb, O), as well as Si (constitutive element of the fused silica substrate) and C (constituting the conductive coating on top of the layers, deposited just before the SEM observation).

is separated into two categories of grains, one composed by a Al-Nb-O compound, which in the HAADF image appear darker, and the other one composed exclusively by Nb and O, which in the HAADF image have a lighter hue. As the Z number of Nb (41) is much larger than the one of Al (13), this color difference is expected, as Nb ions will result in larger scattering probability and, therefore, increased signal. While the color homogeneity suggests the presence of two different compounds only, EDS analysis is not accurate enough to exclude the presence of multiple phases with the same constituting elements, but different stoichiometry, or perhaps crystal structure (i.e. polymorphs of the same compound).

Figure 7.4a shows the superposed distributions of Al, Nb and O atoms, so that the difference between the laser-affected area and the pristine region is more evident. To better quantify the elemental redistribution process, two measures of atomic fraction were done, the first one along scan direction (1), going from the layer-substrate interface to the top surface, and the second one, scan direction (2), going from the pristine layers, through the transition region defined in Fig. 7.2b and ending within the re-crystallized region. For both scans, the atomic fractions are shown on the right side of Fig. 7.4a. Along profile (1), the location of the un-modified layers is clearly indicated by the sharp increase/decrease of Al/Nb content, respectively. Moreover, large oscillations in the Al content along both scan lines confirm that the crystalline grains are constituted by at least two different compounds. Area (3) is magnified in Fig. 7.4b, where the existence of separated phases is highlighted both in the HAADF image (due to the contrast difference), and the EDS maps for Al and Nb atoms distribution.

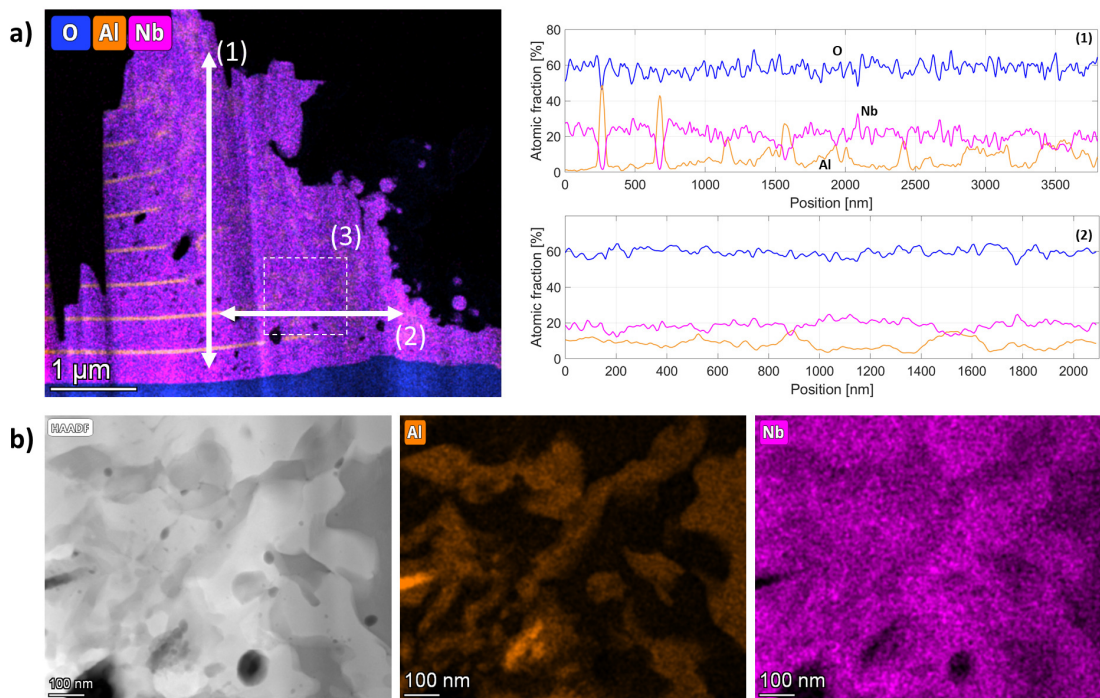


Figure 7.4: a) Combination of EDS elemental maps for O, Al and Nb, showing the elemental distribution within the laser-affected area. The atomic fraction of these three elements along two scan directions, (1) and (2), are shown on the right. Image b) shows a magnification of region (3), highlighted by white dotted borders, as visible in image a). Here, only the HAADF image and the EDS maps of the two main constituting elements of the multilayer sample (Al, Nb) are shown.

The specimens were also characterized with X-ray absorption spectroscopy (XAS) at the μ -XAS beamline at Paul Scherrer Institute, initially with post-mortem studies, then with dynamic studies. The goal of these last experiment was to perform *in situ* observations of the formation of crystalline phases during the laser exposure process, by synchronizing our laser source with the X-ray beam. This analysis was done in transmission mode, through a thin lamella, and in reflection mode, without constraints on the sample thickness.

The surface state of a $\text{Al}_2\text{O}_3/\text{Nb}_2\text{O}_5$ sample analysed in reflection mode is visible in Fig. 7.5a. Several laser-written lines were inscribed on the surface of the specimen, in a 10×10 matrix with increasing pulse energy and focal spot distance from the layers. The repetition rate was set at 100 kHz and the scan speed at 1 mm s^{-1} . The pulse energies of the investigated region were 120 nJ (part above, showing ablated marks) and 100 nJ (part below, showing sub-surface modifications). The spectra were plotted with respect to the 2θ angle between incident and reflected rays, and showed several distinct peaks. Figures 7.5b-d show 2D maps correlating the intensity of individual peaks with the spatial coordinates on the surface. Crystalline signal is observed in both ablated and sub-surface modifications locations, although with different intensities. Specifically, Fig. 7.5c shows no signal coming from the sub-surface modifications area, suggesting the presence of multiple phases, which are not equally distributed between the ablated and non-ablated modifications.

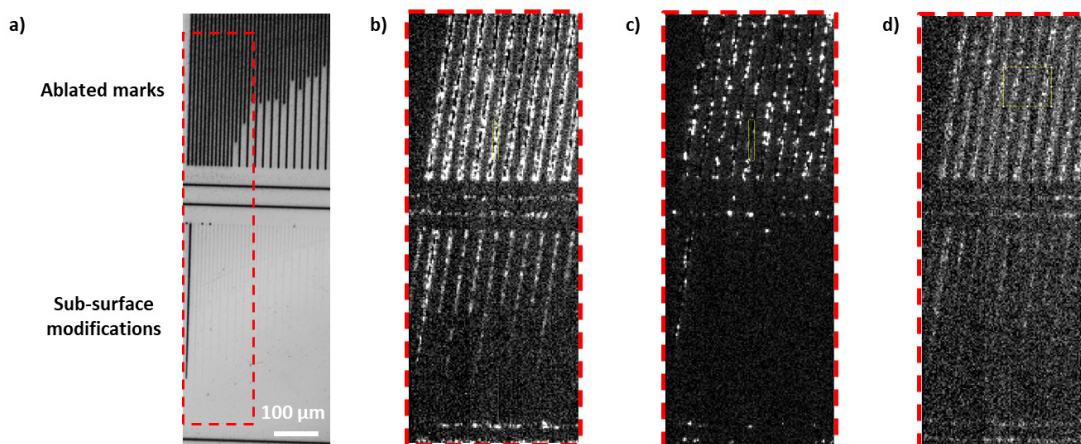


Figure 7.5: X-ray absorption spectroscopy measurements results, in reflection mode. a) Optical micrograph of the sample's surface, showing the upper region with several ablated lines, and the lower region with sub-surface modifications. Images b) - d) show the signal intensity of specific peaks along the 2θ scan, for the region highlighted in red in image a). Every image shows the intensity corresponding to a different peak.

These results confirm the presence of sub-surface crystalline modifications, demonstrating that the crystallization phenomenon can occur without surface ablation. This is a strong case for potential applications, for which ablation-less processing is preferred. Current peak assignment procedures suggest the presence of multiple phases, one of which is potentially a Nb_2O_5 -like phase, possibly with inclusions of a third element, like Al, or a high-pressure polymorph. However, the matching should be investigated further, especially in the case of the ternary Al-Nb-O phase. The analysis is therefore not conclusive on this aspect. Notice that the data pertaining to the XAS observations have not been fully analysed yet, and will be thoroughly presented in separate peer-reviewed publications.

Despite multiple attempts to assign a phase to the different crystalline grains, SAED, EDS, XAS and Astar analysis were not conclusive on the nature of these concurring phases. What can be argued with certainty, based on the chemical mapping of the constituting elements, is that one of the two phase groups belongs to the Nb-O materials system, while the other one consists of at least a Al-Nb-O compound. Candidate phases are AlNbO_4 , for the ternary compound, and NbO_2 , NbO , Nb_2O_5 (which, so far, is the only phase being partially matched with the obtained spectra), and their corresponding polymorphs, for the binary compound. The list is based on the available compounds on the Crystallography Open Database [226], and is not necessarily exhaustive. According to the Al_2O_3 - Nb_2O_5 and the Nb-O phase diagrams [227, 228], other potential phases can be suggested, but their stoichiometry is unlikely to be observed for our multilayer system, as it is far from elemental equilibrium. As a reminder, for every Al_2O_3 molecule, there are three Nb_2O_5 molecules, resulting in a total stoichiometry of $\text{Al}_2\text{Nb}_6\text{O}_{18}$. Using a simplistic calculation, which is not necessarily representative of the real situation, a combination of AlNbO_4 and Nb_2O_5 would respect the stoichiometric proportions. However, further results processing is needed in order to identify the exact nature of these

oxides compounds.

7.4 Discussion

The observation of oxide phases in the laser-affected area, and the absence of indicators of the presence of the Nb₃Al phase, confirmed that the target crystalline polymorph could not be obtained. Evidently, the use of the experimental conditions described above is not enabling the formation of the superconducting phase within the precursor Al₂O₃/Nb₂O₅ multilayer structure. However, the resulting crystallites were still interesting subjects for investigation.

The homogeneity of the phase distribution is remarkable, as elements are, indeed, separated in at least two different phases, but are spread around the laser-affected area without evidence of major element segregation. This is not only observed for the elemental distribution, but also concerns the crystal orientation. As visible in Fig. 7.2c, crystallites with the same planar orientation are well spaced, and no clustering trend is visible. Surprisingly, this suggests that neither the electric field, nor the thermal gradient had a particular influence on the orientation of the grains, or on the redistribution of the elements around the laser-affected zone. The mixing process is also noteworthy, as the total disruption of the layer geometry suggests that a localized plasma state expanded outwards from the beam waist, resulting in the intermixing of the atomic species, similarly to what has been observed in Fig.4.9.

As was suggested in previous cases (notably, for the SiO₂/TiO₂ sample), the phase transition process might occur through a series of intermediate compounds, rather than by a single amorphous-to-crystalline passage. These intermediate states could be formed and then modified depending on the local temperature and their own thermodynamic stability. This could result in the coexistence of several phases with the same elemental composition, but different elemental ratio. It might also be possible that these oxide compounds could act as intermediate phases towards the formation of Nb₃Al, in the case where the processing step would be improved and extended in time.

As was already evidenced in Chapters 4 to 6, femtosecond laser exposure did, under specific experimental conditions, result in the removal of gaseous species from the affected areas. However, all reported cases involved the SiO₂/SiN_x materials system, and the laser-induced modifications resulted in the depletion of nitrogen, not oxygen. Nevertheless, this suggests that removal of oxidizing species is, in principle, possible, with the potential of resulting in purely metallic compounds. For instance, performing larger parametric scans than what has been done so far is a labour-intensive, but potentially rewarding, strategy, which would be easier to implement without the need for additional equipment. Based on the results of Chapter 6, the use of femtosecond lasers at high repetition rates, or of continuous lasers, can also be suggested. Multiple-steps processing is also a potential pathway for the crystallization of the Nb₃Al phase, and could involve an additional fabrication step after (or even before) laser processing, such as annealing or exposure to chemicals. Finally, laser processing at temperatures different than room temperature, or in atmospheres other than air (for example,

in vacuum, or in nitrogen atmosphere) could result in interesting crystallization dynamics. In this framework, the chemistry of the modifications could be controlled by changing the gases composition and pressure. For instance, the choice of the gas environment has been showed to influence the quality of the laser-induced modifications [229]. Moreover, alternating environments during two-steps laser exposure processes was demonstrated to be effective in removing the native oxide in the TiO_2 system [230]. Therefore, experimenting with these techniques on our $\text{Al}_2\text{O}_3/\text{Nb}_2\text{O}_5$ multilayer system could be effective in removing the oxygen species and improve the selectivity of phase formation process.

7.5 Summary

This chapter explored the use of femtosecond laser processing of dielectric multilayers to create specific laser-induced phase transitions, aiming to form localized, functional regions within the multilayer matrix. This case study investigated the feasibility of the technique to obtain the Nb_3Al phase, which exhibits superconducting behaviour below a critical temperature of up to 18.8 K, and is a promising material for high-energy physics and nuclear engineering applications. An $\text{Al}_2\text{O}_3/\text{Nb}_2\text{O}_5$ multilayer sample was designed and fabricated, and a preliminary set of tests and characterization steps were performed to study the modifications phenomena occurring in this materials system.

Experimental observations concluded that crystallization phenomena effectively occurred following laser irradiation. More precisely, TEM imaging showed that under the studied exposure conditions, the laser-affected area consists of a region where elemental intermixing and re-crystallization can be observed. At the interface between this region and the pristine layers, a transition region showing partial intermixing and the formation of nanovoids was observed. Further chemical analysis of the laser-affected area evidenced the presence of distinct oxide phases, homogeneously dispersed within the modified region.

Despite the occurrence of laser-induced crystallization, the desired, Nb_3Al phase could not be found anywhere within the processed volume, consisting of oxide phases only. Nevertheless, there is some leeway in the process, as larger parametric scans have the potential to unravel crystallization paths so-far unexplored. Furthermore, combining femtosecond laser exposure with further processing steps, such as annealing (in an oven, for instance, or laser-mediated) could potentially improve the selectivity of phase formation.

Conclusions **Part III**

8 Conclusions and outlooks

This thesis work focused on the investigation of laser-matter interaction, during femtosecond laser exposure of dielectric multilayers. The interest for laser-processing this specific class of materials resides in the versatility of both elements. While femtosecond laser processing enables localized and precise delivery of energy anywhere in the volume of a transparent material, multilayer structures are advantageous as they consist of precursors of well defined volume, stoichiometry and optical properties. In addition, sample design is flexible and can be adapted to both experimental conditions and desired processing outcomes.

These structures are more sensitive to the laser power than bulk materials. This means operating in a relatively narrow parameter range at the edge of the non-linear absorption threshold. The dimensions, location and orientation of the modifications makes them challenging to characterize, requiring advanced electron microscopy tools for investigation. As demonstrated here, the development of alternative characterization methods, non-destructive and faster than electron microscopy, like THG microscopy, can represent a determining improvement for the study of this materials class.

We designed and deposited several samples, according to our experimental needs, composed by alternating layers of SiO_2 , Si_3N_4 , TiO_2 , Al_2O_3 and Nb_2O_5 , in different combinations. The design steps involved the calculation of the layers reflectance spectra using the transfer matrix method and the simulation of the pulse's propagation inside the layered structures with the FDTD method. The specimens were exposed in different configurations and according to parametric scans, and the resulting laser-induced modifications were investigated using various spectroscopy and microscopy techniques. Laser-induced crystallization was widely and consistently observed, in all the materials systems, and for all the investigated layer designs.

8.1 Main results

At the start of this manuscript, we enunciated three main research questions, which constitute the common thread of this thesis work: the summarized answers to each topic are developed in the following lines.

A) Describe the different kinds of modifications that can be obtained by exposing dielectric multilayers to femtosecond lasers.

Two exposure conditions were considered, top illumination, meaning direct exposure of the layers' surface, and bottom illumination, where the samples are exposed from the backside. The case of layer ablation, occurring for moderate-to-high laser fluences, was briefly presented. In both exposure conditions, the presence of crystallites, dispersed around the laser-affected zone, was demonstrated. A strong elemental intermixing phenomenon was observed, especially in the case of bottom illumination exposure, possibly as a result of a field enhancement effect at the interface between layers and fused silica substrate. Interestingly, in both cases the modified region was much larger than the beam waist, hinting to the occurrence of energy transfer along the layers planes and outside the exposure zone. These findings dealt mostly with the $\text{SiO}_2/\text{SiN}_x$ multilayer system, but they can be correlated for other systems as well, as these modifications were observed in all five samples considered in this work. In addition, under modification confinement conditions, the formation of nanopores was observed.

B) Investigate the modification dynamics by studying the influence of cumulative regimes on the modalities of phase transitions.

The effect of thermal regimes on the crystallization dynamics in multilayer systems was studied under two different laser exposure modalities: high repetition rate femtosecond processing and continuous wave CO laser processing. These two exposure modalities have been compared with the purely non-linear case of low repetition rate, femtosecond irradiation. In the high-frequency femtosecond case, the modification of the layers is more selective than the low repetition rate case, and results in the formation of crystalline Si clusters with a preferential modification of the SiN_x layers. In the CO laser case, layer modifications are larger and result in the formation of crystallites through heat diffusion across the whole layer stack, several microns away from the focal spot location. The laser-matter interaction process results in the formation of different polymorphs, depending on each layer's composition: pure Si crystallites in the SiO_2 layers, and a mix of α - and β - Si_3N_4 in the SiN_x layers. While the Si crystals are relatively randomly oriented, the crystal orientation of the nitride phases is remarkably homogeneous. This study concluded that thermal regimes heavily affect the crystallization dynamics of laser-exposed multilayers, resulting in the formation of various polymorphs during the process. Evidence of laser-induced crystallization was reported even for non-cumulative regimes, and the role of ionization, hindering the recrystallization of nitride compounds, was highlighted.

C) Demonstrate the possibility of introducing confined modifications within the layers stack,

with nanometric dimensions, along the optical axis.

A method for achieving high spatial confinement of laser-induced modifications in multilayered materials exploiting the aperiodic arrangements of the layers was investigated, and the resulting structures were confirmed to be confined along the beam propagation direction, as tightly as in a single layer of the stack. This was done without the use of a tightly focused beam, and the modifications could be confined into one layer of the stack without affecting the material's surface. The method was demonstrated in two different materials systems and was confirmed and predicted using a FDTD propagation model. The presence of laser-induced nano-pores and transversal cracks was also observed. Imaging of the modifications with THG microscopy was demonstrated, opening to the possibility of characterization without the need for destructive techniques; nevertheless, there are still open questions about the correlation between the nature of the modifications and the intensity of the THG signal.

In addition to these three main points, the phenomena discussed above were investigated in the framework of a particular case study, which can be summarized as follows:

D) Study on the feasibility of phase engineering in the Al_2O_3/Nb_2O_5 system.

The goal was to illustrate a first attempt to achieve femtosecond laser-based phase engineering in a dielectric multilayer system, showing the complete process, from layers design through laser processing, to the characterization step. The research objective was to obtain the Nb_3Al phase, which becomes superconducting below 18.8 K, and whose properties are closely linked to its manufacturing process. To this end, an Al_2O_3/Nb_2O_5 multilayer sample was designed and deposited, and subsequently tested under a set of experimental parameters. TEM observations confirmed the presence of crystalline zones within the laser-affected area, showing phase separation into different oxide phases, one composed by Nb and O, and one composed by Al-Nb-O. As the presence of the target Nb_3Al phase could not be observed, further studies on this specific specimen are needed, to verify the possibility of obtaining the desired crystals, and ultimately be able to directly write superconducting patterns within an isolating matrix.

After illustrating the main findings of this work, we conclude that femtosecond laser processing of multilayer materials systems enables precise, localized and, under certain conditions, spatially confined, crystallization within amorphous films and can also promote elemental intermixing.

8.2 Future outlooks and potential applications

The most natural progression, from the work presented here, would be to investigate deeper into the crystallization dynamics, possibly with the help of thermodynamic considerations, and in the kinetic of the crystallization reactions. Exploring the thermodynamic parameters involved in the crystallization process could give insights on the likelihood of occurrence of phase transitions, on the competition between simultaneously occurring phases, and in

general on the potential outcomes of laser processing. The lack of dynamic studies can be addressed by adjusting the exposure parameters to capture different stages of the crystallization process. This is notably the case for low cycle processing, with bursts of a few pulses, which appear to result in the formation of nano-cavities rather than crystallites. As this may offer interesting insights on the early onset of crystallization, a thorough parametric scan with pulse trains with increasing number of pulses, completed with THG, SEM and/or TEM characterization, would certainly be beneficial to better understand the crystallization dynamics inside the multilayers. Last, the role of the oxidizing elements should be investigated further, focusing specifically on compounds other than oxides. For instance, given the observed tendency of nitrogen to decrease in concentration inside the laser-modified zones, it would be interesting to study the exposure of multilayer systems exclusively based on nitrides such as $\text{Si}_3\text{N}_4/\text{TiN}$, which could result in the formation of intermetallics.

In this context, a clear limitation of this work is that results are exclusively issued by "post-mortem" analysis of the laser-modified samples, where the characterization is done *after* the material has been modified. As such, extrapolating information on the (potential) various steps of the modification process is complicated and, too often, relatively speculative. An example of such hurdle is the determination of reliable description of the crystallization paths, which might consist of a single amorphous-to-crystalline process, or might happen through a succession of intermediate metastable phases. To solve this issue, it would be interesting to proceed to in-situ observations, for example at a synchrotron or at an X-FEL facility, in order to improve time resolution and to image the non-linear absorption process as it happens, and its consequent effects on the phase transformation path.

Furthermore, as evidenced in Chapter 5, THG microscopy is a fast and efficient tool to image sub-surface laser-induced modifications. There is an interest in developing this technique further, improving the scan speed, the resolution and the sensitivity of the method. Potentially, developing a correlation between signal intensity and the nature of the modification would enable much faster characterization of the samples with respect to electron microscopy, in a matter of minutes rather than days, in a non-destructive way. In addition, this imaging technique could enable the development of femtosecond laser processing of dielectric multilayers as a data storage medium, as will be explained further below.

Modelling can also be improved, as the FDTD simulations showed in previous chapters are only concerned with the passage of a single pulse, and do not take into consideration non-linear effects, or the cumulative effects of the pulse train. However, the modelling of non-linear absorption in dielectrics is not a trivial feat, as is the integration of the crystallization process into the model. A possible pathway for success could involve the simulation of several pulses, where in between each pulse the layers are locally modified at the locations of high intensity, and the materials parameters in these spots are updated to account for the densification of matter, or the creation of nanovoids. As an example of potential improvement, work performed by Zhang *et al.* [159] suggests a more complete set of modules to compute the propagation of the pulse and the materials modifications in the same simulation package.

8.2 Future outlooks and potential applications

Finally, phase engineering in the $\text{Al}_2\text{O}_3/\text{Nb}_2\text{O}_5$ system lead to interesting observations, but could not ultimately prove that fabrication of the Nb_3Al phase by femtosecond laser processing of these multilayers is achievable. To this end, further parameter exploration is necessary, potentially involving additional steps, like annealing or further continuous-laser processing, or the experimentation of laser exposure under vacuum or other gaseous environments, which might promote a different set of chemical reactions.

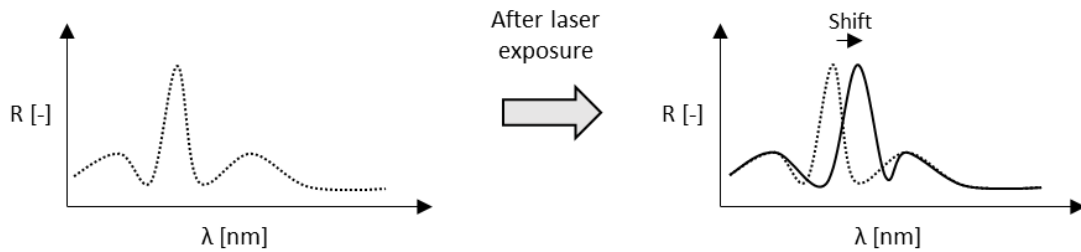


Figure 8.1: Schematics of a potential data storage technique based on femtosecond laser exposure of multilayer dielectric materials. By reading the local change in reflectance of the multilayer stack, it would be possible to encode spectral information into the material, and to retrieve it by measuring its spectrum.

Application-wise, the modification confinement showed in Chapter 5 is particularly interesting in the context of data storage. Due to the exponential rise of computation power and data production, the development of an efficient data storage solution represents an imperative for our civilization. As such, efforts intensified in recent years to find a storage means that would provide a permanent, safer and low-energy consumption alternative to the current state-of-the-art, with potentially a much higher density of information. An example of such device, based on the laser processing method explored in this manuscript, is shown in Fig. 8.1. Here, the promotion of laser-induced modifications inside dielectric multilayers would result in a local shift of optical properties (in the figure, reflectance has been chosen as an example), enabling the writing of datapoints within the layers. Assuming modifications confined to a single, 100 nm thick layer of the stack, and in-plane modification dimensions of $1 \mu\text{m}^2$, the potential data storage capability for such a device, with a surface area of $10 \times 10 \text{ cm}^2$, would be as high as 10 Gbit, or 1.25 GB, per layer. By designing the stack to promote modifications on multiple layers, and by increasing the writing dimensions by considering other parameters such as retardance or crystal orientation, this could result in the development of extremely dense and durable substrates for data storage. Taking inspiration from what has been presented in Section 5.5, methods based on THG signal detection could be explored as potential reading mechanisms, since we demonstrated that THG imaging is a fast and efficient way to probe modified structures under the layers' surface, with a higher degree of precision than optical microscopy.

Furthermore, improving the methodology and the reliability of phase engineering would be an asset for the fabrication of monolithic electro-optical devices, and for the integration of crystalline regions into otherwise amorphous devices, with potential applications in electronics, optics and the medical field. For example, this could enable the conception and the

fabrication of single-photon emitters, the conception of superconducting microcircuits or the development of nanocrystals for anti-microbial surfaces.

Finally, the presence of sub-surface modifications offer interesting perspectives for integration in the luxury industry, especially in the field of anti-counterfeiting. Such structures would be incredibly difficult for competitors to fabricate and, especially, to reverse engineer, resulting in a robust technique to provide proof of authenticity of luxury objects such as watches or jewellery items.

8.3 Personal contributions

This work was done in the framework of a FNS-Synergia collaboration between the laboratories Galatea, of Prof. Y. Bellouard, and LCAV, of Prof. M. Vetterli. The aim of the collaboration was to digitalize the Lippmann photography process. The femtosecond laser processing of dielectric multilayers was one of the explored research axis.

Furthermore, I would like to acknowledge the personal contributions of the following researchers: Dr. Nicolas Descharmes and Dr. Raphaël Barbey, for the deposition of Sample_Si3N4_A. Dr. Simone Frasca, who deposited Sample_TiO2_A, and Dr. Olivier Bernard, who designed, built and debugged the THG imaging setup, and who coded the instructions for the writing of the matrices of points. Samuel Benketaf, who designed, built and operated the laser platform for CO laser processing, and finally Dr. Victor Boureau, who operated the equipment during TEM observations shown in Fig. 4.5, Fig. 4.7, Fig. 4.8 and Fig. 4.9, and helped with the analysis of the corresponding data. Victor also performed the observations and processed the Astar results shown in Fig. 6.8 and Fig. 6.10.

A Samples thickness profiles

The following Table lists the individual layer thicknesses of specimens Sample_Si3N4_B and Sample_TiO2_A, whose structures can be visualized in Fig. 3.3b and Fig. 3.4a, respectively. The nominal refractive index values of each constituting material are also shown. Layer number 1 is the top layer, while layer number 20 is the layer at the interface with the fused silica substrate. In the case of the SiO₂/SiN_x sample, the measured thickness values are compared with the designed values, and the difference in thickness (due to inhomogeneities of the deposition process) is calculated and shown as well. Notice that the SiO₂/TiO₂ sample does not have a column pertaining to the design values, as its geometry is the result of a serendipitous deposition process, where the irregular thickness of the layers was caused by a defective valve at the level of the precursors reservoir. Values of the refractive indexes are taken from [86, 94, 99, 176].

Appendix A. Samples thickness profiles

Layer number	Sample_TiO2_A		Sample_Si3N4_B			
	Thickness [nm]	n [-]	Thickness (design) [nm]	Thickness (measure) [nm]	Deviation [%]	n[-]
1	130.8	1.45	120	116	3.3	1.45
2	133.9	2.48	90	89	1.1	2.01
3	96.6	1.45	110	103	6.4	1.45
4	124.6	2.48	82	81	1.2	2.01
5	59.2	1.45	100	99	1.0	1.45
6	90.3	2.48	74	71	4.1	2.01
7	74.8	1.45	90	92	2.2	1.45
8	74.8	2.48	66	65	1.5	2.01
9	43.6	1.45	80	73	8.8	1.45
10	84.1	2.48	58	57	1.7	2.01
11	56.1	1.45	160	153	4.4	1.45
12	105.9	2.48	58	57	1.7	2.01
13	59.2	1.45	80	74	7.5	1.45
14	93.4	2.48	66	68	3.0	2.01
15	62.3	1.45	90	83	7.8	1.45
16	90.3	2.48	74	73	1.4	2.01
17	90.3	1.45	100	94	6.0	1.45
18	81.0	2.48	82	84	2.4	2.01
19	96.6	1.45	110	106	3.6	1.45
20	77.9	2.48	90	89	1.1	2.01

Table A.1: Individual layer thicknesses of Sample_TiO2_A and Sample_Si3N4_B, and their respective refractive index values. In this notation, layer 1 is the uppermost layer, in contact with air, with increasing layer numbers being closer to the substrate interface.

B Raman spectroscopy

Spectroscopy techniques enable the characterization of materials, compounds and atomic species based on their response to external optical stimulations. To this end, Raman spectroscopy is a powerful and fast tool to assess the occurrence of phase transitions in laser-exposed materials. The scope of the following paragraphs is to familiarize the reader with the basics of Raman spectroscopy, and to illustrate the interest of this technique in the framework of materials characterization.

The occurrence of inelastic scattering of light in materials was first observed and reported by C. V. Raman in 1928 [231], leading to the development of the spectroscopy technique that bears his name. More specifically, he contributed to the description of Stokes and anti-Stokes scattering, a phenomenon where the energy of incident photons is absorbed and excites electrons, which can subsequently fall back emitting a radiation of energy slightly lower (Stokes, see Fig. B.1b) or higher (anti-Stokes, see Fig. B.1c) than their initial energy level. Contrarily to Rayleigh scattering (see Fig. B.1a), the energy balance is not null, so this interaction is inelastic. The molecule is therefore in a different vibrational state, and the nature of the chemical bond under study determines the magnitude of the Raman shift.

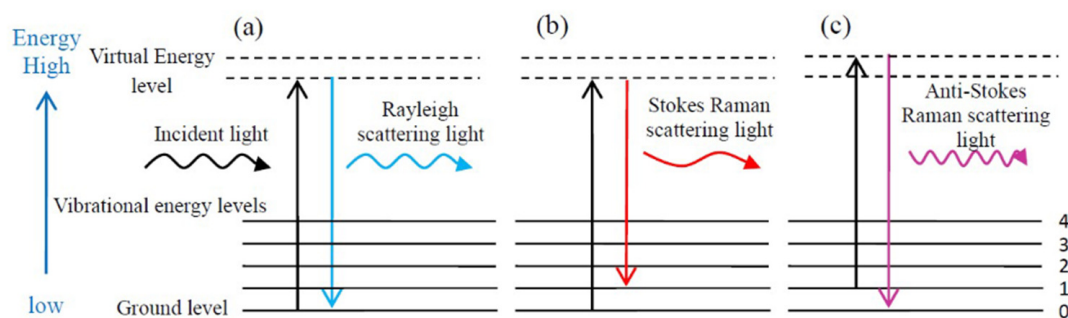


Figure B.1: a) Scheme of Rayleigh scattering, and comparison with both b) Stokes and c) anti-Stokes scattering, which are both Raman scatterings [232].

In summary, this technique relies on the vibrational energy of chemical bonds, which depends

Appendix B. Raman spectroscopy

on the chemical composition and crystallographic structure of the sample [232]. Thus, a variety of materials' parameters can be deduced, at least qualitatively, from the position and the shape of the Raman curves (Fig. B.2a). As a result, Raman spectroscopy is a powerful tool to study the composition of laser-affected zones, and to assess the capability of a determined set of exposure parameters to result in crystallization.

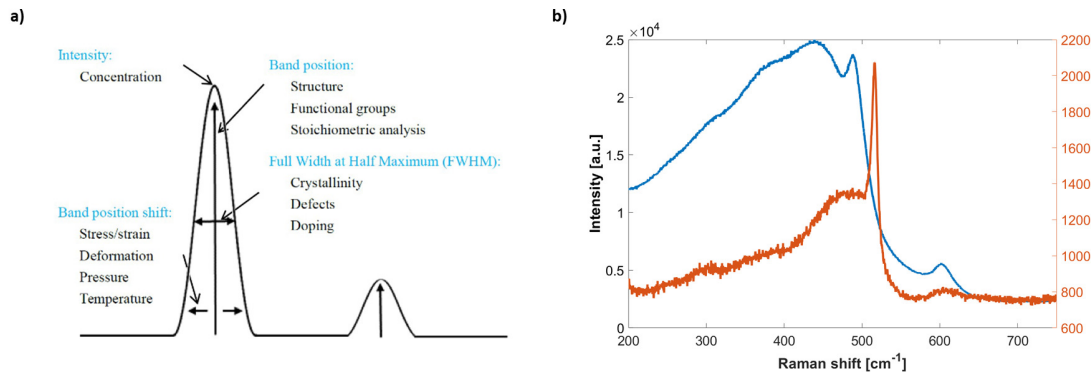


Figure B.2: a) Correlation between peak position, height, width and shape, and the properties of the material under study [232]. b) Example of Raman spectroscopy measures, showing the intensity of the Raman signal as a function of Raman shift (i.e. inverse of the wavelength). Two different curves are shown, in blue the curve of a pristine SiO₂/SiN_x multilayer sample, and in orange the curve corresponding to a laser-affected area on the same material, illustrating the usefulness of the technique in tracking the occurrence of phase transitions.

As shown in Fig. B.2a, the shape, positioning, intensity and shift of the Raman peaks give insightful information on a wide selection of materials' properties, such as the atomic composition, the crystallographic structure, the presence and concentration of different phases in a determined volume, as well as the stress-state of the investigated sample. The presence of specific phases, or the occurrence of a phase transition, can therefore be confirmed by performing Raman spectroscopy on a laser-modified zone and then by comparing the resulting spectrum to the pristine materials spectrum. An example of such methodology is shown in Fig. B.2b, where the spectrum of a pristine SiO₂/SiN_x multilayer (in blue) is compared with the spectrum of the same material after femtosecond laser exposure (in orange). Not only the spectra are different, indicating the occurrence of a laser-induced modification, but the sharp peak appearing in the orange curve also indicates the presence of a crystalline phase. Indeed, the atomic order inherent in a crystalline structure results in much more homogeneous vibrations of the bonds, hence creating a much sharper and localized signal peak.

Bibliography

- [1] B. Russell, *History of Western Philosophy*. London: Routledge, 2004.
- [2] A. Kuwabara, K. Matsunaga, and I. Tanaka, "Lattice dynamics and thermodynamical properties of silicon nitride polymorphs," *Physical Review B*, vol. 78, p. 064104, Aug. 2008.
- [3] A. Greshake, R. Wirth, J. Fritz, T. Jakubowski, and U. Böttger, "Mullite in Libyan Desert Glass: Evidence for high-temperature/low-pressure formation," *Meteoritics & Planetary Science*, vol. 53, pp. 467–481, Mar. 2018.
- [4] J. Bressiani, V. Izhevskiy, and A. H. A. Bressiani, "Development of the microstructure of the silicon nitride based ceramics," *Materials Research*, vol. 2, pp. 165–172, July 1999.
- [5] T. Ishikawa, "Understanding and controlling microstructural evolution in metal forming: An overview," in *Microstructure Evolution in Metal Forming Processes*, pp. 3–16, Elsevier, 2012.
- [6] B. Gidwani, V. Sahu, S. S. Shukla, R. Pandey, V. Joshi, V. K. Jain, and A. Vyas, "Quantum dots: Prospectives, toxicity, advances and applications," *Journal of Drug Delivery Science and Technology*, vol. 61, p. 102308, Feb. 2021.
- [7] Z. Li, ed., *Introduction to Concrete*, ch. 1, pp. 1–22. John Wiley & Sons, Ltd, 2011.
- [8] J. A. Manson, P.-E. Bourban, L. Carlsson, and J.-P. Mercier, *Matériaux composites à matrice organique*. Traité des Matériaux, Lausanne: EPFL Press, 2004.
- [9] S. Kinoshita, S. Yoshioka, and J. Miyazaki, "Physics of structural colors," *Reports on Progress in Physics*, vol. 71, p. 076401, July 2008.
- [10] G. S. Smith, "Structural color of morpho butterflies," *American Journal of Physics*, vol. 77, no. 11, pp. 1010–1019, 2009.
- [11] F. X. Kartner, N. Matuschek, T. Schibli, U. Keller, H. A. Haus, C. Heine, R. Morf, V. Scheuer, M. Tilsch, and T. Tschudi, "Design and fabrication of double-chirped mirrors," 1997.
- [12] N. R. Mavilla, C. S. Solanki, and J. Vasi, "Raman spectroscopy of silicon-nanocrystals fabricated by inductively coupled plasma chemical vapor deposition," *Physica E: Low-dimensional Systems and Nanostructures*, vol. 52, pp. 59–64, Aug. 2013.

Bibliography

- [13] K. Ding, U. Aeberhard, O. Astakhov, F. Köhler, W. Beyer, F. Finger, R. Carius, and U. Rau, "Silicon quantum dot formation in SiC/SiO_x hetero-superlattice," *Energy Procedia*, vol. 10, pp. 249–254, 2011.
- [14] S. G. Cherkova, V. A. Volodin, A. G. Cherkov, A. K. Antonenko, G. N. Kamaev, and V. A. Skuratov, "Light-emitting Si nanostructures formed by swift heavy ions in a-Si:H/SiO₂ multilayer heterostructures," *Mater. Res. Express*, vol. 4, p. 085001, Aug. 2017.
- [15] X. Xu, Y. Q. Cao, P. Lu, J. Xu, W. Li, and K. J. Chen, "Electroluminescence Devices Based on Si Quantum Dots/SiC Multilayers Embedded in PN Junction," *IEEE Photonics J.*, vol. 6, pp. 1–7, Feb. 2014.
- [16] T. Lehnert, S. Tixier, P. Böni, and R. Gotthardt, "A new fabrication process for Ni–Ti shape memory thin films," *Materials Science and Engineering: A*, vol. 273-275, pp. 713–716, Dec. 1999.
- [17] L. Sirleto, M. A. Ferrara, I. Rendina, S. N. Basu, J. Warga, R. Li, and L. D. Negro, "Enhanced stimulated Raman scattering in silicon nanocrystals embedded in silicon-rich nitride/silicon superlattice structures," *Appl. Phys. Lett.*, vol. 93, p. 4, 2008.
- [18] F. Gontad, J. Conde, S. Filonovich, M. Cerqueira, P. Alpuim, and S. Chiussi, "Study on excimer laser irradiation for controlled dehydrogenation and crystallization of boron doped hydrogenated amorphous/nanocrystalline silicon multilayers," *Thin Solid Films*, vol. 536, pp. 147–151, June 2013.
- [19] D. Lehninger, J. Beyer, and J. Heitmann, "A Review on Ge Nanocrystals Embedded in SiO₂ and High-k Dielectrics," *Phys. Status Solidi A*, vol. 215, p. 1701028, Apr. 2018.
- [20] B. Liu, J. Li, W. Yang, X. Zhang, X. Jiang, and Y. Bando, "Semiconductor Solid-Solution Nanostructures: Synthesis, Property Tailoring, and Applications," *Small*, vol. 13, p. 1701998, Dec. 2017.
- [21] F. Priolo, T. Gregorkiewicz, M. Galli, and T. F. Krauss, "Silicon nanostructures for photonics and photovoltaics," *Nature Nanotech*, vol. 9, pp. 19–32, Jan. 2014.
- [22] G. Conibeer, M. Green, E.-C. Cho, D. König, Y.-H. Cho, T. Fangsuwannarak, G. Scardera, E. Pink, Y. Huang, T. Puzzer, S. Huang, D. Song, C. Flynn, S. Park, X. Hao, and D. Mansfield, "Silicon quantum dot nanostructures for tandem photovoltaic cells," *Thin Solid Films*, vol. 516, pp. 6748–6756, Aug. 2008.
- [23] C. Bonafos, M. Carrada, G. Benassayag, S. Schamm-Chardon, J. Groenen, V. Paillard, B. Pecassou, A. Claverie, P. Dimitrakis, E. Kapetanakis, V. Ioannou-Sougleridis, P. Norman, B. Sahu, and A. Slaoui, "Si and Ge nanocrystals for future memory devices," *Materials Science in Semiconductor Processing*, vol. 15, pp. 615–626, Dec. 2012.
- [24] A. Senichev, Z. O. Martin, S. Peana, D. Sychev, X. Xu, A. S. Lagutchev, A. Boltasseva, and V. M. Shalaev, "Room-temperature single-photon emitters in silicon nitride," *Science Advances*, vol. 7, no. 50, p. eabj0627, 2021.

- [25] L. Mangolini, "Synthesis, properties, and applications of silicon nanocrystals," *Journal of Vacuum Science & Technology B, Nanotechnology and Microelectronics: Materials, Processing, Measurement, and Phenomena*, vol. 31, p. 020801, Mar. 2013.
- [26] J. Molina-Reyes, A. Romero-Moran, H. Uribe-Vargas, B. Lopez-Ruiz, J. Sanchez-Salas, E. Ortega, A. Ponce, A. Morales-Sanchez, F. Lopez-Huerta, and C. Zuñiga-Islas, "Study on the photocatalytic activity of titanium dioxide nanostructures: Nanoparticles, nanotubes and ultra-thin films," *Catalysis Today*, vol. 341, pp. 2–12, Feb. 2020.
- [27] R. Osellame, G. Cerullo, and R. Ramponi, eds., *Femtosecond Laser Micromachining: Photonic and Microfluidic Devices in Transparent Materials*. No. v. 123 in Topics in Applied Physics, Berlin ; New York: Springer, 2012.
- [28] C. B. Schaffer, A. Brodeur, and E. Mazur, "Laser-induced breakdown and damage in bulk transparent materials induced by tightly focused femtosecond laser pulses," *Measurement Science and Technology*, vol. 12, pp. 1784–1794, Nov. 2001.
- [29] S. Ruzin and H. Aaron. <https://microscopy.berkeley.edu/tlm/2P/index.html>. Accessed: 2023-04-25.
- [30] A. M. Zheltikov, "Keldysh parameter, photoionization adiabaticity, and the tunneling time," *Physical Review A*, vol. 94, p. 043412, Oct. 2016.
- [31] R. R. Gattass and E. Mazur, "Femtosecond laser micromachining in transparent materials," *Nature Photonics*, vol. 2, pp. 219–225, Apr. 2008.
- [32] A. Kaiser, B. Rethfeld, M. Vicanek, and G. Simon, "Microscopic processes in dielectrics under irradiation by subpicosecond laser pulses," *Physical Review B*, vol. 61, pp. 11437–11450, May 2000.
- [33] S. M. Eaton, G. Cerullo, and R. Osellame, "Fundamentals of Femtosecond Laser Modification of Bulk Dielectrics," in *Femtosecond Laser Micromachining* (R. Osellame, G. Cerullo, and R. Ramponi, eds.), vol. 123, pp. 3–18, Berlin, Heidelberg: Springer Berlin Heidelberg, 2012.
- [34] M. V. Shugaev, C. Wu, O. Armbruster, A. Naghilou, N. Brouwer, D. S. Ivanov, T. J.-Y. Derrien, N. M. Bulgakova, W. Kautek, B. Rethfeld, and L. V. Zhigilei, "Fundamentals of ultrafast laser–material interaction," *MRS Bulletin*, vol. 41, pp. 960–968, Dec. 2016.
- [35] K. Miura, J. Qiu, H. Inouye, T. Mitsuyu, and K. Hirao, "Photowritten optical waveguides in various glasses with ultrashort pulse laser," *Applied Physics Letters*, vol. 71, pp. 3329–3331, Dec. 1997.
- [36] V. R. Bhardwaj, E. Simova, P. P. Rajeev, C. Hnatovsky, R. S. Taylor, D. M. Rayner, and P. B. Corkum, "Optically Produced Arrays of Planar Nanostructures inside Fused Silica," *Physical Review Letters*, vol. 96, p. 057404, Feb. 2006.

Bibliography

- [37] Y. Bellouard, A. Said, M. Dugan, and P. Bado, "Fabrication of high-aspect ratio, microfluidic channels and tunnels using femtosecond laser pulses and chemical etching," *Optics Express*, vol. 12, no. 10, p. 2120, 2004.
- [38] M. Zanaty, T. Fussinger, A. Rogg, A. Lovera, D. Lambelet, I. Vardi, T. J. Wolfensberger, C. Baur, and S. Henein, "Programmable Multistable Mechanisms for Safe Surgical Puncturing," *Journal of Medical Devices*, vol. 13, p. 021002, June 2019.
- [39] L. Borasi, E. Casamenti, R. Charvet, C. Dénéreaz, S. Pollonghini, L. Deillon, T. Yang, F. Ebrahim, A. Mortensen, and Y. Bellouard, "3D metal freeform micromanufacturing," *Journal of Manufacturing Processes*, vol. 68, pp. 867–876, Aug. 2021.
- [40] Y. Lei, M. Sakakura, L. Wang, Y. Yu, H. Wang, G. Shayeganrad, and P. G. Kazansky, "High speed ultrafast laser anisotropic nanostructuring by energy deposition control via near-field enhancement," *Optica*, vol. 8, p. 1365, Nov. 2021.
- [41] E. Casamenti, T. Yang, P. Vlugter, and Y. Bellouard, "Vibration monitoring based on optical sensing of mechanical nonlinearities in glass suspended waveguides," *Optics Express*, vol. 29, p. 10853, Mar. 2021.
- [42] Y. Shimotsuma, P. G. Kazansky, J. Qiu, and K. Hirao, "Self-Organized Nanogratings in Glass Irradiated by Ultrashort Light Pulses," *Physical Review Letters*, vol. 91, p. 247405, Dec. 2003.
- [43] G. Torun, A. Yadav, K. A. Richardson, and Y. Bellouard, "Ultrafast Laser Direct-Writing of Self-Organized Microstructures in Ge-Sb-S Chalcogenide Glass," *Frontiers in Physics*, vol. 10, p. 883319, Apr. 2022.
- [44] Y. Bellouard, A. A. Said, and P. Bado, "Integrating optics and micro-mechanics in a single substrate: A step toward monolithic integration in fused silica," *Optics Express*, vol. 13, p. 6635, Aug. 2005.
- [45] B. Lenssen and Y. Bellouard, "Optically transparent glass micro-actuator fabricated by femtosecond laser exposure and chemical etching," *Applied Physics Letters*, vol. 101, p. 103503, Sept. 2012.
- [46] Nazir and Bellouard, "A Monolithic Gimbal Micro-Mirror Fabricated and Remotely Tuned with a Femtosecond Laser," *Micromachines*, vol. 10, p. 611, Sept. 2019.
- [47] A. Schaap, T. Rohrlack, and Y. Bellouard, "Optical classification of algae species with a glass lab-on-a-chip," *Lab on a Chip*, vol. 12, no. 8, p. 1527, 2012.
- [48] F. He, Y. Liao, J. Lin, J. Song, L. Qiao, Y. Cheng, and K. Sugioka, "Femtosecond Laser Fabrication of Monolithically Integrated Microfluidic Sensors in Glass," *Sensors*, vol. 14, pp. 19402–19440, Oct. 2014.

- [49] E. Casamenti, G. Torun, L. Borasi, M. Lautenbacher, M. Bertrand, J. Faist, A. Mortensen, and Y. Bellouard, "Glass-in-glass infiltration for 3D micro-optical composite components," *Optics Express*, vol. 30, p. 13603, Apr. 2022.
- [50] K. Kumar, K. K. Lee, J. Li, J. Nogami, N. P. Kherani, and P. R. Herman, "Quantized structuring of transparent films with femtosecond laser interference," *Light: Science & Applications*, vol. 3, pp. e157–e157, Mar. 2014.
- [51] J. Bonse and J. Krüger, "Structuring of thin films by ultrashort laser pulses," *Applied Physics A*, vol. 129, p. 14, Jan. 2023.
- [52] V. Csajbók, L. Szikszai, B. J. Nagy, and P. Dombi, "Femtosecond damage resistance of femtosecond multilayer and hybrid mirrors," *Opt. Lett.*, vol. 41, p. 3527, Aug. 2016.
- [53] B. Mangote, L. Gallais, M. Commandré, M. Mende, L. Jensen, H. Ehlers, M. Jupé, D. Ristau, A. Melninkaitis, J. Mirauskas, V. Sirutkaitis, S. Kičas, T. Tolenis, and R. Drazdys, "Femtosecond laser damage resistance of oxide and mixture oxide optical coatings," *Opt. Lett.*, vol. 37, p. 1478, May 2012.
- [54] C. Shunli, Z. Yuan'an, H. Hongbo, and S. Jianda, "Effect of standing-wave field distribution on femosecond laser-induced damage of HfO₂/SiO₂ mirror coating," *Chin. Opt. Lett.*, vol. 9, no. 8, pp. 083101–83104, 2011.
- [55] I. B. Angelov, M. von Pechmann, M. K. Trubetskov, F. Krausz, and V. Pervak, "Optical breakdown of multilayer thin-films induced by ultrashort pulses at MHz repetition rates," *Optics Express*, vol. 21, p. 31453, Dec. 2013.
- [56] D. Schiltz, D. Patel, L. Emmert, C. Baumgarten, B. Reagan, W. Rudolph, J. J. Rocca, and C. S. Menoni, "Modification of multilayer mirror top-layer design for increased laser damage resistance," in *SPIE Laser Damage* (G. J. Exarhos, V. E. Gruzdev, J. A. Menapace, D. Ristau, and M. Soileau, eds.), (Boulder, Colorado, United States), p. 92371G, Dec. 2014.
- [57] D. Lifeng, F. Bo, L. Fengyu, and Z. Rongzhu, "Analysis on laser-induced transient damage behavior in multilayer coating," *Optics Communications*, vol. 358, pp. 120–125, Jan. 2016.
- [58] M. Chorel, T. Lanternier, É. Lavastre, N. Bonod, B. Bousquet, and J. Néauport, "Robust optimization of the laser induced damage threshold of dielectric mirrors for high power lasers," *Optics Express*, vol. 26, p. 11764, Apr. 2018.
- [59] Y. Chai, M. Zhu, H. Wang, H. Xing, Y. Cui, J. Sun, K. Yi, and J. Shao, "Laser-resistance sensitivity to substrate pit size of multilayer coatings," *Sci Rep*, vol. 6, p. 27076, July 2016.
- [60] A. A. Kozlov, J. C. Lambropoulos, J. B. Oliver, B. N. Hoffman, and S. G. Demos, "Mechanisms of picosecond laser-induced damage in common multilayer dielectric coatings," *Scientific Reports*, vol. 9, p. 607, Dec. 2019.

Bibliography

- [61] L. Gallais, X. Cheng, and Z. Wang, "Influence of nodular defects on the laser damage resistance of optical coatings in the femtosecond regime," *Opt. Lett.*, vol. 39, p. 1545, Mar. 2014.
- [62] J. E. Wolfe, S. R. Qiu, and C. J. Stolz, "Fabrication of mitigation pits for improving laser damage resistance in dielectric mirrors by femtosecond laser machining," *Applied Optics*, vol. 50, p. C457, Mar. 2011.
- [63] L. Gallais, B. Mangote, M. Commandré, A. Melninkaitis, J. Mirauskas, M. Jeskevic, and V. Sirutkaitis, "Transient interference implications on the subpicosecond laser damage of multidiellectrics," *Appl. Phys. Lett.*, vol. 97, p. 051112, Aug. 2010.
- [64] G. Long and Y. Zhang, "Fabrication and damage characteristics of low stress HR films for femtosecond laser system," in *Second Symposium on Novel Technology of X-Ray Imaging* (P. Liu, Y. Tian, and T. Xiao, eds.), (Hefei, China), p. 65, SPIE, May 2019.
- [65] D. Lifeng, Z. Xiaobing, and Z. Rongzhu, "The thermal-stress accumulation in anti-reflective coatings with multi-pulse laser irradiation," *Optics Communications*, vol. 350, pp. 263–269, Sept. 2015.
- [66] J. Joannopoulos, S. G. Johnson, J. N. Winn, and R. D. Meade, *Photonic Crystals, Molding the Flow of Light*. Princeton University Press, 2007.
- [67] P. Yeh, *Optical Waves in Layered Media*. J. Wiley and Sons, 1988.
- [68] D. P. Banks, K. Kaur, and R. W. Eason, "Influence of optical standing waves on the femtosecond laser-induced forward transfer of transparent thin films," *Appl. Opt.*, vol. 48, p. 2058, Apr. 2009.
- [69] Y. Wang, Y. Zhao, J. Shao, and Z. Fan, "Effect of native defects and laser-induced defects on multi-shot laser-induced damage in multilayer mirrors," *Chinese Optics Letters*, vol. 9, no. 9, pp. 093102–93105, 2011.
- [70] G. Abromavicius, R. Buzelis, R. Drazdys, A. Melninkaitis, and V. Sirutkaitis, "Influence of electric field distribution on laser induced damage threshold and morphology of high reflectance optical coatings," in *Boulder Damage Symposium XXXIX: Annual Symposium on Optical Materials for High Power Lasers* (G. J. Exarhos, A. H. Guenther, K. L. Lewis, D. Ristau, M. J. Soileau, and C. J. Stolz, eds.), (Boulder, CO), p. 67200Y, Oct. 2007.
- [71] K. Bronnikov, A. Dostovalov, A. Cherepakhin, E. Mitsai, A. Nepomniaschii, S. A. Kulinich, A. Zhizhchenko, and A. Kuchmizhak, "Large-Scale and Localized Laser Crystallization of Optically Thick Amorphous Silicon Films by Near-IR Femtosecond Pulses," *Materials*, vol. 13, p. 5296, Nov. 2020.
- [72] K. N. Astankova, A. S. Kozhukhov, G. K. Krivyakin, Y. A. Zhivodkov, D. V. Sheglov, and V. A. Volodin, "Interaction of low-fluence femtosecond laser pulses with a composite layer containing Ge nanoclusters: A novel type of nanofoam formation," *Journal of Laser Applications*, vol. 34, p. 022002, May 2022.

- [73] V. Volodin, Y. Cheng, A. Bulgakov, Y. Levy, J. Beránek, S. Nagisetty, M. Zukerstein, A. Popov, and N. Bulgakova, "Single-shot selective femtosecond and picosecond infrared laser crystallization of an amorphous Ge/Si multilayer stack," *Optics & Laser Technology*, vol. 161, p. 109161, June 2023.
- [74] S. E. Ahmed, V. M. Poole, J. Igo, Y. Gu, and M. D. McCluskey, "Localized phase transition of TiO₂ thin films induced by sub-bandgap laser irradiation," *Journal of Vacuum Science & Technology A*, vol. 39, p. 053402, Sept. 2021.
- [75] B. Zhang, D. Tan, X. Liu, L. Tong, P. G. Kazansky, and J. Qiu, "Self-Organized Periodic Crystallization in Unconventional Glass Created by an Ultrafast Laser for Optical Attenuation in the Broadband Near-Infrared Region," *Advanced Optical Materials*, vol. 7, p. 1900593, Oct. 2019.
- [76] Y. Liu, B. Zhu, L. Wang, Y. Dai, H. Ma, G. Lakshminarayana, and J. Qiu, "Femtosecond laser direct writing of TiO₂ crystalline patterns in glass," *Applied Physics B*, vol. 93, pp. 613–617, Nov. 2008.
- [77] M. Hébert, L. Simonot, and S. Mazauric, "Matrix method to predict the spectral reflectance of stratified surfaces including thick layers and thin films," p. 21, 2015.
- [78] C. C. Katsidis and D. I. Siapkas, "General transfer-matrix method for optical multilayer systems with coherent, partially coherent, and incoherent interference," *Applied Optics*, vol. 41, p. 3978, July 2002.
- [79] C. L. Mitsas and D. I. Siapkas, "Generalized matrix method for analysis of coherent and incoherent reflectance and transmittance of multilayer structures with rough surfaces, interfaces, and finite substrates," *Applied Optics*, vol. 34, p. 1678, Apr. 1995.
- [80] S. Tjörnhammar, V. Pasiskevicius, and F. Laurell, "Numerical modeling and determination of limiting powers for volume Bragg gratings used in lasers for spectral control," *Journal of the Optical Society of America B*, vol. 30, p. 2326, Aug. 2013.
- [81] M. Born, E. Wolf, A. B. Bhatia, P. C. Clemmow, D. Gabor, A. R. Stokes, A. M. Taylor, P. A. Wayman, and W. L. Wilcock, *Principles of Optics: Electromagnetic Theory of Propagation, Interference and Diffraction of Light*. Cambridge University Press, 7 ed., 1999.
- [82] L. N. Acquaroli, "Matrix method for thin film optics," *arXiv:1809.07708 [physics]*, Sept. 2018.
- [83] A. F. Oskooi, D. Roundy, M. Ibanescu, P. Bermel, J. Joannopoulos, and S. G. Johnson, "Meep: A flexible free-software package for electromagnetic simulations by the FDTD method," *Computer Physics Communications*, vol. 181, pp. 687–702, Mar. 2010.
- [84] A. Taflove and S. C. Hagness, *Computational Electrodynamics: The Finite-Difference Time-Domain Method*. Artech House Antennas and Propagation Library, Boston: Artech House, 3rd ed ed., 2005.

Bibliography

- [85] Kane Yee, "Numerical solution of initial boundary value problems involving maxwell's equations in isotropic media," *IEEE Transactions on Antennas and Propagation*, vol. 14, pp. 302–307, May 1966.
- [86] J. R. DeVore, "Refractive indices of rutile and sphalerite," *J. Opt. Soc. Am.*, vol. 41, pp. 416–419, Jun 1951.
- [87] F. L. Pedrotti, L. M. Pedrotti, and L. S. Pedrotti, *Introduction to Optics*. Cambridge University Press, 3 ed., 2017.
- [88] P. Kabaciński, T. M. Kardaś, Y. Stepanenko, and C. Radzewicz, "Nonlinear refractive index measurement by SPM-induced phase regression," *Optics Express*, vol. 27, p. 11018, Apr. 2019.
- [89] K. Ikeda, R. E. Saperstein, N. Alic, and Y. Fainman, "Thermal and Kerr nonlinear properties of plasma-deposited silicon nitride/ silicon dioxide waveguides," *Optics Express*, vol. 16, p. 12987, Aug. 2008.
- [90] K. Shtyrkova, *Characterization of Third Order Nonlinearities in TiO₂ Waveguides at 1550 Nm*. PhD thesis, MIT, Cambridge, MA, USA, 2013.
- [91] <https://refractiveindex.info/?shelf=main&book=Nb2O5&page=Lemarchand>. Index of Nb₂O₅, based on Lemarchand 2013. Accessed: 2022-11-01.
- [92] M. Al-Kuhaili, "Optical properties of hafnium oxide thin films and their application in energy-efficient windows," *Optical Materials*, vol. 27, pp. 383–387, Dec. 2004.
- [93] R. Boidin, T. Halenkovič, V. Nazabal, L. Beneš, and P. Němec, "Pulsed laser deposited alumina thin films," *Ceramics International*, vol. 42, pp. 1177–1182, Jan. 2016.
- [94] K. Luke, Y. Okawachi, M. R. E. Lamont, A. L. Gaeta, and M. Lipson, "Broadband mid-infrared frequency comb generation in a si₃n₄ microresonator," *Optics Letters*, vol. 40, p. 4823, Nov. 2015.
- [95] Y. Nigara, "Measurement of the Optical Constants of Yttrium Oxide," *Japanese Journal of Applied Physics*, vol. 7, pp. 404–408, Apr. 1968.
- [96] T. N. Nunley, N. S. Fernando, N. Samarasingha, J. M. Moya, C. M. Nelson, A. A. Medina, and S. Zollner, "Optical constants of germanium and thermally grown germanium dioxide from 0.5 to 6.6eV via a multisample ellipsometry investigation," *Journal of Vacuum Science & Technology B, Nanotechnology and Microelectronics: Materials, Processing, Measurement, and Phenomena*, vol. 34, p. 061205, Nov. 2016.
- [97] L. V. Rodríguez-de Marcos, J. I. Larruquert, J. A. Méndez, and J. A. Aznárez, "Self-consistent optical constants of SiO₂ and Ta₂O₅ films," *Optical Materials Express*, vol. 6, p. 3622, Nov. 2016.

- [98] L. V. Rodríguez-de Marcos, J. I. Larruquert, J. A. Méndez, and J. A. Aznárez, "Self-consistent optical constants of MgF₂, LaF₃, and CeF₃ films," *Optical Materials Express*, vol. 7, p. 989, Mar. 2017.
- [99] T. Siefke, S. Kroker, K. Pfeiffer, O. Puffky, K. Dietrich, D. Franta, I. Ohlídal, A. Szeghalmi, E.-B. Kley, and A. Tünnermann, "Materials Pushing the Application Limits of Wire Grid Polarizers further into the Deep Ultraviolet Spectral Range," *Advanced Optical Materials*, vol. 4, pp. 1780–1786, Nov. 2016.
- [100] D. L. Wood and K. Nassau, "Refractive index of cubic zirconia stabilized with yttria," *Applied Optics*, vol. 21, p. 2978, Aug. 1982.
- [101] <https://www.azom.com/properties.aspx?ArticleID=52>. Accessed: 2023-03-15.
- [102] <https://accuratus.com/alumox.html>. Accessed: 2023-03-15.
- [103] <https://progs.coudert.name/elate/mp?query=mp-470>. Accessed: 2023-03-15.
- [104] <https://www.americanelements.com/hafnium-oxide-12055-23-1>. Accessed: 2023-03-15.
- [105] <https://progs.coudert.name/elate/mp?query=mp-352>. Accessed: 2023-03-15.
- [106] https://www.heraeus.com/en/hca/fused_silica_quartz_knowledge_base_1/properties_1/properties_hca.html#tabs-608478-5. Accessed: 2023-03-15.
- [107] <https://www.azom.com/properties.aspx?ArticleID=1179>. Accessed: 2023-03-15.
- [108] https://materials.springer.com/googlecdn/assets/sm_lbs/743/sm_lbs_978-3-540-31361-8_160/sm_lbs_978-3-540-31361-8_160.pdf?trackRequired=true&originUrl=/lb/docs/sm_lbs_978-3-540-31361-8_160. Accessed: 2023-03-15.
- [109] <https://www.azom.com/properties.aspx?ArticleID=133>. Accessed: 2023-03-15.
- [110] M. R. Abernathy, J. Hough, I. W. Martin, S. Rowan, M. Oyen, C. Linn, and J. E. Faller, "Investigation of the Young's modulus and thermal expansion of amorphous titania-doped tantala films," *Applied Optics*, vol. 53, p. 3196, May 2014.
- [111] <https://www.azom.com/properties.aspx?ArticleID=53>. Accessed: 2023-03-15.
- [112] <https://www.cascryst.com/product/detail/22?title=MgF2>. Accessed: 2023-03-15.
- [113] <https://www.crystran.co.uk/optical-materials/magnesium-fluoride-mgf2>. Accessed: 2023-03-15.
- [114] <https://www.coorstek.com/en/materials/technical-ceramics/specialty/yttria/>. Accessed: 2023-03-15.
- [115] K. Kamiya and S. Sakka, "Thermal expansion of TiO₂/SiO₂ and TiO₂/GeO₂ glasses," *Journal of Non-Crystalline Solids*, vol. 52, pp. 357–363, Dec. 1982.

Bibliography

- [116] W. R. Manning, O. Hunter, F. W. Calderwood, and D. W. Stacy, "Thermal Expansion of Nb₂O₅," *Journal of the American Ceramic Society*, vol. 55, pp. 342–347, July 1972.
- [117] O. B. Shcherbina, M. N. Palatnikov, and V. V. Efremov, "Mechanical properties of Nb₂O₅ and Ta₂O₅ prepared by different procedures," *Inorganic Materials*, vol. 48, pp. 433–438, Apr. 2012.
- [118] O. Yeheskel and O. Tevet, "Elastic Moduli of Transparent Ytria," *Journal of the American Ceramic Society*, vol. 82, pp. 136–144, Dec. 2004.
- [119] S. Rajesh and Y. Bellouard, "Towards fast femtosecond laser micromachining of fused silica: The effect of deposited energy," *Opt. Express*, vol. 18, p. 21490, Sept. 2010.
- [120] G. Torun, T. Kishi, and Y. Bellouard, "Direct-write laser-induced self-organization and metallization beyond the focal volume in tellurite glass," *Phys. Rev. Materials*, vol. 5, p. 055201, May 2021.
- [121] B. E. A. Saleh and M. C. Teich, *Fundamentals of photonics; 1st ed.* Wiley series in pure and applied optics, New York, NY: Wiley, 1991.
- [122] S. Aryal, "Electron microscope- definition, principle, types, uses, labeled diagram," 2022.
- [123] W. Zhou, R. Apkarian, Z. L. Wang, and D. Joy, "Fundamentals of scanning electron microscopy (SEM)," in *Scanning Microscopy for Nanotechnology: Techniques and Applications* (W. Zhou and Z. L. Wang, eds.), pp. 1–40, New York, NY: Springer New York, 2007.
- [124] L. Reimer and H. Kohl, *Transmission Electron Microscopy: Physics of Image Formation*. No. 36 in Springer Series in Optical Sciences, New York, NY: Springer, 5th ed ed., 2008.
- [125] H. Demers, N. Poirier-Demers, A. R. Couture, D. Joly, M. Guilmain, N. de Jonge, and D. Drouin, "Three-dimensional electron microscopy simulation with the CASINO Monte Carlo software," *Scanning*, vol. 33, pp. 135–146, May 2011.
- [126] F. Krumeich, "Introduction into Transmission and Scanning Transmission Electron Microscopy," p. 55, 2022.
- [127] B. Cullity, *Elements of X-ray diffraction, 2nd ed.* Addison-Wesley series in metallurgy and materials, Reading, MA: Addison-Wesley Publishing Company, 1978.
- [128] L. A. Giannuzzi and F. A. Stevie, eds., *Introduction to Focused Ion Beams: Instrumentation, Theory, Techniques, and Practice*. New York: Springer, 2005.
- [129] R. Wirth, "Focused Ion Beam (FIB) combined with SEM and TEM: Advanced analytical tools for studies of chemical composition, microstructure and crystal structure in geomaterials on a nanometre scale," *Chemical Geology*, vol. 261, pp. 217–229, Apr. 2009.

- [130] R. Ricca, V. Boureau, and Y. Bellouard, "Ultrafast laser interaction with transparent multi-layer $\text{SiO}_2/\text{Si}_3\text{N}_4$ films," *Journal of Applied Physics*, vol. 130, p. 243105, Dec. 2021.
- [131] L. Yu, E. Barakat, T. Sfez, L. Hvozdar, J. Di Francesco, and H. Peter Herzig, "Manipulating Bloch surface waves in 2D: A platform concept-based flat lens," *Light Sci Appl*, vol. 3, pp. e124–e124, Jan. 2014.
- [132] J. H. Parker, D. W. Feldman, and M. Ashkin, "Raman Scattering by Silicon and Germanium," *Phys. Rev.*, vol. 155, pp. 712–714, Mar. 1967.
- [133] Y. Kang, Y. Qiu, Z. Lei, and M. Hu, "An application of Raman spectroscopy on the measurement of residual stress in porous silicon," *Optics and Lasers in Engineering*, vol. 43, pp. 847–855, Aug. 2005.
- [134] J. F. Cannon, "Behavior of the elements at high pressures," *Journal of Physical and Chemical Reference Data*, vol. 3, no. 3, pp. 781–824, 1974.
- [135] P. Serra and A. Piqué, "Laser-Induced Forward Transfer: Fundamentals and Applications," *Adv. Mater. Technol.*, vol. 4, p. 1800099, Jan. 2019.
- [136] D. Toet, M. O. Thompson, P. M. Smith, and T. W. Sigmon, "Laser-assisted transfer of silicon by explosive hydrogen release," *Appl. Phys. Lett.*, vol. 74, pp. 2170–2172, Apr. 1999.
- [137] A. Narazaki, T. Sato, R. Kurosaki, Y. Kawaguchi, and H. Niino, "Nano- and Microdot Array Formation of FeSi_2 by Nanosecond Excimer Laser-Induced Forward Transfer," *Appl. Phys. Express*, vol. 1, p. 057001, Apr. 2008.
- [138] A. Iqbal, W. B. Jackson, C. C. Tsai, J. W. Allen, and C. W. Bates, "Electronic structure of silicon nitride and amorphous silicon/silicon nitride band offsets by electron spectroscopy," *Journal of Applied Physics*, vol. 61, pp. 2947–2954, Apr. 1987.
- [139] N. Nikolaou, P. Dimitrakis, P. Normand, D. Skarlatos, K. Giannakopoulos, K. Mergia, V. Ioannou-Sougleridis, K. Kukli, J. Niinistö, K. Mizohata, M. Ritala, and M. Leskelä, "Inert ambient annealing effect on MANOS capacitor memory characteristics," *Nanotechnology*, vol. 26, p. 134004, Mar. 2015.
- [140] S. Y. Vetrov, R. G. Bikbaev, N. V. Rudakova, K.-P. Chen, and I. V. Timofeev, "Optical Tamm states at the interface between a photonic crystal and an epsilon-near-zero nanocomposite," *J. Opt.*, vol. 19, p. 085103, Aug. 2017.
- [141] Y. Liao, J. Ni, L. Qiao, M. Huang, Y. Bellouard, K. Sugioka, and Y. Cheng, "High-fidelity visualization of formation of volume nanogratings in porous glass by femtosecond laser irradiation," *Optica*, vol. 2, p. 329, Apr. 2015.

Bibliography

- [142] A. Rudenko, J.-P. Colombier, and T. E. Itina, “From random inhomogeneities to periodic nanostructures induced in bulk silica by ultrashort laser,” *Phys. Rev. B*, vol. 93, p. 075427, Feb. 2016.
- [143] R. Ricca and Y. Bellouard, “Single-Layer Subwavelength Femtosecond-Laser-Induced Confined Nanocrystallization in Multistack Dielectrics,” *Physical Review Applied*, vol. 19, p. 044035, Apr. 2023.
- [144] E. N. Glezer and E. Mazur, “Ultrafast-laser driven micro-explosions in transparent materials,” *Applied Physics Letters*, vol. 71, pp. 882–884, Aug. 1997.
- [145] S. Juodkazis, K. Nishimura, S. Tanaka, H. Misawa, E. G. Gamaly, B. Luther-Davies, L. Hallo, P. Nicolai, and V. T. Tikhonchuk, “Laser-Induced Microexplosion Confined in the Bulk of a Sapphire Crystal: Evidence of Multimegabar Pressures,” *Phys. Rev. Lett.*, vol. 96, p. 166101, Apr. 2006.
- [146] M. Mero, J. Liu, W. Rudolph, D. Ristau, and K. Starke, “Scaling laws of femtosecond laser pulse induced breakdown in oxide films,” *Physical Review B*, vol. 71, p. 115109, Mar. 2005.
- [147] F. Kong, S. Chen, S. Liu, Y. Jin, H. Guan, Y. Du, C. Wei, H. He, and K. Yi, “Laser-induced damage of multilayer dielectric for broadband pulse compression grating,” in *Pacific Rim Laser Damage Symposium: Optical Materials for High Power Lasers* (J. Shao, ed.), (Shanghai, China), p. 82060P, Nov. 2011.
- [148] A. V. Kavokin, I. A. Shelykh, and G. Malpuech, “Lossless interface modes at the boundary between two periodic dielectric structures,” *Physical Review B*, vol. 72, p. 233102, Dec. 2005.
- [149] C. Schmidt, A. Palatnik, M. Sudzius, S. Meister, and K. Leo, “Coupled topological interface states,” *Physical Review B*, vol. 103, p. 085412, Feb. 2021.
- [150] Y. Barad, H. Eisenberg, M. Horowitz, and Y. Silberberg, “Nonlinear scanning laser microscopy by third harmonic generation,” *Applied Physics Letters*, vol. 70, pp. 922–924, Feb. 1997.
- [151] T. Y. F. Tsang, “Optical third-harmonic generation at interfaces,” *Physical Review A*, vol. 52, pp. 4116–4125, Nov. 1995.
- [152] B. Weigelin, G.-J. Bakker, and P. Friedl, “Third harmonic generation microscopy of cells and tissue organization,” *Journal of Cell Science*, p. jcs.152272, Jan. 2016.
- [153] Müller, Squier, Wilson, and Brakenhoff, “3D microscopy of transparent objects using third-harmonic generation,” *Journal of Microscopy*, vol. 191, no. 3, pp. 266–274, 1998.
- [154] J. A. Squier and M. Müller, “Third-harmonic generation imaging of laser-induced breakdown in glass,” *Applied Optics*, vol. 38, no. 27, 1999.

- [155] C. B. Schaffer, J. Aus der Au, E. Mazur, and J. A. Squier, "Micromachining and material change characterization using femtosecond laser oscillators," in *High-Power Lasers and Applications* (G. S. Edwards, J. Neev, A. Ostendorf, and J. C. Sutherland, eds.), (San Jose, California, United States), p. 112, Apr. 2002.
- [156] O. Bernard, A. Kraxner, A. Boukhayma, C.ENZ, Y. Bellouard, and J. Squier, "Third-harmonic generation monitoring of femtosecond laser-induced in-volume functional modifications," *Optica*, 2023.
- [157] D.-W. Kim, N. Enomoto, Z.-e. Nakagawa, and K. Kawamura, "Molecular dynamic simulation in titanium dioxide polymorphs: Rutile, brookite, and anatase," *Journal of the American Ceramic Society*, vol. 79, no. 4, pp. 1095–1099, 1996.
- [158] R. Verma, J. Gangwar, and A. K. Srivastava, "Multiphase TiO₂ nanostructures: A review of efficient synthesis, growth mechanism, probing capabilities, and applications in bio-safety and health," *RSC Advances*, vol. 7, no. 70, pp. 44199–44224, 2017.
- [159] S. Zhang, C. Menoni, V. Gruzdev, and E. Chowdhury, "Ultrafast Laser Material Damage Simulation—A New Look at an Old Problem," *Nanomaterials*, vol. 12, p. 1259, Apr. 2022.
- [160] D. A. H. Hanaor and C. C. Sorrell, "Review of the anatase to rutile phase transformation," *Journal of Materials Science*, vol. 46, pp. 855–874, Feb. 2011.
- [161] M. R. Ranade, A. Navrotsky, H. Z. Zhang, J. F. Banfield, S. H. Elder, A. Zaban, P. H. Borse, S. K. Kulkarni, G. S. Doran, and H. J. Whitfield, "Energetics of nanocrystalline TiO₂," *Proceedings of the National Academy of Sciences*, vol. 99, pp. 6476–6481, Apr. 2002.
- [162] S. J. Smith, R. Stevens, S. Liu, G. Li, A. Navrotsky, J. Boerio-Goates, and B. F. Woodfield, "Heat capacities and thermodynamic functions of TiO₂ anatase and rutile: Analysis of phase stability," *American Mineralogist*, vol. 94, pp. 236–243, Feb. 2009.
- [163] R. Ricca, V. Boureau, and Y. Bellouard, "Influence of ionization and cumulative effects on laser-induced crystallization in multilayer dielectrics," in preparation, 2023.
- [164] C. B. Schaffer, A. Brodeur, J. F. García, and E. Mazur, "Micromachining bulk glass by use of femtosecond laser pulses with nanojoule energy," *Optics Letters*, vol. 26, p. 93, Jan. 2001.
- [165] S. M. Eaton, H. Zhang, P. R. Herman, F. Yoshino, L. Shah, J. Bovatsek, and A. Y. Arai, "Heat accumulation effects in femtosecond laser-written waveguides with variable repetition rate," *Optics Express*, vol. 13, no. 12, p. 4708, 2005.
- [166] J. Kischkat, S. Peters, B. Gruska, M. Semtsiv, M. Chashnikova, M. Klinkmüller, O. Fedosenko, S. Machulik, A. Aleksandrova, G. Monastyrskiy, Y. Flores, and W. Ted Masselink, "Mid-infrared optical properties of thin films of aluminum oxide, titanium dioxide, silicon dioxide, aluminum nitride, and silicon nitride," *Applied Optics*, vol. 51, p. 6789, Oct. 2012.

Bibliography

- [167] E. F. Rauch and L. Dupuy, "Rapid Diffraction Patterns identification through template matching," *Archives of Metallurgy and Materials*, vol. 50, pp. 87–89, 2005.
- [168] D. Viladot, M. Véron, M. Gemmi, F. Peiró, J. Portillo, S. Estradé, J. Mendoza, N. Llorca-Isern, and S. Nicolopoulos, "Orientation and phase mapping in the transmission electron microscope using precession-assisted diffraction spot recognition: State-of-the-art results: REVIEW OF PACOM (ASTAR) APPLICATION," *Journal of Microscopy*, vol. 252, pp. 23–34, Oct. 2013.
- [169] Á. K. Kiss, E. F. Rauch, and J. L. Lábár, "Highlighting material structure with transmission electron diffraction correlation coefficient maps," *Ultramicroscopy*, vol. 163, pp. 31–37, 2016.
- [170] J. Z. Jiang, F. Kragh, D. J. Frost, K. StÅhl, and H. Lindelov, "Hardness and thermal stability of cubic silicon nitride," *Journal of Physics: Condensed Matter*, vol. 13, pp. L515–L520, June 2001.
- [171] V. Klosek, "Crystallographic textures," *EPJ Web of Conferences*, vol. 155, p. 00005, 2017.
- [172] H.-J. Bunge, *Texture Analysis in Materials Science: Mathematical Methods*. London ; Boston: Butterworths, english ed ed., 1982.
- [173] D. de Faoite, D. J. Browne, F. R. Chang-Díaz, and K. T. Stanton, "A review of the processing, composition, and temperature-dependent mechanical and thermal properties of dielectric technical ceramics," *Journal of Materials Science*, vol. 47, pp. 4211–4235, May 2012.
- [174] V. AstaÅauskas, A. Bellissimo, P. Kuksa, C. Tomastik, H. Kalbe, and W. S. Werner, "Optical and electronic properties of amorphous silicon dioxide by single and double electron spectroscopy," *Journal of Electron Spectroscopy and Related Phenomena*, vol. 241, p. 146829, May 2020.
- [175] S.-Y. Ren and W. Y. Ching, "Electronic structures of β - and α -silicon nitride," *Physical Review B*, vol. 23, pp. 5454–5463, May 1981.
- [176] I. H. Malitson, "Interspecimen comparison of the refractive index of fused silica*,†," *J. Opt. Soc. Am.*, vol. 55, pp. 1205–1209, Oct 1965.
- [177] Y.-N. Xu and W. Y. Ching, "Electronic structure and optical properties of α and β phases of silicon nitride, silicon oxynitride, and with comparison to silicon dioxide," *Physical Review B*, vol. 51, pp. 17379–17389, June 1995.
- [178] K. F. Young and H. P. R. Frederikse, "Compilation of the Static Dielectric Constant of Inorganic Solids," *Journal of Physical and Chemical Reference Data*, vol. 2, no. 2, 1973.
- [179] A. Jain, S. P. Ong, G. Hautier, W. Chen, W. D. Richards, S. Dacek, S. Cholia, D. Gunter, D. Skinner, G. Ceder, and K. A. Persson, "Commentary: The Materials Project: A materials

- genome approach to accelerating materials innovation,” *APL Materials*, vol. 1, p. 011002, July 2013.
- [180] D. R. Lide, G. Baysinger, S. Chemistry, L. I. Berger, R. N. Goldberg, and H. V. Kehiaian, *CRC Handbook of Chemistry and Physics*. CRC Press, 2005.
- [181] S. Pramanik, A. Manna, A. Tripathy, and K. K. Kar, “Current Advancements in Ceramic Matrix Composites,” in *Composite Materials* (K. K. Kar, ed.), pp. 457–496, Berlin, Heidelberg: Springer Berlin Heidelberg, 2017.
- [182] B. Champagnon, V. Martinez, C. Martinet, R. Le Parc, and C. Levelut, “Density and density fluctuations anomalies of SiO₂ glass: Comparison and light-scattering study,” *Philosophical Magazine*, vol. 87, pp. 691–695, Jan. 2007.
- [183] P. Richet, “GeO₂ vs SiO₂: Glass transitions and thermodynamic properties of polymorphs,” *Physics and Chemistry of Minerals*, vol. 17, pp. 79–88, Jan. 1990.
- [184] T. Lube and J. Dusza, “A silicon nitride reference material—A testing program of ESIS TC6,” *Journal of the European Ceramic Society*, vol. 27, pp. 1203–1209, Jan. 2007.
- [185] T. Rouxel, “High Temperature Mechanical Behavior of Silicon Nitride Ceramics,” *Journal of the Ceramic Society of Japan*, vol. 109, no. 1270, pp. S89–S97, 2001.
- [186] L. S. Parfen’eva, N. F. Kartenko, B. I. Smirnov, I. A. Smirnov, D. Singh, K. C. Goretta, H. Misiorek, J. Mucha, D. Wlosewicz, A. Jezowski, and A. I. Krivchikov, “Thermal conductivity and heat capacity of Si₃N₄/BN fiber monoliths,” *Physics of the Solid State*, vol. 51, pp. 2274–2281, Nov. 2009.
- [187] H. Ftouni, C. Blanc, D. Tainoff, A. D. Fefferman, M. Defoort, K. J. Lulla, J. Richard, E. Collin, and O. Bourgeois, “Thermal conductivity of silicon nitride membranes is not sensitive to stress,” *Physical Review B*, vol. 92, p. 125439, Sept. 2015.
- [188] A. P. Chojnacka, C. T. Avedisian, and A. Rendtel, “The thermal diffusivity of silicon nitride/silicon carbide nanocomposites using a photothermal deflection technique,” *Proceedings of the Royal Society of London. Series A: Mathematical, Physical and Engineering Sciences*, vol. 455, pp. 2781–2802, Aug. 1999.
- [189] C. Clauser, “8.1 The Earth’s thermal regime,” in *Renewable Energy* (K. Heinloth, ed.), vol. 3C, pp. 493–548, Springer Berlin Heidelberg, 2006.
- [190] O. Koszor, A. Lindemann, F. Davin, and C. Balázs, “Observation of Thermophysical and Tribological Properties of CNT Reinforced Si₃N₄,” *Key Engineering Materials*, vol. 409, pp. 354–357, Mar. 2009.
- [191] M. Shimizu, M. Sakakura, M. Ohnishi, Y. Shimotsuma, T. Nakaya, K. Miura, and K. Hirao, “Mechanism of heat-modification inside a glass after irradiation with high-repetition rate femtosecond laser pulses,” *Journal of Applied Physics*, vol. 108, p. 073533, Oct. 2010.

Bibliography

- [192] J. Cao, M. Lancry, F. Brisset, L. Mazerolles, R. Saint-Martin, and B. Pommellec, "Femtosecond Laser-Induced Crystallization in Glasses: Growth Dynamics for Orientable Nanostructure and Nanocrystallization," *Crystal Growth and Design*, vol. 19, pp. 2189–2205, Apr. 2019.
- [193] M. Cavillon, J. Cao, M. Vallet, F. Brisset, L. Mazerolles, B. Dkhil, M. Lancry, and B. Pommellec, "Thermal and Electron Plasma Effects on Phase Separation Dynamics Induced by Ultrashort Laser Pulses," *Crystals*, vol. 12, p. 496, Apr. 2022.
- [194] X. He, Q. Liu, M. Lancry, F. Brisset, and B. Pommellec, "Space-Selective Control of Functional Crystals by Femtosecond Laser: A Comparison between SrO-TiO₂-SiO₂ and Li₂O-Nb₂O₅-SiO₂ Glasses," *Crystals*, vol. 10, p. 979, Oct. 2020.
- [195] E. Muzi, M. Cavillon, M. Lancry, F. Brisset, R. Que, D. Pugliese, D. Janner, and B. Pommellec, "Towards a Rationalization of Ultrafast Laser-Induced Crystallization in Lithium Niobium Borosilicate Glasses: The Key Role of the Scanning Speed," *Crystals*, vol. 11, p. 290, Mar. 2021.
- [196] T. Komatsu and T. Honma, "Laser patterning and growth mechanism of orientation designed crystals in oxide glasses: A review," *Journal of Solid State Chemistry*, vol. 275, pp. 210–222, July 2019.
- [197] S. V. Lotarev, A. S. Lipatiev, T. O. Lipateva, E. V. Lopatina, and V. N. Sigaev, "Ultrafast Laser-Induced Crystallization of Lead Germanate Glass," *Crystals*, vol. 11, p. 193, Feb. 2021.
- [198] R. C. Dante and C. Kajdas, "A review and a fundamental theory of silicon nitride tribochemistry," *Wear*, vol. 288, pp. 27–38, May 2012.
- [199] D. Chen and B.-H. Yu, "Pressure-induced phase transition in silicon nitride material," *Chinese Physics B*, vol. 22, p. 023104, Feb. 2013.
- [200] Y. Li, L. Wang, S. Yin, F. Yang, and P. Wu, "Rapid Crystallization Process of Amorphous Silicon Nitride," *Journal of the American Ceramic Society*, vol. 94, pp. 4169–4173, Dec. 2011.
- [201] N. Jehanathan, M. Saunders, Y. Liu, and J. Dell, "Crystallization of silicon nitride thin films synthesized by plasma-enhanced chemical vapour deposition," *Scripta Materialia*, vol. 57, pp. 739–742, Oct. 2007.
- [202] R. Riedel and M. Seher, "Crystallization behaviour of amorphous silicon nitride," *Journal of the European Ceramic Society*, vol. 7, pp. 21–25, Jan. 1991.
- [203] G. Gregori, R. Merkle, and J. Maier, "Ion conduction and redistribution at grain boundaries in oxide systems," *Progress in Materials Science*, vol. 89, pp. 252–305, Aug. 2017.

- [204] H. Yoshida, "Control of high temperature mass transport phenomena through grain boundaries in oxide ceramics based on grain boundary chemical composition and external electric field," *Journal of the Ceramic Society of Japan*, vol. 130, pp. 762–769, Sept. 2022.
- [205] N. L. Peterson, "Diffusion mechanisms and structural effects in grain boundaries," *Journal of Vacuum Science & Technology A: Vacuum, Surfaces, and Films*, vol. 4, pp. 3066–3070, Nov. 1986.
- [206] R. H. Willens, T. H. Geballe, A. C. Gossard, J. P. Maita, A. Menth, G. W. Hull, and R. R. Soden, "Superconductivity of Nb₃Al," *Solid State Communications*, vol. 7, pp. 837–841, June 1969.
- [207] C.-Y. Wu, H.-M. Lin, H.-F. Lin, M.-F. Tai, C.-R. Wang, C.-K. Lin, and P. Lee, "Preparation and characterization of nanocrystalline Nb₃Al alloy," *Scripta Materialia*, vol. 44, pp. 1967–1971, May 2001.
- [208] X. Wen, X. Li, H. Zhao, Z. Ma, L. Yu, C. Li, C. Liu, Q. Guo, and Y. Liu, "The phase formation mechanism of Nb₃Al prepared by mechanical alloying and subsequent sintering and its effect on superconducting properties," *Intermetallics*, vol. 103, pp. 33–39, Dec. 2018.
- [209] Z. Liu and B. Wang, "Comparative study on the strain-dependent mechanical and electronic properties of Nb₃Al and Nb₃Sn," *Materials Research Express*, vol. 8, p. 086001, Aug. 2021.
- [210] A. A. A. P. da Silva, G. C. Coelho, C. A. Nunes, J. M. Fiorani, N. David, and M. Vilasi, "Nb-Al Binary System: Reevaluation of the Solubility Limits of the (Nb), Nb₃Al, Nb₂Al and NbAl₃ Phases at High Temperatures," *Materials Research*, vol. 22, no. 5, p. e20190305, 2019.
- [211] T. Takeuchi, A. Kikuchi, N. Banno, H. Kitaguchi, Y. Iijima, K. Tagawa, K. Nakagawa, K. Tsuchiya, C. Mitsuda, N. Koizumi, and K. Okuno, "Status and perspective of the Nb₃Al development," *Cryogenics*, vol. 48, pp. 371–380, July 2008.
- [212] T. Takeuchi, "Nb₃Al conductors for high-field applications," *Superconductor Science and Technology*, vol. 13, pp. R101–R119, Sept. 2000.
- [213] H. Mostaan, F. Karimzadeh, and M. H. Abbasi, "Thermodynamic analysis of nanocrystalline and amorphous phase formation in Nb–Al system during mechanical alloying," *Powder Metallurgy*, vol. 55, pp. 142–147, Apr. 2012.
- [214] H. Sina and S. Iyengar, "Studies on the formation of aluminides in heated Nb–Al powder mixtures," *Journal of Alloys and Compounds*, vol. 628, pp. 9–19, Apr. 2015.
- [215] H. Naghiha, B. Movahedi, M. A. Asadabad, and M. T. Mournani, "Amorphization and nanocrystalline Nb₃Al intermetallic formation during mechanical alloying and subsequent annealing," *Advanced Powder Technology*, vol. 28, pp. 340–345, Feb. 2017.

Bibliography

- [216] T. Takeuchi, "Nb₃Al superconductors," *IEEE Transactions on Applied Superconductivity*, vol. 12, pp. 1088–1093, Mar. 2002.
- [217] H. Kumakura, K. Togano, K. Tachikawa, Y. Yamada, S. Murase, E. Nakamura, and M. Sasaki, "Synthesis of Nb₃Ga and Nb₃Al superconducting composites by laser beam irradiation," *Applied Physics Letters*, vol. 48, pp. 601–603, Mar. 1986.
- [218] H. Kumakura, K. Togano, K. Tachikawa, Y. Yamada, S. Murase, M. Sasaki, and E. Nakamura, "Nb₃Al and Nb₃(Al,Ge) composite tapes fabricated by CO₂ laser beam irradiation," *IEEE Transactions on Magnetics*, vol. 23, pp. 952–955, Mar. 1987.
- [219] W. Schaper, R. Bormann, and H. C. Freyhardt, "Laser processing of Nb₃Al(Ge, Si) high-field superconductors," *Journal of Applied Physics*, vol. 74, pp. 2686–2691, Aug. 1993.
- [220] D.-S. Chung, M. Enoki, and T. Kishi, "Microstructural analysis and mechanical properties of in situ Nb/Nb-aluminide layered materials," *Science and Technology of Advanced Materials*, vol. 3, pp. 129–135, Jan. 2002.
- [221] K. Barmak, K. R. Coffey, D. A. Rudman, and S. Foner, "Phase formation sequence for the reaction of multilayer thin films of nb/al," *Journal of Applied Physics*, vol. 67, no. 12, pp. 7313–7322, 1990.
- [222] A. Jain, S. P. Ong, G. Hautier, W. Chen, W. D. Richards, S. Dacek, S. Cholia, D. Gunter, D. Skinner, G. Ceder, and K. A. Persson, "Commentary: The Materials Project: A materials genome approach to accelerating materials innovation," *APL Materials*, vol. 1, p. 011002, July 2013. Data retrieved from the Materials Project for Al₂O₃ (mp-1245211) from database version v2022.10.28.
- [223] A. Jain, S. P. Ong, G. Hautier, W. Chen, W. D. Richards, S. Dacek, S. Cholia, D. Gunter, D. Skinner, G. Ceder, and K. A. Persson, "Commentary: The Materials Project: A materials genome approach to accelerating materials innovation," *APL Materials*, vol. 1, p. 011002, July 2013. Data retrieved from the Materials Project for Nb₂O₅ (mp-581967) from database version v2022.10.28.
- [224] R. Boidin, T. Halenkovič, V. Nazabal, L. Beneš, and P. Němec, "Pulsed laser deposited alumina thin films," *Ceramics International*, vol. 42, pp. 1177–1182, Jan. 2016.
- [225] M. N. Polyanskiy, "Refractive index database." <https://refractiveindex.info>. Accessed on 2023-01-26.
- [226] S. Gražulis, D. Chateigner, R. T. Downs, A. F. T. Yokochi, M. Quirós, L. Lutterotti, E. Manakova, J. Butkus, P. Moeck, and A. Le Bail, "Crystallography Open Database – an open-access collection of crystal structures," *Journal of Applied Crystallography*, vol. 42, pp. 726–729, Aug. 2009.

- [227] C. Nico, T. Monteiro, and M. Graça, “Niobium oxides and niobates physical properties: Review and prospects,” *Progress in Materials Science*, vol. 80, pp. 1–37, July 2016.
- [228] D. W. Zaidan, B. X. de Freitas, G. C. Coelho, C. A. Nunes, C. dos Santos, E. C. T. Ramos, and A. S. Ramos, “The 1300 °C Isothermal Section in the Al₂O₃-Y₂O₃-Nb₂O₅ System,” *Journal of Phase Equilibria and Diffusion*, vol. 43, pp. 393–400, June 2022.
- [229] S. Hammouti, B. Holybee, W. Zhu, J. P. Allain, B. Jurczyk, and D. N. Ruzic, “Titanium nitride formation by a dual-stage femtosecond laser process,” *Applied Physics A*, vol. 124, p. 411, June 2018.
- [230] J. Lehr, F. de Marchi, L. Matus, J. MacLeod, F. Rosei, and A.-M. Kietzig, “The influence of the gas environment on morphology and chemical composition of surfaces micro-machined with a femtosecond laser,” *Applied Surface Science*, vol. 320, pp. 455–465, Nov. 2014.
- [231] C. V. Raman and K. S. Krishnan, “The Negative Absorption of Radiation,” *Nature*, vol. 122, pp. 12–13, July 1928.
- [232] Z. Xu, Z. He, Y. Song, X. Fu, M. Rommel, X. Luo, A. Hartmaier, J. Zhang, and F. Fang, “Topic Review: Application of Raman Spectroscopy Characterization in Micro/Nano-Machining,” *Micromachines*, vol. 9, p. 361, July 2018.

Curriculum Vitae

Ruben Ricca
June 24th, 1992, Swiss citizen
ruben.ricca@alumni.epfl.ch

Education

- | | |
|-------------|---|
| 2019 - 2023 | PhD in Advanced Manufacturing, <i>Galatea Lab</i> , EPFL , Switzerland |
| 2016 - 2018 | Master in Materials Science and Engineering, EPFL , Switzerland
Master thesis at <i>Research Laboratory of Electronics</i> , MIT , USA |
| 2012 - 2015 | Bachelor in Materials Science and Engineering, EPFL , Switzerland |

Journal publications

- R. Ricca, V. Boureau and Y. Bellouard, *Influence of thermal relaxation on laser-induced modifications in multilayer dielectrics*, in preparation (2023)
- R. Ricca and Y. Bellouard, *Single layer, sub-wavelength, femtosecond laser-induced confined nano-crystallization in a multi-stack dielectrics*, *Physical Review Applied*, vol. 19, p.044035 (2023)
- R. Ricca, V. Boureau, Y. Bellouard, *Ultrafast laser interaction with transparent multi-layer SiO₂/Si₃N₄ films*, *J. Appl. Phys.* 130, 243105 (2021)
- J. Vukajlovic-Plestina, V. G. Dubrovskii, G. Tutuncuoglu, H. Potts, R. Ricca et al. *Molecular beam epitaxy of InAs nanowires in SiO₂ nanotube templates: challenges and prospects for integration of III-Vs on Si*, *Nanotechnology*, vol. 27, num. 45, p. 455601 (2016)

Patents

- R. Ricca, Y. Bellouard, M. Vetterli, *Non-volatile data storage medium and system*, EP22170715.1 (under examination).

Bibliography

Conferences

- 06.2023 LPM, Hirosaki - R. Ricca, Y. Bellouard, *Non-destructive interaction of femtosecond lasers with multilayered dielectrics*
- 06.2023 PULMM, Nikko, Poster presentation - R. Ricca, Y. Bellouard, *On the interaction of femtosecond lasers with layered dielectric structures*
- 02.2023 CIME Day, Lausanne - R. Ricca, V. Boureau, L. Navratilova, R. Therisod, Y. Bellouard, *Laser-induced crystallization in multilayer dielectrics*
- 06.2022 LPM, Dresden - R. Ricca, Y. Bellouard, *Thermal-regime dependence of laser-induced modifications in dielectric multi-layers*
- 05.2022 CLEO, S. José - R. Ricca, Y. Bellouard, *Femtosecond laser-induced confined nanocrystallization in dielectric multilayers*, DOI: 10.1364/CLEO_AT.2022.ATu4C.2
- 10.2021 ICALEO, Online conference - R. Ricca, Y. Bellouard, *Femtosecond laser-induced nano-crystallization in dielectric multilayer systems*
- 09.2021 Euromat, Online conference - R. Ricca, V. Boureau, Y. Bellouard, *Femtosecond laser-induced crystallization in sub-wavelength multilayer systems*
- 02.2020 Photonics West, S. Francisco - R. Ricca, Y. Bellouard, *Investigation of laser-matter interaction in transparent multilayer thin films*